

Photoproduction of Hydrogen by Decamethylruthenocene

THÈSE N° 7690 (2017)

PRÉSENTÉE LE 7 AVRIL 2017

À LA FACULTÉ DES SCIENCES DE BASE

LABORATOIRE D'ÉLECTROCHIMIE PHYSIQUE ET ANALYTIQUE

PROGRAMME DOCTORAL EN CHIMIE ET GÉNIE CHIMIQUE

ÉCOLE POLYTECHNIQUE FÉDÉRALE DE LAUSANNE

POUR L'OBTENTION DU GRADE DE DOCTEUR ÈS SCIENCES

PAR

Lucie Josette Renée RIVIER

acceptée sur proposition du jury:

Prof. J.-E. Moser, président du jury

Prof. H. Girault, directeur de thèse

Prof. M. Robert, rapporteur

Prof. R. Alberto, rapporteur

Prof. X. Hu, rapporteur



ÉCOLE POLYTECHNIQUE
FÉDÉRALE DE LAUSANNE

Suisse
2017

♪ *Don't stop, never give up*

Hold you head high and reach the top

Let the world see what you have got

Bring it all back to you ♪

S Club 7

Acknowledgements

First, I would like to acknowledge my thesis supervisor Prof. Hubert H. Girault who has welcomed me in the Laboratory of Physical Chemistry and Analytical Electrochemistry. Thank you for trusting me, advising me as well as giving me a great freedom and opportunities to travel. I felt honoured by the great responsibilities with which you have entrusted me and I hope that I met your expectations.

I would also like to acknowledge the work of the jury members, Professor Roger Alberto, Professor Xile Hu, Professor Marc Robert and Professor Jacques Moser for taking the time to read the present thesis and providing an interesting discussion and valuable comments.

Thank you also to my colleagues that have been working on this project: Dr. Micheál Scanlon, Dr. Manuel Méndez, Dr. Jane Stockmann and Dr. Pekka Peljo for their guidance, their advices and their support. Thank you also to Dr Heron Vrubel, who has been a valuable help in solving the reaction mechanisms as well as Grégoire Gschwend for the spectroscopic measurements. I would also like to thank Professor Clémence Corminboeuf and Laurent Vannay who provided the DFT calculations presented in this thesis.

Thank you very much to Patricia Byron for her unconditional good mood and her continuous help in any kind of administrative works. I also would like to express my gratitude to Dr. Anne-Sophie Chauvin for her mentoring and for giving me valuable advices to complete successfully this project. Thank you also to Annelene Odegaard for her help in the administrative aspects related to the doctoral school. Thank you to the team of the Magasin CH for being always available to answer any problems concerning orders of components or chemical products and the classification of chemical wastes.

I would like also to express my profound gratitude to my former supervisors: Professor William Skene, Dr. Stéphane Campidelli and Dr. Frédéric Kanoufi for inspiring me to become a researcher and encouraging me in this direction.

I would like to thank every members of the LEPA group that I have known during these four years. A first big thank you to Véronique for your unconditional friendship, your advices and your help

in the difficult periods. Thank you also to all my office mates: Peiyu, Alexandra, Reza, Xiaoqin, Tzu-En, Evgeny, Elena Tobolkina, Liang, Alejandro and Elena Zanzola. I passed a very good time with you, having nice and funny discussions. Thank you also to the people from the lab (that have not been cited above): Mik, Milica, Justyna, Sunny, Andreas, Chris, Alberto, Astrid, Fred, Victor, Natalia, Kass, Fernando, Haiqiang, Jonnathan, Elena Vladimirova, Desiré, Patrick as well as the trainees who have been of great significance to my PhD life: Justine, César, Geraldine, Joana, Encarni and Andrés. I am really grateful for sharing time with you during these last 4 years and I deeply enjoyed working with you.

To conclude, I would like to thank my friends: Véronique, Louise, Margherita, Amita, Elise, Hélène, Jonathan, Virgile, Prisca, Damien, Carole, Marie and a special thanks to Xavier who brought me here today. Thank you for your support and all the cheerful time we have been sharing together before and during my PhD project.

Abstract

Splitting water to produce hydrogen (H_2) fuel appears very promising to address the challenges of solar energy storage and global warming as the only by-product generated is oxygen (O_2). An alternative strategy, called batch water-splitting, based on Interfaces between Two Immiscible Electrolyte Solutions (ITIES) and artificial light-induced water-splitting is presented in the following thesis. This approach consists of two biphasic systems for the photo-production of H_2 and O_2 . The following thesis focuses on the realisation of the H_2 side.

In first instance, the photo-induced hydrogen evolution reaction (HER) by decamethylruthenocene ($Cp_2^*Ru^{(II)}$) is reported as a strategy to facilitate water splitting in biphasic systems. Hydrogen evolution by $Cp_2^*Ru^{(II)}$ was studied in detail. The study highlights that $Cp_2^*Ru^{(II)}$ is an attractive molecule capable of photo-reducing hydrogen without the need for an additional sensitizer. Electrochemical, gas chromatographic and spectroscopic (UV/vis, 1H and ^{13}C NMR) measurements indicate that the production of hydrogen occurs by a two-step process. First, the decamethylruthenocene hydride ($[Cp_2^*Ru^{(IV)}(H)]^+$) is formed in the presence of acids, followed by the reduction of this complex *via* a monometallic reaction leading to a first release of hydrogen. Thereafter, the resultant decamethylruthenocenium ion ($[Cp_2^*Ru^{(III)}]^+$) is further reduced leading to a second release of hydrogen by subtraction of a proton from a methyl group of $[Cp_2^*Ru^{(III)}]^+$. Experimental results showed an excitation of $[Cp_2^*Ru^{(IV)}(H)]^+$ at $\lambda = 243$ nm to evolve H_2 for the first oxidation. $[Cp_2^*Ru^{(III)}]^+$ was produced from the reduction of protons by $Cp_2^*Ru^{(II)}$ at $\lambda = 365$ nm and electrochemically regenerated *in situ* on a Fluorinated Tin Oxide (FTO) electrode surface. A promising internal quantum yield of 25 % was obtained for HER by $Cp_2^*Ru^{(II)}$ combined with electrochemical recycling.

Thereafter, HER by $Cp_2^*Ru^{(II)}$ was performed at ITIES. Shake-flask experiments demonstrated the production of H_2 only when the biphasic system was positively polarized, to favor proton transfer. Kinetics/thermodynamics for decamethylruthenocene hydride formation were electrochemically evaluated at liquid|liquid interface. Simulated curves developed using COMSOL Multiphysics software and compared to experimental data, indicate a modified EC (electrochemical–chemical) mechanism for the $[Cp_2^*Ru^{(IV)}(H)]^+$ formation at polarised interfaces.

In the proposed pathway, $[\text{Cp}_2^*\text{Ru}^{(\text{IV})}(\text{H})]^+$ is sufficiently stable in dichloroethane to transfer at negative potentials to the aqueous phase where it quickly dissociates. Additionally, the SHG response of $[\text{Cp}_2^*\text{Ru}^{(\text{IV})}(\text{H})]^+$ as function of the polarisation applied confirmed this mechanism.

Finally, an alternative method using homogeneous catalysts, $\text{Co}(\text{dmgh})_2(\text{py})\text{Cl}$ and $\text{Fe}_2(\mu\text{-SCH}_2\text{C}_6\text{H}_4\text{CH}_2\text{S})(\text{CO})_6$ at liquid||liquid interfaces was investigated. Coupled with a sacrificial electron donor and a sensitizer, H_2 production was achieved for both catalysts. However, results showed the polarisation was not responsible for the proton transfer and the electron donor was identified as the dominant proton source.

This study represents major progress in the development of the batch water splitting process as it overcomes the use of sacrificial electron donors. Moreover, these investigations provide substantial improvement in the general understanding of the photo-production of H_2 by metallocenes and reactions and characterisations at ITIES.

Keywords: batch water-splitting, decamethylruthenocene, hydrogen evolution reaction, ITIES, metal hydride, metallocenes, water-splitting.

Résumé

La production d'hydrogène (H_2) comme carburant apparaît comme une solution prometteuse afin de répondre aux enjeux liés au réchauffement climatique et au stockage de l'énergie. Une stratégie alternative, nommée « batch water-splitting », basée sur les interfaces entre deux solutions immiscibles d'électrolytes (ITIES) et la photo-oxydation de l'eau artificielle, est présentée au début de cette thèse. Cette approche repose sur deux systèmes biphasiques, visant à la photo-production de l' H_2 et de l'oxygène. La thèse suivante se concentre sur la réalisation de la partie produisant de l' H_2 .

Dans un premier temps, la réaction produisant de l' H_2 de manière photo-induite à partir du decamehtylruthenocene ($Cp_2^*Ru^{(II)}$) est présentée comme une stratégie pour faciliter le batch water-splitting. La production d' H_2 par le $Cp_2^*Ru^{(II)}$ a été étudiée en détail mettant en lumière les possibilités de cette molécule à réduire les protons sans addition d'un photo-sensibilisateur. Les mesures électrochimiques, chromatographiques et spectroscopiques (UV/vis, RMN 1H et ^{13}C) ont indiqué que la réaction se faisait en deux étapes. Dans un premier temps, le l'hydrure de decamethylruthenocène ($[Cp_2^*Ru^{(IV)}(H)]^+$) est formé en présence d'acide. Par la suite, le complexe est réduit *via* une réaction monometallique conduisant à une première libération d' H_2 . L'ion decamethylruthenocenium résultant ($[Cp_2^*Ru^{(III)}]^+$) est alors réduit produisant une deuxième libération d' H_2 en soustrayant un proton provenant de l'un de ses methyl. Les résultats expérimentaux et computationnels montrent qu'une excitation du $[Cp_2^*Ru^{(IV)}(H)]^+$ à $\lambda_{max} = 243$ nm permet d'éliminer l' H_2 au cours de la première réduction. $[Cp_2^*Ru^{(III)}]^+$ produit à partir de la réduction des protons a été régénéré électrochimiquement sur une électrode d'oxyde d'étain dopée. Un rendement prometteur de 25 % a été obtenu pour la réaction de production d' H_2 par $Cp_2^*Ru^{(II)}$ combinée à une régénération électrochimique.

Par la suite, la réaction a été adaptée aux ITIES. La production d' H_2 a été observée uniquement lorsque le système était négativement polarisé ce qui favorise le transfert de protons. Des études cinétiques et thermodynamiques ont été réalisées sur la protonation du $Cp_2^*Ru^{(II)}$ à l'interface. Des simulations, réalisées à l'aide du logiciel COMSOL Multiphysics, ont indiqué la formation du $[Cp_2^*Ru^{(IV)}(H)]^+$ à l'interface *via* un mécanisme EC (electrochimique-chimique). Il a

été démontré que le complexe été suffisamment stable dans le dichloroethane pour être transféré à des potentiels négatifs dans la phase aqueuse. Ce mécanisme a été confirmé par la mesure d'un signal de génération de seconde harmonique à l'interface.

Pour finir, deux catalyseurs, $\text{Co}(\text{dmgh})_2(\text{py})\text{Cl}$ et $\text{Fe}_2(\mu\text{-SCH}_2\text{C}_6\text{H}_4\text{CH}_2\text{S})(\text{CO})_6$, ont été étudiés aux ITIES pour produire de l' H_2 . Associés à un donneur d'électron sacrificiel et à un photo-sensibilisateur, les deux catalyseurs ont montré une capacité à produire de l' H_2 aux ITIES. Cependant, les résultats montrent que la polarisation n'est pas responsable du transfert des protons, qui serait plutôt lié à la présence de l'électron donneur.

Cette étude représente un progrès majeur dans le développement du « batch water-splitting » en évitant l'utilisation d'un donneur d'électron sacrificiel. De plus, ces investigations fournissent une amélioration substantielle de la compréhension des phénomènes mise en jeu lors de la photo-production d' H_2 par les metallocènes ainsi que sur les réactions et caractérisations aux ITIES.

Mots-clés: batch water-splitting, decamethylruthenocene, réaction d'évolution d'hydrogène, ITIES, metal hydride, metallocènes, oxidation de l'eau.

List of Symbols

a : activity

c : concentration

D : diffusion coefficient

E : potential

ε : extinction coefficient

F : Faraday constant

i : current

J : flux

k : rate constant

λ : wavelength

R : gas constant

T : temperature

t : time

μ^\ominus : standard chemical potential

ν : scan rate

z : charge

$\Delta G_{tr}^{\ominus, w \rightarrow o}$: standard Gibbs free energy of ion transfer from water to organic phase

ϕ : inner potential

$\Delta_o^w \phi$ Galvani potential difference

$\Delta_o^w \phi^\ominus$: standard Galvani potential difference

List of Abbreviations

A: acceptor

ACT: aqueous phase complexation followed by transfer

BA: bis(triphenylphosphoranylidene) ammonium

bpy: bipyridine

CE: counter electrode

CV: Cyclic Voltammetry

Cp: cyclopentadienyl

Cp*: methylcyclopentadienyl

D: donor

DCE: 1,2-dichloroethane

dmgh: dimethylglyoxime

FTO: fluorinated thin oxide

GC: Gas Chromatography

HER: Hydrogen Evolution Reaction

NMR: Nuclear Magnetic Resonance

ITIES: Interface between Two Immiscible Electrolyte Solutions

PS: photosensitizer

py: pyridine

SHE: standard hydrogen electrode

SHG: second harmonic generation

TB: tetrakis-(pentafluorophenyl)borate

TBA: tetrabutylammonium

TEA: trimethylamine

TFT: tetrafluorotoluene

TIC: transfer by interfacial complexation

TID: transfer by interfacial dissociation

TOC: transfer to the organic phase followed by complexation

UV/vis: ultraviolet/visible

vs: versus

w: water

Table of Contents

Acknowledgements.....	iiiv
Abstract	vii
Résumé.....	ix
List of Symbols.....	xi
List of Abbreviations.....	xii
1. Introduction	1
1.1 Historical background and goals.....	4
1.1.1 Practical solar water-splitting	4
1.1.2 Batch water-splitting concept	4
1.2 Electrochemistry at the Interface between Two Immiscible Electrolyte Solutions	6
1.2.1 Polarisation control at liquid liquid interfaces.....	6
1.2.1.1 Polarisation induced chemically	8
1.2.1.2 Polarisation induced electrochemically	9
1.2.2 Ion transfers across the interface	11
1.2.2.1 Simple ion transfer reactions	11
1.2.2.2 Assisted ion transfer reactions.....	13
1.2.3 Applications of liquid liquid interface.....	14
1.3 General review on catalytic hydrogen evolution reaction	15
1.3.1 Attractive features of transition metals	15
1.3.2 Photo-catalytic systems.....	16
1.3.3 Efficient catalysts for hydrogen evolution	17
1.3.4 Sensitizers.....	19
1.3.5 Addition of sacrificial electron donors.....	21

1.4	Metallocenes.....	23
1.4.1	Historical background	23
1.4.2	Substituent effects on the reactivity of metallocenes.....	24
1.4.3	Suggested mechanism for HER by metallocenes.....	26
1.5	The scope of the present thesis.....	26
1.6	References	29
2.	Experimental, Instrumentation and Simulations	35
2.1	Chemicals.....	36
2.1.1	Reagents.....	36
2.1.2	Synthesis.....	37
2.1.2.1	Preparation of Bis(triphenyl-phosphoranylidene) ammonium tetrakis(pentafluorophenyl)borate electrolyte (BATB).....	37
2.1.2.2	Preparation of tetrakis(pentafluorophenyl)borate diethyl etherate acid ([H(OEt ₂) ₂]TB).....	37
2.1.2.3	Preparation of Tris(2,2'-bipyridyl)ruthenium(II) tetrakis-(pentafluorophenyl)borate ([RuII(bpy) ₃]TB ₂)	39
2.2	Electrochemical methods.....	39
2.2.1	Three-electrode system	39
2.2.2	Bulk electrolysis experiments	40
2.2.3	Spectroelectrochemistry experiments	40
2.2.4	Four-electrode system.....	41
2.2.5	Electrode preparation	41
2.2.5.1	FTO electrodes washing.....	41
2.2.5.2	Aqueous reference electrodes preparation	42
2.2.5.3	Reference electrode for measurements in organic media	42
2.3	Photo-generation of H ₂ by Cp ₂ *Ru ^(II) in single or biphasic solutions.....	42

2.3.1	Experimental	42
2.3.2	Gas chromatography (GC), UV/vis and NMR spectroscopy	43
2.4	Measurements of the quantum yield and photon flux calculation of the source	43
2.4.1	Photon flux calculation of the source	43
2.4.2	Wavelength dependence of the HER by $\text{Cp}_2^*\text{Ru}^{\text{(II)}}$	44
2.5	Second Harmonic Generation set-up	44
2.6	Water DCE, shake-flask methodology	45
2.7	COMSOL: simulation details	45
2.7.1	Finite Element Simulations of the Photo-Electrocatalysis of Proton Reduction by Decamethylruthenocene	45
2.7.2	Finite Element Simulations of the Proton Reduction by Decamethylruthenocene at w DCE	48
2.8	Computational details	50
2.9	References	52
	Appendix: Transmittance of FTO glass electrode	54
3.	Photo-generation of Hydrogen by Decamethylruthenocene: a non-sacrificial electron donor and sensitizer	51
3.1	Introduction	52
3.2	Electrochemical characterization of $\text{Cp}_2^*\text{Ru}^{\text{(II)}}$	52
3.3	Photo-generation of H_2 from acidified 1,2-dichloroethane using $\text{Cp}_2^*\text{Ru}^{\text{(II)}}$	54
3.4	Multi-step mechanism for the photo-generation of H_2 from acidified organic solutions containing $\text{Cp}_2^*\text{Ru}^{\text{(II)}}$	55
3.4.1	Factors influencing hydride formation in the dark	56
3.4.1.1	General aspects	57
3.4.1.2	Experimental studies of acid strength of $[\text{Cp}_2^*\text{Ru}^{\text{(IV)}}(\text{H})]^+$	58

3.4.2	Light-driven reaction mechanism characterization	63
3.4.2.1	UV/vis characterization	63
3.4.2.2	Identification transient $[\text{Cp}_2^*\text{Ru}^{(\text{III})}]^+$	64
3.4.2.3	The second release of H_2 from the transient $[\text{Cp}_2^*\text{Ru}^{(\text{III})}]^+$ species.....	66
3.4.2.4	Identification of the final photo-product as $[\text{Cp}_2^*\text{Ru}^{(\text{IV})}(\text{C}_5\text{Me}_4\text{CH}_2)]^+$ by NMR spectroscopy.	68
3.4.3	Hydricity.....	72
3.5	Kinetics analysis of the transient $[\text{Cp}_2^*\text{Ru}^{(\text{III})}]^+$ species.....	73
3.5.1	Influence of $\text{Cp}_2^*\text{Ru}^{(\text{II})}$ initial concentration	74
3.5.2	Influence of $[\text{H}(\text{OEt}_2)_2]\text{TB}$ initial concentration	77
3.6	DFT calculations.....	79
3.7	Conclusions.....	81
3.8	References	83
4.	Photoproduction of Hydrogen by Decamethylruthenocene Combined with Electrochemical Regeneration	87
4.1	Introduction.....	88
4.2	Influence of coordinating solvent and of the counter anions on $[\text{Cp}_2^*\text{Ru}^{(\text{III})}]^+$ stability	89
4.3	Preliminary experiments: chemical regeneration	91
4.3.1	Sacrificial electron donor	91
4.3.2	Anionic tetracyanoquinodimethane: non-sacrificial electron donor.....	93
4.4	Electrochemical regeneration	95
4.4.1	Electrochemical characterisation on FTO electrode.....	96
4.4.2	Photo-oxidation of DCE in absence of protons	97
4.4.3	Photo-catalytic hydrogen production with organic protons	98
4.4.3.1	Experimental cyclic voltammetry and constant potential electrolysis	98

4.4.3.2	Control experiments.....	100
4.4.3.3	Simulated constant potential electrolysis	101
4.4.4	Gas chromatography analysis of produced hydrogen.....	101
4.4.5	Quantum yield	104
4.5	Conclusions.....	105
4.6	References	107
5.	Decamethylruthenocene Hydride and Hydrogen Formation at Liquid Liquid Interfaces.....	109
5.1	Introduction.....	110
5.2	Experimental hydrogen evolution at liquid liquid interfaces	111
5.2.1	Shake-flask experiments.....	111
5.2.2	Cyclic voltammetric observations at w DCE interfaces	115
5.2.2.1	Mechanism involved for the proton transfer at w DCE interfaces.....	115
5.2.2.2	Control electrochemical experiments.....	116
5.2.2.2.1	$[\text{Cp}_2^*\text{Ru}^{\text{(III)}}]^+$ transfer across polarized w DCE interfaces.....	116
5.2.2.2.2	Influence of chloride and hydrogen ions presence.....	117
5.2.2.2.3	Influence of counter ion of the aqueous acid at polarized w DCE interfaces ..	118
5.2.2.2.4	Influence of the complexation rate of the hydride formation	119
5.3	Mechanistic analysis using simulated voltammetric curves.....	120
5.3.1	Influence of the rate of $[\text{Cp}_2^*\text{Ru}^{\text{(IV)}}(\text{H})]^+$ formation in the organic phase.....	121
5.3.2	Simulation of the facilitated proton transfer	123
5.3.3	Influence of the rate of $[\text{Cp}_2^*\text{Ru}^{\text{(IV)}}(\text{H})]^+$ dissociation in the organic phase.....	124
5.3.4	Influence of the rate of $[\text{Cp}_2^*\text{Ru}^{\text{(IV)}}(\text{H})]^+$ dissociation in the aqueous phase.....	124
5.3.5	Influence of the rate of $[\text{Cp}_2^*\text{Ru}^{\text{(IV)}}(\text{H})]^+$ association in the aqueous phase	126

5.4	Conclusions.....	126
5.5	References	129
6.	Photo-induced Decamethylruthenocene Hydride: a key intermediate to understand photo production of H₂ by metallocenes	131
6.1	Introduction	132
6.2	Spectroscopy and photochemistry of [Cp ₂ *Ru ^(IV) (H)] ⁺	132
6.2.1	Hydride formation: UV/vis investigations	132
6.2.2	Wavelength dependence of the excitation of [Cp ₂ *Ru ^(IV) (H)] ⁺	134
6.2.3	Computed absorption spectrum of [Cp ₂ *Ru ^(IV) (H)] ⁺	135
6.3	Clarification of the excitation photo-process involved in the mechanism	137
6.4	Second Harmonic Generation	138
6.4.1	Historical background of second harmonic generation	139
6.4.2	General strengths and limitations of second harmonic generation measurements.	140
6.4.3	Application of SHG to the study of assisted proton transfer	141
6.4.3.1	Experimental set-up	141
6.4.3.2	Preliminary results.....	142
6.4.3.3	Limitation and possibilities	145
6.5	Conclusions.....	146
6.6	References	148
7.	Biphasic Hydrogen Evolution Using Classical Systems	151
7.1	Introduction	152
7.2	First investigations on classical systems at soft interfaces	153
7.3	Cyclic voltammetry observations at w DCE interfaces	155
7.4	Mechanistic discussion	156
7.4.1	Energy transfer reactions.....	158

7.4.1.1	Characterisation of Ru(bpy) ₃ TB ₂	158
7.4.1.2	Electrochemical characterisations	159
7.5	Shake-flask experiments.....	161
7.5.1	Reaction and analysis.....	161
7.5.2	Comparison between the catalyst efficiencies at soft interfaces.....	162
7.5.3	Clarification of the proton source	163
7.6	Conclusions.....	163
7.7	References	165
8.	Conclusions and perspectives	167
8.1	References	172
Curriculum Vitae		

1. Introduction

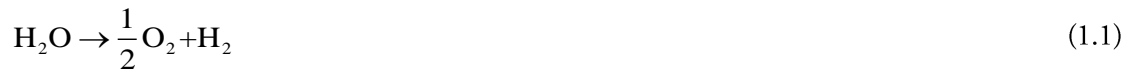
1.1	Historical background and goals	4
1.1.1	Practical solar water-splitting	4
1.1.2	Batch water-splitting concept.....	4
1.2	Electrochemistry at the Interface between Two Immiscible Electrolyte Solutions	6
1.2.1	Polarisation control at liquid liquid interfaces.....	6
1.2.1.1	Polarisation induced chemically	8
1.2.1.2	Polarisation induced electrochemically	9
1.2.2	Ion transfers across the interface	11
1.2.2.1	Simple ion transfer reactions	11
1.2.2.2	Assisted ion transfer reactions.....	13
1.2.3	Applications of liquid liquid interface.....	14
1.3	General review on catalytic hydrogen evolution reaction	15
1.3.1	Attractive features of transition metals	15
1.3.2	Photo-catalytic systems.....	16
1.3.3	Efficient catalysts for hydrogen evolution	17
1.3.4	Sensitizers.....	19
1.3.5	Addition of sacrificial electron donors.....	21
1.4	Metallocenes.....	23
1.4.1	Historical background	23
1.4.2	Substituent effects on the reactivity of metallocenes.....	24
1.4.3	Suggested mechanism for HER by metallocenes.....	26
1.5	The scope of the present thesis.....	26
1.6	References.....	29

For many years, the energy supply has been dominated by fossil fuels such as coal, crude oil and natural gas. These sources of energy take their advantage from a well-developed technology together with a satisfying efficiency. However, fossil fuels reserves will soon be depleted if contemporary rates of consumption are not curbed or alternative energy sources not found. Worldwide stocks of fossil fuels are expected to be totally consumed within the next decades.¹ Furthermore, the recent concern regarding the environmental impact of fossil fuel based energy production, such as the production of CO₂ and other harmful greenhouse gases eliciting global climate change, has driven attention towards the development of cleaner energy technologies. Finally, as access to energy is required for economic development, new energy sources must be sought to provide clean energy alternatives for developing nations to inhibit possible environmental impacts of these emerging economies. This strategy should include an array of energy conversion methods to lessen the dependence towards any single source.

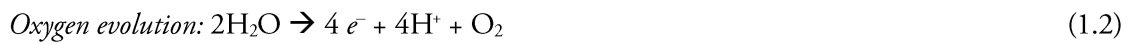
Therefore, to answer the expected 45%-increase of world energy consumption by 2030,² it is crucial to produce more energy while reducing greenhouse gas emissions – that are the main factor responsible for global warming. Furthermore, to increase access to energy throughout the developing world and improve the quality of life within these nations, energy has to be cheap and reliable. To achieve this, new sources of energy must also be sustainable, renewable, environmentally-friendly and of high efficiency to take into account the future evolution of our fast-developing world.

Recently, several renewable energies have been developed such as geothermal energy or biomass utilization. However, these energy sources are limited by their energetic capacities and thus, for now, the field is dominated by nuclear energy.¹ Nevertheless, nuclear energy presents serious safety problems including possible access to atomic weapons, the risk of major nuclear accidents and last but not least, the disposal of long-lived radioactive waste.³ Together with the high cost of this technology, it appears difficult to base the world development on this single source of energy. Besides nuclear energy, solar energy also has promising potential as the amount of solar radiation hitting the earth contains high amounts of energy.⁴ In the past, solar energy conversion has been expensive owing to the utilization of high quality materials such as nanocrystalline silicon.⁵ Moreover, contemporary solar cell efficiency is still limited with single junctions having a projected maximum efficiency of ~40% whilst multi-junctions have demonstrated 40-50%,⁶ and thus, an

avid area of research is the development of alternative methods of solar energy conversion using more common and cheaper alternatives. The development of artificial photo-systems mimicking the photosynthesis process used by plants are currently under heavy scrutiny and could offer a new way to produce energy from sunlight. However, one of the major issues facing the development of renewable energy strategies (solar and wind in particular) is the intermittent nature of the energy production, mostly dependent on climatic conditions. Hydrogen (H_2) as a solar fuel has been proposed as a solution to allow the stock-piling of clean energy produced in excess, with the aim of redistributing it on demand.⁷ H_2 has the advantage that it may be readily obtained in large amounts by “splitting” water⁸, as described through the following equation:



Water, is very abundant, environmentally friendly, and renewable. However, the water splitting process is highly endothermic and thus requires energy.⁸ Plants naturally perform water splitting in photosynthesis. A photon is absorbed and converted into chemical energy *via* a biological complex, the resulting chemical energy is used for water splitting or other chemical transformations. The idea to mimic the natural water splitting by plants to produce hydrogen has led to the development of artificial light-induced water splitting called photocatalytic water splitting.⁸ The concept is to build photoelectrochemical cell (PEC) that, in one side oxidize water and on the other side reduce proton to H_2 .



In this context, the development of simple and efficient methods to produce molecular H_2 is crucial. In this thesis, an alternative strategy, called batch water-splitting, based on polarized liquid||liquid interfaces and artificial light-induced water-splitting, is proposed. The concept and the issues are presented in the following section.

1.1 Historical background and goals

1.1.1 Practical solar water-splitting

Two types of PEC are actually proposed to perform water-splitting. One uses a fixed-electrode design where the light-absorber materials and the catalysts are deposited on the electrode immersed into an electrolyte solution. The other methodology uses in-solution metal complexes where the species are free to move in solution as light-absorbers and catalysts. Extensive studies in PEC have been started from the seminal work by Brattain, Garrett, Gerischer *et al.* in the 50s-60s using materials from the photovoltaics community and metal-oxide materials in fixed-electrode arrangements.^{9,10} At the end of the 70s, investigations into PEC water splitting using particle suspensions in solution were reported.^{11,12} However, despite the potential of the method in solution,¹³⁻¹⁵ the fixed electrodes were far more efficient.^{9,16} Thus, fixed electrodes for PEC have become a booming research area. Nevertheless, PEC in-solution has also remained an active area of research and, recently, it has been projected to be cost-competitive with gasoline sold in the U.S. when operated at the energy-conversion efficiency for solar-to-hydrogen evolution through water splitting of only 5-10 % (compared to ~25% required for fixed electrode).¹⁷ Consequently, alternative methods utilizing metal complexes in solution remains particularly attractive. Two general designs can be considered to performed water-splitting reaction in solution: one which evolves H₂ and O₂ in the same reactor and the other where H₂ and O₂ are produced in separate reactors, generating intermediate chemical species that serve as a redox shuttle between the reactors *via* a Z-scheme mechanism.

1.1.2 Batch water-splitting concept

Inspired by the second design, the long-term objective of the project related to this thesis is to develop a batch water splitting scheme based on two biphasic systems for the photo-production of H₂ and O₂. The set-up consists of an organic electrolyte solution of low water miscibility (typically 1,2-dichloroethane (DCE)) containing a metal complexes donor (D) able to act as light absorber and catalyst to reduce protons, in contact with an acidic aqueous electrolyte solution. Upon polarization of the liquid|liquid interface, either *via* the application of an external voltage or by dissolving a common ion in both phases, protons are pumped into the organic phase where they are reduced to H₂.¹⁸⁻²⁰ The result is the formation of oxidize species (D⁺).



The reversible nature of the metal complex donor is the key as it opens a perspective in solar fuel generation: the oxidized electron donor (D^+) can be regenerated by a reduced electron acceptor species (A^-). The latter can be sourced from a second half-reaction, such as light-driven oxygen evolution in organic media²¹



In theory, both photo-systems will be “reset” by mixing the oil phases after photo-irradiation:



This concept called “batch water-splitting” is illustrated in Figure 1.1.

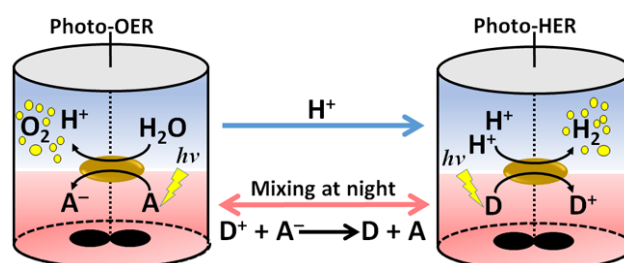


Figure 1.1. Batch water splitting. “A” is a recyclable electron acceptor that is reduced to oxidize water and “D” is a recyclable electron donor oxidized to reduce protons.²²

The key to success in a batch-water splitting arrangement is to ensure that D and A can (i) provide an efficient driving force for the photo-production of H_2 and O_2 , respectively, and (ii) be regenerated easily on mixing. In this regard, electron donors of higher (more positive) redox potentials are desirable, as weaker electron acceptors will be required to reset the photo-system. Significantly, one key advantage of the method is the use of two separate tubes which ensures the effective separation of H_2 and O_2 and, consequently, guarantees safe working conditions.

This thesis focuses on the realization of the hydrogen evolution reaction (HER) side. The choice and the study of the metal complex donor D and its implementation inside biphasic system to perform HER. General concepts of electrochemistry at liquid|liquid interfaces required to develop the batch water-splitting are introduced in the section 1.2. Thereafter, the section 1.3 presents the state-of-the-art on photocatalytic systems for hydrogen production. They generally consist of highly engineered catalyst, photosensitizer and sacrificial electron donor combinations.

A major challenge of this work is to design a simple system, that can be easily implemented at a biphasic interphase, and that can be regenerated by oxygen evolution reaction (OER). Based on Section 1.3, we suggest the use of a simple component, decamethylruthenocene, as the metal complex donor D. Therefore, Section 1.4 presents the chemistry of metallocenes, a class of molecule capable of achieving the complex photo-generation of H_2 by himself without the need of a photosensitizer.

1.2 Electrochemistry at the Interface between Two Immiscible Electrolyte Solutions

The interface between two immiscible electrolyte solutions (ITIES), for example at a water|1,2-dichloroethane (w|DCE) interface, provides alternative electrochemical perspective from which to investigate the HER.

For a long time, scientists have been interested in developing electrochemical membranes as demonstrated by the work of Nernst and Bernstein at the beginning of the 20th century.²³ ITIES has been intensively explored to study ion transfers across a membrane and ion selectivity. The thermodynamics of this interface were characterized by Karpfen and Randles,²⁴ but the first study of ion transfers under electrical current flow was made by Guastalla, Gavach *et al.*²⁵ After extensive studies during the last few decades,^{26,27} a well-defined model of the interface and advanced understanding of the mechanism of the ion transfer at ITIES has been described. The next section described the methods and models of liquid|liquid interfacial polarization.

1.2.1 Polarisation control at liquid|liquid interfaces

The polarisation and charge separation occurring at a liquid|liquid interface is similar to that which takes place at a metal|metal junction or at the interface between a metal and an electrolyte solution as illustrated Figure 1.2 (A) and (B). For example, when two metals are placed in contact, their Fermi levels align and the electrons move from the metal with the lowest work function to the one with the higher one. Additionally, when the metal is placed in an electrolyte solution, a few nanometer thick ionic space charged region appears as described by the Gouy-Chapman theory.²⁸ Similarly, the ITIES may be polarized and two ionic space regions will be created on both sides of the interface as illustrated in Figure 1.2(C).

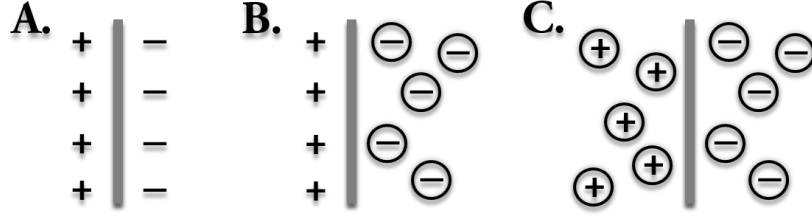


Figure 1.2: Comparison of polarised interfaces. A. MetallMetal, B. MetallSolution and C. SolutionSolution.

From a physicochemical viewpoint, the potential dependence of ion transfer through the influence of the polarization can be expressed using the Nernst equation. Indeed, the standard Gibbs free energy of ion transfer for a species i can be defined, from two immiscible solutions containing electrolytes, one aqueous (w) and one organic (o). It corresponds to the difference between the standard chemical potentials of the species i in organic and aqueous phases.

$$\Delta G_{tr,j}^{\Theta,w \rightarrow o} = \mu_i^{\Theta,o} - \mu_i^{\Theta,w} \quad (1.7)$$

This difference is illustrated in Figure 1.3 for a lipophilic ion i meaning its standard chemical potential is higher (in absolute terms) in the organic phase than in the aqueous phase. Consequently, $\Delta G_{tr,j}^{\Theta,w \rightarrow o}$ is negative. Therefore, the ion i solubilised in the aqueous phase tends to transfer to the organic phase until the system reaches its equilibrium. At the equilibrium, the electrochemical potentials are equal. By developing:

$$\mu_i^{\Theta,w} + RT \ln a_i^w + z_i F \phi^w = \mu_i^{\Theta,o} + RT \ln a_i^o + z_i F \phi^o \quad (1.8)$$

The Nernst equation for ionic exchange is obtained according to the Galvani potential difference across the interface:

$$\Delta_o^w \phi = \phi^w - \phi^o = \Delta_o^w \phi_i^{\Theta,o} + \frac{RT}{z_i F} \ln \left(\frac{a_i^o}{a_i^w} \right) \quad (1.9)$$

$\Delta_o^w \phi_i^{\Theta}$ is the standard ion transfer potential defined as the standard Gibbs free energy divided by $z_i F$.

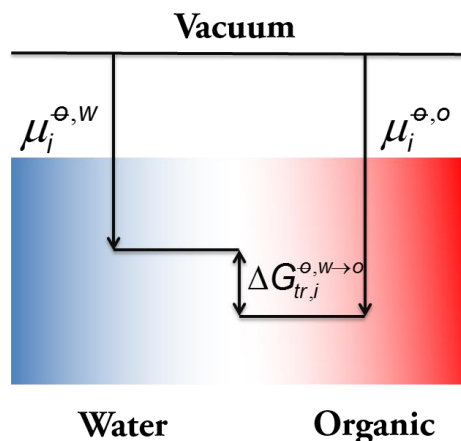


Figure 1.3: Transfer of ion i from water to organic phase. Ion i , more soluble in the organic phase, is firstly solubilized in water. Therefore, when the two phases are in contact, the ion i transfers from water to organic phase.

Concretely, the polarisation and its control is achieved either by applying a potential between the two phases or by distribution of ions across the interface as explained in the next sections.

1.2.1.1 Polarisation induced chemically

Chemical polarisation uses a combination of charged species (*i.e.* ions) which, owing to their solubility properties, are distributed on both sides of the interface. The created polarisation is easily explained and modelled: in the case of a single salt in water in the presence of an organic solvent, if the cation c^+ is more lipophilic than the counterion a^- , c^+ will transfer to the organic phase and will drag a^- until the Galvani potential difference satisfied the Eq. (1.9) for both species. Consequently, Galvani potential difference is created across the interface. Practically, salts in excess are used to fix the polarisation and the species in low concentration distribute according to this polarisation. Some values of commonly used ions and important for the understanding of the Chapter V are presented in Table 1.1 for the water|1,2-dichloroethane interface.²⁹

Table 1.1: Example of standard Gibbs energy transfer of common ions

Cations	$\Delta G_{tr,C^+}^{\Theta,w \rightarrow o} / \text{kJ.mol}^{-1}$	Anions	$\Delta G_{tr,A^-}^{\Theta,w \rightarrow o} / \text{kJ.mol}^{-1}$
BA ⁺	− 66.5	TB [−]	− 67.5
H ⁺	56	OH [−]	67.6
Li ⁺	62.7	Cl [−]	51.8

1.2.1.2 Polarisation induced electrochemically

A traditional four electrode cell is typically used to polarise the interface and characterised charge transfer reactions as described previously.³⁰⁻³² In this case, the polarisation applied between the two phases is controlled through a potentiostat (see Chapter II, Section 2.2.4). Two platinum (Pt) counter electrodes, connected to the working and counter electrode leads of the potentiostat are positioned in the aqueous and organic phases, respectively, to supply the current. An external potential applied between the counter electrodes is controlled with two Ag/AgCl reference electrodes placed in Luggin capillaries. The latter tapered openings are positioned proximal and on opposing sides of the ITIES, as illustrated in Figure 1.4. The Ag/AgCl reference on the organic side is immersed in an aqueous solution containing a common ion with the organic electrolyte to chemically polarize the organic|aqueous reference solution interface.

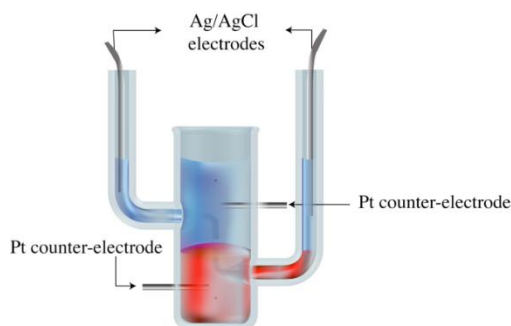


Figure 1.4: Example of a four-electrode cell. The cell includes two silver chloride reference electrodes (Ag/AgCl) and two platinum counter electrodes (Pt).

The interfacial concentration ratio of ions follows the Nernst equation. Consequently, when the Galvani potential is perturbed from the equilibrium potential, ion transfer occurs until the Nernst potential matches the applied Galvani potential difference. Thus, an electric current is created at the counter electrodes terminal to respect the electroneutrality inside the solutions. Commonly, the electron transfers at the interface between a metal electrode and an electrolyte solution is characterized by cyclic voltammetry. Similarly, the charge transfer across a liquid|liquid interface can be investigated by drawing $i = f(E)$ curves. Information including faradaic and non-faradaic processes occurring at the interface can be obtained. Therefore, this method appears as a very useful tool to study the proton coupled electron transfer reaction involving aqueous protons and electron donors.^{33,34} By convention, a positive potential corresponds to the positive polarisation of the aqueous phase. An important difference between ITIES and a metallsolution interface is the

polarisable potential window. Indeed, for metallsolution, the potential window is limited by the solvent reduction or oxidation while, in ITIES, this window is limited by the transfer of the species in excess with the smallest standard of ion transfer potential. In other words, at positive potentials (water *vs* organic) the potential window is limited by the transfer of an aqueous cation or an organic anion as a function of their Gibbs energy of transfer. Similarly, at negative potentials, the window is limited by either the transfer of an aqueous anion or that of an organic cation as illustrated in Figure 1.5.

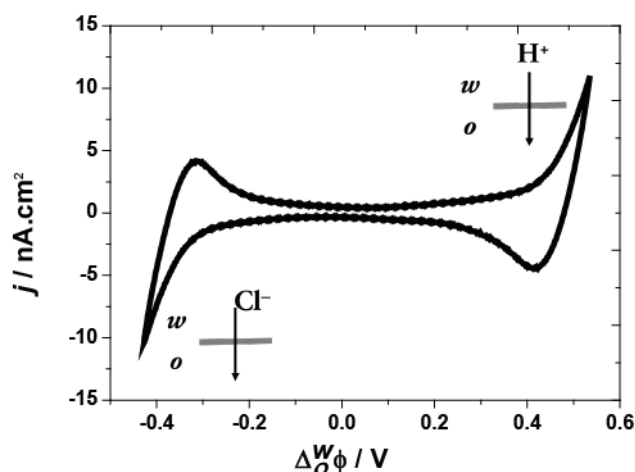


Figure 1.5: Interfacial process within the potential window. Potential window for the cell including HCl and BATB as the supporting electrolytes in the aqueous and in the organic phase, respectively. Considering the standard ion transfer potential of each ion (Table 1.1) the potential window is limited by the transfer of protons at positive potentials and chloride at negative potentials.

In practice, a very lipophilic electrolyte is dissolved in the organic phase. Consequently, the transfer of this salt from organic to water is unfavourable and it guarantees that the potential window is limited by the transfer of the aqueous electrolyte as illustrated in Figure 1.5. Tetrabutylammonium tetrphenylborate (TBATPB) was traditionally used in the oil phase but has been replaced by more hydrophobic salts, such as bis(triphenylphosphoranylidene) ammonium tetrakis(pentafluorophenyl) borate (BATB)⁷⁸ illustrated in Figure 1.6.

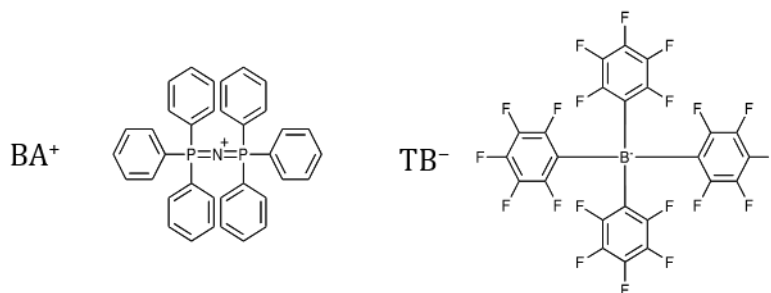


Figure 1.6: Structure of the conventional highly hydrophobic organic electrolyte. Bis(triphenylphosphoranylidene) ammonium (left, BA⁺) and tetrakis(pentafluorophenyl) borate (right, TB⁻).

It is also interesting to note that the potential scale is the absolute Galvani potential difference, and the uncharged interface equivalent to a flat band potential in semiconductor electrochemistry. A reference is necessary to compare different measurements. Usually, a reference ion dissolved in either phase with a known standard Gibbs energy of ion transfer is used to calibrate the potential scale.

1.2.2 Ion transfers across the interface

The transfer of charged species, ions or electrons, across a polarized interface has been studied for a long time. Electron transfer reactions refer to the reaction between two redox couples placed on either side of the interface. In relation to HER, a photo-induced electron transfer between [Ru(bpy)₃]²⁺ sensitizer in water phase and a donor heptyl-4,4'bipyridinium (C₇V²⁺) in organic phase was investigated by Girault *et al.*³⁵ In the same way, De Armond and coworkers³⁶ used [Ru(bpy)₃]²⁺ and methyl viologen in a 4-electrode setup and also observed a photocurrent resulting from the electron transfer. For the present investigation, only ion transfer will be studied. Therefore, some fundamental concepts on ion transfer reactions are presented below.

1.2.2.1 Simple ion transfer reactions

With the application of a Galvani potential difference, as described in the last paragraph, it is possible to drive the transfer of ions from one phase to the other. This transfer does not require a large reorganisation of the solvent and is relatively fast compared to the heterogeneous electron transfer.³⁷

Ion transfer reactions are commonly investigated by cyclic voltammetry with the four-electrode cell set up presented above. An example is given in Figure 1.7 for the transfer of

tetraethylammonium ion (TEA^+). Herein, the positive peak represents TEA^+ transfer from aqueous to organic phase and the negative peak refers to the transfer from organic to water phase. The mass transport conditions are analogous to those for a redox reaction on a metal electrode. Indeed, for a transfer across the interface, the reaction includes a mass transfer step from the bulk aqueous phase towards the interface crossing and a mass transfer step into the bulk organic phase. Thus, all the methodology developed to estimate kinetic parameters and mechanisms of charge transfer reactions at metal electrodes is also applicable to study ion transfer reactions at liquid|liquid interfaces. With a reversible ion transfer, *i.e.* transfer is fast compared to the diffusion, a peak-to-peak separation between the forward and reverse waves of a cyclic voltammogram of 59/ z mV is classically observed with the mid-peak potential corresponding to the standard ion transfer potential.

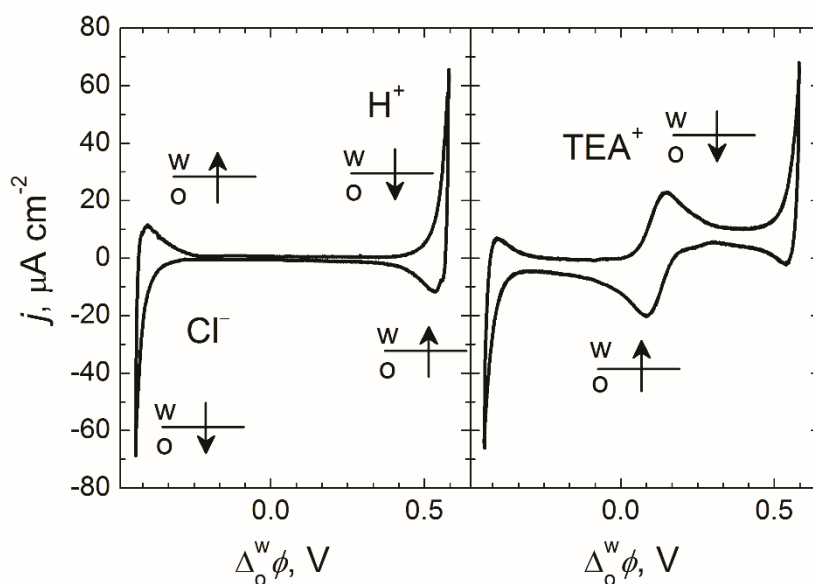


Figure 1.7: Experimental cyclic voltammograms (CVs) illustrating a simple ion transfer. CVs obtained using a cell composed of 10 mM HCl and 5 mM BATB as the supporting electrolytes in the aqueous and in 1,2-dichlorobenzene phase respectively. With (right) and without (left) TEA^+ dissolved in the aqueous phase. (CVs measured by Pekka Peljo, LEPA-EPFL).³⁸

For the transport of the ion across the interface, it is now rather accepted that the solvent deformation accelerates the ion motion. As water is the most coordinating solvent, ions transferring from aqueous to organic phase occurs with a certain co-transport of water molecules after formation of a “hernia” at the interface. This effect is stronger for cations than anions. Inversely, from oil toward water, the ion is probably sucked by water protrusion. This

phenomenon, called harpoon effect, helps to cross the interface.³⁹ These two occurrences are illustrated in Figure 1.8 below.

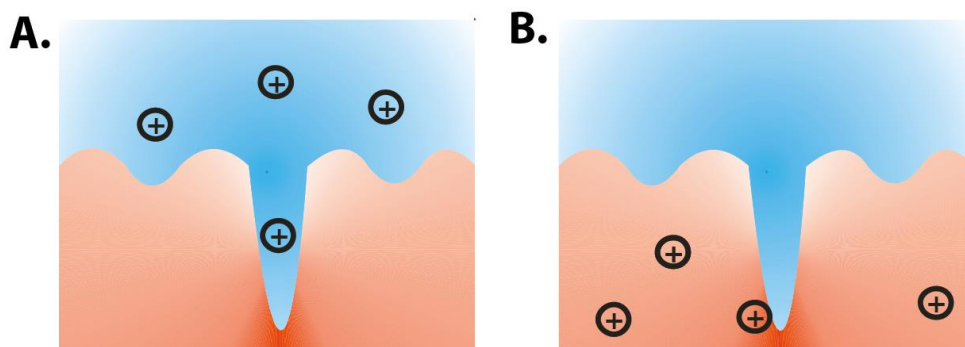


Figure 1.8: Schematic ion transfer reaction mechanism. (A) Transfer of aqueous ion to the organic phase and (B) transfer of organic ion to the aqueous phase via harpoon effect.

1.2.2.2 Assisted ion transfer reactions

In nature, the transfer of ions across the phospholipid bilayer of the cell membrane may be facilitated by a lipid-soluble molecule called an ionophore. Indeed, ionophores may complex ions which result in decreasing of their Gibbs energy of transfer.^{40,41} The first example of assisted, or facilitated, ion transfer reaction at liquid-liquid interface was the study of the transfer of potassium and sodium ions facilitated by a natural antibiotic and a synthetic ionophore reported by Koryta in 1979.⁴⁰ Since the work of Koryta, interfacial complexation reactions have been widely studied^{30,42} four types of reaction mechanisms⁴³ can be distinguished (summarized in Figure 1.9.): the transfer through interfacial complexation/decomplexation (TIC/TID), the transfer of the proton, followed by organic phase complexation (TOC) or aqueous phase complexation followed by transfer (ACT).

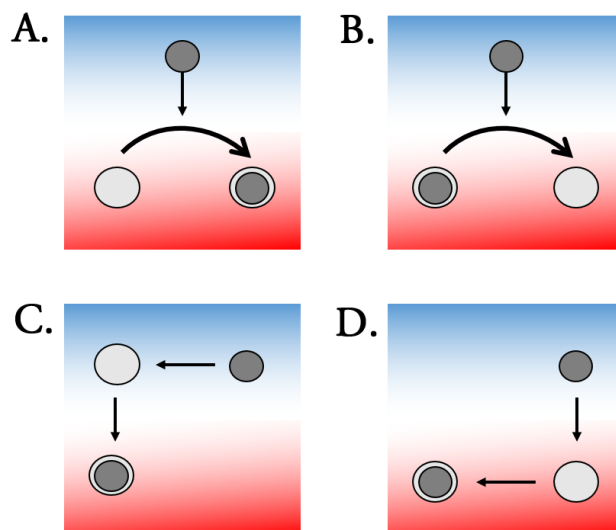


Figure 1.9: Schematic representation of assisted ion transfer reactions. (A) Transfer by interfacial complexation (TIC), (B) Transfer by interfacial decomplexation (TID), (C) Aqueous complexation followed by transfer (ACT) and (D) transfer followed by organic-phase complexation (TOC).

In this thesis, we are particularly interested to reproduce this mechanism to favor the transfer of ions at ITIES and especially the extraction of protons from the water phase with the main goal of performing HER. In this case, a lipophilic base is added to the aqueous phase. Its protonation forms an organic acid which makes the proton easily transferable to the organic phase. This so called “proton pumping” has many applications in pharmacokinetics and biology.⁴⁴ Moreover, molecules with acid-base features may act as ligands to facilitate the proton transfer. It has already been shown using porphyrin derivatives,⁴⁵ decamethylferrocene⁴⁶ and tetrathiafulvalene.⁴⁷

1.2.3 Applications of liquidliquid interface

One of the first application of ITIES was the investigation of drug delivery in membrane. Indeed, by its very nature, ITIES mimics biological membranes and, by this way, is an interesting platform to study drug transfer characteristics and mechanisms across interfaces to design drugs and optimize their performances.^{48,49} Development of amperometric ion sensors have been investigated in the 90s to detect ions by measuring the current induced by ion transfer reactions across polarized interfaces. Applications include the detection of heavy metals where precise analytical tools are of particular importance owing to their high toxicity. The two main advantages are that the selectivity which may be enhanced by the choice of the ionophore (which can be a simple ligand but a also macromolecule such as proteins for biological applications)^{50,51} and by the polarization.^{41,52,53} However, the technique suffered of two major inconvenient: the mechanical

instability of the interface and the large ohmic drop in the organic phase.²⁶ Nowadays, with the development of micro-interfaces, these problems are about to be overcome.²⁷ Other applications such as thermo-electricity²⁶ or Marangoni pump have also been explored. However, the application that appeals our interest, in the aim to provide a novel alternative to produce hydrogen, is the electrocatalysis and solar energy conversion at the ITIES. First works have shown the high photo-reactivity of absorbed porphyrin at liquid|liquid interfaces.^{54,55} In 2010, our group demonstrated the possibility to produce H₂ in the dark using decamethylferrocene (Cp₂⁺Fe^(II); Cp^{*} = C₅Me₅) as an electron donor in a biphasic system.¹⁸ In 2011, we reported that platinum or palladium nanoparticles (NPs),⁵⁶ molybdenum sulfide or carbide NPs either free standing⁵⁷ or supported on mesoporous carbon material⁵⁸ were very efficient in catalyzing aqueous proton reduction by water insoluble electron donors. Motivated by these early findings, we set out to explore the reactivity of other metallocenes as suitable electron donors. Further details are provided in Section 1.4.2.

1.3 General review on catalytic hydrogen evolution reaction

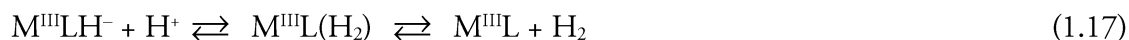
1.3.1 Attractive features of transition metals

Transition metal complexes are known for their excellent properties to catalyze reactions such as coupling⁵⁹ or hydrogenation.⁶⁰ Thus, they are also very well adapted for the photo-induced proton reduction and for the catalysis photo-activation. Indeed, some complexes are excellent photosensitizers because they absorb an important amount of light in the visible wavelengths and have a long-lived excited state allowing efficient electron transfers.⁶¹ Furthermore, metal complexes are efficient catalysts for HER due to their ability to store several electronic charges *via* their different redox states. They can perform multi-electronic reactions such as the two-electron reduction necessary for HER. Therefore, most of the publications on photo-induced hydrogen production are based on these kind of complexes.^{62,63}

In principle, all redox couples with a potential lower than $\text{H}_2\text{O}/\text{H}_2$ (meaning -0.41 V *vs* SHE for pH 7.0) should be able to produce hydrogen in water. Practically, this reaction is very slow without a suitable catalyst. Indeed, as shown in the equations below, the reduction with one or two electrons of H^+ is energetically unfavourable. Thereby, H^\bullet and H^- intermediates have to be stabilized in order to improve the reaction rate. One- and two-electron potentials for H^+ reduction at pH 7 and 25°C are given below for standard state 1 bar and 1 M for other species:



Several studies on hydrogen evolution have highlighted the crucial role of metal hydride d^6 (named $\text{M}^{\text{III}}(\text{L})\text{H}^-$, where M is the metal and L the ligand(s)). The equations below represent the reactions for a d^6 - d^8 (M^{III} - M^{I}) metal based cycle.⁶⁴⁻⁶⁶



The metal complex, initially d^6 or d^7 (M^{III} or M^{II}), is reduced to the d^8 complex (M^{I} , Eq. 1.14 and 1.15) that may undergo an oxidative addition and formation of a d^6 hydride $\text{M}^{\text{III}}\text{L}(\text{H}^-)$ (Eq. 1.16). This hydride complex may now produce hydrogen according to a first order reaction with a proton (Eq. 1.17) or, with a second order reaction with another equivalent of hydride complex (Eq. 1.18). Finally, the hydride complex may be reduced to $\text{M}^{\text{II}}\text{L}(\text{H}^-)$ (Eq. 1.19) if the hydride complex is not reactive enough to form hydrogen as in equations 1.17 and 1.19.

1.3.2 Photo-catalytic systems

Since the late 1970s, various state-of-the-art multi-component photo-systems to generate H_2 were developed and generally consist of highly engineered catalyst (Cat.), photosensitizer (PS) and

sacrificial electron donor (SD) combinations.⁶⁷⁻⁷⁰ Electrons required for the hydride formation are provided by a photosensitizer through a photo-induced transfer; the latter is recycled by a sacrificial electron donor that supplies the necessary electrons for the catalysis.⁷¹ In certain cases, a redox mediator, as methyl viologen is used as an electron relay between the photosensitizer and the catalyst to improve the electron transfer.⁶⁷ Under irradiation, the photosensitizer can be in an excited oxidative or reductive state. Figure 1.10 illustrates the two possible mechanistic pathways to photo-induced hydrogen through a three-component system.

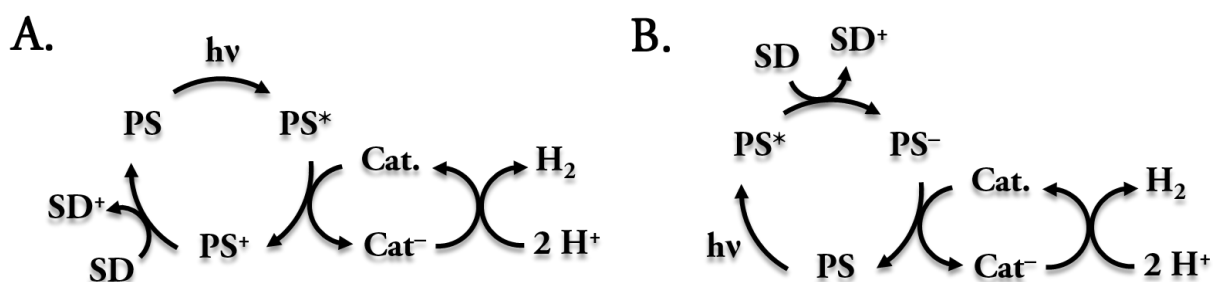


Figure 1.10. Simplified mechanism in a three-component system for hydrogen evolution. (A) Oxidative and (B) reductive mechanism

In both cases, the process begins with the absorption of a photon, which induces the excitation of PS to PS^* . In the oxidative mechanism, PS^* transfers first its electron to the catalyst and PS^+ is generated. The latter is regenerated by reduction with SD. In the reductive mechanism, SD provides an electron to PS^* and generates PS^- which, then, provides the electron to the catalyst. Practically, most of the reactions are performed under anaerobic conditions to avoid the undesirable reaction between PS^* and oxygen – effectively quenching the reaction series. The following sections review the components developed for this system.

1.3.3 Efficient catalysts for hydrogen evolution

Noble metals, such as rhodium,⁷² platinum⁷³ or palladium,⁷⁴ have proven so far to be the best catalysts for H_2 production. Nevertheless, as noble metals are rare and expensive, researchers have developed several new catalysts based on non-expensive compounds for hydrogen production from water at room temperature and pressure. This has led to the development of a bio-inspired chemistry, which aims at mimicking chemical processes implemented by living organisms. These organisms have enzymatic systems, called hydrogenases, that employ hydrogen as an energy source

or produce hydrogen from water. In nature, hydrogenases are divided into two main categories depending on the metal of their active site: NiFe hydrogenases, which are naturally the most abundant and contain nickel and iron metals, as well as FeFe hydrogenases which have only iron.⁷⁵ These enzymes have an efficiency similar to platinum⁷⁶ and their catalytic systems are based on cheap and abundant metals. The two metallic atoms are connected by thiolate bridges and iron atoms are coordinated by carbon monoxide and cyanide (Figure 1.11). This configuration allows facile access of electrons and protons to the metal core.⁷⁷

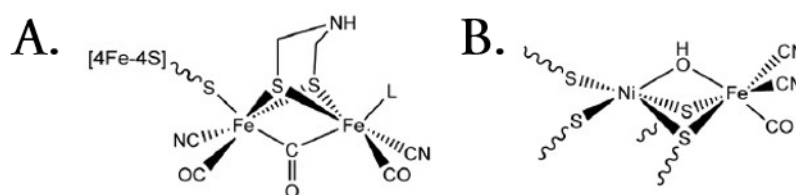


Figure 1.11. Active sites structure of hydrogenases. (A) FeFe hydrogenase and (B) NiFe hydrogenase.

Presently, there is no compound that exactly reproduces all the features of Fe_2S_2 core; however, over the last decade, the synthesis of numerous structural and functional models of the type $\text{Fe}_2(\text{SR})_2(\text{CO})_6$ have been developed^{75,77,78} showing their ability to catalyse H_2 production with good yields.⁷⁵ An example of this type of structures is presented on Figure 1.12(A). Simultaneous research over the past several years has been inspired by this enzyme towards the development of new molecular catalysts – without noble metals – based on iron,⁷⁹ nickel,⁸⁰ cobalt,⁷⁰ or manganese.⁸¹ Thus, cobaloximes are molecular catalysts containing cobalt bonded with dioxime ligands (Figure 1.12(B)) that show good efficiency for HER with low overpotential.^{68,70,82,83} Furthermore, they are relatively easy to prepare.⁸⁴ Nevertheless, several key features of hydrogenases are difficult to reproduce such as the active site playing the role of proton relay. Moreover, the basic dioxime ligand showed stability problems and this class of complexes is difficult to adapt to a large pH range. In 2005, Hinnemann and coworkers demonstrated the potential of MoS_2 particles as active HER catalysts.⁸⁵ Since then, the interest in developing MoS_2 and related metal sulphite catalyst has grown as these materials appear more promising.⁸⁶⁻⁸⁸ Indeed, this compound, while not expensive, is based on an abundant and very stable metal that may be used in acid, neutral or basic pH while also demonstrating good efficiency. Its structure is composed of a sulfur-surrounded first-row transition metal which is similar to the hydrogenase thiolate bridges.

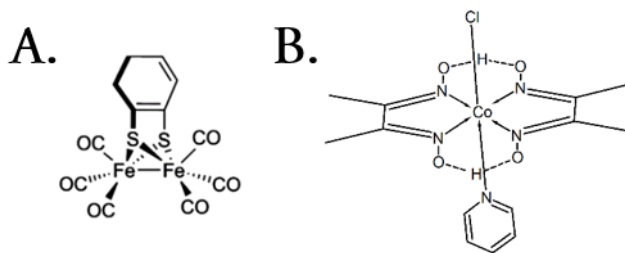


Figure 1.12. Structure example of HER catalysts. (A) $\text{Fe}_2(\text{SR})_2(\text{CO})_6$ and (B) $\text{Co}(\text{dmg})_2(\text{py})\text{Cl}$ (dmg: dimethylglyoxime)

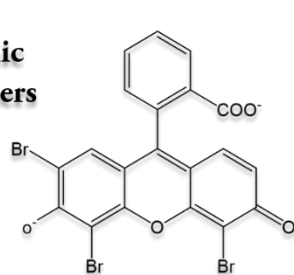
1.3.4 Sensitizers

The role of the sensitizer is to transform light energy into chemical energy and transfer it, under favourable conditions, to perform the HER. First, sensitizers must have excellent light harvesting properties. In other words, the extinction coefficient of the molecule must be high in order to reach a significant theoretical photocurrent.⁸⁹ Presently, sensitizers can be divided in two categories: molecular sensitizer (composed of organic dyes and inorganic sensitizers) and semiconductors.⁴¹ The latter are now intensively studied since the successful achievement of photoelectrolysis of water with TiO_2 by Honda and Fujishima in 1972.⁶⁹ A number of semiconductors have already exhibited excellent photocatalytic performance such as ZnO , Fe_2O_3 , CdS and ZnS .⁹⁰ These materials each have different advantages. Firstly, they are very stable, and secondly, their band gap is adjustable by changing the metal or its environment. Finally, it is possible to exploit multiple exciton generation to obtain high efficiency.⁹¹ Nevertheless, the maximum wavelength of excitation is relatively small ($\lambda \leq 387 \text{ nm}$ for TiO_2) resulting a poor absorption of direct free sunlight.⁹² This notable problem has to be solved and with one avenue of research focused on exploring novel methods through the use of a molecular sensitizer (and especially ruthenium complexes) to extend the photoresponse of TiO_2 into the visible region.^{93,94}

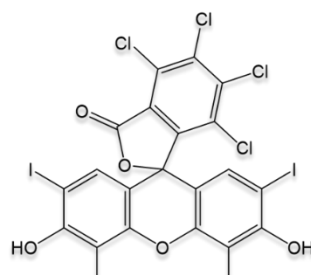
Molecular sensitizers are another well characterized class of compounds used for the photosensitization due to their ease of handling. Also, inorganic sensitizers have a long and rich history in photochemistry.⁹⁵ The two most studied classes of molecules are porphyrin and phthalocyanine macrocycles⁹⁶ inspired by natural photosynthetic systems and polypyridyl metals such as $[\text{Rh}^{\text{III}}(\text{bpy})_3]^{2+}$, iridium coordination complexes^{97,98} and the popular $[\text{Ru}^{\text{II}}(\text{bpy})_3]^{2+}$. Indeed, the extensive redox chemistry exhibited by $[\text{Ru}^{\text{II}}(\text{bpy})_3]^{2+}$ has demonstrated several times that this

complex is known to be an efficient photosensitizer for HER.⁹⁹ Its absorption band at 452 nm allows systems to work in the visible range while the triplet excited state is generated with a high quantum efficiency and is long-lived (~890 ns in acetonitrile) to increase the probability for the reaction to occur.¹⁰⁰ Various examples of inorganic dyes are presented in Figure 1.13.

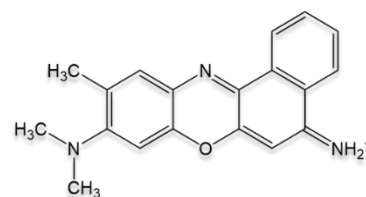
Besides inorganic compounds, organic dyes are also promising compounds owing to their low cost and low toxicity.¹⁰¹ Several molecules have demonstrated good ability as photosensitizers such as eosin Y, riboflavin, rose Bengal, cyanine, cresyl violet, hemicyanine and merocynine.^{62,102} Unfortunately, the huge limitation of these dyes is their very poor stability,¹⁰³ thus preventing their intensive use as photosensitizers.

Organic sensitizers

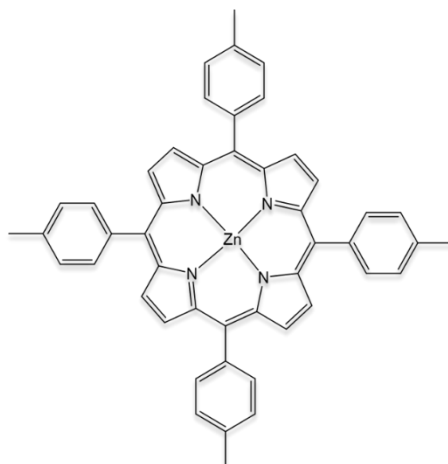
Eosin Y



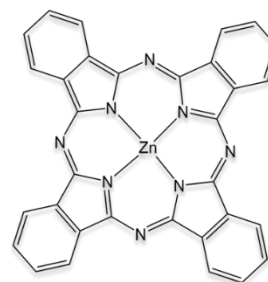
Rose Bengale



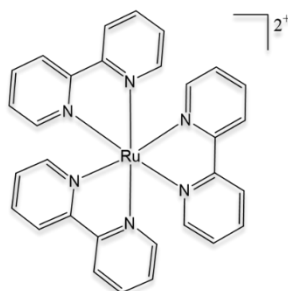
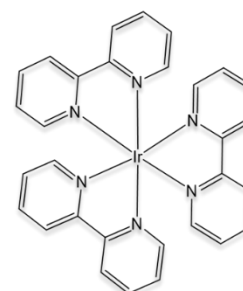
Cresyl violet

Inorganic sensitizers

Zinc porphyrin



Zinc phthalocyanine

 $[Ru^{II}(bpy)_3]^{2+}$  $[Ir^I(bpy)_3]^+$ **Figure 1.13. Structure of various organic and inorganic sensitizers****1.3.5 Addition of sacrificial electron donors**

One of the main barriers of the photocatalytic system is the rapid recombination of the photo-generated electron/hole pairs as well as the backward reactions.¹⁰⁴ One response to these deficiencies is the utilisation of a sacrificial reagent. This compound reacts irreversibly with the photo-generated PS^* to enhance the photocatalytic electron/hole separation resulting in a higher quantum efficiency. This task is generally achieved with tertiary amines such as triethanolamine,

triethylamine dimethylaniline or ethylene diamine which decompose after oxidation by PS* avoiding the back electron transfer.¹⁰⁵ Nevertheless, hydrogen is one of their decomposition products thus obscuring the obtained hydrogen yield. Other inorganic redox couples such as IO_3^-/I^- or $\text{S}^{2-}/\text{SO}_3^{2-}$ were used to play the role of electron donor especially when the sensitizer was a semiconductor.^{106,107}

The utilisation of a sacrificial electron donor makes it easier the study of the HER half-reaction. However, continual addition of electron donors is required to sustain hydrogen production since the electron donor is consumed during the reaction. Consequently, from the principle of water splitting, oxygen evolution is often envisaged to bring an electron to contribute to HER. Nevertheless, the electron that oxygen evolution may supply is not at a favourable energy to reduce PS*. In an ideal case, it should be coupled with another sensitizer to increase this energy but actually, systems are limited by the communication between all components. Another approach already envisaged is to employ pollutants such as oxalic acid, formic acid or formaldehyde to produce clean hydrogen fuel.¹⁰⁸

To conclude, the developed multi-component systems tend towards highly engineered catalyst, photosensitizer and sacrificial electron donor combinations. This sophisticated approach is complicated to implement in biphasic systems where the reaction requires also two solvents and the control of the polarization. Furthermore, the major challenge is to design systems where the electron donor can be regenerated either chemically or electrochemically. Within this context, metallocenes appear as an attractive class of molecules capable of achieving the complex photo-generation of H_2 by themselves. Indeed, these complexes have the capacity to provide electrons, undergo photo-activation and the metal centre has the ability to reduce protons. Therefore, these all-in-one molecules offer an interesting alternative to state-of-the-art multi-component systems, involving multiple electron transfer steps. Our choice to work specifically with decamethylruthenocene is explained and supported in the next paragraph.

1.4 Metallocenes

1.4.1 Historical background

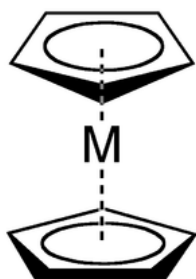


Figure 1.14: Metallocene structure.

Metallocenes are organometallic complexes composed of a transition metal such as iron, ruthenium or osmium linked only to two cyclopentadienyl ligands arranged in parallel as shown in Figure 1.14.¹⁰⁹ Ferrocene was the first compound discovered in this category and also the most well-known. Since its discovery in 1951 simultaneously by Keally and Pauson¹¹⁰ along with Miller *et al.*,¹¹¹ many derivatives of metallocenes were described to be active catalysts for olefin polymerization or to prepare catalysts allowing the synthesis of very promising polymers such as polyethylene with high molecular weight or plastomeres.⁹⁹

Additionally, metallocenes are attractive class of molecules because they are simple, easy to synthesize, with ligands and metal centres that may be tuned to obtain certain desired properties, such as tailored:

- (i) solubility, attractive to implement them in biphasic systems,
- (ii) absorbance wavelength, meaning they can be maximized to use sunlight to drive a thermodynamically uphill reaction,
- (iii) redox potentials, to make it advantageous to both have enough driving force to performed the desired reaction and recover the metallocenes at a favourable potential.

Therefore, metallocenes are compounds full of promise for photo-catalytic systems. It became obvious to suggest metallocenes with d^6 metal centres (*i.e.* group 8) as potential candidates to reduce protons into hydrogen. For example, Mueller-Westerhoff and Nazzari investigated successfully a binuclear metallocene complex to perform the HER in 1984.¹¹² From that time, various metallocenes containing different transition metals such as cobalt¹¹³, iron¹¹⁴ and osmium^{19,115} have been studied in different systems to reduce or photo-reduce protons. As well as the three-component systems presented above, a judiciously chosen catalyst may be added to improve the system performance.⁵⁸ If the potential is not reductive enough, the complex is activated by light.¹⁹

Thus, no photosensitizer is required. These all-in-one molecules would offer an interesting alternative to state-of-the-art multi-component systems involving multiple electron transfer steps, as a system with fewer barriers to negotiate may potentially be faster. However, only scattered works have proposed the use of a single molecule to achieve the complex photocatalytic H₂ evolution process. Cole-Hamilton¹¹⁶ reported H₂ photo-production from a platinum phosphine complex, while both Miller¹¹⁷ and Gray¹¹⁸ used iridium chloride complexes. Nevertheless, the use of this type of complexes is attractive to replace the catalyst and the sensitizer present in conventional system to photo-produce H₂ at liquid|liquid interfaces and facilitate the batch water-splitting implementation.

1.4.2 Substituent effects on the reactivity of metallocenes

Substituents to Cp ligands impacts metal complexes in several ways. Both the steric bulk and the electronic features of the substituents affect the metal complexes. They induce effects on the molecular structure, physical and chemical properties, spectroscopic properties, electrochemical properties and catalytic activity and selectivity of a complex and can be exploited to optimize metallocenes towards HER as discussed above. Steric effects impact the orientation of the metallocene molecules and the approach of the reactants towards the metal. For example, complexes that include triisopropylcyclopentadienyl ligands ((C₃H₇)₃C₅H₂) are highly air sensitive while the tetraisopropylcyclopentadienyl analogues ((C₃H₇)₄C₅H) are less reactive towards air and nucleophiles. Indeed, the additional C₃H₇ masks the metal active site and prevent the approach of reactants.¹¹⁹ The control of the size and position of substituent on metallocenes was used in polyolefins polymerization to control the molecular weight and the isospecificity of the synthesized polymers.^{120,121} Interestingly, the electronic properties of substituents, either electron donating or electron withdrawing, influences the physical properties of metallocenes complexes and they reactivity. Several metallocenes including various metal centres and Cp ligands or Cp* ligands are summarized in Figure 1.15 with their redox potentials measured in DCE. For the metallocenes including Cp*, the methyl electron-donating groups increase the electron density around the metal centre, making the metal less electrophilic. Thus, these complexes show a lower redox potential (*i.e.* the oxidation of the metal centre is easier). Consequently, when these metallocenes are used for HER, they reduce protons at a lower potential. Electron-withdrawing groups would have the opposite effect, drawing the electron density away from the metal centre, making the metal more

electrophilic and the redox potential higher. This conclusion is corroborated by the work of Mason on phenylferrocenes, which displayed increased redox potential with incorporation of electron-withdrawing group such as NO_2 , COMe , and Br in the structure.¹²²

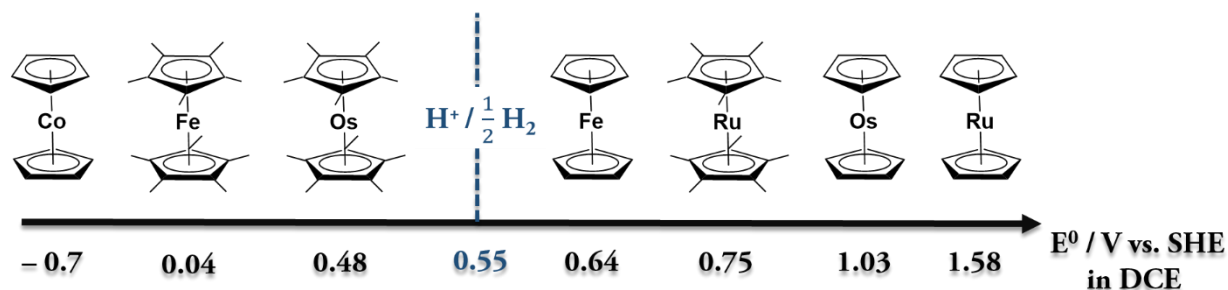
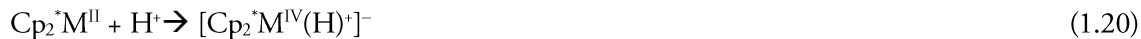


Figure 1.15. Standard redox potential of various metallocenes and protons in DCE.

Cobaltocene ($\text{Cp}_2\text{Co}^{\text{II}}$, $\text{Cp} = \text{C}_5\text{H}_5$) was the first metallocene reported by Grätzel *et al.* to produce H_2 in the dark in 1988.¹¹³ Since this study, our group demonstrated the possibility to performed HER in the dark using $\text{Cp}_2^*\text{Fe}^{\text{II}}$ as an electron donor in a biphasic system.¹¹⁴ Motivated by these early findings, we set out to explore the reactivity of other metallocenes with higher redox potential as suitable electron donors that are easily recoverable. The presence of methyl groups on the Cp^* ring appeared advisable, not only to tailor the redox potential, but also to avoid the formation of dimers during the reaction. However, this particular point was an essential advantage in the case of osmocene ($\text{Cp}_2\text{Os}^{\text{II}}$),¹¹⁵ which splits water by forming the dimer $[\text{Cp}_2\text{Os}^{\text{III}}-\text{Os}^{\text{III}}\text{Cp}_2]^{2+}$. Decamethylosmocene ($\text{Cp}_2^*\text{Os}^{\text{II}}$)¹⁹ also demonstrated capabilities to produce H_2 upon light irradiation. Indeed, both of these metallocenes have higher (more positive) formal redox potentials than $\text{Cp}_2^*\text{Fe}^{\text{II}}$ and they cannot produce H_2 in the dark. Furthermore, as $\text{Cp}_2\text{Os}^{\text{II}}$ ($[E^\circ_{[\text{Cp}_2\text{Os}^{\text{III}}]^{+}/\text{Cp}_2\text{Os}^{\text{II}}}]^{\text{DCE}} = 1.03 \text{ V vs. SHE}$)¹¹⁵ has a high redox potential compared to protons reduction in DCE, the reaction has little driving force (even after photo-activation). Herein, we propose to investigate and to implement in the batch water-splitting the use of decamethylruthenocene ($\text{Cp}_2^*\text{Ru}^{\text{II}}$) as a light-activated electron donor. $\text{Cp}_2^*\text{Ru}^{\text{II}}$ has an intermediate redox potential between that of $\text{Cp}_2\text{Os}^{\text{II}}$ and $\text{Cp}_2^*\text{Os}^{\text{II}}$, which is suitably high to facilitate both the photo-system reset after photo-irradiation and efficient photo-production of H_2 .

1.4.3 Suggested mechanism for HER by metallocenes

The first step of the reaction is the spontaneous formation of a metal hydride in the dark in presence of protons:



This step is well-understood and has been characterized by ^1H NMR measurements.^{19,115} However, the formation of hydrogen during a second step as well as the contribution of light, when metallocene has a too high potential (*i.e.* a too low energy) to induce the electron transfer to generate hydrogen in the dark, were not fully understood yet.

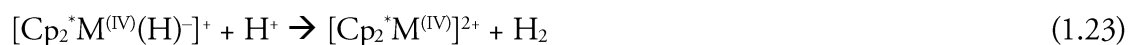
Three different mechanisms were proposed to explain the production of hydrogen from metal hydride metallocenes in the dark or photo-induced. The first possibility is a bimolecular homolytic pathway, known as a Tafel reaction, where two protonated metallocenium ions react to release hydrogen as shown below:



Another possibility is a first reduction of the hydride followed by a protonation allowing the formation of $\text{Cp}_2^*\text{M}^{\text{III}}$ and H_2 :



The last possibility envisaged is a proton attack on the hydride also called a hetero-dissociation reaction resulting in a metallocenium di-hydride which may release H_2 and form a metallocenium ion:



Although the bimolecular pathway is unlikely due to sterically hindered methyl on Cp rings, to date, no experimental result could support or contradict one mechanism more than another. Thus, one goal of this thesis is to clarify the mechanism involved.

1.5 The scope of the present thesis

Chapter II presents experimental details, including instruments and set-ups, synthesis of chemicals, calculations and computational details. The primary aim of this study was to evaluate the suitability

of decamethylruthenocene as the metallocene of choice towards applications in “batch-water splitting”. Therefore, **Chapter III** investigates in detail the photo-production of H_2 by $\text{Cp}_2^*\text{Ru}^{\text{(II)}}$ as a sacrificial electron donor. This chapter sheds light on the reaction mechanisms. Every step is characterised and discussed to provide guidelines to study and compare metallocenes as electron donors for HER. The elucidation of the mechanism indicates that the production of hydrogen occurs by a two-step process. First the formation of decamethylruthenocene hydride ($[\text{Cp}_2^*\text{Ru}^{\text{(IV)}}(\text{H})]^+$) followed by the reversible reduction of this complex *via* a photon excitation process leading to a first release of hydrogen. However, the formed decamethylruthenocenium ion ($[\text{Cp}_2^*\text{Ru}^{\text{(III)}}]^+$) is not stable in these conditions and the complex reduced a second time leading to a second release of hydrogen by subtraction of a proton from a methyl group of $[\text{Cp}_2^*\text{Ru}^{\text{(III)}}]^+$. The reaction leading to the final product ($[\text{Cp}_2^*\text{Ru}^{\text{(IV)}}(\text{C}_5\text{Me}_4\text{CH}_2)]^+$) is not reversible. Therefore, the **Chapter IV** consists of stabilized the transient $[\text{Cp}_2^*\text{Ru}^{\text{(III)}}]^+$ to favour its reduction and recovery the original $\text{Cp}_2^*\text{Ru}^{\text{(II)}}$. The use of weakly coordinating solvent and counter ions provided optimal experimental conditions to achieve this goal. Preliminary experiments investigate the chemical regeneration of synthesized $[\text{Cp}_2^*\text{Ru}^{\text{(III)}}]^+$ by titration. Then, the transient $[\text{Cp}_2^*\text{Ru}^{\text{(III)}}]^+$ generated during the HER was electrochemically regenerated *in-situ* on a Fluorinated Tin Oxide (FTO) electrode surface with a positive onset potential compare to the direct proton reduction on Pt thanks to the photo-activation. Additionally, a promising internal quantum yield of 25 % was obtained. These results in hands, **Chapter V** presents the implementation of the photo-HER by $\text{Cp}_2^*\text{Ru}^{\text{(II)}}$ at the liquid|liquid interface. This Chapter demonstrates that $\text{Cp}_2^*\text{Ru}^{\text{(II)}}$ can act as an electron donor to produce H_2 at chemically polarised soft interfaces. The data recorded by polarisation of the interface by an external voltage compared with COMSOL simulations provide key elements on the mechanism involved to the formation of $[\text{Cp}_2^*\text{Ru}^{\text{(IV)}}(\text{H})]^+$ at the interface. To complete these investigations, **Chapter VI** studies the spectroscopic phenomena during the photo-HER by $\text{Cp}_2^*\text{Ru}^{\text{(II)}}$. In a first stage, in bulk solution to investigate the role of the light excitation in $[\text{Cp}_2^*\text{Ru}^{\text{(IV)}}(\text{H})]^+$ oxidation. In a second stage, at a liquid|liquid interface to characterize the formation $[\text{Cp}_2^*\text{Ru}^{\text{(IV)}}(\text{H})]^+$ from transferred protons. Finally, **Chapter VII** is an opening to adapt HER at liquid|liquid interface to classical systems. A highly hydrophobic sensitizer consisting of a $\text{Ru}(\text{bpy})_3(\text{TB})_2$ salt was introduced to the organic phase. In the presence of TEA, as sacrificial

electron donor, two catalysts inspired by the hydrogenase protein and composed of non-noble metals, were used for the first time at a liquid|liquid interface to perform HER. Each compound was separately studied inside the system. This investigation provides the foundation of an all-purpose soft interface, adaptable to various components and reactions.

To conclude, this thesis provides the foundation of the production of H_2 by $\text{Cp}_2^*\text{Ru}^{(\text{II})}$ in the batch water-splitting while also enhancing our understanding of the chemistry of metallocenes, and especially the metal hydride formation, and the hydrogen evolution reaction. This work is a very significant step forward the spread of photo-HER with metallocenes and the implementation of $\text{Cp}_2^*\text{Ru}^{(\text{II})}$ and metal complex species at liquid|liquid interfaces demonstrates a possible “real world” application of such a system.

1.6 References

- (1) Hoffert, M. I.; Caldeira, K.; Benford, G.; Criswell, D. R.; Green, C.; Herzog, H.; Jain, A. K.; Khesghi, H. S.; Lackner, K. S.; Lewis, J. S. *Science* **2002**, *298*, 981.
- (2) Hayward, T. *Oil and Gas Journal* **2009**, 25 November.
- (3) Shoesmith, D. W. *Journal of Nuclear Materials* **2000**, *282*, 1.
- (4) Morton, O. *Nature* **2006**, *443*, 19.
- (5) Chung, I.; Lee, B.; He, J.; Chang, R. P.; Kanatzidis, M. G. *Nature* **2012**, *485*, 486.
- (6) King, R.; Bhusari, D.; Larrabee, D.; Liu, X. Q.; Rehder, E.; Edmondson, K.; Cotal, H.; Jones, R.; Ermer, J.; Fetzer, C. *Progress in Photovoltaics: Research and Applications* **2012**, *20*, 801.
- (7) Lewis, N. S.; Nocera, D. G. *Proceedings of the National Academy of Sciences* **2006**, *103*, 15729.
- (8) Bard, A. J.; Fox, M. A. *Accounts of Chemical Research* **1995**, *28*, 141.
- (9) Brattain, W.; Garrett, C. *Bell System Technical Journal* **1955**, *34*, 129.
- (10) Gerischer, H. *Annual Review of Physical Chemistry* **1961**, *12*, 227.
- (11) Schrauzer, G.; Guth, T. *Journal of the American Chemical Society* **1977**, *99*, 7189.
- (12) Van Damme, H.; Hall, W. K. *Journal of the American Chemical Society* **1979**, *101*, 4373.
- (13) Kalyanasundaram, K.; Grätzel, M. *Angewandte Chemie International Edition in English* **1979**, *18*, 701.
- (14) Kalyanasundaram, K.; Borgarello, E.; Duonghong, D.; Grätzel, M. *Angewandte Chemie International Edition in English* **1981**, *20*, 987.
- (15) Lehn, J.; Sauvage, J.; Ziessel, R. *New Journal of Chemistry* **1980**; Vol. 4, p 623.
- (16) Kudo, A.; Miseki, Y. *Chemical Society Reviews* **2009**, *38*, 253.
- (17) Fabian, D. M.; Hu, S.; Singh, N.; Houle, F. A.; Hisatomi, T.; Domen, K.; Osterloh, F. E.; Ardo, S. *Energy & Environmental Science* **2015**, *8*, 2825.
- (18) Su, B.; Hatay, I.; Ge, P. Y.; Mendez, M.; Corminboeuf, C.; Samec, Z.; Ersoz, M.; Girault, H. H. *Chemical Communications* **2010**, *46*, 2918.
- (19) Ge, P.; Olaya, A. J.; Scanlon, M. D.; Hatay Patir, I.; Vrubel, H.; Girault, H. H. *ChemPhysChem* **2013**, *14*, 2308.
- (20) Scanlon, M. D.; Bian, X.; Vrubel, H.; Amstutz, V.; Schenk, K.; Hu, X.; Liu, B.; Girault, H. H. *Physical Chemistry Chemical Physics* **2013**, *15*, 2847.
- (21) Hidalgo-Acosta, J. C.; Mendez, M. A.; Scanlon, M. D.; Vrubel, H.; Amstutz, V.; Adamiak, W.; Opallo, M.; Girault, H. H. *Chemical Science* **2015**, *6*, 1761.
- (22) Rivier, L.; Vannay, L.; Mendez, M.; Peljo, P.; Vrubel, H.; Corminboeuf, C.; Scanlon, M. D.; Girault, H. H. **2017**, submitted.
- (23) Nernst, W.; Riesenfeld, E. H. *Annalen der Physik* **1902**, *313*, 600.
- (24) Karpfen, F.; Randles, J. *Transactions of the Faraday Society* **1953**, *49*, 823.
- (25) Gavach, C.; Mlodnick, T.; Guastall, J. *Comptes Rendus Hebdomadaires Des Seances De L Academie Des Sciences Serie C* **1968**, *266*, 1196.
- (26) Reymond, F.; Fermin, D.; Lee, H. J.; Girault, H. H. *Electrochimica acta* **2000**, *45*, 2647.
- (27) Peljo, P.; Girault, H. H. *Encyclopedia of Analytical Chemistry* **2012**.

- (28) Su, B.; Eugster, N.; Girault, H. H. *Journal of Electroanalytical Chemistry* **2005**, *577*, 187.
- (29) Olaya, A. J.; Méndez, M. A.; Cortes-Salazar, F.; Girault, H. H. *Journal of Electroanalytical Chemistry* **2010**, *644*, 60.
- (30) Stockmann, T. J.; Deng, H.; Peljo, P.; Kontturi, K.; Opallo, M.; Girault, H. H. *J. Electroanal. Chem.* **2014**, *729*, 43.
- (31) Ge, P.; Todorova, T. K.; Patir, I. H.; Olaya, A. J.; Vrubel, H.; Mendez, M.; Hu, X.; Corminboeuf, C.; Girault, H. H. *Proc. Natl. Acad. Sci. U. S. A., Early Ed.* **2012**, *1*.
- (32) Samec, Z.; Langmaier, J.; Kakiuchi, T. *Pure Appl. Chem.* **2009**, *81*, 1473.
- (33) Hatay, I.; Su, B.; Li, F.; Méndez, M. A.; Khoury, T.; Gros, C. P.; Barbe, J.-M.; Ersoz, M.; Samec, Z.; Girault, H. H. *Journal of the American Chemical Society* **2009**, *131*, 13453.
- (34) Su, B.; Hatay, I.; Trojánec, A. n.; Samec, Z.; Khoury, T.; Gros, C. P.; Barbe, J.-M.; Daina, A.; Carrupt, P.-A.; Girault, H. H. *Journal of the American Chemical Society* **2010**, *132*, 2655.
- (35) Thomson, F. L.; Yellowlees, L. J.; Girault, H. H. *Journal of the Chemical Society, Chemical Communications* **1988**, 1547.
- (36) Marecek, V.; De Armond, A. H.; De Armond, M. K. *Journal of the American Chemical Society* **1989**, *111*, 2561.
- (37) Osakai, T.; Ogata, A.; Ebina, K. *The Journal of Physical Chemistry B* **1997**, *101*, 8341.
- (38) Peljo, P. Thesis: *Proton Transfer Controlled Reactions at Liquid-Liquid Interfaces*, Aalto University, **2013**.
- (39) Kornyshev, A. A.; Kuznetsov, A. M.; Urbakh, M. *The Journal of Chemical Physics* **2002**, *117*, 6766.
- (40) Koryta, J. *Electrochimica Acta* **1979**, *24*, 293.
- (41) Volkov, A. G.; Deamer, D. W. *Liquid-Liquid Interfaces Theory and Methods*; CRC press, 1996.
- (42) Nestor, U.; Wen, H.; Girma, G.; Mei, Z.; Fei, W.; Yang, Y.; Zhang, C.; Zhan, D. *Chemical Communications* **2014**, *50*, 1015.
- (43) Shao, Y.; Osborne, M. D.; Girault, H. H. *Journal of Electroanalytical Chemistry and Interfacial Electrochemistry* **1991**, *318*, 101.
- (44) Stedman, C.; Barclay, M. *Alimentary pharmacology & therapeutics* **2000**, *14*, 963.
- (45) Kasuno, M.; Uehara, A.; Ichieda, N.; Kitano, T.; Banu, K.; Kihara, S. *Journal of Electroanalytical Chemistry* **2005**, *579*, 223.
- (46) Su, B.; Nia, R. P.; Li, F.; Hojeij, M.; Prudent, M.; Corminboeuf, C.; Samec, Z.; Girault, H. H. *Angewandte Chemie* **2008**, *120*, 4753.
- (47) Olaya, A. J.; Ge, P.; Gonthier, J. F.; Pechy, P.; Corminboeuf, C.; Girault, H. H. *Journal of the American Chemical Society* **2011**, *133*, 12115.
- (48) Conradi, R. A.; Burton, P. S.; Borchardt, R. T. In *Lipophilicity in Drug Action and Toxicology*; Wiley-VCH **2008**, p 233.
- (49) Taylor, J. B.; Kennewell, P. D. *Modern Medicinal Chemistry*; Ellis Horwood Limited, **1993**.
- (50) Arrigan, D. W. *Analytical letters* **2008**, *41*, 3233.
- (51) Herzog, G.; Arrigan, D. W. *Analyst* **2007**, *132*, 615.
- (52) Girault, H. In *Modern Aspects of Electrochemistry*; Springer: **1993**, p 1.

- (53) Senda, M. In *Frontiers in Biosensorics I*; Springer: 1997, p 193.
- (54) Cheng, Y.; Schiffrin, D. J. *Journal of the Chemical Society, Faraday Transactions* 1993, 89, 199.
- (55) Fermín, D. J.; Duong, H. D.; Ding, Z.; Brevet, P.-F.; Girault, H. H. *Journal of the American Chemical Society* 1999, 121, 10203.
- (56) Nieminen, J. J.; Hatay, I.; Ge, P.; Mendez, M. A.; Murtomaki, L.; Girault, H. H. *Chemical Communications* 2011, 47, 5548.
- (57) Hatay, I.; Ge, P. Y.; Vruble, H.; Hu, X.; Girault, H. H. *Energy & Environmental Science* 2011, 4, 4246.
- (58) Ge, P.; Scanlon, M. D.; Peljo, P.; Bian, X.; Vubrel, H.; O'Neill, A.; Coleman, J. N.; Cantoni, M.; Hu, X.; Kontturi, K.; Liu, B.; Girault, H. H. *Chemical Communications* 2012, 48, 6484.
- (59) Dyker, G. *Angewandte Chemie International Edition* 1999, 38, 1698.
- (60) Bolm, C. *Angewandte Chemie International Edition in English* 1993, 32, 232.
- (61) Kalyanasundaram, K.; Grätzel, M. *Coordination chemistry reviews* 1998, 177, 347.
- (62) Zhang, P.; Wang, M.; Dong, J.; Li, X.; Wang, F.; Wu, L.; Sun, L. *The Journal Of Physical Chemistry C* 2010, 114, 15868.
- (63) Okura, I. *Biochimie* 1986, 68, 189.
- (64) Sutin, N.; Creutz, C. *Pure and Applied Chemistry* 1980, 52, 2717.
- (65) Brothers, P. J. *Progress in Inorganic Chemistry, Volume 28* 1981, 1.
- (66) Ramasami, T.; Espenson, J. H. *Inorganic Chemistry* 1980, 19, 1523.
- (67) Kalyanasundaram, K.; Kiwi, J.; Grätzel, M. *Helvetica Chimica Acta* 1978, 61, 2720.
- (68) Hawecker, J.; LEHN, J. M.; Ziessel, R. *Chemischer Informationsdienst* 1983, 14.
- (69) Esswein, A. J.; Nocera, D. G. *Chemical Reviews* 2007, 107, 4022.
- (70) Dempsey, J. L.; Brunschwig, B. S.; Winkler, J. R.; Gray, H. B. *Accounts of Chemical Research* 2009, 42, 1995.
- (71) Zeitler, K. *Angewandte Chemie International Edition* 2009, 48, 9785.
- (72) Smiljanić, M.; Srejić, I.; Grgur, B.; Rakočević, Z.; Štrbac, S. *Electrochemistry Communications* 2013, 28, 37.
- (73) Kiwi, J.; Grätzel, M. 1979.
- (74) Sreethawong, T.; Yoshikawa, S. *Catalysis Communications* 2005, 6, 661.
- (75) Wang, M.; Chen, L.; Li, X.; Sun, L. *Dalton Transactions* 2011, 40, 12793.
- (76) Jones, A. K.; Sillery, E.; Albracht, S. P.; Armstrong, F. A. *Chemical Communications* 2002, 866.
- (77) Tard, C.; Pickett, C. J. *Chemical Reviews* 2009, 109, 2245.
- (78) Capon, J.-F.; Gloaguen, F.; Schollhammer, P.; Talarmin, J. *Coordination chemistry reviews* 2005, 249, 1664.
- (79) Ott, S.; Kritikos, M.; Åkermark, B.; Sun, L.; Lomoth, R. *Angewandte Chemie-International Edition* 2004, 116, 1024.
- (80) Manor, B. C.; Rauchfuss, T. B. *Journal of the American Chemical Society* 2013, 135, 11895.
- (81) El Kadiri, M. Y.; El Ghachtouli, S.; Guillot, R.; Billon, L.; Charlot, M. F.; Framery, E.; Andrioletti, B.; Aukauloo, A. *ChemSusChem* 2012, 5, 2147.

- (82) Hu, X.; Brunschwig, B. S.; Peters, J. C. *Journal of the American Chemical Society* **2007**, *129*, 8988.
- (83) Fihri, A.; Artero, V.; Razavet, M.; Baffert, C.; Leibl, W.; Fontecave, M. *Angewandte Chemie International Edition* **2008**, *47*, 564.
- (84) Kolawole, G. A.; Ndahi, N. P. *Synthesis and Reactivity in Inorganic and Metal-Organic Chemistry* **2004**, *34*, 1563.
- (85) Hinnemann, B.; Moses, P. G.; Bonde, J.; Jørgensen, K. P.; Nielsen, J. H.; Horch, S.; Chorkendorff, I.; Nørskov, J. K. *Journal of the American Chemical Society* **2005**, *127*, 5308.
- (86) Merki, D.; Fierro, S.; Vrubel, H.; Hu, X. *Chemical Science* **2011**, *2*, 1262.
- (87) Liao, L.; Zhu, J.; Bian, X.; Zhu, L.; Scanlon, M. D.; Girault, H. H.; Liu, B. *Advanced Functional Materials* **2013**, *23*, 5326.
- (88) Lukowski, M. A.; Daniel, A. S.; Meng, F.; Forticaux, A.; Li, L.; Jin, S. *Journal of the American Chemical Society* **2013**, *135*, 10274.
- (89) Zhang, C.-R.; Han, L.-H.; Zhe, J.-W.; Jin, N.-Z.; Wang, D.-B.; Wang, X.; Wu, Y.-Z.; Chen, Y.-H.; Liu, Z.-J.; Chen, H.-S. *Computational and Theoretical Chemistry* **2013**, *1017*, 99.
- (90) Chen, X.; Shen, S.; Guo, L.; Mao, S. S. *Chemical reviews* **2010**, *110*, 6503.
- (91) Hodes, G. *The Journal of Physical Chemistry C* **2008**, *112*, 17778.
- (92) Ni, M.; Leung, M. K.; Leung, D. Y.; Sumathy, K. *Renewable and Sustainable Energy Reviews* **2007**, *11*, 401.
- (93) Cheung, S. T.; Fung, A. K.; Lam, M. H. *Chemosphere* **1998**, *36*, 2461.
- (94) Pérez León, C.; Kador, L.; Peng, B.; Thelakkat, M. *The Journal of Physical Chemistry B* **2006**, *110*, 8723.
- (95) Teplý, F. *Collection of Czechoslovak Chemical Communications* **2011**, *76*, 859.
- (96) Bonnett, R. *Chemical Society Reviews* **1995**, *24*, 19.
- (97) Kirch, M.; Lehn, J. M.; Sauvage, J. P. *Helvetica Chimica Acta* **1979**, *62*, 1345.
- (98) Goldsmith, J. I.; Hudson, W. R.; Lowry, M. S.; Anderson, T. H.; Bernhard, S. *Journal of the American Chemical Society* **2005**, *127*, 7502.
- (99) Britovsek, G. J.; Gibson, V. C.; Wass, D. F. *Angewandte Chemie International Edition* **1999**, *38*, 428.
- (100) Montalti, M.; Credi, A.; Prodi, L.; Gandolfi, M. T. *Handbook of photochemistry*; CRC press, 2006.
- (101) Mishra, A.; Fischer, M. K.; Bäuerle, P. *Angewandte Chemie International Edition* **2009**, *48*, 2474.
- (102) Li, Y.; Xie, C.; Peng, S.; Lu, G.; Li, S. *Journal of Molecular Catalysis A: Chemical* **2008**, *282*, 117.
- (103) Nowakowska, M.; Sterzel, M.; Zapotoczny, S.; Kot, E. *Applied Catalysis B: Environmental* **2005**, *57*, 1.
- (104) Balzani, V.; Credi, A.; Venturi, M. *ChemSusChem* **2008**, *1*, 26.
- (105) Ozawa, H.; Haga, M.-a.; Sakai, K. *Journal of the American Chemical Society* **2006**, *128*, 4926.
- (106) Sayama, K.; Mukasa, K.; Abe, R.; Abe, Y.; Arakawa, H. *Journal of Photochemistry and Photobiology A: Chemistry* **2002**, *148*, 71.
- (107) Koca, A.; Şahin, M. *International Journal of Hydrogen Energy* **2002**, *27*, 363.
- (108) Li, Y.; Lu, G.; Li, S. *Chemosphere* **2003**, *52*, 843.

- (109) Moss, G. P.; Smith, P. A. S.; Tavernier, D. *Pure and Applied Chemistry* **1995**; Vol. 67, p 1307.
- (110) Kealy, T.; Pauson, P. *Nature* **1951**, 168, 1039.
- (111) Miller, S. A.; Tebboth, J. A.; Tremaine, J. F. *Journal of the Chemical Society (Resumed)* **1952**, 632.
- (112) Mueller-Westerhoff, U. T.; Nazzari, A. *Journal of the American Chemical Society* **1984**, 106, 5381.
- (113) Koelle, U.; Infelta, P. P.; Graetzel, M. *Inorganic Chemistry* **1988**, 27, 879.
- (114) Hatay, I.; Su, B.; Li, F.; Partovi-Nia, R.; Vrubel, H.; Hu, X.; Ersoz, M.; Girault, H. H. *Angewandte Chemie International Edition* **2009**, 48, 5139.
- (115) Ge, P.; Todorova, T. K.; Patir, I. H.; Olaya, A. J.; Vrubel, H.; Mendez, M.; Hu, X.; Corminboeuf, C.; Girault, H. H. *Proceedings of the National Academy of Sciences* **2012**, 109, 11558.
- (116) Jones, R. F.; Cole-Hamilton, D. J. *Journal of the Chemical Society, Chemical Communications* **1981**, 1245.
- (117) Pitman, C. L.; Miller, A. J. M. *ACS Catalysis* **2014**, 4, 2727.
- (118) Gray, H. B.; Maverick, A. W. *Science* **1981**, 214, 1201.
- (119) Burkey, D. J.; Hays, M. L.; Duderstadt, R. E.; Hanusa, T. P. *Organometallics* **1997**, 16, 1465.
- (120) Obora, Y.; Stern, C. L.; Marks, T. J.; Nickias, P. N. *Organometallics* **1997**, 16, 2503.
- (121) Giardello, M. A.; Eisen, M. S.; Stern, C. L.; Marks, T. J. *Journal of the American Chemical Society* **1995**, 117, 12114.
- (122) Mason, J. G.; Rosenblum, M. *Journal of the American Chemical Society* **1960**, 82, 4206.

2. Experimental, Instrumentation and Simulations

2.1	Chemicals.....	36
2.1.1	Reagents	36
2.1.2	Synthesis.....	37
2.1.2.1	Preparation of Bis(triphenyl-phosphoranylidene) ammonium tetrakis(pentafluorophenyl)borate electrolyte (BATB).....	37
2.1.2.2	Preparation of tetrakis(pentafluorophenyl)borate diethyl etherate acid ([H(OEt ₂) ₂]TB).....	37
2.1.2.3	Preparation of Tris(2,2'-bipyridyl)ruthenium(II) tetrakis(pentafluorophenyl)-borate ([RuII(bpy) ₃]TB ₂)	39
2.2	Electrochemical methods.....	39
2.2.1	Three-electrode system	39
2.2.2	Bulk electrolysis experiments	40
2.2.3	Spectroelectrochemistry experiments	40
2.2.4	Four-electrode system.....	41
2.2.5	Electrode preparation	41
2.2.5.1	FTO electrodes washing.....	41
2.2.5.2	Aqueous reference electrodes preparation	42
2.2.5.3	Reference electrode for measurements in organic media	42
2.3	Photo-generation of H ₂ by Cp ₂ *Ru ^(II) in single or biphasic solutions.....	42
2.3.1	Experimental	42
2.3.2	Gas chromatography (GC), UV/vis and NMR spectroscopy	43
2.4	Measurements of the quantum yield and photon flux calculation of the source	43
2.4.1	Photon flux calculation of the source.....	43

2.4.2	Wavelength dependence of the HER by $\text{Cp}_2^*\text{Ru}^{\text{III}}$	44
2.5	Second Harmonic Generation set-up.....	44
2.6	Water DCE, shake-flask methodology.....	45
2.7	COMSOL: simulation details.....	45
2.7.1	Finite Element Simulations of the Photo-Electrocatalysis of Proton Reduction by Decamethylruthenocene.....	45

2.1 Chemicals

2.1.1 Reagents

All chemicals were used as received without further purification. All aqueous solutions were prepared with ultrapure water (Millipore Milli-Q, specific resistivity 18.2 M Ω cm). The solvents used were 1,2-dichloroethane (DCE, ≥ 99.8 %, Fluka), α, α, α -trifluorotoluene (TFT, ≥ 99 %, Sigma-Aldrich), deuterated dichloromethane (CD_2Cl_2 , 99.8+ atom % D, Merck), hydrochloric acid (HCl, 37 %, Merck) and sulfuric acid (H_2SO_4 , 98 %, Merck). Decamethylruthenocene ($\text{Cp}_2^*\text{Ru}^{\text{III}}$, 99 %) was supplied by ABCR and stored in a N_2 -filled glove-box until use. Ferrocenium hexafluorophosphate ($[\text{Cp}_2^*\text{Fe}^{\text{III}}]\text{PF}_6$, 97%), trifluoromethanesulfonic acid ($\text{CF}_3\text{SO}_3\text{H}$, 98 %), trifluoroacetic acid ($\text{CF}_3\text{CO}_2\text{H}$, ≥ 99.0 %), tetrabutylammonium hexafluorophosphate (TBAPF₆, ≥ 99.0 %) and dichloromethane (DCM, 99,9 %) were obtained from Sigma-Aldrich. Bis(triphenylphosphoranylidene)ammonium chloride (BACl, 98%) was purchased from Fluka. Lithium tetrakis-(pentafluorophenyl)borate ethyl etherate ($\text{Li}(\text{OEt}_2)_2\text{TB}$ purum) was purchased from Boulder Scientific. Anhydrous lithium chloride (LiCl , ≥ 99 %), anhydrous sodium sulfate (Na_2SO_4 , ≥ 99 %), and tetraethylammonium chloride (TEACl, ≥ 98 %) were obtained from Fluka. MoS_2 grown on mesoporous carbon was obtained through Professor Baohong Liu (Fudan University, Shanghai, China) and $\text{Fe}_2(\mu\text{-SCH}_2\text{C}_6\text{H}_4\text{CH}_2\text{S})(\text{CO})_6$ was provided by Frédéric Gloaguen (Université de Bretagne Occidentale, Brest, France). Chloro(pyridine)bis(dimethylglyoximate)cobalt(III) was purchased from Aldrich.

2.1.2 Synthesis

2.1.2.1 Preparation of Bis(triphenyl-phosphoranylidene) ammonium tetrakis(pentafluorophenyl)borate electrolyte (BATB)

1.4 g of $[\text{Li}(\text{OEt}_2)_2]\text{TB}$ and 918 mg of BACl were separately dissolved in water. Then, the two solutions were mixed (final volume ≈ 60 mL). The obtained white precipitate from the metathesis reaction was separated by filtration and washed with water before complete dilution in acetone to obtain a clear solution. Then, water was added and the solution became turbid. The acetone was evaporated under reduced pressure and the obtained white product was filtrated and dried overnight under reduced pressure.

2.1.2.2 Preparation of tetrakis(pentafluorophenyl)borate diethyl etherate acid ($[\text{H}(\text{OEt}_2)_2]\text{TB}$)

- *Synthesis of $[\text{H}(\text{OEt}_2)_2]\text{TB}$*

3 g of $[\text{Li}(\text{OEt}_2)_2]\text{TB}$ was dissolved in 30 mL of 6 M HCl to prepare $[\text{H}(\text{OEt}_2)_2]\text{TB}$. To ensure that the $\text{H}(\text{OEt}_2)_2^{2+}$ cation was formed a few mLs of ether were added to this mixture. The latter is a critical step in the synthesis as the non-etherated version of this acid, $[\text{H}]\text{TB}$, although predicted to be an exceptionally strong acid,¹ cannot be synthesised as the TB^- is unstable with respect to B-phenyl bond cleavage.² The diethyl etherate prepared here is a weaker acid than the theoretical non-etherated $[\text{H}]\text{TB}$ but much more stable.³⁻⁵ Next, $[\text{H}(\text{OEt}_2)_2]\text{TB}$ from the metathesis reaction was extracted by addition of DCM (30 mL) and the aqueous layer was further washed with DCM (2×15 mL) after phase separation. The combined organic layers were dried over sodium sulfate (Na_2SO_4 , Reactolab). Finally, Na_2SO_4 was removed by filtration and DCM evaporated under reduced pressure to yield the organic soluble acid $[\text{H}(\text{OEt}_2)_2]\text{TB}$ as a white powder.

- *Characterization of $[\text{H}(\text{OEt}_2)_2]\text{TB}$*

^1H NMR measurements in Figure 2.1.(A) & (B) confirm the presence of hydrogen bonding on the diethyl ether oxygen atom of $[\text{H}(\text{OEt}_2)_2]\text{TB}$ acid. In spectra (A), $[\text{H}(\text{OEt}_2)_2]\text{TB}$, in presence of a base in excess (here, $\text{Cp}_2^*\text{Ru}^{(\text{III})}$), is entirely deprotonated. The signal for the protonated base is labelled as ▼. The signal for unreacted base (labelled with ●) is small, indicating the majority, but not all, of the base in the NMR tube has reacted to form the hydride. Two distinct signals

appear for protons of the non-protonated diethyl ether at 1.15 and 3.43 ppm, corresponding to the protons of the $-\text{CH}_3$ and $-\text{CH}_2$ groups, respectively. Their multiplicity due to the spin coupling is well-defined. However, in spectra (B), where $[\text{H}(\text{OEt}_2)_2]\text{TB}$ is present in excess compared to the base, significant amounts of protonated diethyl ether remain in the NMR tube. Thus, with protonated diethyl ether the chemical shifts are strongly affected by the hydrogen bonding on oxygen atom. The phenomena is more pronounced for the $-\text{CH}_2$ group located closer of the oxygen. This signal broadens and the multiplicity is smeared, owing to the labile nature of the hydrogen bonding. As the $-\text{CH}_3$ and $-\text{CH}_2$ groups become electron poor, this causes the signals to move downfield to 1.33 and 3.85 ppm, respectively.

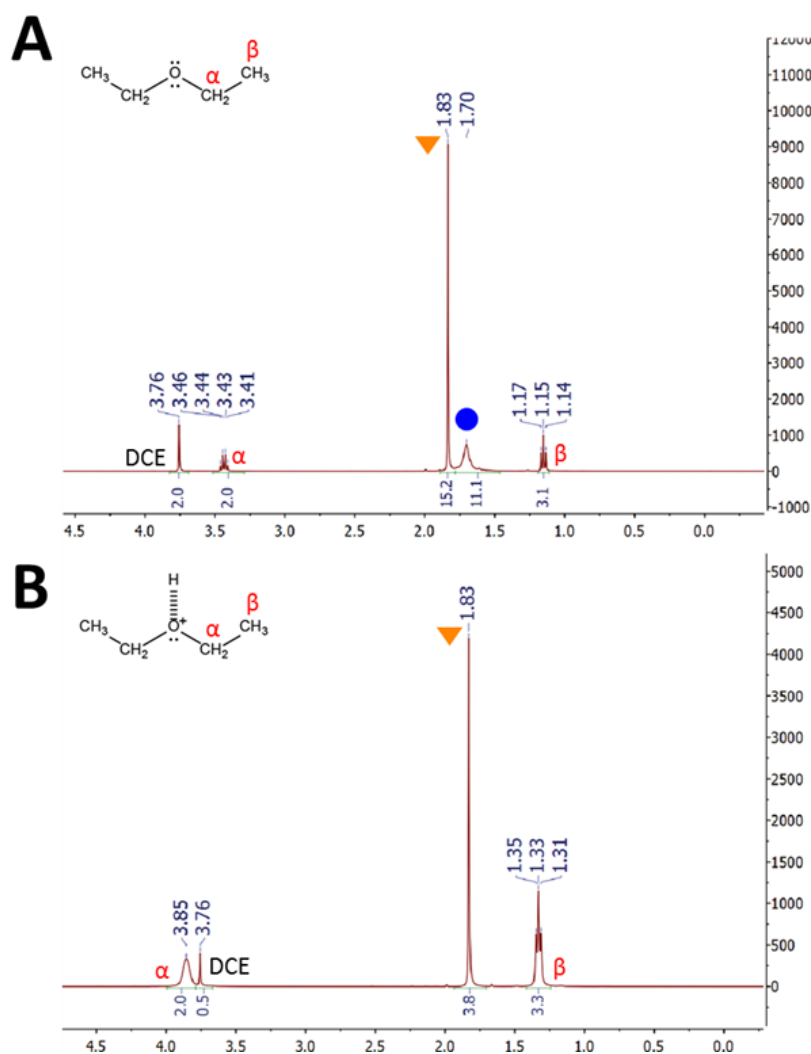


Figure 2.1. ^1H NMR spectra of (A) 15 mM organic base and 12.5 mM $[\text{H}(\text{OEt}_2)_2]\text{TB}$, and (B) 15 mM organic base and excess (50 mM) $[\text{H}(\text{OEt}_2)_2]\text{TB}$.

2.1.2.3 Preparation of Tris(2,2'-bipyridyl)ruthenium(II) tetrakis(pentafluorophenyl)borate ([RuII(bpy)₃]TB₂)

[Ru^{II}(bpy)₃]TB₂ was synthesized by metathesis. 1 equivalent of lithium tetrakis(pentafluorophenyl)borate ethyl etherate (LiTB-DEE) dissolved in a minimum of water was added drop by drop to a concentrated water solution of 1 eq of tris(2,2'-bipyridyl)ruthenium(II) chloride hexahydrate ([Ru^{II}(bpy)₃]Cl₂·6H₂O) supplied by Sigma-Aldrich. The solution was stirred during 2 hours. The obtained orange precipitate was filtered and washed with water and then dried under vacuum for 12 hours.

2.2 Electrochemical methods

2.2.1 Three-electrode system

Cyclic voltammetry (CV) and chronoamperometry experiments were performed in a three-electrode configuration using a PGSTAT 30 potentiostat (Metrohm, CH) under anaerobic conditions in a N₂-filled glove-box and at ambient temperatures. CVs were calibrated *versus* the formal reduction potential of Cp₂*Fe^(III) in DCE on the standard hydrogen electrode (SHE) scale ($[E^0_{\text{Cp}_2\text{Fe}(\text{III})^+/\text{Cp}_2\text{Fe}(\text{III})}]^{\text{DCE}} = 0.07 \text{ V vs. SHE}$).⁶

Chapter III and Chapter VII. A glassy carbon working electrode (2 mm diameter) was immersed in a solution of DCE containing 100 or 10 mM TBAPF₆ as supporting electrolyte. CVs were obtained using silver and platinum wires as the reference and counter electrodes.

Chapter IV. A fluorinated tin oxide (FTO) working electrode (15 Ω per sq, 2.2 mm thickness, Solaronix) was contacted with a solution of DCE containing 0.1 M TBAPF₆ as supporting electrolyte. CVs were obtained using a platinum (Pt) wire (for electrochemical measurements) or Pt disk (2 mm Ø, for gas measurements) as the counter electrode. For the controlled potential electrolysis experiments, a potential of 0.50 V *vs.* SHE was applied, *i.e.*, a sufficiently negative potential to regenerate [Cp₂*Ru^(III)]⁺ but not so negative as to spontaneously evolve H₂ on the FTO electrode surface in the dark. The cell was illuminated by a 365 nm LED (Thorlabs, M365L2) through the FTO electrode as illustrated in Figure 2.2.

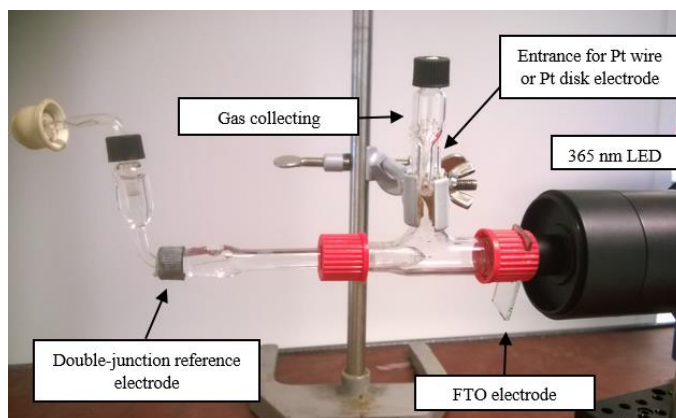


Figure 2.2. Cell used for photo-electrochemical measurements and collection of H₂ gas.

2.2.2 Bulk electrolysis experiments

Bulk oxidative electrolysis of Cp₂*Ru^(II) was carried out using a PGSTAT 30 potentiostat (Metrohm, CH) under anaerobic conditions in a N₂-filled glove-box and at ambient temperatures. A classic bulk electrolysis cell configuration was employed using Duocel[®] reticulated vitreous carbon (RVC, pores/inch = 30; relative density 3%, supplied by ERG Aerospace Corporation, USA) as the working and counter electrodes, respectively, and a Ag/Ag⁺ wire organic reference electrode. The single-junction Ag/Ag⁺ organic reference electrode was constructed by immersing a Ag wire in a solution containing 20 mM BATB and separating this solution from the anodic compartment using a porous Vycor[®] tip (BASi). The anodic chamber was filled with de-oxygenated DCE containing Cp₂*Ru^(II) and 20 mM BATB as supporting electrolyte. Meanwhile the cathodic compartment was filled with a solution of ferrocenium cations (specifically [Cp₂*Fe^(III)]PF₆) to reduce the total voltage between the working and the counter electrodes, again with 20 mM BATB as supporting electrolyte. The compartments were separated by a glass wool plug to prevent re-reduction of Cp₂*Ru^(II) at the RVC counter electrode. The volume of the anodic compartment was 7 mL. Once more, the potentials applied by chronoamperometry are reported *vs.* aqueous SHE in DCE and calibrated relative to $[E^0_{[\text{Cp}_2\text{Fe}(\text{III})]^+/\text{Cp}_2\text{Fe}(\text{III})}]^{\text{DCE}}$ *vs.* SHE.

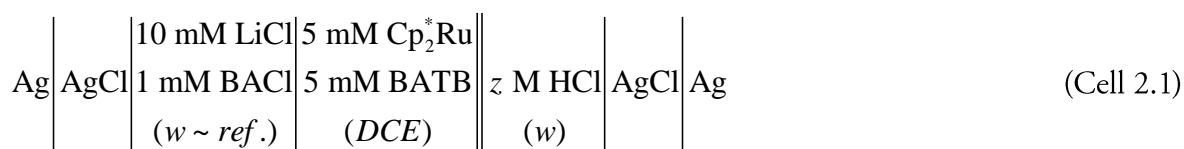
2.2.3 Spectroelectrochemistry experiments

A 6 mM solution of Cp₂*Ru^(II) in DCE with 20 mM BATB as supporting electrolyte, was placed in a thin-layer quartz cuvette with a path length of 1 mm (BASi, USA). The cell configuration was composed of a Pt mini-grid as the working electrode, a Pt wire as the counter electrode and reference electrode described below. The solution was oxidized using chronoamperometry for 120

s at a series of applied potentials spaced at regular intervals between 0.22 and 0.91 V (*vs.* SHE). The response was followed by UV/vis spectroscopy.

2.2.4 Four-electrode system

Charge transfer reactions between water and DCE were characterized using a traditional four electrode, electrolytic cell, as described previously,⁷⁻⁹ with an interfacial surface area of $\sim 1.53 \text{ cm}^2$, and controlled through a PGSTAT 30 potentiostat (Metrohm, CH). Two platinum counter electrodes, connected to the working and counter electrode leads of the potentiostat were positioned in the aqueous and organic phases, respectively, and supplied the current. An external potential was applied by means of Ag/AgCl reference electrodes placed in Luggin capillaries whose tapered openings were positioned proximal and on opposing sides of the ITIES. This configuration can be described through Cell 2.1 as an example below:



The measured Galvani potential difference across the w|DCE interface, $\Delta_o^w \phi$, was calibrated relative to the formal ion transfer potential of the tetraethylammonium cation (TEA^+), taken to be 0.019 V,¹⁰ excepted for the determination of the formal ion transfer potential of the $[\text{Cp}_2^*\text{Ru}^{(\text{III})}]^+$ ion, $\Delta_o^w \phi_{[\text{Cp}_2^*\text{Ru}^{(\text{III})}]^+}^{o'}$, which was calibrated relative to the formal ion transfer potential ($\Delta_o^w \phi^{o'}$) of tetramethylammonium cation (TMA^+), taken to be 0.160 V.¹¹ The half-wave ion transfer potentials ($\Delta_o^w \phi_{1/2}$) of TEA^+ and TMA^+ were determined using CV. Experiments were performed with aqueous and organic phases thoroughly degassed using nitrogen, under anaerobic conditions in a nitrogen filled glove box, in the dark, and at an ambient temperature, unless otherwise stated.

2.2.5 Electrode preparation

2.2.5.1 FTO electrodes washing

FTO plates were immersed in 4.7% KOH in ethanol/water (4:1) mixture and sonicated for 5 minutes. Then, the plates were washed with water and immersed in 0.1 M H_2SO_4 . Subsequently, they were washed a second time with water and finally dried.

2.2.5.2 Aqueous reference electrodes preparation

The reference electrodes, Ag/AgCl and Ag/Ag₂SO₄, were prepared by electrolysis of a clean silver wire as anode and platinum wire as cathode in a 0.1 M HCl and 5 mM Li₂SO₄ solution respectively, at a output voltage of 1.5 V.

2.2.5.3 Reference electrode for measurements in organic media

The reference electrode used for measurements in organic media was a double-junction reference electrode encompassing a Pt wire. The inner chamber contained a Pt wire in a solution of 0.1 M TBAPF₆ in acetonitrile and was separated by from the outer chamber containing the same solution by a porous silica bead, replacing the typically used Vycor(R) porous glass frit. The cracked Pt junction connected the electrochemical cell and the outer chamber.

2.3 Photo-generation of H₂ by Cp₂*Ru^(II) in single or biphasic solutions

2.3.1 Experimental

Test solutions for photochemical reactions analyzed by either gas chromatography or UV/vis spectroscopy were prepared in degassed DCE solvent under anaerobic conditions in a N₂-filled glove-box and at ambient temperatures. Anaerobic conditions were necessary to avoid any potential competing side reactions of Cp₂*Ru^(II) with O₂. Degassed solutions were transferred into a quartz cell (Hellma), with an optical path length of 1 cm and containing a small magnetic stirrer and sealed with Suba-seal® septa (Sigma-Aldrich). Once filled and sealed, the quartz cells were removed from the glove-box and all photochemical reactions were performed by irradiation with white light from a 500 W Xenon lamp (Oriel, Research Arc Lamp Source) or a 365 nm LED (Thorlabs, M365L2) under stirring conditions as specified in respective chapters.

Test solutions for photochemical reactions analysed by ¹H NMR and ¹³C NMR spectroscopy in Chapter III were also prepared under anaerobic conditions but directly in glass NMR tubes using degassed CD₂Cl₂ as solvent. The NMR tubes were also sealed, removed from the glove-box and irradiated with white light while being agitated using a vortex. Also, the species in the reaction mixture after photo-irradiation of acidified organic solutions of Cp₂*Ru^(II) were separated by column chromatography (DCM/hexane, 6:4 and then 8:2) and an orange powder was obtained as the final product for NMR analysis.

2.3.2 Gas chromatography (GC), UV/vis and NMR spectroscopy

- *GC*

1 mL samples of the headspace gas were obtained by using a lock-in syringe with a push–pull valve (SGE Analytical Sciences) and subsequently analyzed by a Thermo Scientific gas chromatograph (Trace 1300, equipped with a 20 μ L loop, HAYESEP DB and an 100/120 mesh) for Chapter IV and a PerkinElmer gas chromatograph (Clarus 400, equipped with a 20 μ L loop, 5 Å molecular sieves and an 80/100 mesh) for Chapter III, V and VII. Both were equipped with a thermal conductivity detector (TCD) and argon as the carrier gas.

- *UV/vis spectroscopy*

An Ocean Optics USB 2000+ fiber optic spectrophotometer was employed for kinetics experiments. All other UV/vis analysis, including spectro-electrochemical analysis (discussed *vide infra*), was performed on an Agilent Carry 8453 photodiode array spectrophotometer.

- *^1H and ^{13}C NMR analysis*

All NMR analysis was performed on a Bruker Biospin Avance-400 spectrometer. Chemical shifts are expressed in parts per million (ppm) relative to CD_2Cl_2 ($\delta = 5.32$ ppm for ^1H NMR and $\delta = 53.84$ ppm for ^{13}C NMR spectra).¹² DCE was used as an internal standard and added at a concentration of 31.2 mM.

2.4 Measurements of the quantum yield and photon flux calculation of the source

2.4.1 Photon flux calculation of the source

In Chapter IV, the photon flux was calculated by measuring the LED power, which was adjusted to a desired value and measured using a Newport 918D-UV-OD3 assuming all photons had the same wavelength of 365 nm (5.45×10^{-19} Joule/photon). In this adjustment of the power we accounted for the irradiated area over the sample, as well as for the absorption of the reaction cell window and other minor losses in the setup.

The LED wavelength (λ) used was 365 nm; therefore the energy each photon carries is:

$$E_{\text{photon}} = (h \cdot c) / \lambda = 6.626 \times 10^{-34} (\text{J} \cdot \text{s}^{-1}) \cdot 3 \times 10^8 (\text{m} \cdot \text{s}^{-1}) / 365 \times 10^{-9} (\text{m}) \quad (2.1)$$

$$E_{\text{photon}} = 5.45 \times 10^{-19} \text{ J / photon} \quad (2.2)$$

where h is Planck's constant and c is the speed of light.

The LED power was set to 11 mW, thus the photon flux (amount of photons per second) is given by:

$$\begin{aligned}\text{Photon flux} &= \text{LED power} / E_{\text{photon}} \\ &= 11 \times 10^{-3} \text{ (J} \cdot \text{s}^{-1}) / 5.45 \times 10^{-19} \text{ (J / photon)} \\ &= 2.0 \times 10^{16} \text{ photons} \cdot \text{s}^{-1}\end{aligned}\tag{2.3}$$

In Chapter IV, the transmittance observed from the transmittance spectrum presented in the appendix, was used to calculate the External Quantum Yield (EQY).

2.4.2 Wavelength dependence of the HER by $\text{Cp}_2^*\text{Ru}^{\text{III}}$

A solution of 6 mM $\text{Cp}_2^*\text{Ru}^{\text{III}}$ with 12 mM $[\text{H}(\text{OEt}_2)_2]\text{TB}$ was prepared inside a glove box, introduced in a quartz cell and sealed with a septa. Then, the cell was illuminated outside the glove box under stirring conditions for 10 min. at various wavelengths with a Ekspla PL2230 Series combined with a Ekspla PG400 Series OPG laser. The power was modulated in order to keep the number of emitted photon constant and equal to 1.8 μmol .

2.5 Second Harmonic Generation set-up

The setup consisted of an Ekspla PG400 Series OPG laser pumped by an Ekspla PL2230 Series laser producing ≈ 30 ps long pulses at a frequency of 50Hz in the range of 210 – 1600 nm. The delay between the pulses was controlled by a BNC 575 pulse delay generator. The precision of the delay was limited by the lasers' jitter (10 ns according to the manufacturer). The energy of the probe pulses, typically of the order of 100 μJ , was decreased to 10 μJ by a neutral density filter to avoid damaging the interface. The linear polarisation of the probe beam was modified thanks to a half-wave plate (Thorlabs AHWP05M-980). Its orientation was automatically controlled. The pulses were then filtered by a long pass colour filter (Thorlabs FGL 780) just before the interface to remove any unwanted second harmonic signal generated by the optical components. Then, the beam was focused on the interface in a spot of *ca.* 0:01 cm^2 . The fundamental beam was subsequently filtered by a bandpass filter (Thorlabs FGB37S), while the second harmonic signal was collected by a lens (Thorlabs LA 4380) and arrived to the monochromator (Monochromator Triax 320). Therefore, the light was detected by a photomultiplier (Hamamatsu R928), whose

signal is amplified and sent to a boxcar triggered by the probe laser. Finally, the SHG is recorded by a “Labview” (National Instrument) software that also control the half-wave plate, the probe laser and the delay generator. The polarization of the interface was controlled by a four-electrode cell as described in Section 2.2.4.

2.6 Water|DCE, shake-flask methodology

All anaerobic experiments were prepared using aqueous and organic solutions previously saturated with nitrogen and transferred to a nitrogen filled glove box; wherein, samples were either placed in a black box for dark conditions or illuminated with white-light using a 500 W Xenon lamp (Oriel, Research Arc Lamp Source).

Two-phase – so-called ‘shake-flask’ – experiments were performed in septum-sealed glass vials with a solution comprised of an oil (o) phase of DCE and an aqueous (w) phase whose compositions are exemplified schematically in Vial 2.1, below:



After combining the two phases, a magnetic stirrer was added, the vial was sealed, and then stirred for 60 min at ambient temperature.

1 mL portions of the headspace gas from shake-flask vials were sampled using a lock-in syringe and subsequently analysed *via* injection into a Gas Chromatograph (PerkinElmer GC).

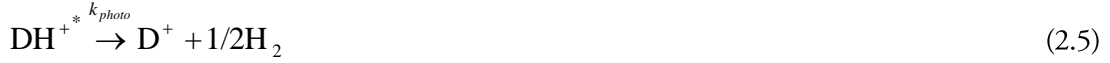
UV/Vis spectra were recorded with an Agilent Carry 8453 photodiode array spectrophotometer employing a quartz cell with an optical path length of 1 cm.

2.7 COMSOL: simulation details

2.7.1 Finite Element Simulations of the Photo-Electrocatalysis of Proton Reduction by Decamethylruthenocene

The simulations were made by Dr. Pekka Peljo, a fellow scientist at LEPA. A finite element model was constructed within COMSOL Multiphysics software (v.5.1) utilizing a 1D geometry to simulate the system performance, with the light entering the cell at the back of the transparent electrode. In the system, the photo-excited decamethylruthenocene hydride DH^+ will form the

photo-excited state DH^{+*} , that will either undergo homolytic bond cleavage to produce hydrogen or relax back to DH^+ .



The oxidised decamethylruthenocene D^+ can be reduced to decamethylruthenocene D at the electrode ($x = 0$), and D can be protonated to regenerate DH^+ , with the equilibrium constant $K = k_1/k_{-1}$.



The absorption of light by species i is described by eq. 2.10 (resulting in Lambert-Beer law).^[18–20]

$$\nabla \cdot I = - \sum \epsilon_i c_i I \quad (2.10)$$

where I is the molar flux of photons expressed as $\text{mol} \cdot \text{cm}^{-2} \cdot \text{s}^{-1}$, ϵ_i the extinction coefficient of i and c_i is the concentration of i . The light at the intensity of I_0 is shining through the light electrode at $x = 0$. The transient transport equations including the reactions can be written for all the species participating in the reaction:

$$\frac{\partial c_{\text{DH}^+}}{\partial t} = \nabla \cdot (D_{\text{DH}^+} \nabla c_{\text{DH}^+}) - \epsilon_{\text{DH}^+} c_{\text{DH}^+} I + k_{\text{rec}} c_{\text{DH}^{+*}} + k_1 c_{\text{D}} c_{\text{H}^+} - k_{-1} c_{\text{DH}^+} \quad (2.11)$$

Where, $\epsilon_{\text{DH}^+} c_{\text{DH}^+} I$ is the rate of the photo-excitation, k_{rec} is the relaxation rate constant of the excited state (2.6) and k_1 and k_{-1} are the forwards and backwards reaction rate constants of the protonation/deprotonation reactions (2.8-2.9). To have the correct units for all the terms in eq. 2.11, the light intensity has to be expressed as molar flux of photons ($\text{mol} \cdot \text{cm}^{-2} \cdot \text{s}^{-1}$), as described earlier by Alberly *et al.*¹³ and by us.^{14,15} Correspondingly for other species:

$$\frac{\partial c_D}{\partial t} = \nabla \cdot (D_D \nabla c_D) - k_1 c_D c_{H^+} + k_{-1} c_{DH^+} \quad (2.12)$$

$$\frac{\partial c_{H^+}}{\partial t} = \nabla \cdot (D_{H^+} \nabla c_{H^+}) - k_1 c_D c_{H^+} + k_{-1} c_{DH^+} \quad (2.13)$$

$$\frac{\partial c_{D^+}}{\partial t} = \nabla \cdot (D_{D^+} \nabla c_{D^+}) + k_{photo} c_{DH^{+*}} \quad (2.14)$$

$$\frac{\partial c_{DH^{+*}}}{\partial t} = \nabla \cdot (D_{DH^{+*}} \nabla c_{DH^{+*}}) + \varepsilon_{DH^+} c_{DH^+} I - k_{rec} c_{DH^{+*}} + k_{photo} c_{DH^{+*}} \quad (2.15)$$

The electrochemical reaction of D^+/D at the electrode was implemented with the Butler-Volmer kinetics, as a flux boundary condition as described below:

$$D_D \left(\frac{\partial c_D}{\partial x} \right)_{x=0} = -D_{D^+} \left(\frac{\partial c_{D^+}}{\partial x} \right)_{x=0} = k_{ox} c_{D^+} - k_{red} c_D \quad (2.16)$$

where the rate constants of the oxidation and reduction reactions follow the Butler-Volmer kinetics:

$$k_{ox} = k^0 \exp[\alpha f n (E - E^0)] \quad (2.17)$$

$$k_{red} = k^0 \exp[(\alpha - 1) f n (E - E^0)] \quad (2.18)$$

Where k^0 is the apparent standard rate constant of the electrode reaction, α is the charge transfer coefficient (here taken as 0.5), $f = F/RT$, n is the number of transferred electrons (here $n = 1$), E^0 is the formal potential of the D^+/D redox couple and E is the potential at the electrode.

The parameters are listed in the Table 2.1.

Table 2.1. Parameters used in the model

Parameter	Value	Justification
k_{photo}	$1 \times 10^6 \text{ s}^{-1}$	Fitted in this work
k_{rec}	$1.5 \times 10^6 \text{ s}^{-1}$	Calculated from the QY of 40 %
K	$1 \times 10^5 \text{ L mol}^{-1}$	Fitted in this work, ref. 16
k_1	$100 \text{ L mol}^{-1} \text{ s}^{-1}$	Fitted in this work
k_{-1}	$1 \times 10^{-3} \text{ s}^{-1}$	Calculated from K and k_1
ε_D	$15 \text{ L mol}^{-1} \text{ cm}^{-1}$	Measured at $\lambda = 365 \text{ nm}$
ε_{DH^+}	$3.5 \text{ L mol}^{-1} \text{ cm}^{-1}$	Measured at $\lambda = 365 \text{ nm}$
ε_D^+	$900 \text{ L mol}^{-1} \text{ cm}^{-1}$	Measured at $\lambda = 365 \text{ nm}$
I_0	$5.8 \times 10^{-3} \text{ mol m}^{-2} \text{ s}^{-1}$	Calculated from the power of the LED of 227 mW cm ⁻² at $\lambda = 365 \text{ nm}$, penetrating the FTO electrode.
$D_D = D_D^+ = D_{DH^+} = D_{DH^{+*}}$	$15 \times 10^6 \text{ cm}^2 \text{ s}^{-1}$	Fitted from the voltammetry of D ⁺ /D at the glassy carbon electrode.
k^0	$5 \times 10^{-4} \text{ cm s}^{-1}$	Fitted in this work

2.7.2 Finite Element Simulations of the Proton Reduction by Decamethylruthenocene at w|DCE

The simulations were made by Dr. Jane Stockmann, a fellow post-doc at LEPA. Herein, Fick's laws were used to describe diffusion of the various chemical species; for example, species i of concentration c_i with a diffusion coefficient D_i through the following relation:

$$\frac{\partial c_{i,w}(x,t)}{\partial t} = D_{i,w} \nabla c_{i,w}(x) = D_{i,w} \frac{\partial c_{i,w}(x)}{\partial x} \quad (2.19)$$

Equation (1) has been written for an ion dissolved in the aqueous phase (w); however, an equivalent equation can be for the 1,2-dichloroethane (DCE) or organic phase (o). The electrochemical flux of ions across the ITIES was simulated using the Butler-Volmer kinetic equations in the form of (2.20) and (2.21), below:

$$k_f = k^0 \exp \left[-\alpha f (\Delta_o^w \phi - \Delta_o^w \phi^{o'}) \right] \quad (2.20)$$

$$k_b = k^0 \exp \left[(1 - \alpha) f (\Delta_o^w \phi - \Delta_o^w \phi^{o'}) \right] \quad (2.21)$$

Such that k^0 , α , and $\Delta_o^w \phi^{o'}$ represent the standard rate constant, the transfer coefficient, and the formal ion transfer potential, respectively. $\Delta_o^w \phi$ is the Galvani potential difference across the interface; while experimentally this is controlled externally through a potentiostat, it was replicated in the simulation through application of a triangular waveform. Ultimately, k_f and k_b represent the electrochemical rate of simple ion transfer as shown in eq. 2.22:



Finally, the current was related to the overall flux of ions across the interface through eq. 2.23:

$$J(x, t) = FA \sum_i z_i D_{i,w} \nabla c_{i,w}(x, t) \quad (2.23)$$

Where the electrode area, A , was chosen so as to be reflective of the experimental and defined by a circle of radius 0.7 cm. The simulation mesh was validated using simple IT and comparison of the peak current to the Randles-Sevcik equation^{17,18} as demonstrated recently.¹⁹

A list of the parameters and coefficients employed have been provided in Table 2.2.

.

Table 2.2. List of the terms and coefficients employed in the simulations.

Term	Initial Values	Description
$c_{\text{H}^+,aq}^*$	1, 10, 100, and 1000 mM	Initial aqueous proton concentration
$c_{\text{DMRc},org}^*$	5 mM	Initial organic phase DMRc concentration
$D_{\text{H}^+,aq}$	$9.4 \times 10^{-5} \text{ cm}^2 \cdot \text{s}^{-1}$	Aqueous proton diffusion coefficient
$D_{\text{H}^+,org}$	$1 \times 10^{-5} \text{ cm}^2 \cdot \text{s}^{-1}$	H^+ diffusion coefficient in the organic phase
$D_{\text{DMRc},org} = D_{\text{DMRc},aq}$	$7.26 \times 10^{-6} \text{ cm}^2 \cdot \text{s}^{-1}$	Diffusion coefficient of DMRc^+
k_{cf1}	$1 \times 10^5 \text{ L} \cdot \text{mol}^{-1} \cdot \text{s}^{-1}$	Rate of hydride formation in the organic phase
k_{cb1}	1 s^{-1}	Rate of hydride dissociation in the organic phase
k_{cf2}	$1 \text{ L} \cdot \text{mol}^{-1} \cdot \text{s}^{-1}$	Rate of hydride formation in the aqueous phase
k_{cb2}	$1 \times 10^5 \text{ s}^{-1}$	Rate of hydride dissociation in the aqueous phase
k_{pf}	$1 \times 10^{-6} \text{ cm} \cdot \text{s}^{-1}$	Rate of DMRc (neutral) from the aqueous to organic phase
k_{pb}	$1 \times 10^{-10} \text{ cm} \cdot \text{s}^{-1}$	Rate of DMRc (neutral) from the organic to aqueous phase
v	$0.050 \text{ V} \cdot \text{s}^{-1}$	Scan rate

[†]These were used to describe $[\text{Cp}_2^*\text{Ru}^{\text{(III)}}]^+$ in either phase.

2.8 Computational details

DFT calculations were provided by Laurent Vannay and Prof. Clémence Corminboeuf from the Laboratory for Computational Molecular Design (LCMD) at EPFL. Geometries were optimized in the gas phase at the M06/def2-TZVP level,²⁰⁻²² using an ultrafine grid for numerical integrations in Gaussian09.²³ For Ru the LanL2DZ effective core potential²⁴ was used. Single point energies were computed using the dispersion corrected hybrid PBE0-dDsC and a TZ2P basis set²⁵⁻²⁹ in the ADF package.³⁰ Solvent effects were accounted for the frozen gas phase geometries using the COSMO-RS model³¹ (relative permittivity $\epsilon_r = 10.125$ for DCE). All spin multiplicities were computed to ensure lowest ground state electronic configuration. All the stationary points were verified by analytic computation of vibrational frequencies that were also used for the zero point energies and 298 K thermal contributions to the Gibbs energy, using the usual rigid-rotator

harmonic oscillator approximation. The low-lying excited state of $[\text{Cp}_2^*\text{Ru}^{(\text{III})}]^+$ was obtained using the time dependent density functional theory (TDDFT) formalism³² at the $\omega\text{B97X-D/def2-TZVP}$ level³³ and a LanL2DZ pseudopotential on Ru. Solvation effects on excitation energies were accounted using the SMD model³⁴ for DCE in Gaussian09.

2.9 References

- (1) Stoyanov, E. S.; Kim, K.-C.; Reed, C. A. *Journal of the American Chemical Society* **2006**, *128*, 8500.
- (2) Reed, C. A.; Kim, K.-C.; Stoyanov, E. S.; Stasko, D.; Tham, F. S.; Mueller, L. J.; Boyd, P. D. W. *Journal of the American Chemical Society* **2003**, *125*, 1796.
- (3) Jutzi, P.; Müller, C.; Stammer, A.; Stammer, H.-G. *Organometallics* **2000**, *19*, 1442.
- (4) Reed, C. A. *Accounts of Chemical Research* **2010**, *43*, 121.
- (5) Reed, C. A. *Accounts of Chemical Research* **2013**, *46*, 2567.
- (6) Eugster, N.; Fermín, D. J.; Girault, H. H. *The Journal of Physical Chemistry B* **2002**, *106*, 3428.
- (7) Stockmann, T. J.; Deng, H.; Peljo, P.; Kontturi, K.; Opallo, M.; Girault, H. H. *J. Electroanal. Chem.* **2014**, *729*, 43.
- (8) Ge, P.; Todorova, T. K.; Patir, I. H.; Olaya, A. J.; Vrubel, H.; Mendez, M.; Hu, X.; Corminboeuf, C.; Girault, H. H. *Proc. Natl. Acad. Sci. U. S. A., Early Ed.* **2012**, *1*.
- (9) Samec, Z.; Langmaier, J.; Kakiuchi, T. *Pure Appl. Chem.* **2009**, *81*, 1473.
- (10) Wandlowski, T.; Mareček, V.; Samec, Z. *Electrochim. Acta* **1990**, *35*, 1173.
- (11) Sabela, A.; Mareček, V.; Samec, Z.; Fuoco, R. *Electrochim. Acta* **1992**, *37*, 231.
- (12) Fulmer, G. R.; Miller, A. J. M.; Sherden, N. H.; Gottlieb, H. E.; Nudelman, A.; Stoltz, B. M.; Bercaw, J. E.; Goldberg, K. I. *Organometallics* **2010**, *29*, 2176.
- (13) Albery, W. J.; Archer, M. D. *Nature* **1977**, *270*, 399.
- (14) Mendez, M. A.; Peljo, P.; Scanlon, M. D.; Vrubel, H.; Girault, H. H. *J. Phys. Chem. C* **2014**, *118*, 16872.
- (15) Bourdon, R.; Peljo, P.; Mendez, M. A.; Olaya, A. J.; De Jonghe-Risse, J.; Vrubel, H.; Girault, H. H. *J. Phys. Chem. C* **2015**, *119*, 4728.
- (16) Rivier, L.; Stockmann, T. J.; Méndez, M. A.; Scanlon, M. D.; Peljo, P.; Opallo, M.; Girault, H. H. *The Journal of Physical Chemistry C* **2015**, *119*, 25761.
- (17) Randles, J. E. B. *Trans. Faraday Soc.* **1948**, *44*, 327.
- (18) Bard, A. J.; Faulkner, L. R. *Electrochemical Methods: Fundamentals and Applications*; 2nd ed.; Wiley, **2001**.
- (19) Stockmann, T. J.; Deng, H.; Peljo, P.; Kontturi, K.; Opallo, M.; Girault, H. H. *J. Electroanal. Chem.* **2014**, *729*, 28.
- (20) Zhao, Y.; Truhlar, D. *Theor Chem Account* **2008**, *120*, 215.
- (21) Weigend, F.; Ahlrichs, R. *Physical Chemistry Chemical Physics* **2005**, *7*, 3297.
- (22) Weigend, F. *Physical Chemistry Chemical Physics* **2006**, *8*, 1057.

- (23) Frisch, M. J.; Trucks, G. W.; Schlegel, H. B.; Scuseria, G. E.; Robb, M. A.; Cheeseman, J. R.; Scalmani, G.; Barone, V.; Mennucci, B.; Petersson, G. A.; Nakatsuji, H.; Caricato, M.; Li, X.; Hratchian, H. P.; Izmaylov, A. F.; Bloino, J.; Zheng, G.; Sonnenberg, J. L.; Hada, M.; Ehara, M.; Toyota, K.; Fukuda, R.; Hasegawa, J.; Ishida, M.; Nakajima, T.; Honda, Y.; Kitao, O.; Nakai, H.; Vreven, T.; Montgomery Jr., J. A.; Peralta, J. E.; Ogliaro, F.; Bearpark, M. J.; Heyd, J.; Brothers, E. N.; Kudin, K. N.; Staroverov, V. N.; Kobayashi, R.; Normand, J.; Raghavachari, K.; Rendell, A. P.; Burant, J. C.; Iyengar, S. S.; Tomasi, J.; Cossi, M.; Rega, N.; Millam, N. J.; Klene, M.; Knox, J. E.; Cross, J. B.; Bakken, V.; Adamo, C.; Jaramillo, J.; Gomperts, R.; Stratmann, R. E.; Yazyev, O.; Austin, A. J.; Cammi, R.; Pomelli, C.; Ochterski, J. W.; Martin, R. L.; Morokuma, K.; Zakrzewski, V. G.; Voth, G. A.; Salvador, P.; Dannenberg, J. J.; Dapprich, S.; Daniels, A. D.; Farkas, Ö.; Foresman, J. B.; Ortiz, J. V.; Cioslowski, J.; Fox, D. J.; Gaussian, Inc.: Wallingford, CT, USA, **2009**.
- (24) Wadt, W. R.; Hay, P. J. *J. Chem. Phys.* **1985**, *82*, 284.
- (25) Adamo, C.; Barone, V. *The Journal of Chemical Physics* **1999**, *110*, 6158.
- (26) Steinmann, S. N.; Corminboeuf, C. *Journal of Chemical Theory and Computation* **2011**, *7*, 3567.
- (27) Steinmann, S. N.; Corminboeuf, C. *The Journal of Chemical Physics* **2011**, *134*, 044117.
- (28) Steinmann, S. N.; Corminboeuf, C. *Journal of Chemical Theory and Computation* **2010**, *6*, 1990.
- (29) Van Lenthe, E.; Baerends, E. J. *J. Comput. Chem.* **2003**, *24*, 1142.
- (30) te Velde, G.; Bickelhaupt, F. M.; Baerends, E. J.; Fonseca Guerra, C.; van Gisbergen, S. J. A.; Snijders, J. G.; Ziegler, T. *J. Comput. Chem.* **2001**, *22*, 931.
- (31) Pye, C. C.; Ziegler, T.; van Lenthe, E.; Louwen, J. N. *Can. J. Chem.-Rev. Can. Chim.* **2009**, *87*, 790.
- (32) Runge, E.; Gross, E. K. U. *Physical Review Letters* **1984**, *52*, 997.
- (33) Chai, J.-D.; Head-Gordon, M. *Physical Chemistry Chemical Physics* **2008**, *10*, 6615.
- (34) Marenich, A. V.; Cramer, C. J.; Truhlar, D. G. *The Journal of Physical Chemistry B* **2009**, *113*, 6378.

Appendix: Transmittance of FTO glass electrode

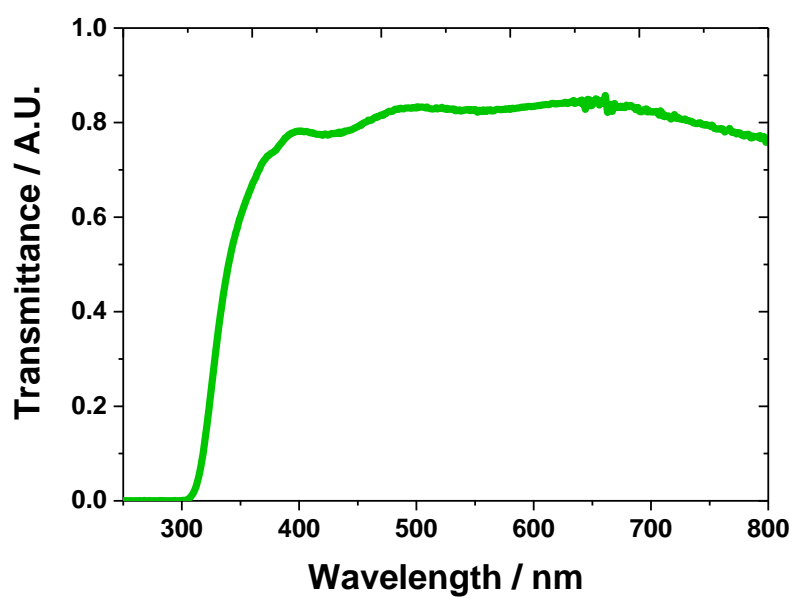


Figure 2.3. Transmittance spectrum of FTO glass electrode. Air was taken as blank. A transmittance of 69.7 % was observed at 365 nm.

3. Photo-generation of Hydrogen by Decamethylruthenocene: a non-sacrificial electron donor and sensitizer

3.1	Introduction	52
3.2	Electrochemical characterization of $\text{Cp}_2^*\text{Ru}^{\text{(II)}}$	52
3.3	Photo-generation of H_2 from acidified 1,2-dichloroethane using $\text{Cp}_2^*\text{Ru}^{\text{(II)}}$	54
3.4	Multi-step mechanism for the photo-generation of H_2 from acidified organic solutions containing $\text{Cp}_2^*\text{Ru}^{\text{(II)}}$	55
3.4.1	Factors influencing hydride formation in the dark.	56
3.4.1.1	General aspects.....	57
3.4.1.2	Experimental studies of acid strength of $[\text{Cp}_2^*\text{Ru}^{\text{(IV)}}(\text{H})]^+$	58
3.4.2	Light-driven reaction mechanism characterization	63
3.4.2.1	UV/vis characterization	63
3.4.2.2	Identification transient $[\text{Cp}_2^*\text{Ru}^{\text{(III)}}]^+$	64
3.4.2.3	The second release of H_2 from the transient $[\text{Cp}_2^*\text{Ru}^{\text{(III)}}]^+$ species.....	66
3.4.2.4	Identification of the final photo-product as $[\text{Cp}_2^*\text{Ru}^{\text{(IV)}}(\text{C}_5\text{Me}_4\text{CH}_2)]^+$ by NMR spectroscopy.	68
3.4.3	Hydricity.....	72
3.5	Kinetics analysis of the transient $[\text{Cp}_2^*\text{Ru}^{\text{(III)}}]^+$ species.....	73
3.5.1	Influence of $\text{Cp}_2^*\text{Ru}^{\text{(II)}}$ initial concentration	74
3.5.2	Influence of $[\text{H}(\text{OEt}_2)_2]\text{TB}$ initial concentration	77
3.6	DFT calculations.....	79
3.7	Conclusions.....	81
3.8	References.....	83

3.1 Introduction

In Chapter I, we demonstrated the potential of metallocenes to perform photo-HER. Their adaptability allows us to envisage a long-term strategy to develop this type of catalyst.

In this context, we suggested to investigate and to implement in the batch water-splitting the use of $\text{Cp}_2^*\text{Ru}^{\text{(II)}}$ as a light-activated electron donor. $\text{Cp}_2^*\text{Ru}^{\text{(II)}}$ has an intermediate redox potential between that of $\text{Cp}_2\text{Os}^{\text{(II)}}$ ($[E^{0'}_{[\text{Cp}_2\text{Os}^{\text{(III)}}]/[\text{Cp}_2\text{Os}^{\text{(II)}}]}]^{\text{DCE}} = 1.03 \text{ V vs. SHE})^1$ and $\text{Cp}_2^*\text{Os}^{\text{(II)}}$ ($[E^{0'}_{[\text{Cp}_2\text{Os}^{\text{(III)}}]/[\text{Cp}_2\text{Os}^{\text{(II)}}]}]^{\text{DCE}} = 0.48 \text{ V vs. SHE})^2$ which is suitably high to facilitate both the photo-system reset after photo-irradiation and efficient photo-production of H_2 .

The objectives of this chapter are to (i) demonstrate the possibility to evolve H_2 with $\text{Cp}_2^*\text{Ru}^{\text{(II)}}$, (ii) identified the reaction mechanisms and (iii) characterize every step in order to facilitate the implementation of the reaction at liquid|liquid interfaces. Thus, we investigate the photo-reduction of organic protons in a single organic phase, 1,2-dichloroethane, by $\text{Cp}_2^*\text{Ru}^{\text{(II)}}$. The multi-step photo-mechanism leading to H_2 evolution with $\text{Cp}_2^*\text{Ru}^{\text{(II)}}$ in organic media is fully elucidated using electrochemical, gas chromatographic (GC) and spectroscopic (UV/vis, ^1H and ^{13}C NMR) experimental approaches, with corroboration by density functional theory (DFT) computations. A comprehensive guide describing the influences of the nature of $\text{Cp}_2^*\text{Ru}^{\text{(II)}}$ itself (in comparison to similar experiments performed with $\text{Cp}_2^*\text{Os}^{\text{(II)}}$) and the organic acid on each step of the photo-generation of H_2 in acidified organic media is presented. However, with the aim to recycle the reaction, our investigations were particularly focused on the reversible steps.

3.2 Electrochemical characterization of $\text{Cp}_2^*\text{Ru}^{\text{(II)}}$

As demonstrated in Chapter I, section 1.4, redox potentials can be used to predict the feasibility of redox reactions. Thus, electrochemical characterisation of $\text{Cp}_2^*\text{Ru}^{\text{(II)}}$ in 1,2-dichloroethane, to be in the conditions for the batch-water splitting, was performed to characterise the electron donating ability of $\text{Cp}_2^*\text{Ru}^{\text{(II)}}$.

Cyclic voltammograms (CVs) of $\text{Cp}_2^*\text{Ru}^{\text{(II)}}$ obtained at a glassy-carbon working electrode, with TBAPF_6 as the supporting electrolyte and under anaerobic conditions at ambient temperatures (Figure 3.1., black CV) show a quasi-reversible $\text{Ru}^{\text{(III)}}/\text{Ru}^{\text{(II)}}$ redox process with the formal redox potential of $\text{Cp}_2^*\text{Ru}^{\text{(II)}}$, $[E^{0'}_{[\text{Cp}_2^*\text{Ru}^{\text{(III)}}]/[\text{Cp}_2^*\text{Ru}^{\text{(II)}}]}]^{\text{DCE}}$, determined as 0.75 V versus the aqueous standard

hydrogen electrode (SHE). Consequently, $\text{Cp}_2^*\text{Ru}^{\text{(II)}}$ has an intermediate redox potential between that of $\text{Cp}_2\text{Os}^{\text{(II)}}$ and $\text{Cp}_2^*\text{Os}^{\text{(II)}}$, discussed in Chapter I, which is suitably high to facilitate both the photo-system reset after photo-irradiation and efficient photo-production of H_2 . The oxidation proceeds by a quasi-reversible $1 e^-$ process in a weakly coordinating (low donor) organic solvent. The influence of the solvent and the supporting electrolyte anions are discussed in more detail in Chapter IV, Section 4.2. Further oxidation of the $\text{Ru}^{\text{(III)}}$ species to $\text{Ru}^{\text{(IV)}}$ at 1.81 V *vs.* SHE was irreversible. The precise identification of this oxidation product, possibly $[\text{Cp}_2^*\text{Ru}^{\text{(IV)}}(\text{C}_5\text{Me}_4\text{CH}_2)]^+$, discussed in detail *vide infra*, or $[\text{Cp}_2^*\text{Ru}^{\text{(IV)}}]^{2+}$ is outside the scope of this study. The irreversible loss of a part of the $\text{Ru}^{\text{(III)}}$ species at these highly oxidising potentials resulted in the reduction peak current on the reverse scan (i_{pc}) being significantly smaller than the oxidation peak current (i_{pa}) for the $\text{Ru}^{\text{(III)}/\text{Ru}^{\text{(II)}}$ redox transition. However, the reversible nature of the $\text{Ru}^{\text{(III)}/\text{Ru}^{\text{(II)}}$ redox transition was confirmed by limiting the potential window to exclude the irreversible process at 1.81 V *vs.* SHE (Figure 3.1., red CVs). Furthermore, two very small irreversible reduction peaks were observed at potentials more negative than the $\text{Ru}^{\text{(III)}/\text{Ru}^{\text{(II)}}$ redox potential and attributed to decomposition products of the irreversible oxidation of $\text{Ru}^{\text{(III)}}$, as these peaks were absent when the potential sweep was reversed before the oxidation of $\text{Ru}^{\text{(III)}}$ (not shown).

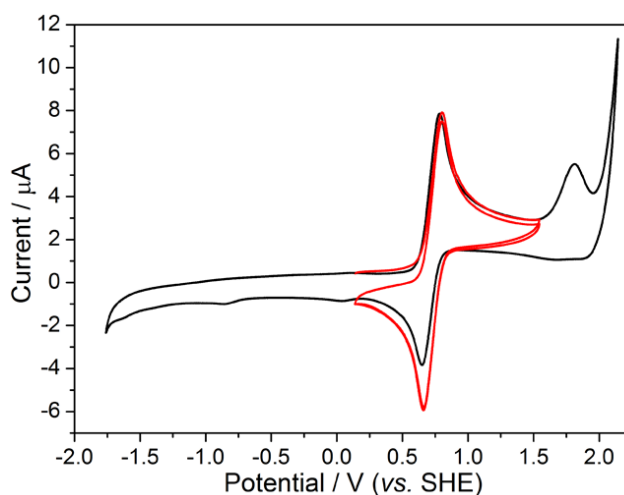


Figure 3.1. Cyclic voltammetry (CV) at $50 \text{ mV}\cdot\text{s}^{-1}$ of $0.5 \text{ mM } \text{Cp}_2^*\text{Ru}^{\text{(II)}}$ at a glassy carbon electrode immersed in a de-oxygenated solution of DCE containing 100 mM TBAPF_6 as supporting electrolyte. CVs were obtained under anaerobic conditions at ambient temperatures using silver and platinum wires as the reference and counter electrodes, respectively. CVs were calibrated versus the standard reduction potential of $\text{Cp}_2^*\text{Fe}^{\text{(II)}}$ in DCE on the SHE scale ($[E^0_{[\text{Cp}_2^*\text{Fe}^{\text{(III)}}]/[\text{Cp}_2^*\text{Fe}^{\text{(II)}}]}]^{\text{DCE}} = 0.07 \text{ V vs. SHE}$).³

3.3 Photo-generation of H₂ from acidified 1,2-dichloroethane using Cp₂*Ru^(II)

Considering that organic solubilized protons in DCE have a redox potential, $[E^{0'}_{\text{H}^+/1/2\text{H}_2}]^{\text{DCE}}$ *vs.* SHE, of 0.55 V,⁴ thermodynamically Cp₂*Ru^(II) is not capable of evolving H₂ in the dark, as previously observed for Cp₂Os^(II) ($[E^{0'}_{\text{Cp}_2\text{Os(III)}^+/\text{Cp}_2\text{Os(II)}}]^{\text{DCE}}$ *vs.* SHE = 1.03 V)¹ and Cp₂*Os^(II) ($[E^{0'}_{\text{Cp}_2^*\text{Os(III)}^+/\text{Cp}_2^*\text{Os(II)}}]^{\text{DCE}}$ = 0.48 V *vs.* SHE).² However, H₂ is evolved to a minor extent by Cp₂Os^(II) and stoichiometrically by Cp₂*Os^(II) with white light illumination under anaerobic conditions in the presence of organic solubilised protons.^{1,2}

Preliminary GC experiments under white light illumination, that involved sampling the head-space of a septum-sealed glass-vial containing a stirred solution of 4 μmol Cp₂*Ru^(II) and an excess of strong [H(OEt₂)₂]TB organic acid dissolved in de-oxygenated DCE, yielded considerable H₂ evolution after 2 hours (Figure 3.2.A, red trace). Experimental details are outlined in the Chapter II, section 2.3. The photo-production of H₂ under anaerobic conditions was confirmed by the absence of any measurable H₂ gas in a control experiment under identical conditions but left in the dark for 2 hours (Figure 3.2.(A), black trace). Interestingly, monitoring the photo-production of H₂ as a function of illumination time (up to 4 hours) revealed that 4 μmol H₂ was evolved in total in the presence of excess organic protons (Figure 3.2.(B)). This represented a 200 % yield of H₂ based on the clearly erroneous initial assumption that Cp₂*Ru^(II) would act as a 1 e⁻ donor and react with organic protons in a stoichiometric 1:1 ratio (as previously observed for Cp₂*Fe^(II), $[E^{0'}_{\text{Cp}_2^*\text{Fe(III)}^+/\text{Cp}_2^*\text{Fe(II)}}]^{\text{DCE}}$ = 0.07 V *vs.* SHE, in the dark and in the presence of a suitable H₂ evolution catalyst).⁵⁻¹¹ These initial GC experiments invited further in-depth mechanistic studies to fully elucidate the underlying factors leading to the Cp₂*Ru^(II) molecule seemingly acting as a 2 e⁻ donor.

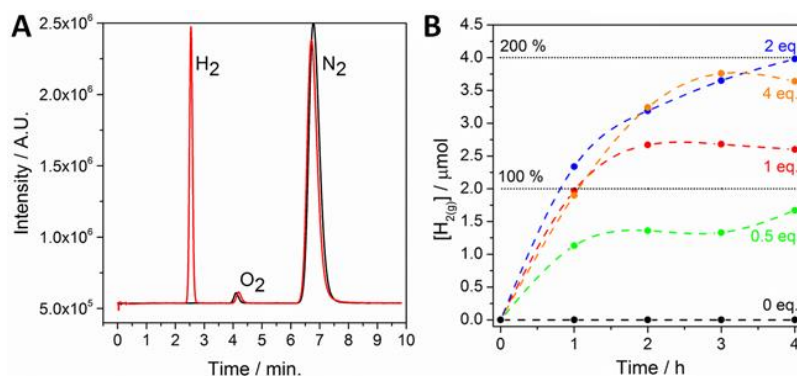
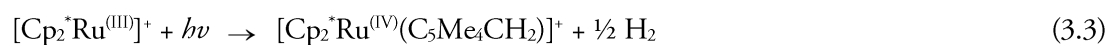
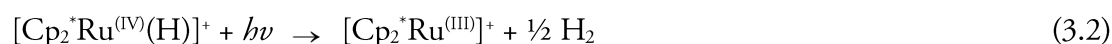
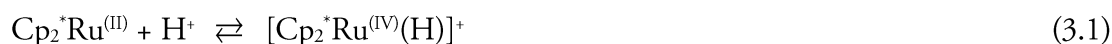


Figure 3.2. Photo-production of H₂ gas from solutions of Cp₂*Ru^(II) dissolved in DCE as a function of organic proton concentrations and irradiation time. **(A)** Gas chromatograms of the headspace of a septum-sealed stirring solution of 4 μmol Cp₂*Ru^(II) and excess organic protons (16 μmol [H(OEt₂)₂]TB; 4 equivalents) dissolved in DCE under anaerobic conditions with (red trace) and without (black trace) irradiation by a 500 W Xe lamp. **(B)** Summary of the quantities of H₂ gas evolved (μmol) in the presence of various equivalents of organic protons (0, 2, 4, 8, and 16 μmol [H(OEt₂)₂]TB) as a function of irradiation time by a 500 W Xe lamp. The horizontal lines represent the theoretical % yields assuming that Cp₂*Ru^(II) would act as a 1 e⁻ donor and react with organic protons in a stoichiometric 1:1 ratio.

3.4 Multi-step mechanism for the photo-generation of H₂ from acidified organic solutions containing Cp₂*Ru^(II)

A large body of work has emanated from the A. N. Nesmeyanov Institute of Organoelement Compounds (Moscow, Russian Federation) over the past 30 years on the organometallic chemistry of metallocenes, especially decamethylmetallocenes,¹²⁻¹⁹ including the UV photolysis of Cp₂*Ru^(II) in acidic organic solutions.^{20,21} A focus of these previous studies was the synthesis and characterization of cationic derivatives of Cp₂*Ru^(II), especially with regard to the stabilization of up to three carbocationic sites (CH₂⁺) on the cyclopentadienyl rings by a single ruthenium metal atom^{15,16} and the reactivity of these cations towards strong nucleophiles.^{17,19} The proposed mechanism was divided into three steps, Ru^(IV) hydride formation in the dark (eq.(3.1)), generation of a transient Ru^(III) cationic intermediate (eq. (3.2)), and the breakdown of the latter to a cationic Ru^(IV) species (eq. (3.3)) that contains a stabilized CH₂⁺ site.



The net reaction results in the generation of a single H₂ molecule per Cp₂*Ru^(III) in solution as one proton comes from the organic acid and another is sourced from a methyl-group on one of the Cp₂*Ru^(III) cyclopentadienyl rings (eq. (3.4)).



While these earlier studies provided key clues to predict the behaviour of photo-activated Cp₂*Ru^(III) in acidic organic media, we use alternative experimental characterization techniques, especially (spectro)electrochemistry and GC, and corroborate the present experimental findings with DFT calculations. Thus, we focus our attention much more on: (i) quantitative analytical determination of H₂ gas evolved (typically considered a by-product in previous studies), as shown already in Figure 3.2, (ii) determining all of the possible factors that influence hydride formation (eq. (3.1)), from the Brønsted basicity of Cp₂*Ru^(III), to the choice of acid, and the p*K_a* of [Cp₂*Ru^(IV)(H)]⁺, and (iii) providing new mechanistic insights by spectroelectrochemistry into the kinetics of the previously unobserved transient [Cp₂*Ru^(III)]⁺ intermediate generated *in situ* during photo-irradiation (eq. (3.2) & (3.3)), (iv) resolving the mechanism involved in the H₂ formation.

The comprehensive nature of the study allows us to determine if the characteristics of Cp₂*Ru^(III) are suitable for its implementation as a reversible electron donor in the “biphasic H₂ evolution” section of a batch-water splitting arrangement, and if so, what acid is most suitable to use with Cp₂*Ru^(III) in this regard.

3.4.1 Factors influencing hydride formation in the dark.

The first step in the mechanism of H₂ evolution in acidified organic solutions with any metallocene, either light-activated or not, is the protonation at the metal to form the cationic hydride in the dark,²² as described by eq. (3.1) for Cp₂*Ru^(III). The proton transfer reactions – to and from the hydride – are crucial steps to achieve the H₂ evolution reaction (HER).^{23,24} The basicity of the metal has to be sufficient to allow the coordination of a proton on the metal centre but at the same time, the formed bond should not be too strong as to hamper the elimination of H₂. Moreover, the Brønsted basicity of Cp₂*Ru^(III) is of particular importance for the design of catalytic H₂ evolution processes, as it provides thermodynamic information for rationally choosing the acid source. Thus, the strength of organic acid to facilitate protonation of the metal centre is a crucial factor when designing experiments to accurately determine the maximum experimental yields of H₂ gas evolved

per $\text{Cp}_2^*\text{Ru}^{\text{(II)}}$ molecule present. Ideally, a strong organic acid that reacts in a 1:1 ratio with $\text{Cp}_2^*\text{Ru}^{\text{(II)}}$ to facilitate 100 % conversion to $[\text{Cp}_2^*\text{Ru}^{\text{(IV)}}(\text{H})]^+$ is desirable in order to remove any ambiguity as to whether all of the $\text{Cp}_2^*\text{Ru}^{\text{(II)}}$ present is converted to $[\text{Cp}_2^*\text{Ru}^{\text{(IV)}}(\text{H})]^+$ and preclude an underestimation of the maximum possible experimental yields of H_2 gas.

3.4.1.1 General aspects

In the common studies of acid strength of organic compounds, UV/vis and NMR detection are used to determine the acid dissociation constants K_a (eq. (3.5)).²⁵⁻²⁷ In organic solvents, the measurements of activity of solvated hydrogen ion $\text{H}(\text{S})^+$ are problematic. To overcome this issue, the equilibria (eq. (3.6)) between the acid and protonated bases of known K_a (eq. (3.7)) can be studied.²⁸ The result is a relative acidity reported as $\text{p}K_a$ value (eq. (3.8)).



$$\text{p}K_a^{\text{MHL}_n^+} = \text{p}K_a^{\text{BH}^+} - \text{p}K_{eq} \quad (3.8)$$

Here, ^1H NMR spectroscopy was applied to monitor the conversion of $\text{Cp}_2^*\text{Ru}^{\text{(II)}}$ to $[\text{Cp}_2^*\text{Ru}^{\text{(IV)}}(\text{H})]^+$ (another study using UV/vis spectroscopy corroborating ^1H NMR results is detailed in Chapter VI, Section 6.2.1). ^1H NMR spectra were obtained in deuterated dichloromethane (CD_2Cl_2) using DCE (31.2 mM) as an internal standard, in the dark, at ambient temperatures and under anaerobic conditions. The similarities of the two solvents, CD_2Cl_2 and DCE, in terms of being weakly coordinating, having similar dielectric constants, *etc.* were such that the trends seen by NMR in CD_2Cl_2 were expected to accurately reflect the processes that occur in DCE under otherwise identical experimental conditions. Commonly, solvents with high relative permittivity, such as acetonitrile ($\epsilon_r = 37.5$ at 20°C)²⁹, are strongly recommended to reduce problems associated with ion pairing that can influence equilibria of interest. They minimize the electrostatic attraction between oppositely charged ions and facilitate the dissociation of ion pairs into free solvated ions. The use of dichloromethane or dichloroethane, (respectively $\epsilon_r = 9.08$ and

10.6 at 20°C)²⁹ is challenging because of ion pairing and homo-association. The last is particularly important when the base and its conjugate acid form a hydrogen bond (eq. (3.9)).



Nevertheless, they have been already employed for pK_a measurements at low concentrations to avoid aggregation of ion pairs.^{30,31} DCE is a weakly basic solvent but previous studies have conclusively shown that DCE is not protonated even by strong organic acids such as $\text{CF}_3\text{SO}_3\text{H}$.³² Thus, organometallic hydride species of relatively low basicity, such as $\text{Cp}_2^*\text{Ru}^{\text{(II)}}$, exhibit acid/base equilibria therein.³²⁻³⁵

3.4.1.2 Experimental studies of acid strength of $[\text{Cp}_2^*\text{Ru}^{\text{(IV)}}(\text{H})]^+$

Firstly, the ^1H NMR spectrum of pristine $\text{Cp}_2^*\text{Ru}^{\text{(II)}}$ was obtained prior to the addition of organic acid, see Figure 3.3(A). All of the protons of the methyl groups on each cyclopentadienyl ring for $\text{Cp}_2^*\text{Ru}^{\text{(II)}}$ have chemically equivalent spins, showing a characteristic singlet chemical shift (δ) at 1.62 ppm, in agreement with previous studies.^{20,22} The ^1H NMR spectrum of $[\text{Cp}_2^*\text{Ru}^{\text{(IV)}}(\text{H})]^+$, formed *in situ* by reaction with an excess of 1.3 equivalents of the known strong Brønsted acid $[\text{H}(\text{OEt}_2)_2]\text{TB}$, shows a singlet peak at -8.38 ppm corresponding to the hydridic $\text{Ru}-\text{H}$ proton, see Figure 3.3(B). In addition, the signal for the protons of the methyl groups on each cyclopentadienyl ring is shifted positively to 1.83 ppm. The latter is due to the electron density on the cyclopentadienyl rings being reduced to compensate the Ru oxidation, leading to the slight de-shielding of the protons of the methyl groups. The ^1H NMR spectrum of $[\text{Cp}_2^*\text{Ru}^{\text{(IV)}}(\text{H})]^+$ generated by $[\text{H}(\text{OEt}_2)_2]\text{TB}$ is in close, but not perfect, agreement with those of $[\text{Cp}_2^*\text{Ru}^{\text{(IV)}}(\text{H})]^+$ species generated *in situ* with either excess $\text{CF}_3\text{SO}_3\text{H}$ (Figure 3.3(C)) or $\text{CF}_3\text{CO}_2\text{H}$ (Figure 3.3(D)) acting as the organic acid. These slight discrepancies are related to the influence of the different organic counter-anions in solution.^{20,22}

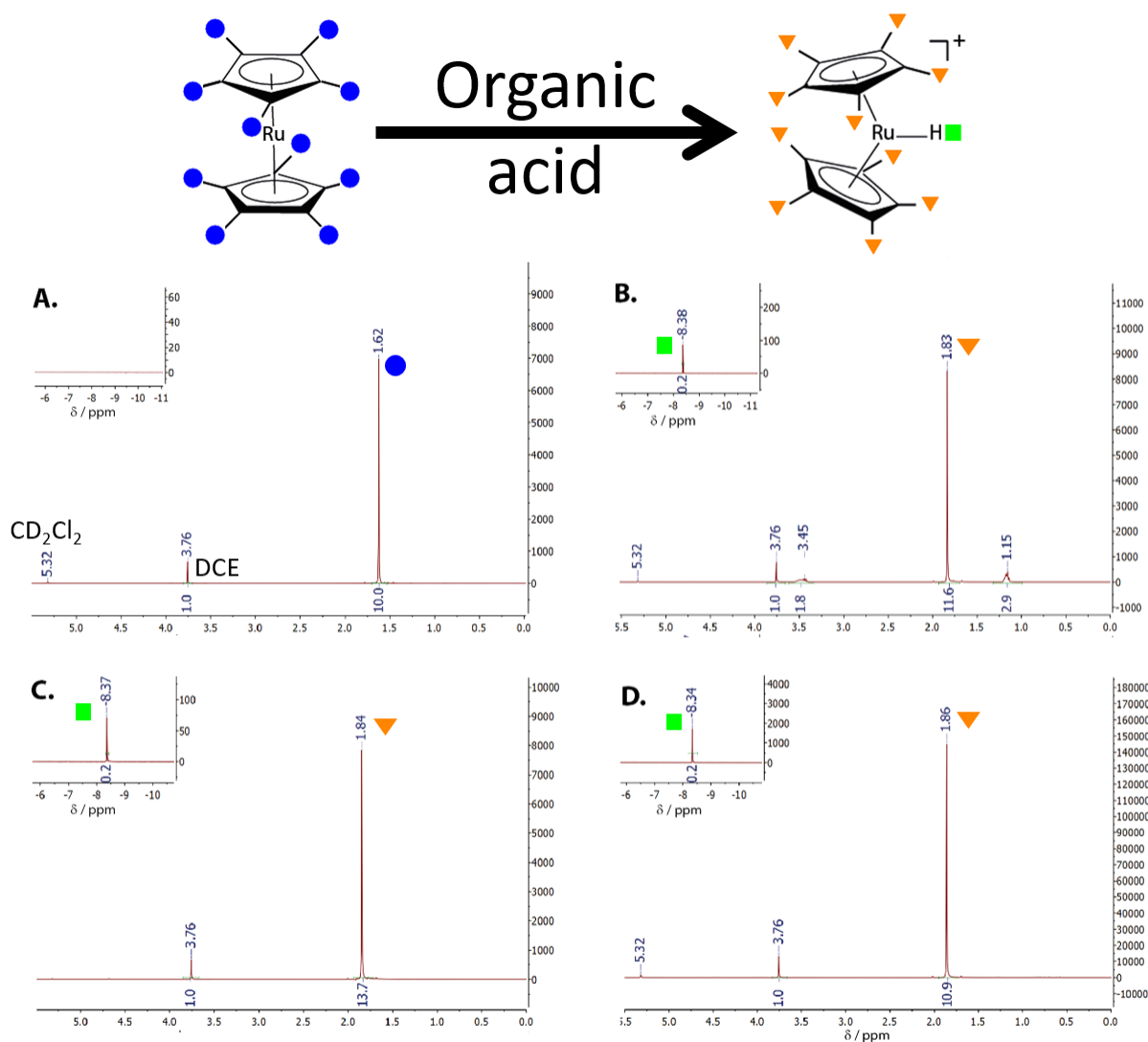


Figure 3.3. ^1H NMR spectra of (A) 15 mM $\text{Cp}_2^*\text{Ru}^{\text{II}}$, and 15 mM $[\text{Cp}_2^*\text{Ru}^{\text{IV}}(\text{H})]^+$ generated by reacting 15 mM $\text{Cp}_2^*\text{Ru}^{\text{II}}$ with (B) 20 mM HTB, (C) 2.25 M $\text{CF}_3\text{CO}_2\text{H}$ and (D) 210 mM $\text{CF}_3\text{SO}_3\text{H}$. ^1H NMR spectra were obtained in deuterated dichloromethane (CD_2Cl_2) solvent using DCE (31.2 mM) as an internal standard, in the dark, at ambient temperatures and under anaerobic conditions.

In Figure 3.4, the raw NMR data as a function of increasing organic acid concentration is illustrated on the right and outlines the appearance of the signal corresponding to the hydridic proton (green squares) at a characteristic negative value of -8.38 ppm. In addition, the disappearance of the methyl group of $\text{Cp}_2^*\text{Ru}^{\text{II}}$ (blue circles, $\delta = 1.62$ ppm) and the concurrent appearance at more positive chemical shift values (orange inverted triangles; $\delta = 1.85$ ppm) of the equivalent protons for $[\text{Cp}_2^*\text{Ru}^{\text{IV}}(\text{H})]^+$ are illustrated in Figure 3.5. As a consequence, comparing the efficiency of conversion of $\text{Cp}_2^*\text{Ru}^{\text{II}}$ to $[\text{Cp}_2^*\text{Ru}^{\text{IV}}(\text{H})]^+$ was possible by monitoring the positive shift in the signal for the protons of the methyl groups on the cyclopentadienyl ring (Figure 3.5)

and the appearance of the signal corresponding to the hydridic proton (Figure 3.4) as a function of increasing concentrations of organic acid. In this manner, it was clearly demonstrated that $[\text{H}(\text{OEt}_2)_2]\text{TB}$ and $\text{CF}_3\text{SO}_3\text{H}$ ($\text{p}K_a = -11.4$ in DCE relative to picric acid)^{34,35} are sufficiently strong acids in DCE that one equivalent of acid was adequate to fully convert all $\text{Cp}_2^*\text{Ru}^{\text{(II)}}$ molecules present into $[\text{Cp}_2^*\text{Ru}^{\text{(IV)}(\text{H})}]^+$ (*i.e.*, the conjugate Brønsted acid). Meanwhile, $\text{CF}_3\text{CO}_2\text{H}$ is a weaker acid, requiring 10 equivalents to achieve full conversion (Figure 3.4 and Figure 3.5).

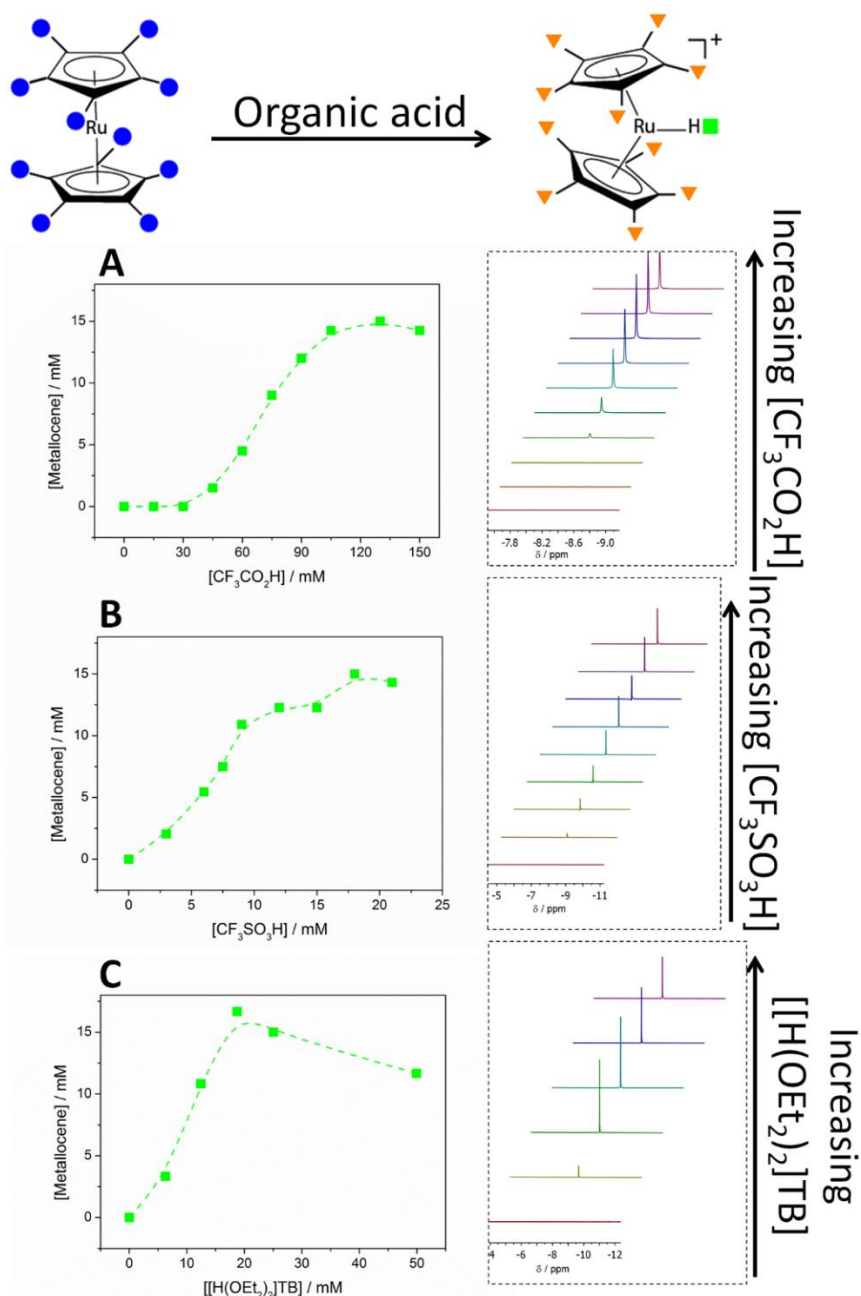


Figure 3.4. Metal hydride formation followed by ^1H NMR of the hydride proton in the presence of various organic acids. The efficiency of conversion of $\text{Cp}_2^*\text{Ru}^{\text{(II)}}$ (15 mM) to $[\text{Cp}_2^*\text{Ru}^{\text{(IV)}(\text{H})}]^+$, in terms of the number of equivalents of acid required to achieve 100 % conversion, was monitored by ^1H NMR spectroscopy in the presence of the organic acids (A) $\text{CF}_3\text{CO}_2\text{H}$, (B) $\text{CF}_3\text{SO}_3\text{H}$ and (C) $[\text{H}(\text{OEt}_2)_2]\text{TB}$.

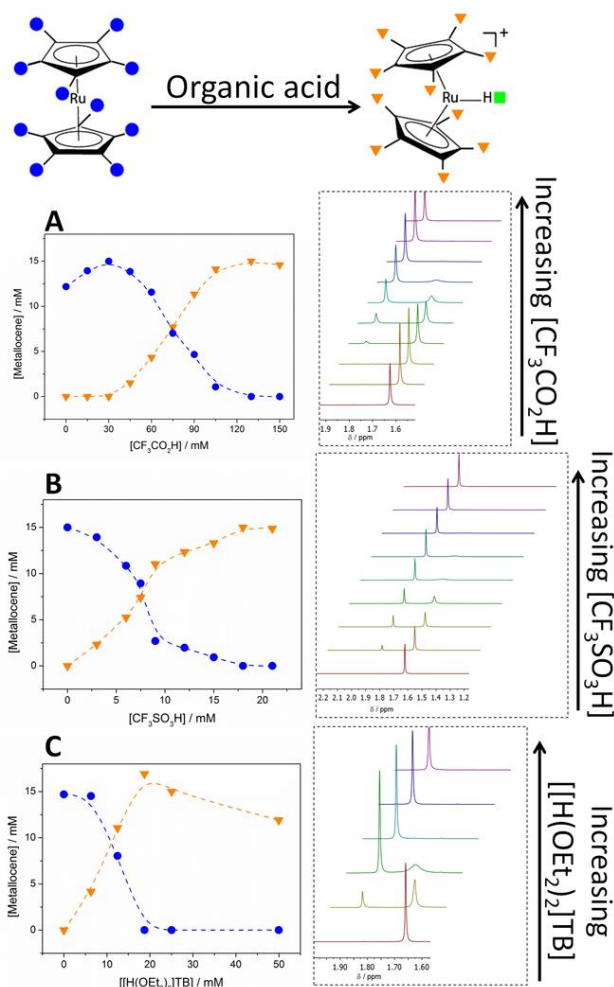
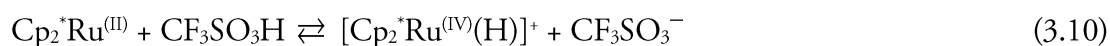


Figure 3.5. Identifying strong organic acids capable of stoichiometrically protonating the relatively weak Brønsted base $\text{Cp}_2^*\text{Ru}^{\text{II}}$ to form the cationic hydride species. The efficiency of conversion of $\text{Cp}_2^*\text{Ru}^{\text{II}}$ (15 mM) to $[\text{Cp}_2^*\text{Ru}^{\text{IV}}(\text{H})]^+$, in terms of the number of equivalents of acid required to achieve 100 % conversion, was monitored by ^1H NMR spectroscopy of the hydrogen in the methyl groups in the presence of the organic acids (A) $\text{CF}_3\text{CO}_2\text{H}$, (B) $\text{CF}_3\text{SO}_3\text{H}$ and (C) $[\text{H}(\text{OEt})_2]\text{TB}$. ^1H NMR spectra were obtained in deuterated dichloromethane (CD_2Cl_2) solvent using DCE (31.2 mM) as an internal standard, in the dark and under anaerobic conditions.

Herein, to further aid the rational design of the HER in DCE involving $\text{Cp}_2^*\text{Ru}^{\text{II}}$ with regard to the appropriate choice of organic acid, the $\text{p}K_a$ of $[\text{Cp}_2^*\text{Ru}^{\text{IV}}(\text{H})]^+$ in DCE was investigated by measurement of the proton-transfer equilibria between $\text{Cp}_2^*\text{Ru}^{\text{II}}$ and $\text{CF}_3\text{SO}_3\text{H}$ as outlined in eq. (3.10):



$\text{CF}_3\text{SO}_3\text{H}$ was selected as the organic acid as it is (i) demonstrably a stronger acid than $[\text{Cp}_2^*\text{Ru}^{\text{IV}}(\text{H})]^+$, requiring just one equivalent to fully convert all $\text{Cp}_2^*\text{Ru}^{\text{II}}$ present to the hydride,

and (ii) well-studied in the literature, with a known pK_a of -11.4 in DCE relative to picric acid.^{34,35} Inconveniently, it turned out that the equilibrium constant of the reaction was dependent of the quantity of acid added. It is a strong indication of the formation of ion pairing and/or homoassociation during the reaction. Therefore, too many unknown parameters were involved in the process and it was not possible to accurately estimate the pK_a .

Nevertheless, Angelici and co-workers have determined the trend of increasing Brønsted basicity for Group 8 decamethylmetallocenes as follows: $\text{Cp}_2^*\text{Fe}^{(\text{II})} < \text{Cp}_2^*\text{Ru}^{(\text{II})} < \text{Cp}_2^*\text{Os}^{(\text{II})}$.^{32,36} The latter is supported (a) by direct comparison of the heats of protonation (ΔH_{HM}) of $\text{Cp}_2^*\text{Os}^{(\text{II})}$ ($\Delta H_{\text{HM}} = -111.3$ kJ/mol) and $\text{Cp}_2^*\text{Ru}^{(\text{II})}$ ($\Delta H_{\text{HM}} = -79.5$ kJ/mol) by $\text{CF}_3\text{SO}_3\text{H}$ in DCE, (ΔH_{HM} for $\text{Cp}_2^*\text{Fe}^{(\text{II})}$ could not be determined). Moreover, a theoretical study using valence-bond concepts to predict the valence bond energies of all three rows of transition metal hydride cations by Ohanessian and Goddard³⁷ demonstrated that the M–H bond energies increased in the order $\text{Ru} < \text{Fe} < \text{Os}$ for Group 8 transition metals primarily due to factors associated with the change in atomic exchange energy and the promotion energy to obtain an atomic configuration suitable for bonding. Thus, the much lower bond strength of the Ru–H bond in comparison to the Os–H has the practical consequence that $[\text{Cp}_2^*\text{Ru}^{(\text{IV})}(\text{H})]^+$ is not a very stable species, and considerably less so than its group 8 analogue $[\text{Cp}_2^*\text{Os}^{(\text{IV})}(\text{H})]^+$. Additionally, to date, $[\text{Cp}_2^*\text{Ru}^{(\text{IV})}(\text{H})]^+$ has only been generated transiently *in situ*. $[\text{Cp}_2^*\text{Os}^{(\text{IV})}(\text{H})]^+$ on the other hand is an isolable species.²² Peiyu Ge *et al.*² determined $\text{Cp}_2^*\text{Os}^{(\text{II})}$ pK_a at 8.35. Therefore, we can conclude that the pK_a of $\text{Cp}_2^*\text{Ru}^{(\text{II})}$ should be higher. Simulations were performed in this Chapter in the section 2.5 and give a computed $\Delta G_{\text{H}^+}^0$, DFT. Additionally, a pK_a with an aqueous proton at liquid|liquid interface was obtained by fitting of the experimental data with simulated ones in Chapter V.

Finally, $[\text{H}(\text{OEt}_2)_2]\text{TB}$ and $\text{CF}_3\text{SO}_3\text{H}$ are both sufficiently strong organic acids to both facilitate $[\text{Cp}_2^*\text{Ru}^{(\text{IV})}(\text{H})]^+$ formation in a stoichiometric 1:1 fashion. However, in order to facilitate the batch-water splitting process, $[\text{H}(\text{OEt}_2)_2]\text{TB}$ was chosen as the organic acid of choice for all subsequent mechanistic studies, in part due to its additional potential advantage of being a particularly poor nucleophile, discussed in the next Chapter.³⁸

3.4.2 Light-driven reaction mechanism characterization

3.4.2.1 UV/vis characterization

To understand the mechanism involved for the photo-hydrogen production by $\text{Cp}_2^*\text{Ru}^{\text{(II)}}$, the reaction was first followed by UV/vis spectroscopy, as shown in Figure 3.6.

In the absence of $[\text{H}(\text{OEt}_2)_2]\text{TB}$, and hence $[\text{Cp}_2^*\text{Ru}^{\text{(IV)}(\text{H})}]^+$, no significant changes of the UV/vis spectra were observed. With increased illumination time, some increase in the absorbance between 300 and 400 nm did occur, indicating that $\text{Cp}_2^*\text{Ru}^{\text{(II)}}$ may decompose to a certain extent with prolonged exposure to white light. In the presence of an excess of $[\text{H}(\text{OEt}_2)_2]\text{TB}$ (2 and 4 equivalents), a clear initial increase of the absorbance at 500 nm was observed during the early stages of the reaction corresponding to the formation of a first non-identified pink species expected to be $[\text{Cp}_2^*\text{Ru}^{\text{(III)}}]^+$ from eq. (3.2). After a certain period of time, approximately 50 min, the maximum absorbance was reached and the reaction proceeded accompanied by a gradual decrease of the band at 500 nm. Two isosbestic points were observed at 460 and 557 nm, and after 4 hours of illumination, a significant absorbance below 400 nm and a broad band at 450 nm were indicative of the presence of a final product, expected to be $[\text{Cp}_2^*\text{Ru}^{\text{(IV)}}(\text{C}_5\text{Me}_4\text{CH}_2)]^+$ from eq. (3.3). However, when $[\text{H}(\text{OEt}_2)_2]\text{TB}$ was the limiting reagent (0.5 and 1 equivalent), fast decomposition of $[\text{Cp}_2^*\text{Ru}^{\text{(III)}}]^+$ occurred with the clear absorbance peak at 500 nm quickly giving way to a series of ill-defined absorbance bands. The latter suggests that the compound decomposes under light illumination and in the absence of protons.

In the following paragraphs, UV/vis and NMR spectroscopy studies were carried out to identify $[\text{Cp}_2^*\text{Ru}^{\text{(IV)}}(\text{C}_5\text{Me}_4\text{CH}_2)]^+$ and, for the first time, $[\text{Cp}_2^*\text{Ru}^{\text{(III)}}]^+$.

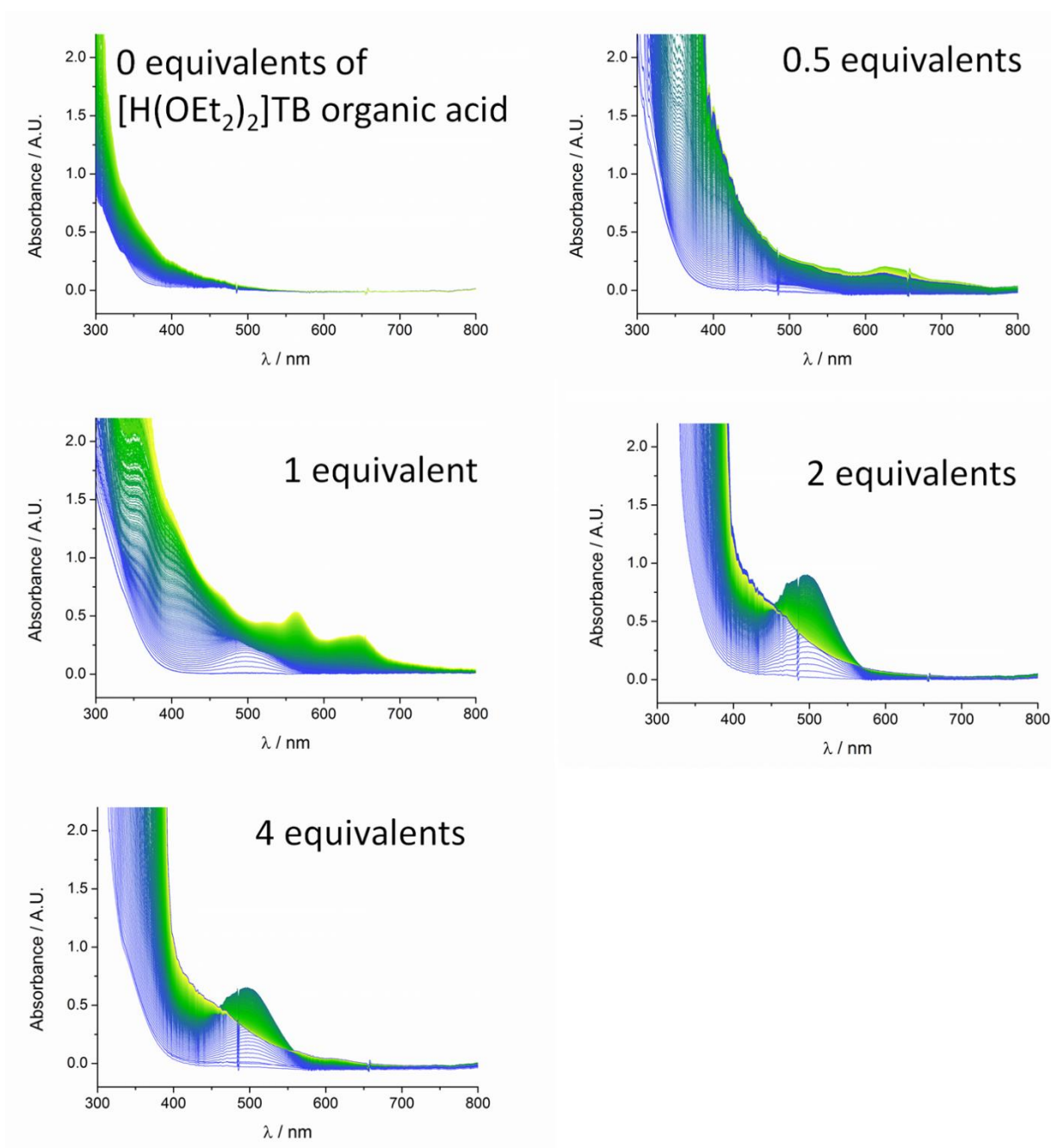


Figure 3.6. Irradiation of an acidified organic solution of $\text{Cp}_2^*\text{Ru}^{\text{(III)}}$ with white light monitored by UV/vis spectroscopy. The influence of the number of equivalents of the strong organic acid $[\text{H}(\text{OEt}_2)_2]\text{TB}$ on the evolution of the UV/vis spectra was monitored for solutions of $\text{Cp}_2^*\text{Ru}^{\text{(III)}}$ (1.875 mM) in DCE subjected to white light illumination by a 500 W Xe lamp. UV/vis spectra were taken every minute in a glovebox under anaerobic conditions.

3.4.2.2 Identification transient $[\text{Cp}_2^*\text{Ru}^{\text{(III)}}]^+$

The identification and characterisation of $[\text{Cp}_2^*\text{Ru}^{\text{(III)}}]^+$, assumed to be generated *in situ* during irradiation of $\text{Cp}_2^*\text{Ru}^{\text{(III)}}$ in acidified organic solutions (eq. (3.2)),^{17,20,21,39} was obstructed in previous studies due to its high instability and a very short life time. In these studies, $[\text{Cp}_2^*\text{Ru}^{\text{(III)}}]^+$ was assumed to convert rapidly to $[\text{Cp}_2^*\text{Ru}^{\text{(IV)}}(\text{C}_5\text{Me}_4\text{CH}_2)]^+$. As discussed above and detailed in the

next Chapter, it appears that counter-anions are highly detrimental to the stability of the $[\text{Cp}_2^*\text{M}^{(\text{III})}]^+$ ($\text{M} = \text{Os}$ or Ru) species and, indeed, several studies reporting the formation of $[\text{Cp}_2^*\text{M}^{(\text{III})}]^+$ in the presence of nucleophilic counter highlight the instability of the oxidized metallocenes under these experimental conditions.^{40,20,41} Furthermore, breakdown of $[\text{Cp}_2^*\text{M}^{(\text{III})}]^+$ is accelerated in the presence of coordinating solvents such as acetonitrile and tetrahydrofuran.^{39,42} As TB^- is less nucleophilic than the other counter-anions reported until now, we attempted to prepare the potentially stabilised $[\text{Cp}_2^*\text{Ru}^{(\text{III})}]\text{TB}$ species by oxidation of $\text{Cp}_2^*\text{Ru}^{(\text{II})}$ in a solution of DCE (a non-coordinating solvent) containing bis(triphenylphosphoranylidene)ammonium tetrakis-(pentafluorophenyl) borate (BATB) supporting electrolyte.

The spectroscopic identification of the transient $[\text{Cp}_2^*\text{Ru}^{(\text{III})}]^+$ species was achieved by preparing $[\text{Cp}_2^*\text{Ru}^{(\text{III})}]\text{TB}$ *via* oxidation of 6 mM $\text{Cp}_2^*\text{Ru}^{(\text{II})}$ in a solution of DCE containing BATB as a supporting electrolyte. The solution was oxidized for 120 s at a series of applied potentials spaced at regular intervals between 0.22 and 0.91 V (*vs.* SHE). The response at each applied potential was followed by UV/vis spectroscopy. As seen Figure 3.7, a characteristic absorbance, with a maximum (λ_{max}) centred at 500 nm, appeared confirming the presence of $[\text{Cp}_2^*\text{Ru}^{(\text{III})}]\text{TB}$ as an intermediate during the catalysis. On the time-scale of this experiment (120 s), at 0.75 V *vs.* SHE, all $\text{Cp}_2^*\text{Ru}^{(\text{II})}$ molecules present were converted to $[\text{Cp}_2^*\text{Ru}^{(\text{III})}]^+$. This was reflected in the observed plateau in absorbance at 500 nm and by a decrease of the current beyond this applied potential. Finally, the molar extinction coefficient of $[\text{Cp}_2^*\text{Ru}^{(\text{III})}]^+$ in DCE was determined using the Beer-Lambert Law as $0.960 \text{ mM}^{-1}\cdot\text{cm}^{-1}$, with an optical path length of 1 mm, and an absorbance of 0.576 at an applied potential of 0.75 V (*vs.* SHE) that corresponds to 6 mM of $[\text{Cp}_2^*\text{Ru}^{(\text{III})}]^+$ generated by exhaustive electrolysis.

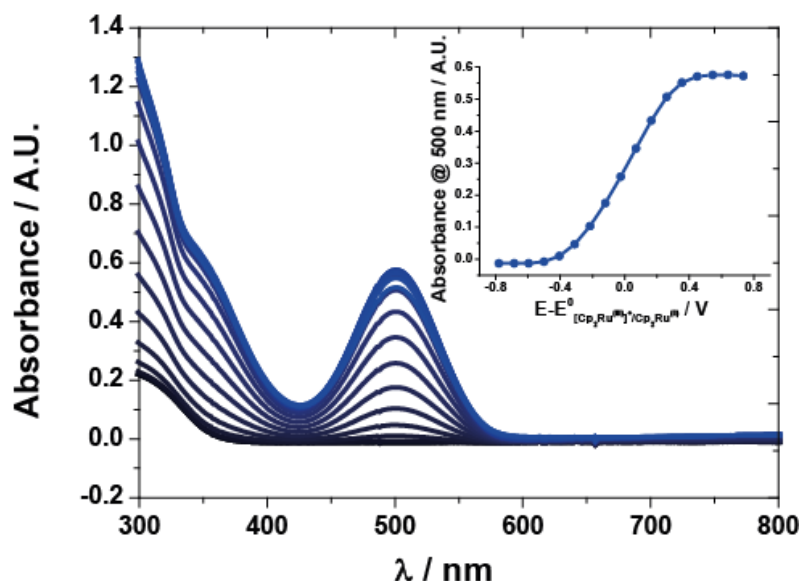


Figure 3.7. Spectroelectrochemical characterisation of the generation of $[\text{Cp}_2^*\text{Ru}^{\text{(III)}}]^+$ as a function of the applied potential. Oxidation of a 6 mM solution of $\text{Cp}_2^*\text{Ru}^{\text{(II)}}$ in de-oxygenated DCE with 20 mM BATB as supporting electrolyte, was performed by applying various potentials at regular intervals between 0.22 and 0.91 V (*vs.* SHE) for 120 s under anaerobic conditions. $[\text{Cp}_2^*\text{Ru}^{\text{(III)}}]^+$ has a UV/vis absorbance maximum (λ_{max}) at 500 nm. Inset, the variation of absorbance at 500 nm plotted as a function of applied potential.

3.4.2.3 The second release of H_2 from the transient $[\text{Cp}_2^*\text{Ru}^{\text{(III)}}]^+$ species

$[\text{Cp}_2^*\text{Ru}^{\text{(III)}}]^+$, a previously unattainable species due to its instability in the presence of slightly nucleophilic counter-anions, was synthesized by bulk electrolysis and its capability to produce hydrogen under illumination was investigated. The monitoring of the electrochemical reaction is illustrated in Figure 3.8. A potential of 1.2 V (*vs.* SHE) was applied for 65 min to a solution of 28 μmol $\text{Cp}_2^*\text{Ru}^{\text{(II)}}$. After 50 min, current no longer flowed and charge reached a maximum of 2.9 C. This quantity of charge is in excellent agreement with that required to generate the theoretical number of moles of $[\text{Cp}_2^*\text{Ru}^{\text{(III)}}]^+$ expected ($n([\text{Cp}_2^*\text{Ru}^{\text{(III)}}]^+)$) for exhaustive electrolysis of 28 μmol $\text{Cp}_2^*\text{Ru}^{\text{(II)}}$, as determined from Faraday's law, $n([\text{Cp}_2^*\text{Ru}^{\text{(III)}}]^+) = Q/zF$, where z , the number of electrons transferred per $\text{Cp}_2^*\text{Ru}^{\text{(II)}}$ molecule oxidised, is equal to 1, confirming the total conversion of $\text{Cp}_2^*\text{Ru}^{\text{(II)}}$ to $[\text{Cp}_2^*\text{Ru}^{\text{(III)}}]^+$ under these experimental conditions. Thus, it would seem that the generated $[\text{Cp}_2^*\text{Ru}^{\text{(III)}}]^+\text{TB}$ species was stable. This is a significant result as previous studies have noted the immediate decomposition of $[\text{Cp}_2^*\text{Ru}^{\text{(III)}}]^+$ in the presence of other electrolyte counter-anions.

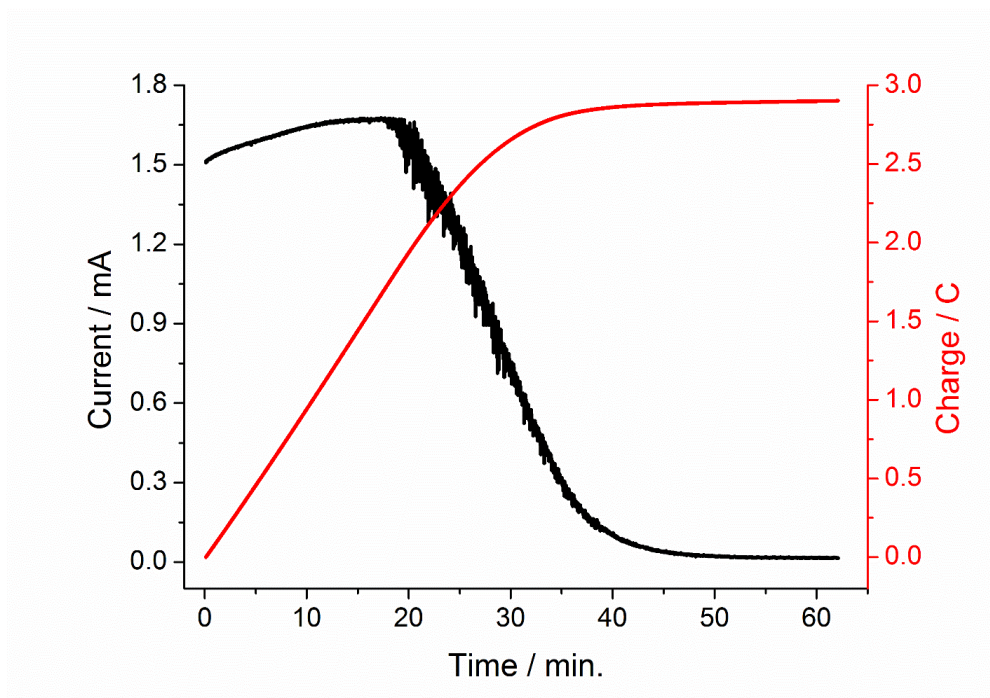


Figure 3.8. Monitoring the electro-synthesis of $[\text{Cp}_2^*\text{Ru}^{\text{III}}]^+$ by bulk electrolysis in the presence of the TB^- counter-ion. Current (black line) and charge (red line) shown as a function of electrolysis time during the oxidation of 28 μmol $\text{Cp}_2^*\text{Ru}^{\text{II}}$ in 1,2-DCE with 20 mM BATB as supporting electrolyte.

Solutions of $[\text{Cp}_2^*\text{Ru}^{\text{III}}]^+$ were subsequently illuminated in the presence of protons to investigate if H_2 could be produced with $[\text{Cp}_2^*\text{Ru}^{\text{III}}]^+$ as the initial form of the metallocene present. Indeed, H_2 was evolved and detected by GC with illumination and in the presence of acid (see Figure 3.9). The latter is a powerful validation of the mechanism proposed by the A. N. Nesmeyanov Institute of Organoelement Compounds.¹²⁻¹⁹ Furthermore, the necessity to add protons to the solution is a confirmation that the generation of a single H_2 molecule involves one proton coming from the organic acid and the other from a methyl-group on one of the $[\text{Cp}_2^*\text{Ru}^{\text{III}}]^+$ cyclopentadienyl rings.

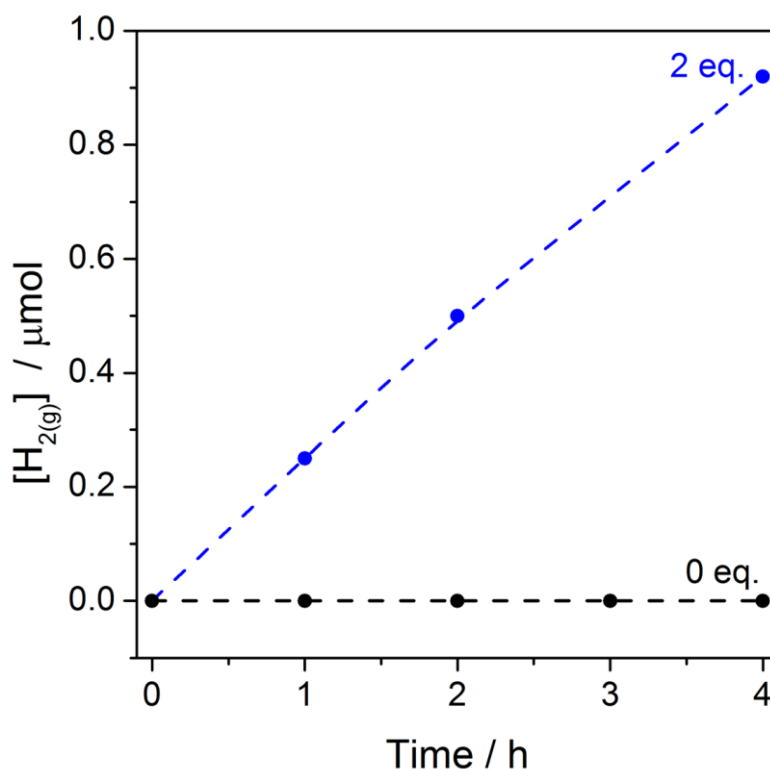


Figure 3.9. Monitoring the photo-production of H₂ gas from solutions of [Cp₂*Ru^(III)]⁺ dissolved in DCE as a function of organic proton concentration and irradiation time. Summary of the quantities of H₂ gas evolved (μmol) determined by sampling the headspace of septum-sealed stirring solutions of 4 μmol [Cp₂*Ru^(III)]⁺ dissolved in DCE in the absence (black trace) and presence (blue trace) of organic protons (8 μmol HTB) as a function of irradiation time with white light from a 500 W Xe lamp. [Cp₂*Ru^(III)]⁺ was generated by bulk electrolysis of Cp₂*Ru^(II) in DCE in the dark under anaerobic conditions (see Figure 3.8).

3.4.2.4 Identification of the final photo-product as [Cp₂*Ru^(IV)(C₅Me₄CH₂)]⁺ by NMR spectroscopy.

The photo-irradiation of Cp₂*Ru^(III) in acidified solutions (eq. (3.4)) was monitored by ¹H NMR spectroscopy, complementing the earlier GC experiments for this reaction where significant H₂ was detected (see Figure 3.2). The goal of these ¹H NMR experiments was to unambiguously identify the final form of the metallocene after photo-irradiation in acidified organic solutions. The NMR analysis involved preparing a solution of Cp₂*Ru^(III) in CD₂Cl₂ (with 31.2 mM DCE present as the internal standard) containing excess [H(OEt₂)₂]TB (4 equivalents). The tube was illuminated and the reaction monitored by ¹H NMR, as shown in Figure 3.10. After 360 min of illumination the signals characteristic of [Cp₂*Ru^(IV)(H)]⁺ (see Figure 3.3) had disappeared, to be replaced by new ¹H NMR signals at δ = 1.50, 1.74, 1.83 and 4.30 ppm (see Figure 3.10). The final ¹H NMR spectra outlining the complete disappearance of the signal corresponding to the hydridic proton (green square) at a characteristic negative value of −8.38 ppm.

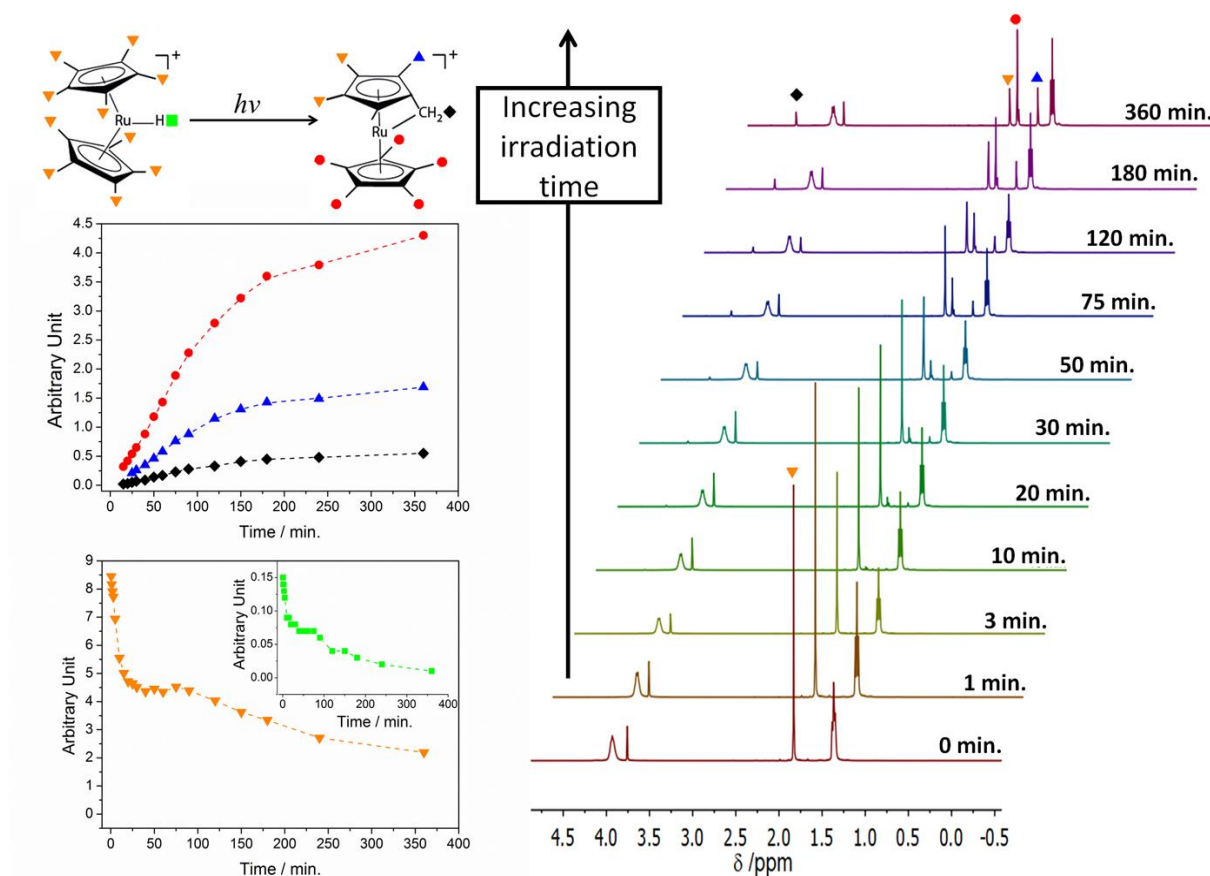
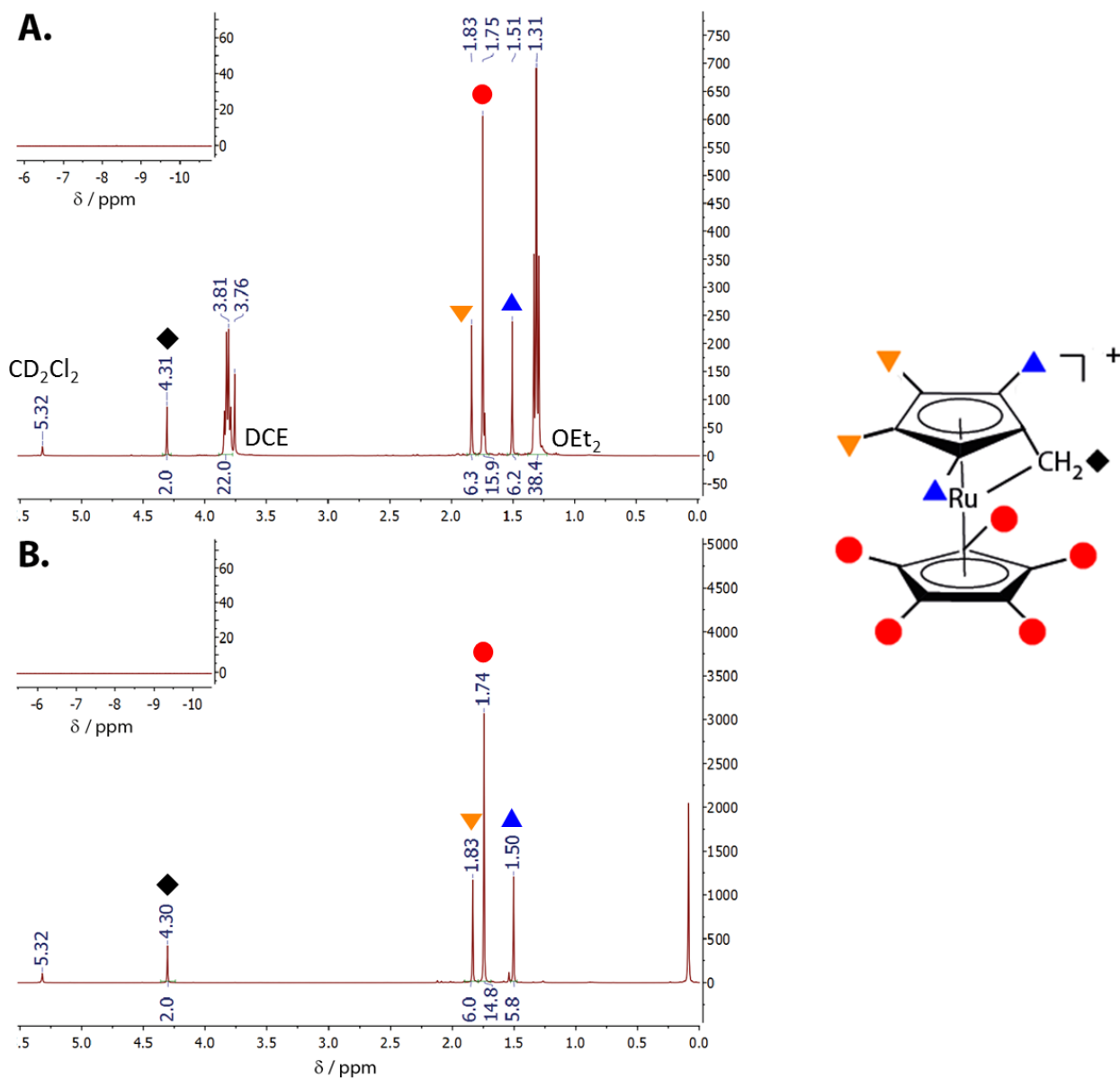


Figure 3.10. Formation of $[\text{Cp}^*\text{Ru}^{\text{IV}}(\text{C}_5\text{Me}_4\text{CH}_2)]^+$ from $[\text{Cp}_2^*\text{Ru}^{\text{IV}}\text{H}]^+$ monitored by ^1H NMR spectroscopy as function of irradiation time. ^1H NMR spectra were recorded every minute (shown on the right) for a solution of 15 mM $\text{Cp}_2^*\text{Ru}^{\text{III}}$ in CD_2Cl_2 containing 60 mM $[\text{H}(\text{OEt}_2)_2]\text{TB}$ (4 equivalents) and illuminated for 360 min by a 500 W Xe lamp. Solutions were prepared under anaerobic conditions and 31.2 mM DCE was used as the internal standard.

After further purification by column chromatography with DCM/hexane, 6:4, and then 8:2 eluent (see Chapter II, Section 2.3.1), the formed product was unambiguously identified as $[\text{Cp}^*\text{Ru}^{\text{IV}}(\text{C}_5\text{Me}_4\text{CH}_2)]^+$ by ^1H and ^{13}C and DEPT-135 NMR analysis, in agreement with previous studies (see Figure 3.11).²⁰ Based on the integrals on ^1H NMR spectra (Figure 3.11(B)), the signals at 1.50, 1.74 and 1.83 ppm were assigned to chemically non-equivalent protons of three different sets of methyl groups on the cyclopentadienyl rings, designated \bullet , \blacktriangle and \blacktriangledown , and assigned as shown in Figure 3.11(A) and (B). The signal at 4.30 ppm was assigned to a stabilized metallocenyl carbocationic CH_2 group, consistent with the formation of $[\text{Cp}_2^*\text{Ru}^{\text{IV}}(\text{C}_5\text{Me}_4\text{CH}_2)]^+$. Additionally, the ^{13}C NMR of the purified product in Figure 3.11(C) revealed four peaks between 95 and 110 ppm corresponding to the quaternary carbons of $[\text{Cp}_2^*\text{Ru}^{\text{IV}}(\text{C}_5\text{Me}_4\text{CH}_2)]^+$. The presence of the

ethyl at 74.26 ppm was highlighted by performing DEPT 135 spectra, as illustrated Figure 3.11(D), and the methyl group gave three signals below 15 ppm.



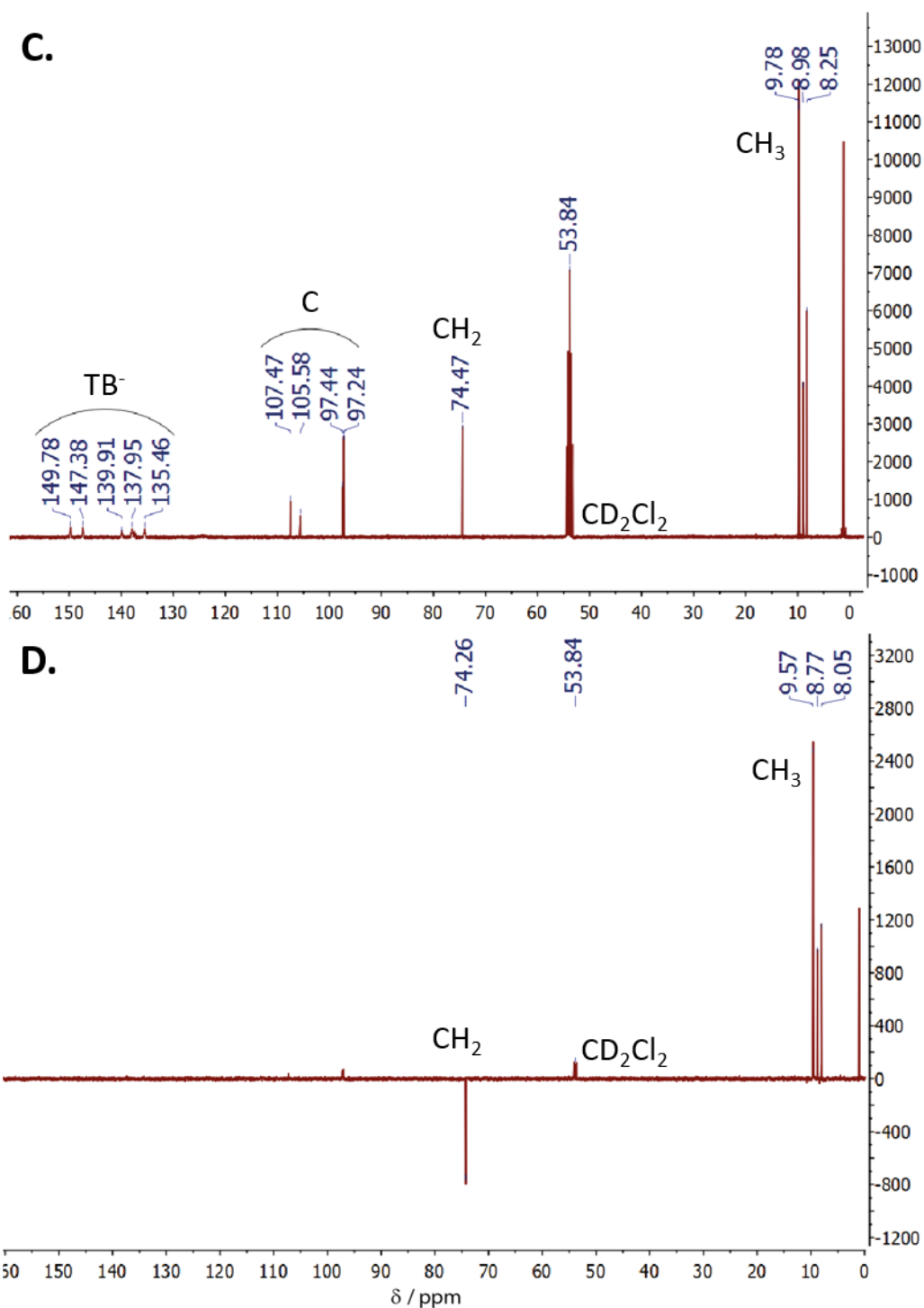


Figure 3.11. ^1H NMR and ^{13}C NMR spectra of the purified final product obtained after irradiation of 15 mM $[\text{Cp}_2^+\text{Ru}^{(\text{IV})}(\text{H})]^+$ for 360 min: before (A) and after (B) purification. (C) Standard ^{13}C and (D) DEPT-135. NMR spectra were obtained in CD_2Cl_2 solvent in the dark and under anaerobic conditions. Purification was achieved by separating the reaction products after irradiation by column chromatography using DCM/hexane (initially with a 6:4 ratio, and subsequently an 8:2 ratio) as the eluent. An orange powder was obtained as a final product. OEt_2 = diethylether, present in $[\text{H}(\text{OEt}_2)_2]\text{TB}$ due to its synthesis from $\text{Li}(\text{OEt}_2)_2\text{TB}$. The negative peak observed in the DEPT-135 spectra reveals the presence of CH_2 .

3.4.3 Hydricity

As explained above, M-H bond plays a crucial role in HER. To further investigate the bond breaking occurring in the mechanistic pathway, the hydricity of $[\text{Cp}_2^*\text{Ru}^{\text{(IV)}}(\text{H})]^+$ was investigated. The hydricity represents the Gibbs energy required to cleave an M-H bond to generate a hydride ion (H^-).⁴³ It is a useful experimentally measurable parameter that can help predict the reactivity of metal hydride and thereby, assist in comparing metallocenes for HER amongst themselves. Experimental methods widely used for thermodynamic hydricity determination include: (i) the H_2 heterolysis method⁴⁴ to determine hydricity values relative to the hydricity of H_2 , (ii) the potential – $\text{p}K_a$ method⁴⁵ using reduction potential of the complex and its acid strength and (iii) the hydride transfer method⁴⁵ measuring the equilibrium constant between the hydride donor of interest ($[\text{Cp}_2^*\text{Ru}^{\text{(IV)}}(\text{H})]^+$) and a reference hydride acceptor with a known hydricity.

The first method was not possible to implement due to the photo-activation step involved. The potential – $\text{p}K_a$ method requires to know the $\text{p}K_a$ and the reduction potential cannot be accurately estimated from irreversible electrochemical waves. Therefore, hydricity of $[\text{Cp}_2^*\text{Ru}^{\text{(IV)}}(\text{H})]^+$ was investigated from trityl cation (Ph_3C^+) hydride acceptor. $\text{Cp}_2^*\text{Ru}^{\text{(II)}}$ was mixed with Ph_3C^+ in CD_2Cl_2 in the absence (Figure 3.12) and presence (not shown) of protons. Unexpectedly, ^1H NMR shows the appearance of $[\text{Cp}_2^*\text{Ru}^{\text{(IV)}}(\text{C}_5\text{Me}_4\text{CH}_2)]^+$ with the formation of triphenylmethane in both cases. Thus, the determination of the hydricity of $[\text{Cp}_2^*\text{Ru}^{\text{(IV)}}(\text{H})]^+$ was inaccessible. Nevertheless, it reveals the hydridic nature of the methyl hydrogens in $\text{Cp}_2^*\text{Ru}^{\text{(II)}}$. Their hydricity was estimated from the ^1H NMR spectra in the absence of protons (Figure 3.12). The hydricity of $\text{Cp}_2^*\text{Ru}^{\text{(II)}}$ determined as $\Delta G_{\text{H}^-}^0(\text{Cp}_2^*\text{Ru}^{\text{(II)}}) = 398 \text{ kJ/mol}$ was expressed from the thermodynamics cycle shown in Table 3.1, by taking into account the hydricity of Ph_3C^+ ($\Delta G_{\text{H}^-}^0(\text{Ph}_3\text{CH}) = 414.5 \text{ kJ/mol}$) and the Gibbs energy of the reaction ($\Delta G_{\text{H}^-}^0(\text{eq.}) = -16 \text{ kJ/mol}$).

Table 3.1. Thermodynamic cycle to express the hydricity, $\Delta G_{\text{H}^-}^0(\text{Cp}_2^*\text{Ru}^{\text{(II)}})$.

$\text{Cp}_2^*\text{Ru}^{\text{(II)}} + \text{Ph}_3\text{C}^+ \rightarrow [\text{Cp}_2^*\text{Ru}^{\text{(IV)}}(\text{C}_5\text{Me}_4\text{CH}_2)]^+ + \text{Ph}_3\text{CH}$	$\Delta G_{\text{H}^-}^0(\text{eq.})$
$\text{Ph}_3\text{CH} \rightarrow \text{Ph}_3\text{C}^+ + \text{H}^-$	$\Delta G_{\text{H}^-}^0(\text{Ph}_3\text{CH})$
$\text{Cp}_2^*\text{Ru}^{\text{(II)}} \rightarrow [\text{Cp}_2^*\text{Ru}^{\text{(IV)}}(\text{C}_5\text{Me}_4\text{CH}_2)]^+ + \text{H}^-$	$\Delta G_{\text{H}^-}^0(\text{Cp}_2^*\text{Ru}^{\text{(II)}}) = \Delta G_{\text{H}^-}^0(\text{Ph}_3\text{CH}) + \Delta G_{\text{H}^-}^0(\text{eq.})$

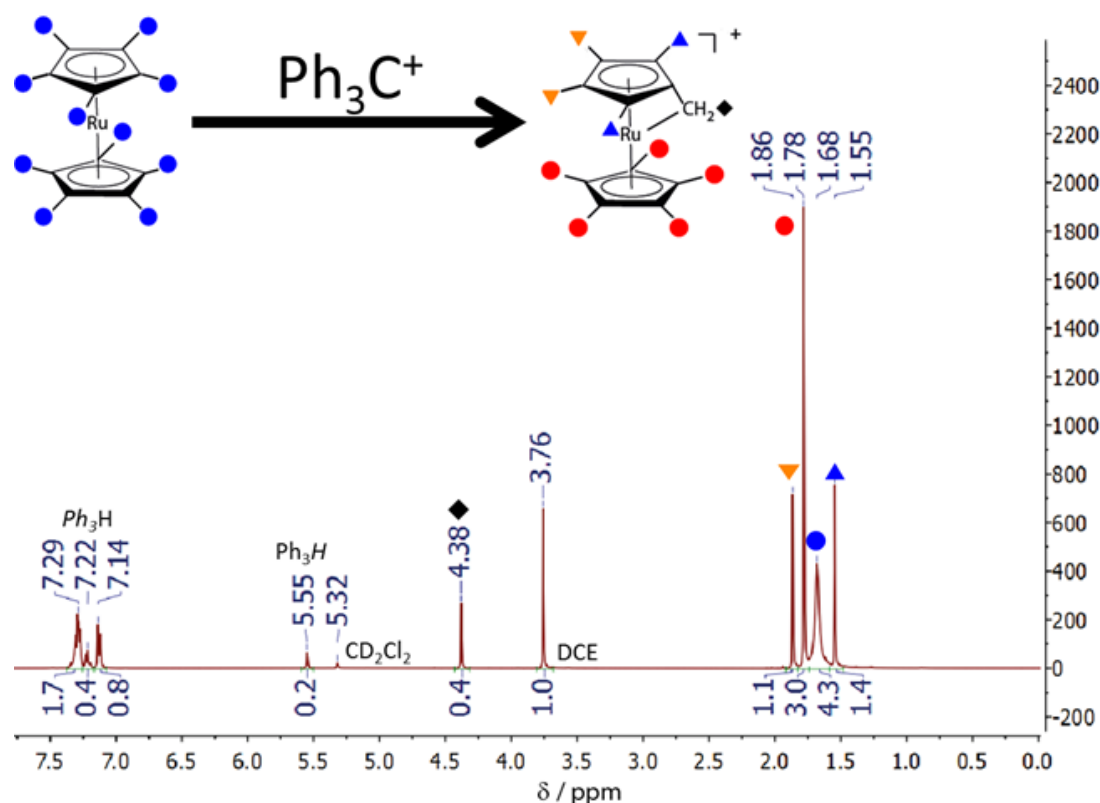


Figure 3.12. ^1H NMR spectra of the equilibrium obtained by mixing 15 mM $\text{Cp}_2^*\text{Ru}^{(\text{II})}$ and Ph_3CPF_6 . ^1H NMR spectra were obtained in CD_2Cl_2 using DCE (31.2 mM) as an internal standard, in the dark and under anaerobic conditions. Hydricity was determined thanks to the concentrations of present species at the equilibrium: $c_{\text{Cp}_2^*\text{Ru}^{(\text{II})}} = 6.47$ mM, $c_{[\text{Cp}_2^*\text{Ru}^{(\text{IV})}(\text{H})]^+} = 8.53$ mM, $c_{\text{Ph}_3\text{CH}} = 14.7$ mM and $c_{\text{Ph}_3\text{C}^+}$, eq. = 0.03 mM.

3.5 Kinetics analysis of the transient $[\text{Cp}_2^*\text{Ru}^{(\text{III})}]^+$ species

In the present experimental conditions, both the relative stability of $[\text{Cp}_2^*\text{Ru}^{(\text{III})}]^+$ in DCE in the presence of TB^- and the clear identification of the UV/vis absorbance peak of $[\text{Cp}_2^*\text{Ru}^{(\text{III})}]^+$ in DCE provided an opportunity to study the behaviour of the $[\text{Cp}_2^*\text{Ru}^{(\text{III})}]^+$ intermediate generated *in situ* during irradiation of $\text{Cp}_2^*\text{Ru}^{(\text{II})}$ in DCE solutions acidified with $[\text{H}(\text{OEt}_2)_2]\text{TB}$. The goals of these experiments is to distinguish the mechanism that is involved during the formation of hydrogen by irradiation of the solution of $[\text{Cp}_2^*\text{Ru}^{(\text{III})}]^+$. As described in Chapter I, Section 1.4.3, three different mechanisms were proposed to explain the production of hydrogen by metallocenes. The first possibility is a bimolecular homolytic pathway, known as a Tafel reaction where two protonated metallocenium ions react to release hydrogen. The two other possibilities are a two steps process which involves an oxidation and a protonation of the complex.

3.5.1 Influence of $\text{Cp}_2^*\text{Ru}^{\text{(II)}}$ initial concentration

The initial rates were used to determine the kinetics of disappearance of $[\text{Cp}_2^*\text{Ru}^{\text{(IV)}}(\text{H})]^+$, generated *in situ* in the dark in a de-oxygenated DCE solution containing excess $[\text{H}(\text{OEt}_2)_2]\text{TB}$ under anaerobic conditions, and on illumination with white light. To achieve this, the rate of change of the absorbance at $\lambda_{\text{max}} = 500 \text{ nm}$, corresponding to the concentration of $[\text{Cp}_2^*\text{Ru}^{\text{(III)}}]^+$ generated by reaction of $[\text{Cp}_2^*\text{Ru}^{\text{(IV)}}(\text{H})]^+$ as described in eq. (3.2), was monitored with spectra taken every 10 s. Thus,

$$v = \frac{d\left(c_{[\text{Cp}_2^*\text{Ru}^{\text{(III)}}]^+}\right)}{dt} = k_{\text{app}} \left(c_{[\text{Cp}_2^*\text{Ru}^{\text{(III)}}]^+}\right)^n \quad (3.11)$$

where k_{app} is the apparent rate constant of the reaction and n is reaction order.⁹

Experiments were performed with various initial concentrations of $[\text{Cp}_2^*\text{Ru}^{\text{(IV)}}(\text{H})]^+$, in the range of 1.4 to 2.8 mM, while keeping the $[\text{H}(\text{OEt}_2)_2]\text{TB}$ concentration in significant excess (42.2 mM), see Figure 3.13. First, the initial rate (v , $\text{mM}\cdot\text{s}^{-1}$) of the reaction described by eq. (3.2) was determined for each starting concentration of $[\text{Cp}_2^*\text{Ru}^{\text{(IV)}}(\text{H})]^+$ from the slopes of a plot of $c[\text{Cp}_2^*\text{Ru}^{\text{(IV)}}(\text{H})]^+$ *versus* time (see Figure 3.13). Results are compared in Figure 3.14.

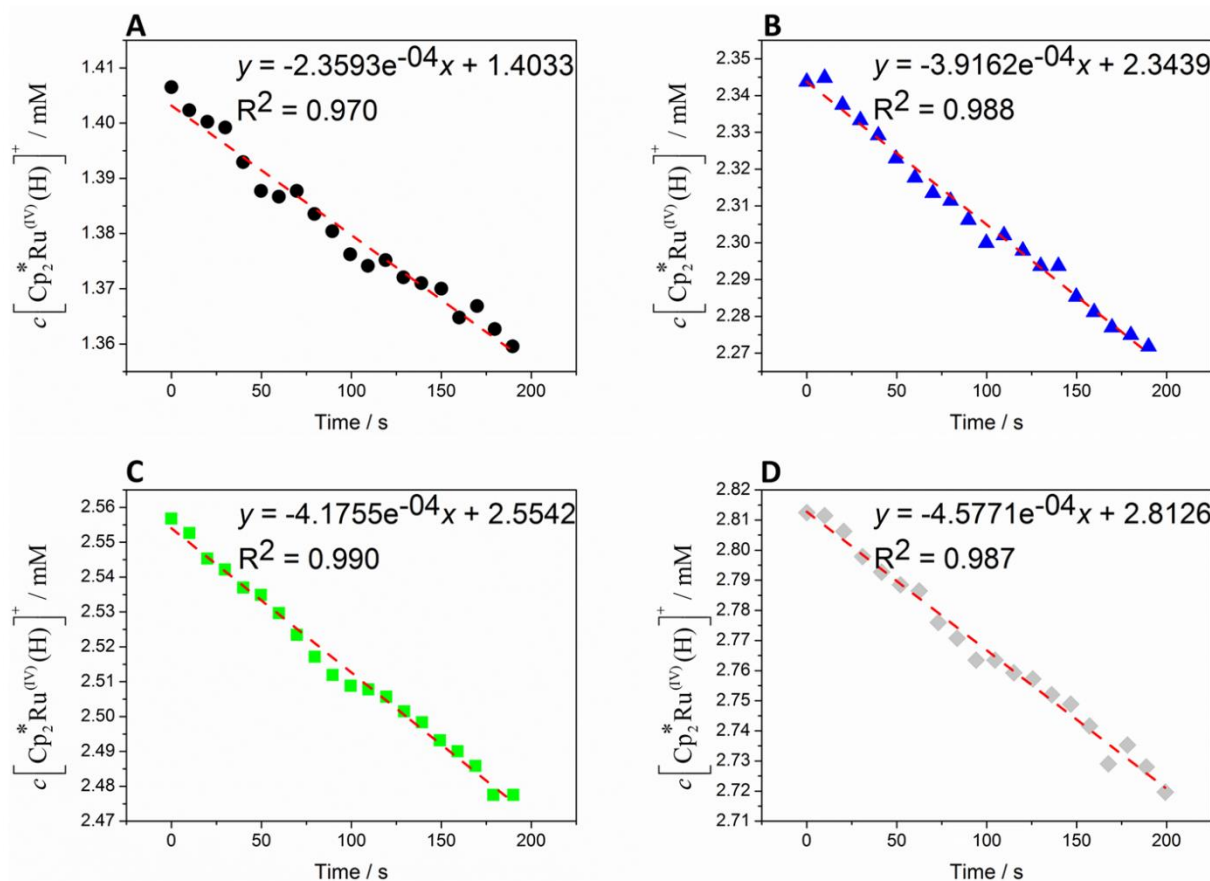


Figure 3.13. The initial rate (v , $\text{mM} \cdot \text{s}^{-1}$) of the reaction described by eq. (2) was determined for each starting concentration of $[\text{Cp}_2^*\text{Ru}^{(\text{IV})}(\text{H})]^+$, (A) 1.40 (black circles), (B) 2.34 (blue triangles), (C) 2.55 (green squares) and (D) 2.81 (grey diamonds) mM, in the presence of excess protons (42.20 mM $[\text{H}(\text{OEt})_2]$ TB) upon commencing irradiation of the organic DCE solution with white light. The slope of each plot corresponds to the initial rate for that starting concentration of $[\text{Cp}_2^*\text{Ru}^{(\text{IV})}(\text{H})]^+$.

Next, the reaction order (n) and k_{app} were determined by plotting $\ln(v)$ vs $\ln([\text{Cp}_2^*\text{Ru}^{(\text{IV})}(\text{H})]^+)$, Figure 3.14 (inset). The slope signified that the reaction was first order with respect to $c[\text{Cp}_2^*\text{Ru}^{(\text{IV})}(\text{H})]^+$ and k_{app} was determined from the intercept (*i.e.*, $\ln(k_{app})$), as $1.7 \times 10^{-4} \text{ s}^{-1}$. This calculated value of k_{app} was used to determine the theoretical first order decrease in the concentration of $[\text{Cp}_2^*\text{Ru}^{(\text{IV})}(\text{H})]^+$ as a function of illumination time (dashed red lines, Figure 3.14), with the integrated rate law for a first order reaction being

$$k_{app}t = \ln\left(\frac{a}{a-x}\right) \quad (3.12)$$

where a is the initial concentration of $[\text{Cp}_2^*\text{Ru}^{(\text{IV})}(\text{H})]^+$ in solution prior to illumination and x is the concentration of $[\text{Cp}_2^*\text{Ru}^{(\text{IV})}(\text{H})]^+$ remaining after a period of illumination time.

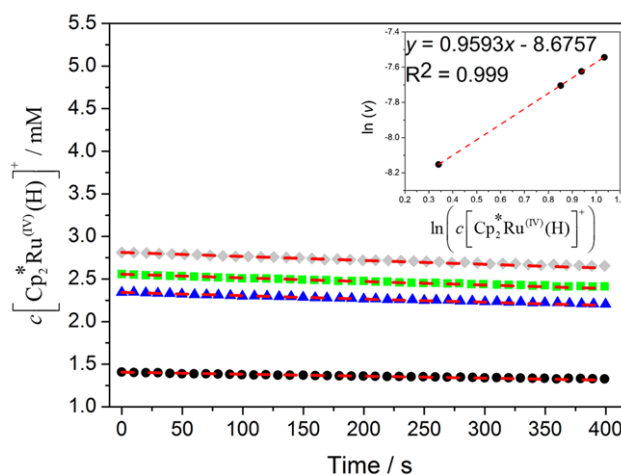


Figure 3.14. Comparison of the experimentally observed kinetics of the disappearance of $[\text{Cp}_2^*\text{Ru}^{\text{(IV)}}(\text{H})]^+$ with the theoretical rate law for a first-order reaction with an apparent rate constant of $1.7 \times 10^{-4} \text{ s}^{-1}$ (dashed red lines). The disappearance of $[\text{Cp}_2^*\text{Ru}^{\text{(IV)}}(\text{H})]^+$ was determined by monitoring the appearance of the UV/vis absorbance peak corresponding to the reaction product $[\text{Cp}_2^*\text{Ru}^{\text{(III)}}]^+$ at $\lambda_{\text{max}} = 500 \text{ nm}$ upon commencing irradiation of the organic DCE solution with white light (see eq. (3.2)). The initial concentrations of $[\text{Cp}_2^*\text{Ru}^{\text{(IV)}}(\text{H})]^+$ present were 1.40 (black circles), 2.34 (blue triangles), 2.55 (green squares) and 2.81 (grey diamonds) mM. The organic acid $[\text{H}(\text{OEt}_2)_2]\text{TB}$ was present in excess at 42.20 mM in each instance. **Inset:** Reaction order and rate constant determination with respect to $[\text{Cp}_2^*\text{Ru}^{\text{(IV)}}(\text{H})]^+$ in the presence of excess protons: plot of $\ln(v)$ *vs.* $\ln([\text{Cp}_2^*\text{Ru}^{\text{(IV)}}(\text{H})]^+)$; the slope signifies the reaction order and the apparent rate constant ($k_{\text{app.}}$) was determined from the intercept, $\ln(k_{\text{app.}})$. The initial rate (v , $\text{mM} \cdot \text{s}^{-1}$) was determined for each starting concentration of $[\text{Cp}_2^*\text{Ru}^{\text{(IV)}}(\text{H})]^+$ as shown in Figure 3.13.

Finally, to highlight the excellent match between theory and experimental data for the initial rates of reaction, the experimental kinetic data was re-plotted on a logarithmic scale *versus* the theoretically derived data in Figure 3.15, thereby confirming that the assumed rate equations correspond with the experimental data.

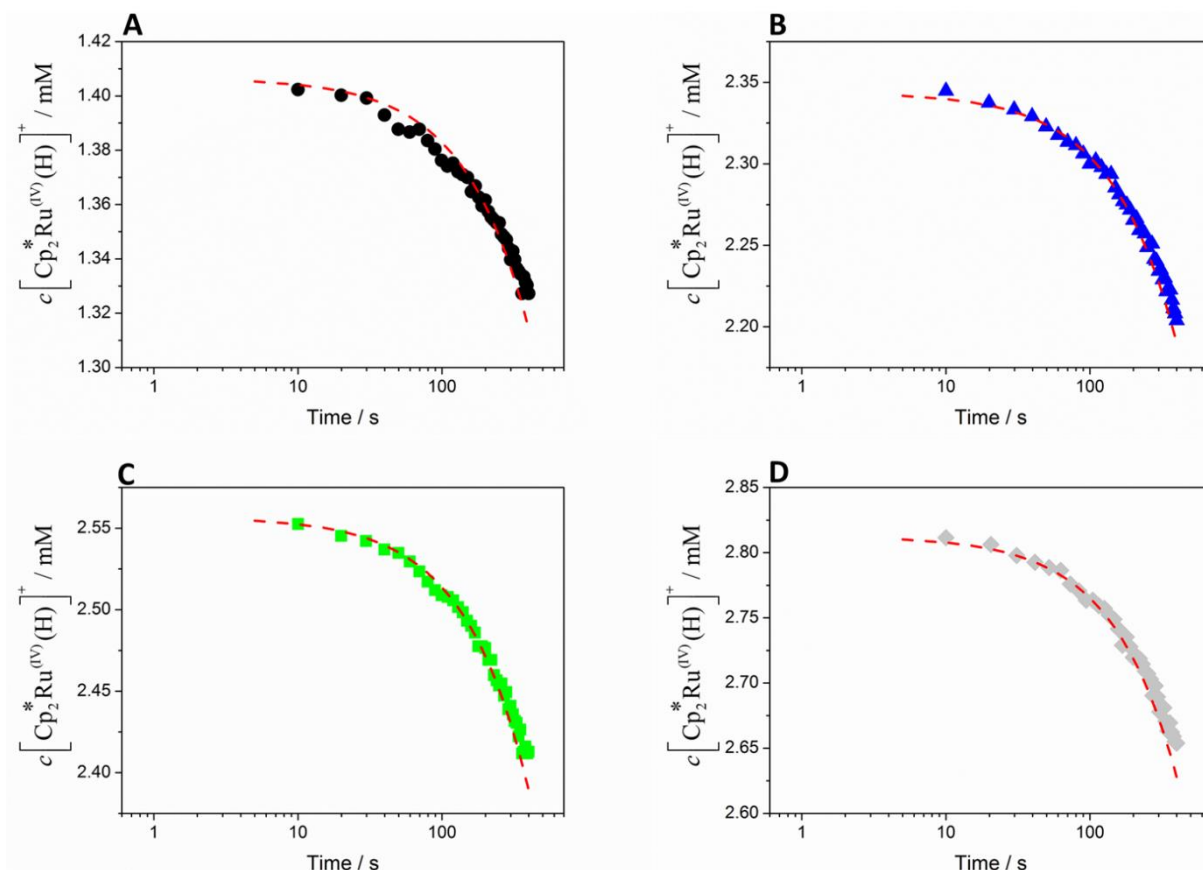


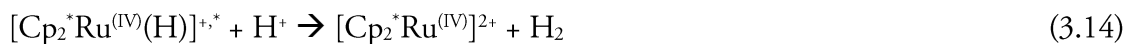
Figure 3.15. The excellent match of the experimentally determined initial kinetics (symbols) with the theoretical fits (dashed red lines) for each starting concentration of $[\text{Cp}_2^*\text{Ru}^{(\text{IV})}(\text{H})]^+$ were clarified graphically by using a logarithmic scale for the reaction time. The initial concentrations of $[\text{Cp}_2^*\text{Ru}^{(\text{IV})}(\text{H})]^+$ were (A) 1.40 (black circles), (B) 2.34 (blue triangles), (C) 2.55 (green squares) and (D) 2.81 (grey diamonds) mM, in the presence of excess protons (42.2 mM $[\text{H}(\text{OEt}_2)_2]\text{TB}$). The fits were obtained using the apparent rate constant, $k_{app.} = 1.7 \cdot 10^{-4} \text{ s}^{-1}$, determined in Figure 3.14 (inset) of the main text for first-order reactions that commence upon irradiation of the organic DCE solution with white light.

From the first order of the reaction, one can conclude that a bimolecular homolytic pathway (*i.e.* Tafel reaction) where two $[\text{Cp}_2^*\text{Ru}^{(\text{IV})}(\text{H})]^+$ would react to release hydrogen, as described in eq. (3.13), is excluded.

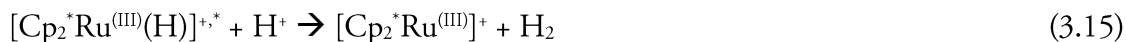


3.5.2 Influence of $[\text{H}(\text{OEt}_2)_2]\text{TB}$ initial concentration

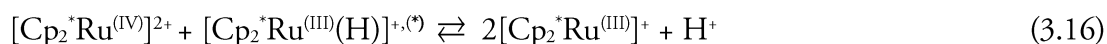
As the Tafel reaction was excluded, a monometallic reaction, consisting to a proton directly reacting with $[\text{Cp}_2^*\text{Ru}^{(\text{IV})}(\text{H})]^+$ or the reduced $[\text{Cp}_2^*\text{Ru}^{(\text{III})}(\text{H})]^+$, was envisaged. The reaction, taking to account the excitation of the hydride required to make the reaction occur,⁴⁶ is described in the eq. (3.14):



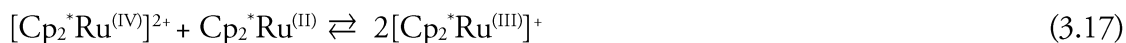
Or a reduced $[\text{Cp}_2^*\text{Ru}^{(\text{III})}(\text{H})]^+$ can directly react with protons:



Furthermore, two possibilities exist that may explain the reduction of $[\text{Cp}_2^*\text{Ru}^{(\text{IV})}]^{2+}$ to the $[\text{Cp}_2^*\text{Ru}^{(\text{III})}]^+$ observed by UV/vis. One possibility involves $[\text{Cp}_2^*\text{Ru}^{(\text{IV})}]^{2+}$ reacting with $[\text{Cp}_2^*\text{Ru}^{(\text{IV})}(\text{H})]^+$ or a photo-activated $[\text{Cp}_2^*\text{Ru}^{(\text{IV})}(\text{H})]^+$ to comproportionate into two equivalents of $[\text{Cp}_2^*\text{Ru}^{(\text{III})}]^+$ (eq. (3.16))



Alternatively, $[\text{Cp}_2^*\text{Ru}^{(\text{IV})}]^{2+}$ can react with the original $\text{Cp}_2^*\text{Ru}^{(\text{II})}$, eq.(3.17), the concentration of which depends on the equilibrium of the eq. (3.1):



Therefore, both pathways are disfavoured by the presence of free protons, the results herein do not allow the distinction between mechanisms involved in eq. (3.15) and (3.16).

In the same way, $[\text{Cp}_2^*\text{Ru}^{(\text{IV})}(\text{H})]^+$ can react with the original $\text{Cp}_2^*\text{Ru}^{(\text{II})}$ to form the $[\text{Cp}_2^*\text{Ru}^{(\text{III})}(\text{H})]^+$ presents in eq (1.15).

Due to solubility constraints, it was not possible to add $\text{Cp}_2^*\text{Ru}^{(\text{II})}$ in excess to determine the partial H^+ order. Nevertheless, the influence of the number of equivalents of $[\text{H}(\text{OEt}_2)_2]\text{TB}$ present relative to the initial concentration of $\text{Cp}_2^*\text{Ru}^{(\text{II})}$ in solution on the observed absorbance at 500 nm as a function of illumination time is shown in Figure 3.16. As noted earlier, details of the actual UV/vis spectra are shown in Figure 3.6, Section 3.3.2.1. Interestingly, although the maximum absorbance at 500 nm was reached after near identical periods of illumination time with both 2 and 4 equivalents of $[\text{H}(\text{OEt}_2)_2]\text{TB}$ present, the maximum magnitude of absorbance was greater for 2 equivalents which is in agreement with the achievement of a monometallic reaction.

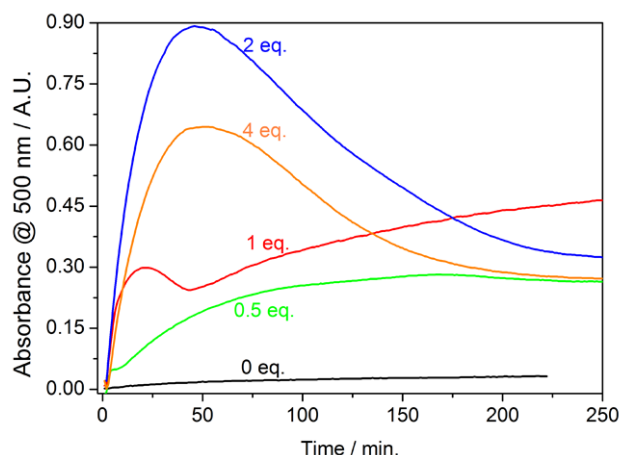


Figure 3.16. Plots of the absorbance at 500 nm *versus* time for UV/vis spectra taken during the generation and subsequent breakdown of the reaction intermediate $[\text{Cp}_2^*\text{Ru}^{(\text{III})}]^+$ upon irradiating an acidified organic solution of $\text{Cp}_2^*\text{Ru}^{(\text{II})}$ with white light. The influence of the number of equivalents of the strong organic acid $[\text{H}(\text{OEt}_2)_2]\text{TB}$ on the evolution of the UV/vis spectra was monitored for solutions of $\text{Cp}_2^*\text{Ru}^{(\text{II})}$ (1.875 mM) in DCE subjected to white light illumination by a 500 W Xe lamp. UV/vis spectra were taken every minute under anaerobic conditions (see Figure 3.6).

Additionally, the influence of the initial proton concentration was investigated by keeping the $\text{Cp}_2^*\text{Ru}^{(\text{II})}$ concentration constant, as shown in Figure 3.17. Similarly, the initial rate of the reaction decreased as the H^+ concentration increase.

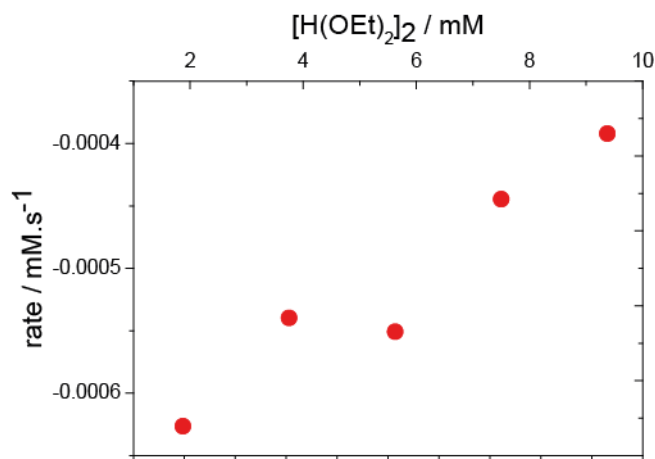


Figure 3.17. The initial rate (v , $\text{mM}\cdot\text{s}^{-1}$) of the reaction described by eq. (3.11) was determined for each starting concentration of $[\text{H}(\text{OEt}_2)_2]\text{TB}$ (1.875, 3.75, 5.625, 7.5 and 9.375 mM), in the presence of 1.875 mM $\text{Cp}_2^*\text{Ru}^{(\text{II})}$ upon commencing irradiation of the organic DCE solution with white light.

3.6 DFT calculations.

DFT calculations were performed in collaboration with the group of Prof. Clémence Corminboeuf to gain insights into the energetics of the different reaction steps (see Figure 3.18). It

has to be stressed that the counter-anion TB^- was not taken into account in the computation, although it certainly has a strong influence on the reaction energies as it stabilizes the charged complexes. Nevertheless, the computed results were in reasonable agreement with phenomena observed experimentally for the production of H_2 by $\text{Cp}_2^*\text{Ru}^{\text{(II)}}$. For instance, in agreement with experimental observations, the formation of $[\text{Cp}_2^*\text{Ru}^{\text{(IV)}(\text{H})}]^+$ from $\text{Cp}_2^*\text{Ru}^{\text{(II)}}$ and $\text{CF}_3\text{SO}_3\text{H}$ is spontaneous in DCE at the PBE0-dDsC. While the $\text{p}K_a$ could not be determined experimentally, the computed Gibbs energy of association was found to be $\Delta G^0_{\text{H}^+, \text{DFT}} = -70 \text{ kJ/mol}$ meaning a $\text{p}K_a$ of -12.3 . Calculations also corroborate that the first step associated with H_2 release (eq. (3.2)), leading to $[\text{Cp}_2^*\text{Ru}^{\text{(III)}}]^+$, is endergonic ($\Delta G^0 = 108 \text{ kJ/mol}$) in the ground state. It was found experimentally that the process only occurs if the reactants were excited by light. While the explicit interactions between the conjugated base and $\text{Cp}_2^*\text{Ru}^{\text{(II)}}$ may play a crucial role in the second reaction, these subtle effects were not accounted for computationally. The second H_2 release (eq. (3.3)) forming the final product $[\text{Cp}^*\text{Ru}^{\text{(IV)}(\text{C}_5\text{Me}_4\text{CH}_2)]^+$ is thermoneutral (-4 kJ/mol). The reaction between $\text{Cp}_2^*\text{Ru}^{\text{(II)}}$ and Ph_3C^+ is exergonic (-86 kJ/mol at the PBE0-dDsC level). Similar results were obtained using different computational levels. This energy, which is not in line with the experimental value (-155 kJ/mol), might again reflect the presence of environmental effects (*e.g.*, interaction with the counter-ion).

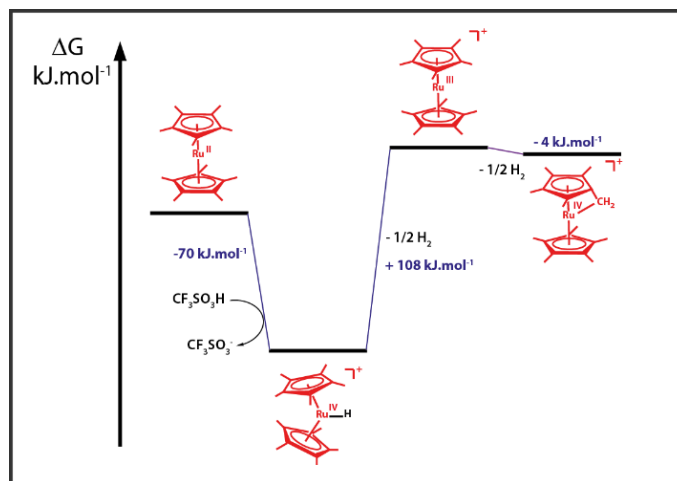


Figure 3.18. Schematic representation of the computed Gibbs energy involved in the photo-production of H_2 by $\text{Cp}_2^*\text{Ru}^{\text{(II)}}$ in DCE.

The computed UV/vis spectrum of $[\text{Cp}_2^*\text{Ru}^{\text{(III)}}]^+$ shows a maximum absorbance peak around 420 nm at the $\omega\text{B97X-D/def2-TZVP}$ level but similar trends are obtained using other functionals (*e.g.*, PBE0/def2-TZVP). While the $\omega\text{B97X-D}$ absorption is commonly blue shifted as compared

to experimental values, the large magnitude of the present shift (0.47eV) once more suggests a strong interaction with the environment. This would be consistent with the metal to ligand electron transfer character of the transition (see Figure 3.19). The difference may be explained by the strong influence of the counter ion which was not taken into account.

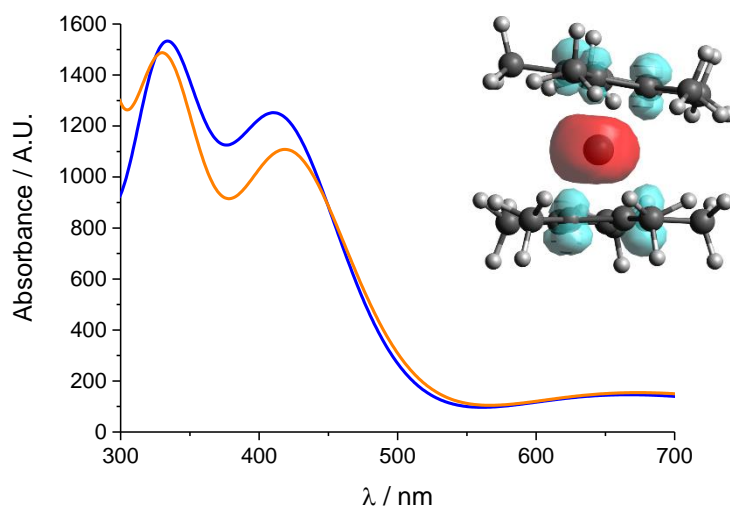


Figure 3.19. Computed UV/vis spectrum of $[\text{Cp}_2^*\text{Ru(III)}]^+$ at the TDDFT $\omega\text{B97X-D}$ (blue trace) and PBE0-D3 (orange trace) level. Inset: Density difference $\Delta\rho = \text{excited state} - \text{ground state density}$ of $[\text{Cp}_2^*\text{Ru(III)}]^+$ for the main transition at 426 nm at the PBE0/TZP level; $\Delta\rho = -0.001$ (red), $\Delta\rho = +0.001$ (blue).

3.7 Conclusions

The two-step process evolving H_2 was monitored by gas chromatography, ^1H and ^{13}C NMR and UV/vis spectroscopies while the subsequent DFT computations corroborate the experimental results. The mechanism of H_2 evolution was probed with unprecedented depth as, for the first time, a key intermediate of the photo-reaction, the $[\text{Cp}_2^*\text{Ru(III)}]^+$ species, was generated under conditions that prevented its immediate decomposition. The latter was achieved by exhaustive oxidative electrolysis of $\text{Cp}_2^*\text{Ru(II)}$ using a non-coordinating organic solvent (DCE) and non-nucleophilic electrolyte anions (TB^-) under anaerobic conditions. $[\text{H}(\text{OEt}_2)_2]\text{TB}$ was identified as an ideal acid for mechanistic studies of H_2 evolution reactions involving metallocenes as, firstly, it is a strong enough acid to efficiently form the metallocene hydride and, secondly, the counter anion TB^- is non-nucleophilic to the extent that it does not lead to the rapid decomposition of intermediate cationic species.

$\text{Cp}_2^*\text{Ru}^{(\text{II})}$ is a weak base but the $\text{p}K_a$ could not be determined, although evidence of ion pairing or homo-association was found. Further spectroscopic investigations are provided in Chapter VI to discriminate the process involved. As a result, in acidified media, the complex is spontaneously protonated in the dark. Subsequently, the resulting hydride species, $[\text{Cp}_2^*\text{Ru}^{(\text{IV})}(\text{H})]^+$, releases H_2 under illumination forming a $[\text{Cp}_2^*\text{Ru}^{(\text{III})}]^+$ species. The latter has a characteristic absorbance at $\lambda_{\text{max}} = 500 \text{ nm}$, easily observable by UV/vis. The reaction is first order with respect to the concentration of $[\text{Cp}_2^*\text{Ru}^{(\text{IV})}(\text{H})]^+$ ($k_{\text{app.}} = 1.7 \cdot 10^{-4} \text{ s}^{-1}$). Therefore, we exclude a homolytic bimolecular pathway and we proposed a monometallic reaction.

The $[\text{Cp}_2^*\text{Ru}^{(\text{III})}]^+$ intermediate is capable of generating a second release of H_2 when illuminated, but only in the presence of protons. The final form of the metallocene was identified as $[\text{Cp}^*\text{Ru}^{(\text{IV})}(\text{C}_5\text{Me}_4\text{CH}_2)]^+$. Investigations into the hydricity of $\text{Cp}_2^*\text{Ru}^{(\text{II})}$ show the hydridic nature of protons located on methyl groups of the cyclopentadienyls ($\Delta G^0_{\text{H}^+} \text{, DFT} = 259.4 \text{ kJ/mol}$). Thus, in the last step, H_2 is produced by one proton abstracted from the complex and another coming from the acidified media.

Although DFT computations do not take into account the counter ion, the theoretical results are in good agreement with the experimental data. The protonation is also spontaneous ($\Delta G^0_{\text{H}^+} \text{, DFT} = -70 \text{ kJ/mol}$) while the two oxidation steps require an input of energy to occur (46.1 and 0.5 kJ/mol respectively).

Electrochemical studies highlight the reversibility of $[\text{Cp}_2^*\text{Ru}^{(\text{III})}]^+$ to $\text{Cp}_2^*\text{Ru}^{(\text{II})}$. As electrochemical or chemical reduction of $[\text{Cp}_2^*\text{Ru}^{(\text{III})}]^+$ is straightforward, $\text{Cp}_2^*\text{Ru}^{(\text{II})}$ is an attractive candidate for performing photo-induced hydrogen evolution for batch water-splitting but the formation of the irreversible $[\text{Cp}^*\text{Ru}^{(\text{IV})}(\text{C}_5\text{Me}_4\text{CH}_2)]^+$ product was not expected. In this regard, the evaluation of the regeneration of $[\text{Cp}_2^*\text{Ru}^{(\text{III})}]^+$ by electrochemical reduction (meaning before the formation of $[\text{Cp}^*\text{Ru}^{(\text{IV})}(\text{C}_5\text{Me}_4\text{CH}_2)]^+$) is studied in the next chapter.

3.8 References

- (1) Ge, P.; Todorova, T. K.; Patir, I. H.; Olaya, A. J.; Vrubel, H.; Mendez, M.; Hu, X.; Corminboeuf, C.; Girault, H. H. *Proceedings of the National Academy of Sciences* **2012**, *109*, 11558.
- (2) Ge, P.; Olaya, A. J.; Scanlon, M. D.; Hatay Patir, I.; Vrubel, H.; Girault, H. H. *ChemPhysChem* **2013**, *14*, 2308.
- (3) Eugster, N.; Fermín, D. J.; Girault, H. H. *The Journal of Physical Chemistry B* **2002**, *106*, 3428.
- (4) Hatay, I.; Su, B.; Li, F.; Partovi-Nia, R.; Vrubel, H.; Hu, X.; Ersoz, M.; Girault, H. H. *Angewandte Chemie International Edition* **2009**, *48*, 5139.
- (5) Hatay, I.; Ge, P. Y.; Vrubel, H.; Hu, X.; Girault, H. H. *Energy & Environmental Science* **2011**, *4*, 4246.
- (6) Nieminen, J. J.; Hatay, I.; Ge, P.; Mendez, M. A.; Murtomaki, L.; Girault, H. H. *Chemical Communications* **2011**, *47*, 5548.
- (7) Ge, P.; Scanlon, M. D.; Peljo, P.; Bian, X.; Vubrel, H.; O'Neill, A.; Coleman, J. N.; Cantoni, M.; Hu, X.; Kontturi, K.; Liu, B.; Girault, H. H. *Chemical Communications* **2012**, *48*, 6484.
- (8) Bian, X.; Scanlon, M. D.; Wang, S.; Liao, L.; Tang, Y.; Liu, B.; Girault, H. H. *Chemical Science* **2013**, *4*, 3432.
- (9) Scanlon, M. D.; Bian, X.; Vrubel, H.; Amstutz, V.; Schenk, K.; Hu, X.; Liu, B.; Girault, H. H. *Physical Chemistry Chemical Physics* **2013**, *15*, 2847.
- (10) Aslan, E.; Hatay Patir, I.; Ersoz, M. *ChemCatChem* **2014**, *6*, 2832.
- (11) Aslan, E.; Patir, I. H.; Ersoz, M. *Chemistry – A European Journal* **2015**, *21*, 4585.
- (12) Fedin, E. I.; Blumenfeld, A. L.; Petrovskii, P. V.; Kreindlin, A. Z.; Fadeeva, S. S.; Rybinskaya, M. I. *Journal of Organometallic Chemistry* **1985**, *292*, 257.
- (13) Kreindlin, A. Z.; Petrovskii, P. V.; Rybinskaya, M. I.; Yanovskii, A. I.; Struchkov, Y. T. *Journal of Organometallic Chemistry* **1987**, *319*, 229.
- (14) Rybinskaya, M. I.; Kreindlin, A. Z.; Kiseleva, L. N.; Kruglova, N. V.; Kamyshova, A. A.; Petrovskii, P. V.; Turpeinen, U. *Journal of Organometallic Chemistry* **1997**, *536–537*, 257.
- (15) Rybinskaya, M. I.; Kamyshova, A. A.; Kreindlin, A. Z.; Petrovskii, P. V. *Mendeleev Communications* **2000**, *10*, 85.
- (16) Rybinskaya, M. I.; Kreindlin, A. Z.; Kamyshova, A. A. *Russian Chemical Bulletin* **2002**, *51*, 1616.
- (17) Kreindlin, A. Z.; Rybinskaya, M. I. *Russian Chemical Reviews* **2004**, *73*, 417.
- (18) Kreindlin, A. Z.; Petrovskii, P. V.; Suponitsky, K. Y.; Starikova, Z. A. *Russ Chem Bull* **2009**, *58*, 810.

- (19) Muratov, D. V.; Romanov, A. S.; Kudinov, A. R. *Mendeleev Communications* **2015**, 25, 109.
- (20) Kamyshova, A. A.; Kreindlin, A. Z.; Rybinskaya, M. I.; Petrovskii, P. V. *Russian Chemical Bulletin* **1999**, 48, 581.
- (21) Kamyshova, A. A.; Kreindlin, A. Z.; Rybinskaya, M. I.; Petrovskii, P. V. *Russian Chemical Bulletin* **2000**, 49, 520.
- (22) Albers, M. O.; Liles, D. C.; Robinson, D. J.; Shaver, A.; Singleton, E.; Wiege, M. B.; Boeyens, J. C. A.; Levendis, D. C. *Organometallics* **1986**, 5, 2321.
- (23) Du, P.; Schneider, J.; Luo, G.; Brennessel, W. W.; Eisenberg, R. *Inorganic Chemistry* **2009**, 48, 4952.
- (24) Liu, T. B.; DuBois, D. L.; Bullock, R. M. *Nature Chemistry* **2013**, 5, 228.
- (25) Kaljurand, I.; Kütt, A.; Sooväli, L.; Rodima, T.; Mäemets, V.; Leito, I.; Koppel, I. A. *The Journal of Organic Chemistry* **2005**, 70, 1019.
- (26) Pearson, R. G. *Chemical Reviews* **1985**, 85, 41.
- (27) Kolthoff, I. M. *Analytical Chemistry* **1974**, 46, 1992.
- (28) Morris, R. H. *Chemical Reviews* **2016**, 116, 8588.
- (29) Maryott, A. A.; Smith, E. R. *Table of dielectric constants of pure liquids*; U.S. Govt. Print. Off., 1951.
- (30) Jia, G.; Lau, C.-P. *Coordination Chemistry Reviews* **1999**, 190–192, 83.
- (31) Morris, R. H. *Journal of the American Chemical Society* **2014**, 136, 1948.
- (32) Angelici, R. J. *Accounts of Chemical Research* **1995**, 28, 51.
- (33) Pedersen, A.; Skagestad, V.; Mats, T. *Acta Chemica Scandinavica* **1995**, 49, 632.
- (34) Kütt, A.; Rodima, T.; Saame, J.; Raamat, E.; Mäemets, V.; Kaljurand, I.; Koppel, I. A.; Garlyauskayte, R. Y.; Yagupolskii, Y. L.; Yagupolskii, L. M.; Bernhardt, E.; Willner, H.; Leito, I. *The Journal of Organic Chemistry* **2011**, 76, 391.
- (35) Raamat, E.; Kaupmees, K.; Ovsjannikov, G.; Trummal, A.; Kütt, A.; Saame, J.; Koppel, I.; Kaljurand, I.; Lipping, L.; Rodima, T.; Pihl, V.; Koppel, I. A.; Leito, I. *Journal of Physical Organic Chemistry* **2013**, 26, 162.
- (36) Sowa, J. R.; Bonanno, J. B.; Zanoliti, V.; Angelici, R. J. *Inorganic Chemistry* **1992**, 31, 1370.
- (37) Ohanessian, G.; Goddard, W. A. *Accounts of Chemical Research* **1990**, 23, 386.
- (38) Mendez, M. A.; Partovi-Nia, R.; Hatay, I.; Su, B.; Ge, P.; Olaya, A.; Younan, N.; Hojeij, M.; Girault, H. H. *Physical Chemistry Chemical Physics* **2010**, 12, 15163.
- (39) Rybinskaya, M. I.; Kreindlin, A. Z.; Hoffmann, R.; Minyaev, R. M. *Russian Chemical Bulletin* **1994**, 43, 1605.
- (40) O'Hare, D.; Green, J. C.; Chadwick, T. P.; Miller, J. S. *Organometallics* **1988**, 7, 1335.

- (41) Kölle, V.; Grub, J. *Journal of Organometallic Chemistry* **1985**, *289*, 133.
- (42) Kreindlin, A. Z.; Petrovskii, P. V.; Rybinskaya, M. I. *Russian Chemical Bulletin* **1987**, *36*, 1498.
- (43) Wiedner, E. S.; Chambers, M. B.; Pitman, C. L.; Bullock, R. M.; Miller, A. J. M.; Appel, A. M. *Chemical Reviews* **2016**, *116*, 8655.
- (44) Curtis, C. J.; Miedaner, A.; Ellis, W. W.; DuBois, D. L. *Journal of the American Chemical Society* **2002**, *124*, 1918.
- (45) Berning, D. E.; Noll, B. C.; DuBois, D. L. *Journal of the American Chemical Society* **1999**, *121*, 11432.
- (46) Rivier, L.; Peljo, P.; Vannay, L.; Grégoire, G.; Mendez, M.; Corminboeuf, C.; Scanlon, M. D.; Girault, H. *Angewandte Chemie International Edition* **2017**, *56*, 2324

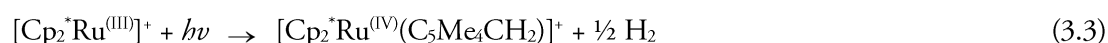
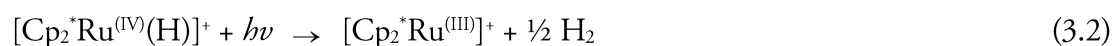
4. Photoproduction of Hydrogen by Decamethylruthenocene Combined with Electrochemical Regeneration

Adapted with permission from Photoproduction of Hydrogen by Decamethylruthenocene Combined with Electrochemical Regeneration, *Angew. Chem. Int. Ed.*, 2017, (56), in Press, Copyright (2017) Wiley.

4.1	Introduction.....	88
4.2	Influence of coordinating solvent and of the counter anions on $[\text{Cp}_2^*\text{Ru}^{\text{(III)}}]^+$ stability.....	89
4.3	Preliminary experiments: chemical regeneration	91
4.3.1	Sacrificial electron donor	91
4.3.2	Anionic tetracyanoquinodimethane: non-sacrificial electron donor.....	93
4.4	Electrochemical regeneration	95
4.4.1	Electrochemical characterisation on FTO electrode.....	96
4.4.2	Photo-oxidation of DCE in absence of protons	97
4.4.3	Photo-catalytic hydrogen production with organic protons.....	98
4.4.3.1	Experimental cyclic voltammetry and constant potential electrolysis	98
4.4.3.2	Control experiments.....	100
4.4.3.3	Simulated constant potential electrolysis.....	101
4.4.4	Gas chromatography analysis of produced hydrogen.....	101
4.4.5	Quantum yield	104
4.5	Conclusions.....	105
4.6	References.....	107

4.1 Introduction

From the results obtained in Chapter III, the applicability of $\text{Cp}_2^*\text{Ru}^{(\text{II})}$ in real and sustainable photoelectrochemical cell or in the batch water-splitting for the production of H_2 appeared impossible because the complex is irreversibly consumed during the reaction. Indeed, $\text{Cp}_2^*\text{Ru}^{(\text{II})}$ undergoes two oxidations which generate a first recoverable $[\text{Cp}_2^*\text{Ru}^{(\text{III})}]^+$ intermediate followed by the irreversible formation of $[\text{Cp}_2^*\text{Ru}^{(\text{IV})}(\text{C}_5\text{Me}_4\text{CH}_2)]^+$ as detailed below:¹



Thus, the reduction of the $[\text{Cp}_2^*\text{Ru}^{(\text{III})}]^+$ is mandatory to regenerate $\text{Cp}_2^*\text{Ru}^{(\text{II})}$ and achieve the catalytic photo-generation of H_2 by $\text{Cp}_2^*\text{Ru}^{(\text{II})}$ as presented in Figure 4.1.

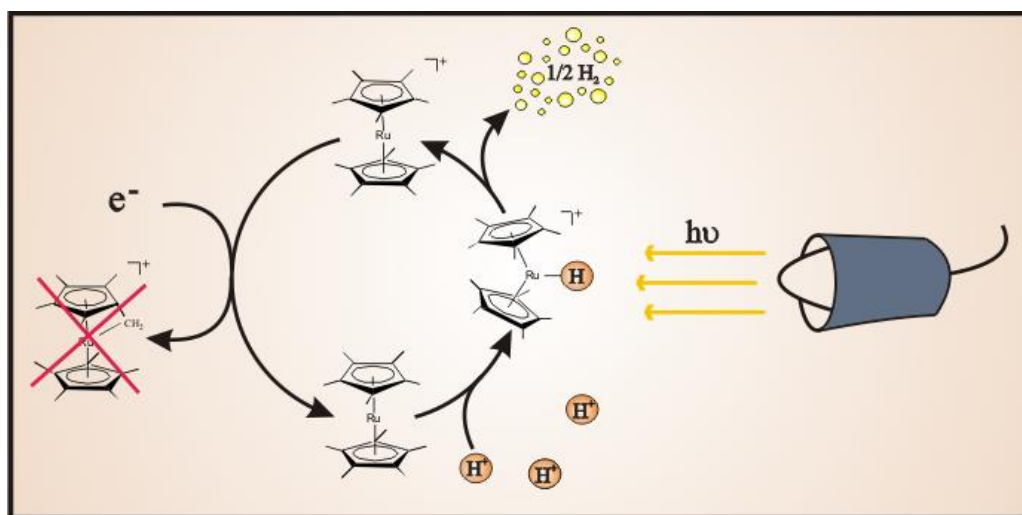


Figure 4.1: Regeneration of $\text{Cp}_2^*\text{Ru}^{(\text{II})}$ in photo-HER by reducing $[\text{Cp}_2^*\text{Ru}^{(\text{III})}]^+$ ion to avoid the formation of $[\text{Cp}_2^*\text{Ru}^{(\text{IV})}(\text{C}_5\text{Me}_4\text{CH}_2)]^+$

Other works have proposed the use of a single molecule to achieve this reaction. For example, Cole-Hamilton² reported a platinum phosphine compound, while both Miller³ and Gray⁴ used iridium chloride complexes. Nevertheless, metallocenes appear as an attractive class of molecules because they are simple, easily synthesized molecules, with ligands and metal centres that may be tuned to obtain certain desired properties, such as tailored solubility, absorbance wavelength or redox potentials. This adaptability allows us to envisage a long-term strategy to develop this type of catalyst.

The electrochemical characterisation, in Chapter III, Section 3.2, shows a quasi-reversible $\text{Ru}^{(\text{III})}/\text{Ru}^{(\text{II})}$ redox process with the formal redox potential of $\text{Cp}_2^*\text{Ru}^{(\text{II})}$, $[E^{\circ}_{[\text{Cp}_2^*\text{Ru}^{(\text{III})+}/\text{Cp}_2^*\text{Ru}^{(\text{II})}]}]^{\text{DCE}}$, determined as 0.75 V *versus* SHE.¹ It suggests that the transient $[\text{Cp}_2^*\text{Ru}^{(\text{III})}]^+$ could be reduced to recover the original $\text{Cp}_2^*\text{Ru}^{(\text{II})}$. The final goal of this investigation is to prove the feasibility to scavenge $[\text{Cp}_2^*\text{Ru}^{(\text{III})}]^+$ to recover the original $\text{Cp}_2^*\text{Ru}^{(\text{II})}$.

In this chapter, the stability of $[\text{Cp}_2^*\text{Ru}^{(\text{III})}]^+$ was first discussed to choose the right conditions to stabilize the species long enough to allow its regeneration. First attempts to regenerate $[\text{Cp}_2^*\text{Ru}^{(\text{III})}]^+$ were done by reducing agents before to study the electrochemical regeneration. Both reactions (chemical or electrochemical) were expected to be similar. In the chemical system, electrons are supplied by a chemical donor, while in the electrochemical system, the electrons are supplied *via* an electrode.⁵ It is established in this chapter that $\text{Cp}_2^*\text{Ru}^{(\text{II})}$ is the first metallocenes that can be electrochemically recovered after photo-generation of H_2 at a reduction potential higher (*i.e.*, more positive) than that of proton reduction. The $[\text{Cp}_2^*\text{Ru}^{(\text{III})}]^+$ reduction was proven by electrochemical studies and a quantum yield of 25 % was achieved.

4.2 Influence of coordinating solvent and of the counter anions on $[\text{Cp}_2^*\text{Ru}^{(\text{III})}]^+$ stability

As it was introduced in the previous chapter, the identification and characterisation of $[\text{Cp}_2^*\text{Ru}^{(\text{III})}]^+$ has been obstructed in previous studies due to its high instability and very short life time. As a result, $[\text{Cp}_2^*\text{Ru}^{(\text{III})}]^+$ was assumed to convert rapidly to $[\text{Cp}_2^*\text{Ru}^{(\text{IV})}(\text{C}_5\text{Me}_4\text{CH}_2)]^+$.⁶⁻⁹ Therefore, we focused our efforts to optimize the right conditions to stabilize the transient $[\text{Cp}_2^*\text{Ru}^{(\text{III})}]^+$ species long enough to allow its electrochemical regeneration and thus obtain a catalytic generation of H_2 .

From previous worked, Hashidzume *et al.* have speculated that complexation of $[\text{Cp}_2^*\text{Ru}^{(\text{III})}]^+$ with acetonitrile (ACN) can drastically shift the $\text{Ru}^{(\text{III})}/\text{Ru}^{(\text{IV})}$ redox potential.¹⁰ Complexation increases the ease of oxidation of the $\text{Ru}^{(\text{III})}$ species to the extent that $[\text{Cp}_2^*\text{Ru}^{(\text{III})}\cdot\text{ACN}]^+$ oxidises more easily than $\text{Cp}_2^*\text{Ru}^{(\text{II})}$. Thus, $[\text{Cp}_2^*\text{Ru}^{(\text{III})}\cdot\text{ACN}]^+$ species formed after the oxidation of $\text{Cp}_2^*\text{Ru}^{(\text{II})}$ will be instantly oxidised to $[\text{Cp}_2^*\text{Ru}^{(\text{IV})}\cdot\text{ACN}]^{2+}$ at the same potential. This gives rise to an apparent $2 e^-$ oxidation of $\text{Cp}_2^*\text{Ru}^{(\text{II})}$. However, due to steric hindrances from the permethylated cyclopentadienyl rings, complexation with ACN is proposed to be an equilibrium reaction with the

majority of the species non-complexed. Thus, the apparent observed electron transfer should be less than 2 on the forward (oxidising) sweep. This gives rise to a large first reduction peak on the reverse sweep, corresponding to the reduction of uncomplexed $[\text{Cp}_2^*\text{Ru}^{(\text{III})}]^+$ to $\text{Cp}_2^*\text{Ru}^{(\text{II})}$, and a much smaller second reduction peak, due to the reduction of the small amount of $[\text{Cp}_2^*\text{Ru}^{(\text{IV})}\cdot\text{ACN}]^{2+}$ present to $[\text{Cp}_2^*\text{Ru}^{(\text{III})}\cdot\text{ACN}]^+$. The latter complex will lose its ACN ligand and, as the electrode potential is already at a lower (more negative) value than the standard potential of the $\text{Ru}^{(\text{II})}/\text{Ru}^{(\text{III})}$ redox couple, $[\text{Cp}_2^*\text{Ru}^{(\text{III})}]^+$ will be further reduced to $\text{Cp}_2^*\text{Ru}^{(\text{II})}$ in an Electrochemical-Chemical-Electrochemical (ECE) mechanism.¹⁰ Further studies would be beneficial to clarify this mechanism. For example, if the $\text{Ru}^{(\text{III})}/\text{Ru}^{(\text{IV})}$ redox potential is not in fact significantly shifted on complexation of $[\text{Cp}_2^*\text{Ru}^{(\text{III})}]^+$ with ACN, then the small irreversible reduction wave at more negative potentials on the reverse sweep may alternatively be due to the reduction of $[\text{Cp}_2^*\text{Ru}^{(\text{III})}\cdot\text{ACN}]^+$. In this case the minor amount of formed $[\text{Cp}_2^*\text{Ru}^{(\text{III})}\cdot\text{ACN}]^+$ may be more stable than the uncomplexed $[\text{Cp}_2^*\text{Ru}^{(\text{III})}]^+$ species, shifting the $\text{Ru}^{(\text{II})}/\text{Ru}^{(\text{III})}$ redox potential for the former to lower potentials.

It is worth noting that, with the exception of extremely weakly coordinating anions such as TB^- and $\text{B}(\text{C}_6\text{H}_3(\text{CF}_3)_2)_4^-$, coordination by many typical supporting electrolyte anions, such as Cl^- , ClO_4^- , BF_4^- , or PF_6^- , dramatically influences the electrochemistry of the less sterically hindered ruthenocene ($\text{Cp}_2\text{Ru}^{(\text{II})}$) complex.¹¹⁻¹³ Ultimately this leads to the observation of irreversible $2 e^-$ oxidation of $\text{Cp}_2\text{Ru}^{(\text{II})}$ by various proposed mechanisms (*i.e.*, rapid dimerization of $[\text{Cp}_2\text{Ru}^{(\text{III})}]^+$ followed by disproportionation or, alternatively, disproportionation of $[\text{Cp}_2\text{Ru}^{(\text{III})}]^+$ in the presence of even weakly coordinating ligands).

As discussed above and in the previous chapter, it appears that $[\text{Cp}_2^*\text{M}^{(\text{III})}]^+$ ($\text{M} = \text{Os}$ or Ru) species can be stabilized by utilizing soft weakly complexing counter-anions and weakly coordinating solvents. In this work, we utilized TB^- to stabilize the $[\text{Cp}_2^*\text{M}^{(\text{III})}]^+$ in DCE solution (a non-coordinating solvent).

4.3 Preliminary experiments: chemical regeneration

4.3.1 Sacrificial electron donor

A review of sacrificial electron donors employed to investigate artificial photosynthesis systems was presented in Chapter I, Section 1.3.5. Tertiary aliphatic amines were widely used to provide electrons because they can irreversibly oxidized into inert molecules that not interfere with the studied photo-reactions.^{14,15} In this category, TEA is certainly the amine the most used and appeared to work in various conditions (*e.g.* pH, solvent, concentration).¹⁶⁻¹⁸ Its success is due to its irreversible oxidation potential at 0.93 V *vs.* SHE in water at pH 11.9 that makes TEA able to thermodynamically reduce a majority of photosensitizers (excited or not, for reductive or oxidative quenching, respectively).^{14,17} Consequently, a first regeneration of transient $[\text{Cp}_2^*\text{Ru}^{\text{(III)}}]^+$ was attempted with TEA. In order to follow the reaction by ^1H NMR, 15 mM $\text{Cp}_2^*\text{Ru}^{\text{(II)}}$ was dissolved in CD_2Cl_2 in presence of an excess of $[\text{H}(\text{OEt}_2)_2]\text{TB}$. The NMR tube was illuminated during 10 minutes and 70 % of $[\text{Cp}_2^*\text{Ru}^{\text{(IV)}}(\text{H})]^+$ disappeared to form $[\text{Cp}_2^*\text{Ru}^{\text{(III)}}]^+$ (no $[\text{Cp}_2^*\text{Ru}^{\text{(IV)}}(\text{C}_5\text{Me}_4\text{CH}_2)]^+$ was observed by ^1H NMR, Figure 4.2 (A) and (B)). Thereafter, TEA was added to the solution leading to an additional consumption of $[\text{Cp}_2^*\text{Ru}^{\text{(IV)}}(\text{H})]^+$ instead of the reduction of $[\text{Cp}_2^*\text{Ru}^{\text{(III)}}]^+$ (Figure 4.2 (C)). TEA was characterized electrochemically in DCE (see Chapter VII, Section 7.4.1.2) and it shows an irreversible reduction peak at 1.11 V *vs.* SHE. It appears that TEA shows a potential much more positive in chlorinated solvent than in water making its oxidation by $\text{Cp}_2^*\text{Ru}^{\text{(II)}}$ thermodynamically impossible. At the opposite, the disappearance of $[\text{Cp}_2^*\text{Ru}^{\text{(IV)}}(\text{H})]^+$ without the reappearance of $\text{Cp}_2\text{Ru}^{\text{(II)}}$ peak is probably due to oxidation of $\text{Cp}_2\text{Ru}^{\text{(II)}}$ in presence of TEA.

A.

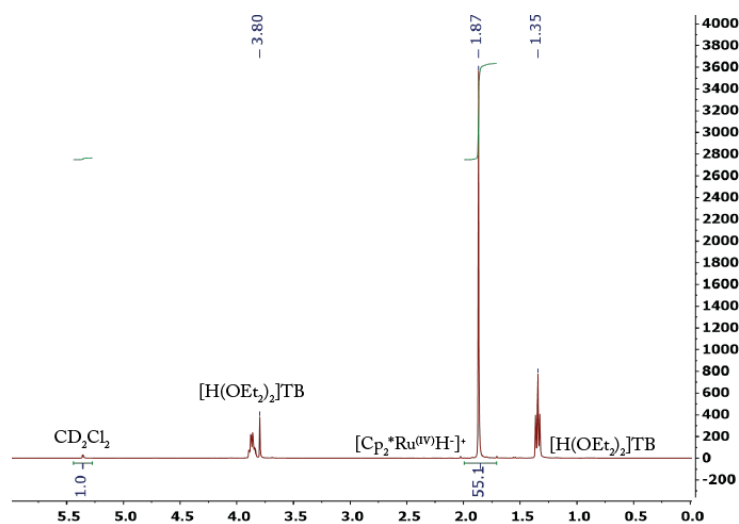
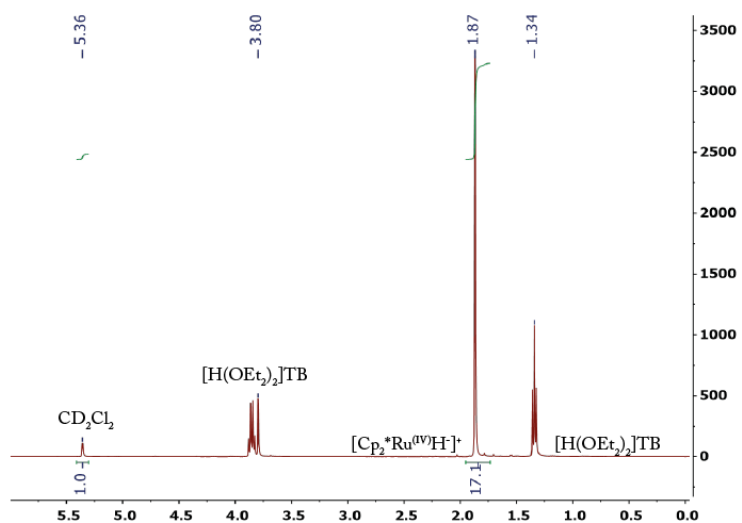
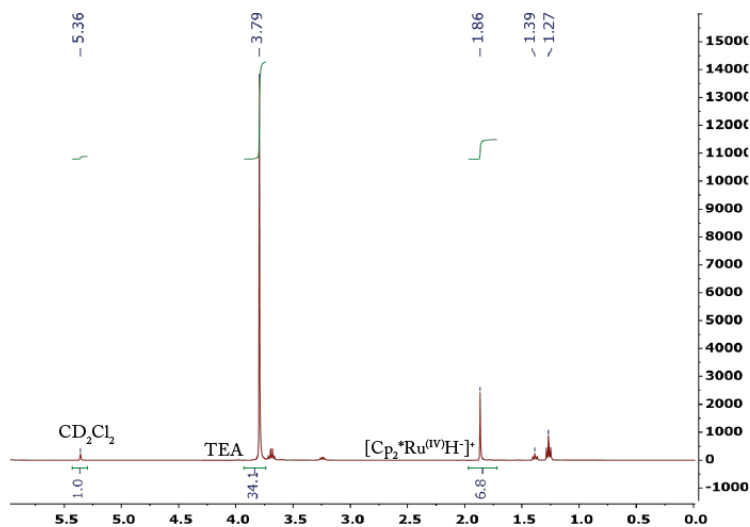


Figure 4.2: ^1H NMR characterization of $\text{Cp}_2\text{Ru}^{\text{III}}$ regeneration by TEA. 15 mM $\text{Cp}_2\text{Ru}^{\text{III}}$ with 4 mM $[\text{H}(\text{OEt}_2)_2]\text{TB}$ in CD_2Cl_2 solution (A) before illumination, (B) after illumination during 10 min and, (C) addition of a drop of TEA in (B).

B.



C.



4.3.2 Anionic tetracyanoquinodimethane: non-sacrificial electron donor

TCNQ is one of the strongest organic electron acceptors. Indeed, it is composed of four peripheral cyano groups and a central hexagonal ring as illustrated in Figure 4.3.¹⁹ In its neutral form, the ring is not aromatic. The ability of TCNQ to accept electrons is eased by: (i) its rigid structure due to the succession of multiple and single bonds, (ii) the presence of cyano functional groups known as π -acceptors

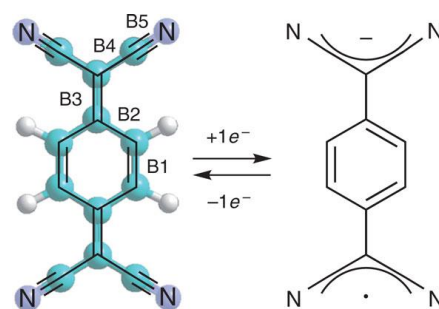


Figure 4.3: Chemical structures of TCNQ and TCNQ⁻.

and, (iii) the enhancing of the conformational freedom of the molecule owing to the aromatization of the central ring when the molecule is reduced to TCNQ⁻ (see Figure 4.3). Thus, TCNQ species has been widely exploited to study charge-transfer interactions.²⁰ Its electrical and optical properties has made it attractive for optical and electrical recording, sensors, electrochromic and magnetic devices as well as energy and data storage.

The formal redox potential of TCNQ in DCE, $[E^0_{\text{TCNQ/TCNQ}^-}]^{\text{DCE}}$, determined as 0.29 V *vs.* SHE, makes TCNQ⁻ form able to reduce $[\text{Cp}_2^*\text{Ru}^{(\text{III})}]^+$. Furthermore, Prof. Alan M. Bond and co-worker have recently achieved the photo-oxidation of water to oxygen in ionic liquid using TCNQ as a sacrificial electron acceptor.²¹ Therefore, this molecule appears very attractive towards water-splitting coupled with $\text{Cp}_2^*\text{Ru}^{(\text{II})}$ to perform HER.

Herein, the regeneration of $\text{Cp}_2^*\text{Ru}^{(\text{II})}$ was achieved by reacting the reduced electron acceptor TCNQ⁻ with $[\text{Cp}_2^*\text{Ru}^{(\text{III})}]^+$ according to the following equation:



The two species were synthesized together by bulk electrolysis from the reduction a solution of TCNQ on the working electrode side and the oxidation of a solution of $\text{Cp}_2^*\text{Ru}^{(\text{II})}$ on the counter electrode side in DCE by applying a potential of - 1 V *vs.* SHE as described in Figure 4.4. Spectroscopic characteristics of $\text{Cp}_2^*\text{Ru}^{(\text{II})}$ and $[\text{Cp}_2^*\text{Ru}^{(\text{III})}]^+$ were already investigated in the previous chapter. Colorless $\text{Cp}_2^*\text{Ru}^{(\text{II})}$ did not show absorbance in the visible spectrum while $[\text{Cp}_2^*\text{Ru}^{(\text{III})}]^+$ had a distinctive band at $\lambda = 500$ nm. Yellow TCNQ shows characteristic absorbance band at $\lambda = 377$ and 401 nm while green TCNQ⁻ absorbs at $\lambda = 423, 440, 487, 676, 749, 851$ nm in DCE

from UV/vis analysis recorded before and after TCNQ reduction. These results are in agreement with the analysis of earlier results.²¹

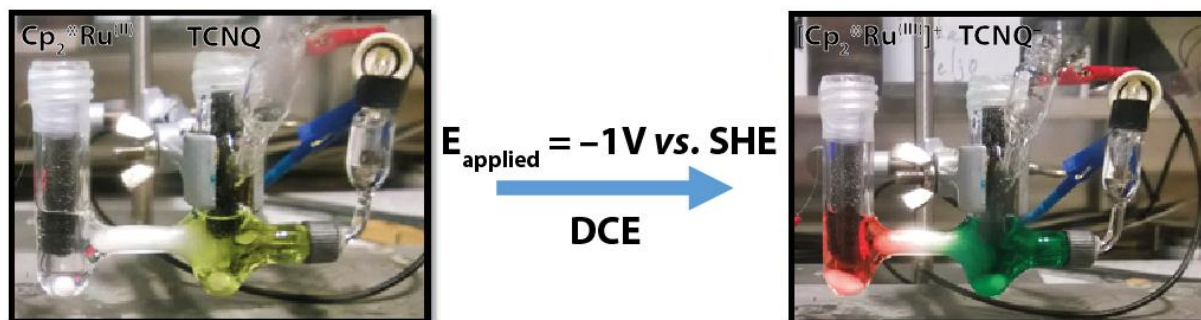


Figure 4.4: Electro-synthesis of $[\text{Cp}_2^*\text{Ru}^{\text{(III)}}]^+$ and TCNQ^- by bulk electrolysis. Left picture: oxidation of 4 mM $\text{Cp}_2^*\text{Ru}^{\text{(II)}}$ (left chamber, colorless: no absorption observed in the visible range) and oxidation of 4 mM TCNQ (right chamber, yellow: $\lambda = 377, 401 \text{ nm}$) in DCE with 0.1 M TBAPF₆ as supporting electrolyte. A potential of -1V (*vs.* SHE) was applied until the current disappeared. Right picture: product obtained: $[\text{Cp}_2^*\text{Ru}^{\text{(III)}}]^+$ (left chamber, pink: $\lambda = 500 \text{ nm}$) and TCNQ^- (right chamber, green: $\lambda = 423, 440, 487, 676, 749, 851 \text{ nm}$).

Thus, the regeneration of $\text{Cp}_2^*\text{Ru}^{\text{(II)}}$ to $[\text{Cp}_2^*\text{Ru}^{\text{(III)}}]^+$ by TCNQ^- was followed by UV/vis spectroscopy. Solutions containing $130 \mu\text{M}$ $[\text{Cp}_2^*\text{Ru}^{\text{(III)}}]^+$ and various amounts of TCNQ^- were prepared and analysed (Figure 4.5 (A)). The resulting colours of the solutions are shown in Figure 4.5 (C) and illustrate the transition from a pink solution of $[\text{Cp}_2^*\text{Ru}^{\text{(III)}}]^+$, turned into a yellow solution of converted TCNQ and $\text{Cp}_2^*\text{Ru}^{\text{(II)}}$ to a green final solution induced by an excess of unreacted TCNQ^- . Indeed, before the addition of TCNQ^- , the UV/vis spectrum showed the characteristic absorbance band of $[\text{Cp}_2^*\text{Ru}^{\text{(III)}}]^+$ at $\lambda = 500 \text{ nm}$ (Figure 4.5 (A), blue line). Then, when TCNQ^- was added, a band at 401 nm appeared while the band relative to $[\text{Cp}_2^*\text{Ru}^{\text{(III)}}]^+$ decreased (Figure 4.5, green lines) until its complete disappearance after the addition of 1 equivalent of TCNQ^- (see the evolution of the absorbance at $\lambda = 500 \text{ nm}$ in Figure 4.5 (B)). After the equivalence, TCNQ^- was not consumed anymore and characteristic bands relative to TCNQ^- species appeared including the one at 487 nm which makes the absorbance at 500 nm increase again. Same results were obtained with $[\text{Cp}_2^*\text{Ru}^{\text{(III)}}]^+$ in presence of protons meaning the protons should not affect the *in-situ* regeneration of the transient $[\text{Cp}_2^*\text{Ru}^{\text{(III)}}]^+$ during the reaction (not shown).

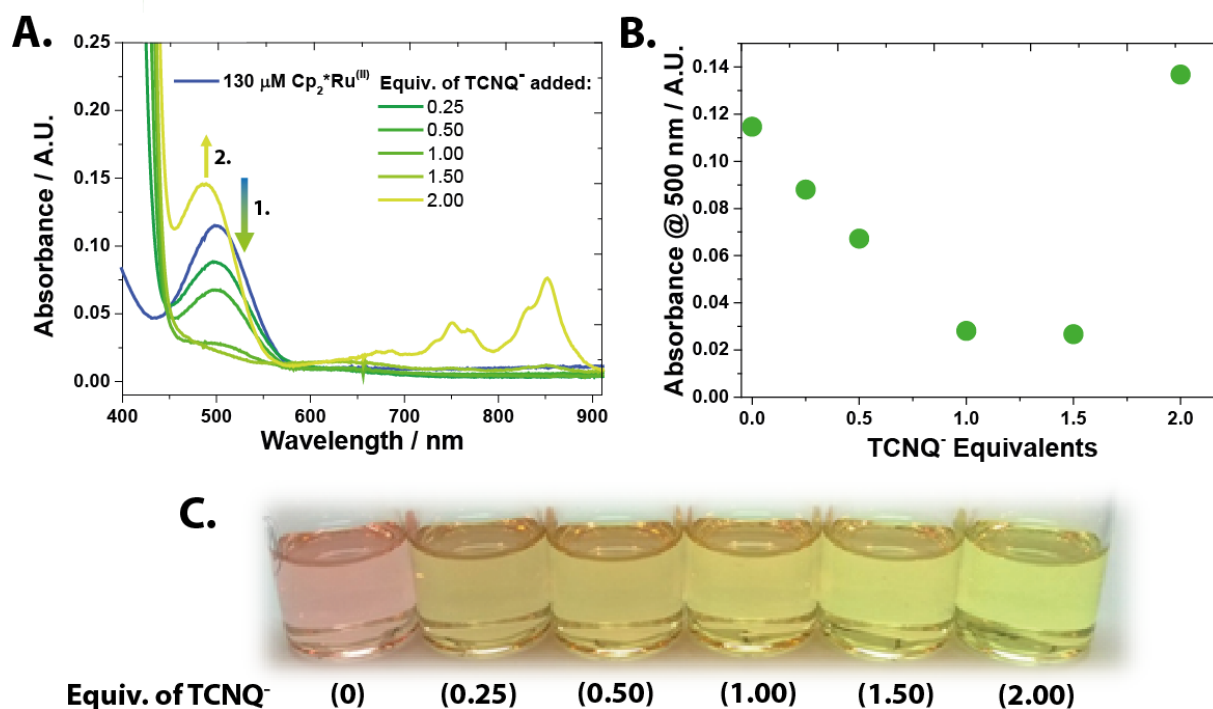


Figure 4.5: Chemical regeneration of $\text{Cp}_2^*\text{Ru}^{(\text{III})}$ to $[\text{Cp}_2^*\text{Ru}^{(\text{III})}]^+$ by TCNQ^- followed by UV/vis spectroscopy. Titration was achieved by preparing solutions containing 130 μM $[\text{Cp}_2^*\text{Ru}^{(\text{III})}]^+$ and various equivalents of TCNQ^- (i.e. 0, 0.25, 0.50, 1.00, 1.50 and, 2.00) in DCE. (A) Solutions analysed by UV/vis spectroscopy show the disappearance of the band relative to $[\text{Cp}_2^*\text{Ru}^{(\text{III})}]^+$ (1.) and the appearance of TCNQ^- spectrum (2.), (B) Absorbance recorded at $\lambda = 500\text{nm}$ as function of TCNQ^- equivalents, (C) Illustration of the colour of the solutions for various equivalents of TCNQ^- .

4.4 Electrochemical regeneration

With these preliminary results in hand, the regeneration was investigated by electrochemical techniques, namely cyclic voltammetry and chronoamperometry. The set-up consisted of a transparent FTO working electrode in contact with a solution of $\text{Cp}_2^*\text{Ru}^{(\text{II})}$ acidified by $[\text{H}(\text{OEt}_2)_2]\text{TB}$ with TBAPF_6 used as an electrolyte. All experiments were performed under inert conditions in a glove box. Details of the experiments are provided in Chapter II, section 2.2. Here, the electrode played the role of a heterogeneous electron donor. Therefore, the solution was illuminated through the FTO electrode which produced molecular H_2 and $[\text{Cp}_2^*\text{Ru}^{(\text{III})}]^+$ close to the electrode. Then, by applying a reductive potential at the FTO electrode, $\text{Cp}_2^*\text{Ru}^{(\text{II})}$ was recovered and the reaction was carried on *via* a catalytic Electrochemical, Chemical, Chemical mechanism (ECC' mechanism) described in Figure 4.6.

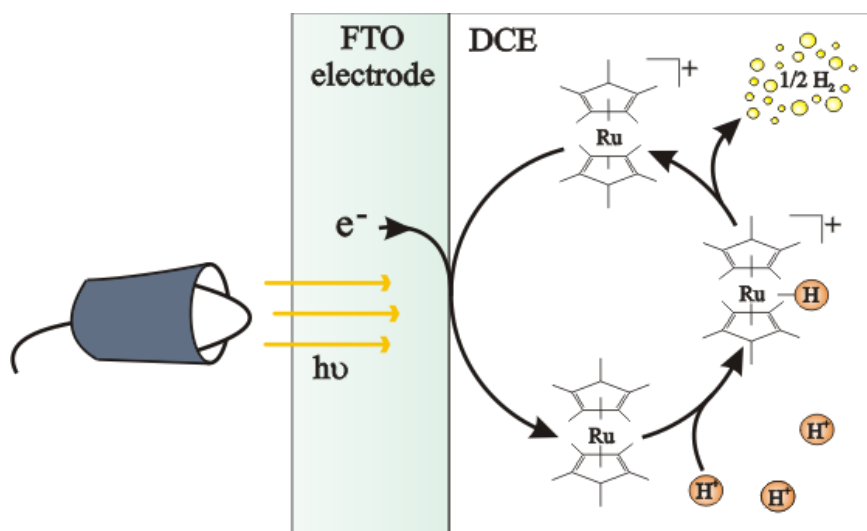


Figure 4.6: Photoproduction of hydrogen by decamethylruthenocene combined with electrochemical recycling at FTO electrode interface.

Poorly stabilized $[\text{Cp}_2^*\text{M}^{(\text{III})}]^+$ may oxidize a second time and form breakdown products as shown in the previous chapter. Therefore, in this work, $[\text{Cp}_2^*\text{Ru}^{(\text{III})}]^+$ species is stabilized (at least on the time-scale of the electrolysis experiments) by utilizing soft tetrakis(pentafluorophenyl) borate counter anion in DCE, a non-coordinated solvent do limit the formation of breakdown products accelerated in the presence of coordinating solvents and counter-anions.

4.4.1 Electrochemical characterisation on FTO electrode

Electrochemical characterisation of $\text{Cp}_2^*\text{Ru}^{(\text{II})}$ was first performed at a FTO working electrode to compare with the results obtained in the previous chapter at a glassy carbon electrode. CVs of $\text{Cp}_2^*\text{Ru}^{(\text{II})}$ obtained with TBAPF_6 as the supporting electrolyte (Figure 4.7) clearly show an oxidation and a reduction peak for the $\text{Ru}^{(\text{III})}/\text{Ru}^{(\text{II})}$ redox process with a current linearly dependent on the square root of the scan rate, characteristic of a diffusion limited electron transfer. The formal redox potential of $\text{Cp}_2^*\text{Ru}^{(\text{II})}$, $[E^0_{[\text{Cp}_2\text{Ru}^{(\text{III})}]^+/\text{Cp}_2\text{Ru}^{(\text{II})}}]^{\text{DCE}}$, was determined as 0.75 V *vs.* SHE. Experimental conditions were reported in Chapter II, section 2.2.

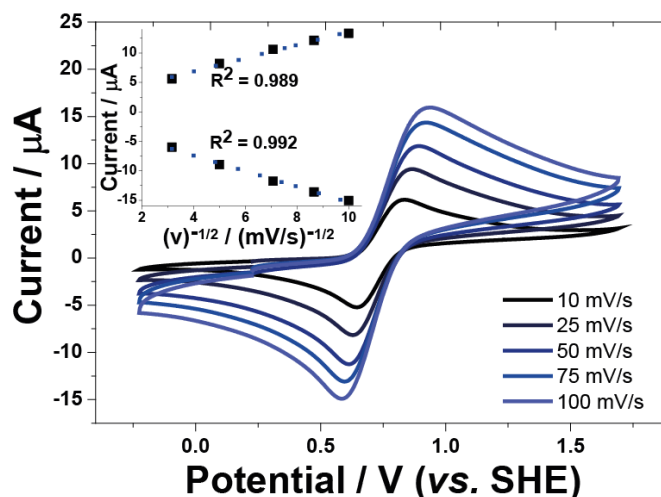


Figure 4.7: CVs of 1 mM $\text{Cp}_2^*\text{Ru}^{\text{II}}$ at an FTO electrode at different scan rates. $\text{Cp}_2^*\text{Ru}^{\text{II}}$ was dissolved in DCE containing 0.1 M TBAPF₆. Measurements were recorded under a N₂ atmosphere at ambient temperature using platinum wire as the counter electrode and a double-junction reference electrode as described in Chapter II were calibrated *vs.* the formal reduction potential of $\text{Cp}_2^*\text{Fe}^{\text{II}}$ in DCE on the SHE scale ($[E^0_{[\text{Cp}_2^*\text{Fe}^{\text{III}]} + / \text{Cp}_2^*\text{Fe}^{\text{II}}]}^{\text{DCE}} = 0.07 \text{ V vs. SHE}$).

4.4.2 Photo-oxidation of DCE in absence of protons

A control electrochemical experiment was performed to characterise the behavior of $\text{Cp}_2^*\text{Ru}^{\text{II}}$ in the electrochemical cell under illumination at $\lambda = 365 \text{ nm}$. CVs in the absence of organic acid, with only $\text{Cp}_2^*\text{Ru}^{\text{II}}$ and the supporting electrolyte present in the DCE solution, exhibited an oxidative catalytic wave under illumination (Figure 4.8). This wave is most probably due to the catalytic oxidation of DCE by $\text{Cp}_2^*\text{Ru}^{\text{II}}$. However, the precise identification of this catalytic oxidation was outside the scope of this study. This side-reaction, while interesting, did not interfere with the present interpretation of the CVs and controlled potential electrolysis (CPE) data obtained in the next paragraphs during the photo-electrocatalytic reduction of protons in the presence of $\text{Cp}_2^*\text{Ru}^{\text{II}}$. Therefore, the investigations were not extended.

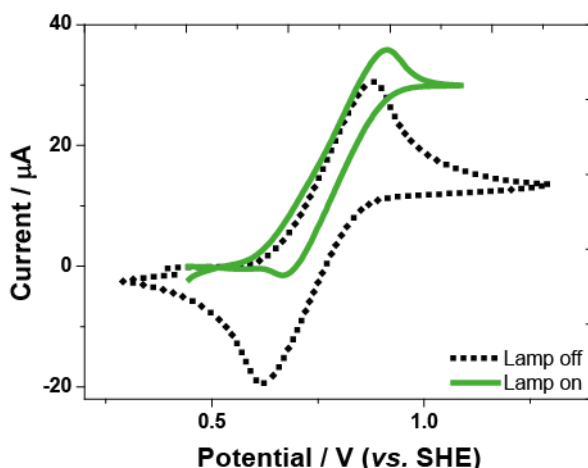


Figure 4.8: CVs of 1 mM $\text{Cp}_2^*\text{Ru}^{\text{(III)}}$ without (dark dot) and with (green line) illumination at $\lambda = 365$ nm. CVs were obtained at $5 \text{ mV}\cdot\text{s}^{-1}$ at an FTO electrode in contact with a solution of DCE containing 0.1 M TBAPF_6 as supporting electrolyte.

4.4.3 Photo-catalytic hydrogen production with organic protons

4.4.3.1 Experimental cyclic voltammetry and constant potential electrolysis

Photo-electrocatalytic H_2 generation by $\text{Cp}_2^*\text{Ru}^{\text{(II)}}$ was achieved directly from $[\text{H}(\text{OEt}_2)_2]\text{TB}$ acid in DCE. As it was monitored by ^1H NMR spectroscopy in the previous Chapter, $\text{Cp}_2^*\text{Ru}^{\text{(II)}}$ does not need a reductive activation step to be protonated. Thus, in acidified organic solutions, $\text{Cp}_2^*\text{Ru}^{\text{(II)}}$ is spontaneously converted to $[\text{Cp}_2^*\text{Ru}^{\text{(IV)}}(\text{H})]^+$ in the dark as described by eq.(4.2):



Therefore, the voltammetry after the addition of acid in excess did not show any electrochemical activity inside the potential window due to the production of the $\text{Ru}^{\text{(IV)}}$ species. Subsequently, upon light illumination through the FTO working electrode using an LED light source at $\lambda = 365$ nm, a clear catalytic current corresponding to the reduction of the photogenerated $[\text{Cp}_2^*\text{Ru}^{\text{(IV)}}]^+$ to $\text{Cp}_2^*\text{Ru}^{\text{(II)}}$ appeared with an onset potential slightly positive of the $[\text{Cp}_2^*\text{Ru}^{\text{(III)}}]^+/\text{Cp}_2^*\text{Ru}^{\text{(II)}}$ redox transition (Figure 4.9 (A), green solid line). No return peak was observed suggesting a fast protonation of the $\text{Cp}_2^*\text{Ru}^{\text{(II)}}$. As shown in Figure 4.9 (A), photo-electrocatalysis with $\text{Cp}_2^*\text{Ru}^{\text{(II)}}$ on an FTO electrode surface takes place at a potential 0.20 V higher (more positive) than direct electrocatalysis on the Pt electrode surface. Such a positive onset potential makes the use of $\text{Cp}_2^*\text{Ru}^{\text{(II)}}$ very attractive towards water splitting applications.

The appearance of the reductive catalytic current in the presence of organic protons, $\text{Cp}_2^*\text{Ru}^{\text{III}}$ and light was also confirmed by constant potential electrolysis done at 0.50 V *vs.* SHE (Figure 4.9 (B)). Initially, prior to illumination, almost no current apart from the double-layer charging was observed, in agreement with the CVs generated under these conditions in Figure 4.9 (A). Upon illumination, $\text{Cp}_2^*\text{Ru}^{\text{III}}$ was immediately oxidised (and H_2 evolved, as shown by head-space analysis with a gas chromatograph) causing the negative current to quickly increase in magnitude due to the regeneration of $[\text{Cp}_2^*\text{Ru}^{\text{III}}]^+$ species at the FTO electrode surface. When the LED was switched off, the current immediately began to drop with the disappearance of the $[\text{Cp}_2^*\text{Ru}^{\text{III}}]^+$ species in the vicinity of the FTO electrode on conversion to $\text{Cp}_2^*\text{Ru}^{\text{II}}$ and subsequent immediate protonation by $[\text{H}(\text{OEt}_2)_2]\text{TB}$.

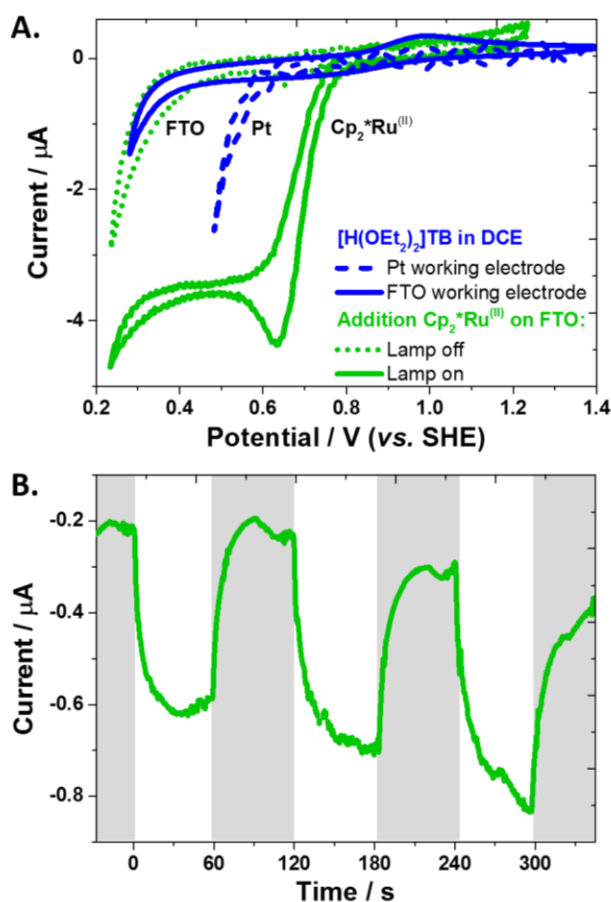


Figure 4.9: (A) Cyclic voltammograms of 4 mM $[\text{H}(\text{OEt}_2)_2]\text{TB}$ in DCE with 0.1 M TBAPF_6 supporting electrolyte without (FTO – solid blue and Pt – dashed blue lines) or with 1 mM $\text{Cp}_2^*\text{Ru}^{\text{III}}$ (green CVs with and without illumination). Scan rate 5 $\text{mV}\cdot\text{s}^{-1}$. (B) Controlled potential electrolysis of the same solution of 1 mM $\text{Cp}_2^*\text{Ru}^{\text{III}}$ and excess $[\text{H}(\text{OEt}_2)_2]\text{TB}$ in DCE with 0.1 M TBAPF_6 as supporting electrolyte on an FTO electrode at 0.50 V *vs.* SHE with the LED illumination switched periodically on (white) and off (grey).

The solution turned from colourless to pink after exposure to the LED light. Upon illumination, $[\text{Cp}_2^*\text{Ru}^{\text{(III)}}]^+$ was also produced in the bulk solution, much too far from the electrode surface to be reduced back to $\text{Cp}_2^*\text{Ru}^{\text{(II)}}$ on the timescale of the experiment. Subsequent analysis by UV/vis spectroscopy revealed a characteristic absorbance band at 500 nm (see Figure 4.14), identified as the $[\text{Cp}_2^*\text{Ru}^{\text{(III)}}]^+$ species (see Chapter III, Figure 3.7).

4.4.3.2 Control experiments

A series of further control electrochemical experiments were performed to fully characterise the behaviour of each species in the electrochemical cell. Firstly, CVs in the absence of organic acid, with only $\text{Cp}_2^*\text{Ru}^{\text{(II)}}$ and the supporting electrolyte present in the DCE solution was shown in section 4.4.2. Subsequently, CVs of an electrochemical cell with only $[\text{H}(\text{OEt}_2)_2]\text{TB}$ and the supporting electrolyte present in the DCE solution did not show any response change under dark conditions and with LED illumination (Figure 4.10 (A) and (B)). Finally, CPE data obtained during the photo-electrocatalytic reduction of protons in the presence of $\text{Cp}_2^*\text{Ru}^{\text{(II)}}$ (Figure 4.10 (B)).

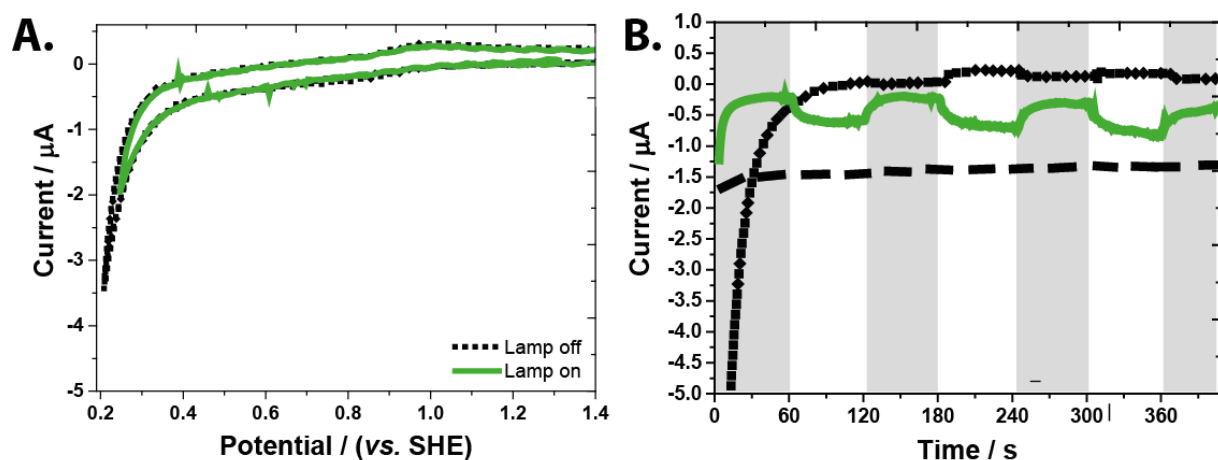


Figure 4.10: Control electrochemical experiments. All CVs were obtained at $5 \text{ mV}\cdot\text{s}^{-1}$ at an FTO electrode in contact with a solution of DCE containing 0.1 M TBAPF_6 as supporting electrolyte. CVs were obtained under anaerobic conditions at ambient temperatures using platinum wire as the counter electrode and a double-junction reference electrode, as described in Chapter II, section 2.2.5.3. (A) CVs of $4 \text{ mM } [\text{H}(\text{OEt}_2)_2]\text{TB}$ without (dark dot) and with (green line) illumination at $\lambda = 365 \text{ nm}$. (B) Chronoamperometry periodically turning the light off (grey) and on (white) with $1 \text{ mM } \text{Cp}_2^*\text{Ru}^{\text{(II)}}$ in solution at 0.50 V vs. SHE (dark dotted line), $1 \text{ mM } \text{Cp}_2^*\text{Ru}^{\text{(II)}}$ and $4 \text{ mM } [\text{H}(\text{OEt}_2)_2]\text{TB}$ in solution at 0.50 V vs. SHE (green line), and $4 \text{ mM } [\text{H}(\text{OEt}_2)_2]\text{TB}$ in solution at 0.35 V (dashed line).

4.4.3.3 Simulated constant potential electrolysis

This electrochemical study is completed and corroborated by a quantitative finite element model through comparison of experimental and simulated constant potential electrolysis.^{25,26} The latter was generated using a 1D geometry developed within COMSOL Multiphysics software (see Figure 4.11). The photoexcited decamethylruthenocene hydride DH^+ formed the photoexcited state DH^{+*} , that either underwent homolytic bond cleavage to produce hydrogen or relax back to DH^+ . Further simulation details are provided in Chapter II. The model shows that the reaction is not sensitive to the rate of the photoreaction, with practically no variation observed when the reaction rate was varied between 1 to 10^9 s^{-1} . However, if the ratio of the photoreaction and relaxation was adjusted to change the quantum yield, higher photocurrents were obtained with higher quantum yield. Hence, the absolute values of the rate constants cannot be accurately determined by simulations. The photocurrent is mostly governed by the mass transport because of the low absorption of incoming light by the DH^+ species results in slow kinetics of the photoreaction.

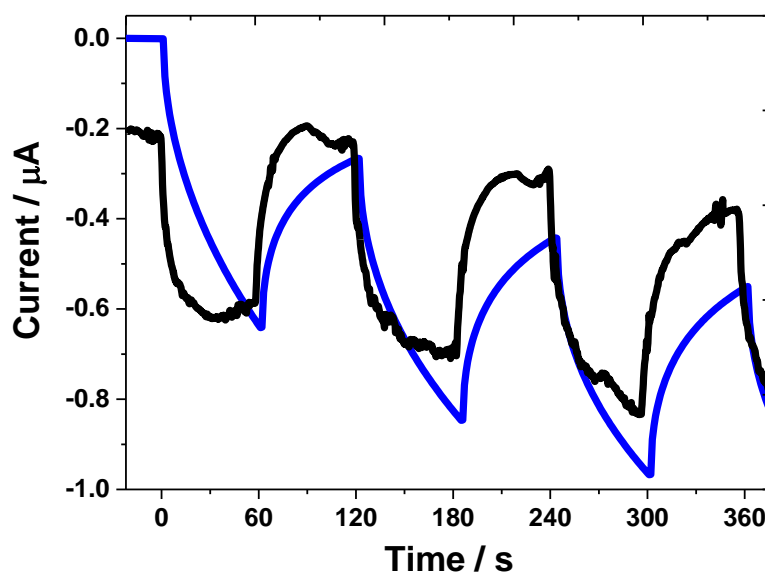


Figure 4.11: Simulations of the photo-electrocatalytic hydrogen production, showing partial agreement between the experiment and simulations.

4.4.4 Gas chromatography analysis of produced hydrogen

The generation of H_2 in the presence of organic protons, $\text{Cp}_2^*\text{Ru}^{(\text{II})}$ and light was definitively proven by photo-electrolysis at an applied potential of 0.50 V *vs.* SHE. The headspace of the electrochemical cell was monitored by gas chromatography and clearly showed the formation of H_2

(see Figure 4.12). The quantity of the evolved H_2 was compared with that for a reaction running without electrochemical regeneration (also Figure 4.12).

As it was demonstrated in the previous chapter, without regeneration, $\text{Cp}_2^*\text{Ru}^{\text{III}}$ acts as an electron donor capable of producing two equivalents of H_2 for each equivalent of $\text{Cp}_2^*\text{Ru}^{\text{III}}$ present in solution. Briefly, one equivalent corresponds to the oxidation of the hydride. The second equivalent is due to the extraction of a proton from one of the methyl groups on the cyclopentadienyl rings. In other words, the permethylated cyclopentadienyl (Cp^*) group is converted from ($\eta^5\text{-C}_5\text{Me}_5$) to a methylenecyclopentadienyl ($\eta^5\text{-C}_5\text{Me}_4\text{CH}_2$) ligand.^{1,27}

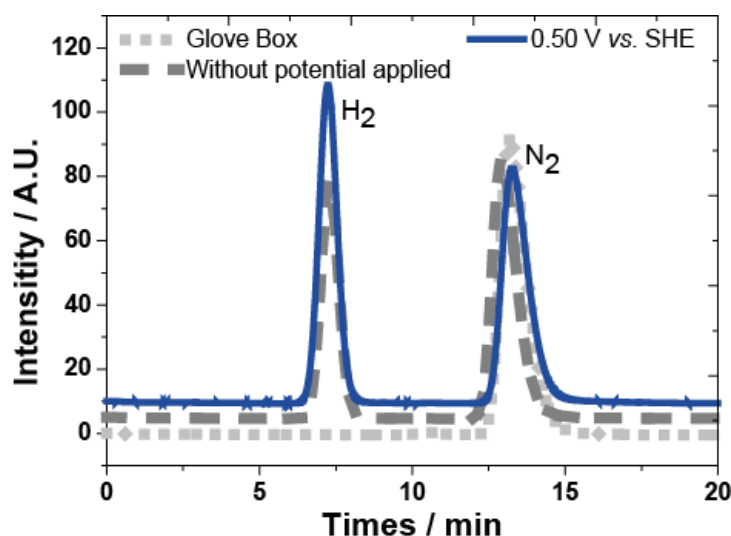


Figure 4.12: Gas chromatogram of the photo-production of H_2 gas from a solution of 1 mM $\text{Cp}_2^*\text{Ru}^{\text{III}}$ with 6 mM $[\text{H}(\text{OEt})_2]_2\text{TB}$ in DCE. The solution was put in contact with an FTO electrode, stirred and illuminated overnight at $\lambda = 365$ nm using the LED during 10 hours. A potential of 0.50 V *vs.* SHE was applied at the FTO electrode during the first 4 hours. The electrochemical cell used is depicted in Chapter II, Figure 2.2, with a platinum wire counter electrode and a double-junction reference electrode. The headspace of the airtight cell was analysed after 10 hours (blue line). To compare, an identical experiment was performed without applying a potential (grey dash). A noticeable enhancement of the H_2 production was observed while the potential was applied. The atmosphere inside the gloves box was analysed as a control experiment for each reaction (grey dot). No hydrogen or oxygen was observed.

The quantities of evolved H_2 without regeneration are in good, but not perfect, agreement with the previous Chapter studying the reaction mechanism of the photoproduction of H_2 with $\text{Cp}_2^*\text{Ru}^{\text{III}}$ in a single acidified organic phase.^{1,27} Despite the caution taken to entirely seal the electrochemical cell, a small amount of H_2 permeated through the electrochemical cell. Indeed, because H_2 is a leaky small molecule, the quantification of the long term H_2 release from the electrode junction with an electrochemical cell is an issue for these kinds of measurements.²⁸ Nevertheless, a noticeable enhancement in H_2 production was observed when the potential was

applied at the FTO electrode for 4 hours (see Figure 4.12 and Figure 4.13) meaning the electro-regeneration occurred.

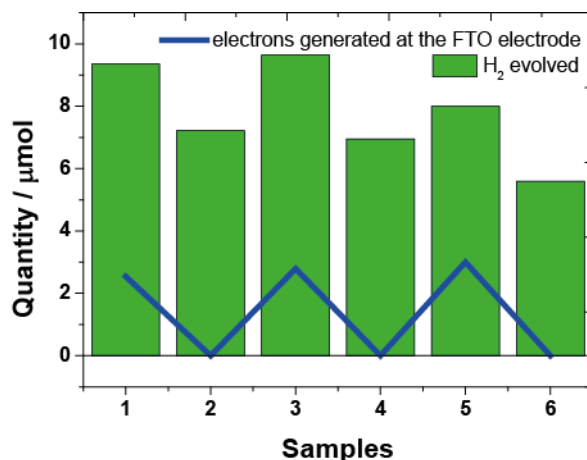


Figure 4.13: Comparison of H₂ production with or without electrochemical regeneration. A solution of 1 mM Cp₂*Ru^(II) with 6 mM [H(OEt)₂]₂TB was placed in the electrochemical cell presented in Figure 2.2 and illuminated for 10 hours under LED illumination. The head space of the cell was analysed (green bar). The result clearly shows the enhancement of the H₂ production while a potential of 0.50 V *vs.* SHE was applied (the quantity of electrons passing through the FTO electrode is signified by the blue line).

The colour of the organic solution turned from colourless to pink during the reaction. Subsequent analysis by UV/vis spectroscopy revealed a characteristic absorbance band at 500 nm (see Figure 4.14), identified as the [Cp₂*Ru^(III)]⁺ species in Chapter III in Figure 3.7. Additionally, a broad band appeared at a higher wavelength which indicated the decomposition of [Cp₂*Ru^(III)]⁺ was beginning to take place (Figure 4.14). After 6 hours without regeneration, decomposition of [Cp₂*Ru^(III)]⁺ occurred giving way to a series of ill-defined absorbance bands (Figure 4.14).

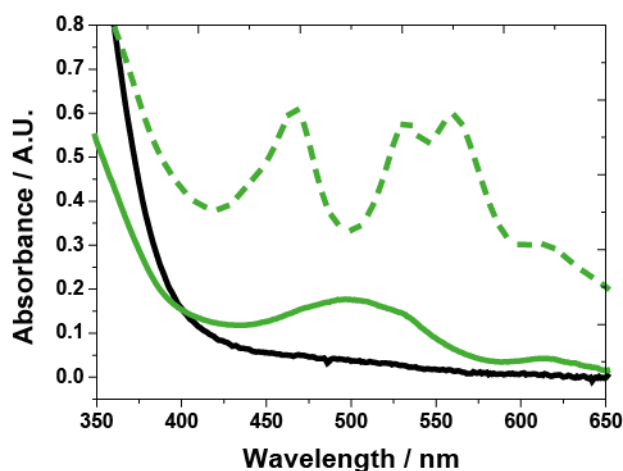


Figure 4.14: Uv/vis spectra of a solution containing 1 mM Cp₂*Ru^(III) and 4 mM [H(OEt)₂]₂TB before the reaction (dark line) and during controlled potential electrolysis at 0.50 V *vs.* SHE under LED illumination

(green line) and 6 hours after controlled potential electrolysis (green dash). A rise of absorbance at 500 nm is induced by the generation of $[\text{Cp}_2\text{Ru}^{(\text{III})}]^+$ (characterised by spectroelectrochemistry in Chapter III, Figure 3.7).

4.4.5 Quantum yield

The quantum yield (QY) for the photo-electrocatalytic generation of H_2 from an acidified organic solution of $\text{Cp}_2^*\text{Ru}^{(\text{II})}$ is defined as $\text{QY} = 2n_{\text{H}_2} / n_{\text{hv}} = n[\text{Cp}_2^*\text{Ru}^{(\text{III})}]^+ / n_{\text{hv}}$. The QY was determined by quantifying the amount of $[\text{Cp}_2^*\text{Ru}^{(\text{III})}]^+$ evolved from a 2 mM $\text{Cp}_2^*\text{Ru}^{(\text{II})}$ solution in DCE with protons in excess (4 mM) at a given photon flux of 2.0×10^{16} photons $\cdot\text{s}^{-1}$ by UV/vis spectroscopy (see Figure 4.15, details of the proton flux calculation are provided in Chapter II, section 2.4.1). The absorbance observed from the UV/vis spectra presented in Figure S8 at 500 nm was converted to concentration of $[\text{Cp}_2^*\text{Ru}^{(\text{III})}]^+$ by applying the Beer-Lambert law, $A = l \varepsilon c$, with $l = 4.2$ cm and $\varepsilon = 0.960$ mM $\cdot\text{cm}^{-1}$ (determined previously during the spectroelectrochemical experiment shown in Figure 3.7, Chapter III). The length of the cell was selected in order to guarantee the absorption of the entire the incident light.

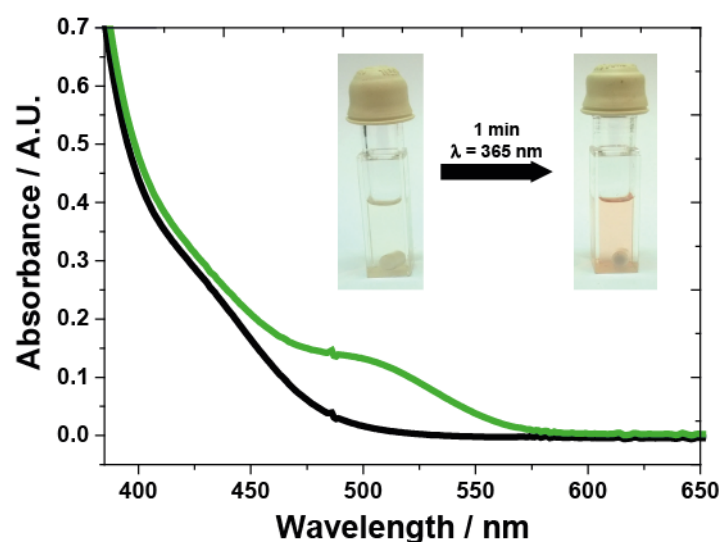


Figure 4.15: Uv/vis spectra of a solution containing 2 mM $\text{Cp}_2^*\text{Ru}^{(\text{II})}$ and 8 mM $[\text{H}(\text{OEt})_2]\text{TB}$. Before the reaction (dark line) and after one minute of illumination with a 365 nm LED (green line). Generation of $[\text{Cp}_2\text{Ru}^{(\text{III})}]^+$ under illumination induces to the rise of absorbance at 500 nm. The production of $[\text{Cp}_2\text{Ru}^{(\text{III})}]^+$ was quantified using the extinction coefficient determined spectroelectrochemically in Chapter III, Figure 3.7 by applying the Beer-Lambert law. The quantified $[\text{Cp}_2\text{Ru}^{(\text{III})}]^+$ was then used to calculate the quantum yield of the photo-reaction.

At 11 mW of power we obtained a concentration of 32.8 μM $[\text{Cp}_2\text{Ru}^{(\text{III})}]^+$ for 15 mL, meaning 3.0×10^{17} molecules were produced.

Next, we calculated the production rate as number of $[\text{Cp}_2\text{Ru}^{(\text{III})}]^+$ molecules per second:

$$3.0 \times 10^{17} / 60 \text{ s} = 4.9 \times 10^{15} \text{ s}^{-1}$$

Thus, the internal QY of the sample is defined as $\text{IQY} = n [\text{Cp}_2^*\text{Ru}^{(\text{III})}]^+ / n_{\text{hv}}$

$$\text{IQY} = 100 \% \cdot (4.9 \times 10^{15} / 2.0 \times 10^{16}) = 24.7 \%$$

However, in the experimental conditions, the light pass through the FTO electrode before to illuminate the sample solution. From the transmittance spectrum at 365 nm, the maximum production rate expected as the number of $[\text{Cp}_2\text{Ru}^{(\text{III})}]^+$ molecules per second when the cell is illuminated through the FTO electrode is given by:

$$4.9 \times 10^{15} \cdot \text{s}^{-1} \times 0.697 = 3.4 \times 10^{15} \text{ photons} \cdot \text{s}^{-1}$$

Therefore, the maximum EQY expected was directly obtained from the new production rate:

$$\text{EQY} = 100 \% \cdot (3.4 \times 10^{15} / 2.0 \times 10^{16}) = 17.0 \%$$

Importantly, by following the appearance of $[\text{Cp}_2^*\text{Ru}^{(\text{III})}]^+$ spectroscopically to determine the QY, overestimations by incorporation of any H_2 that may have been produced by degradation of the catalyst were avoided.

4.5 Conclusions

In summary, $\text{Cp}_2^*\text{Ru}^{(\text{II})}$ is a single molecule that performs the reaction of reduction of protons by photo-activation. The transient $[\text{Cp}_2\text{Ru}^{(\text{III})}]^+$ formed when H_2 is evolved was stabilised by employing a weak coordinating solvent and electrolyte (DCE and TB^- ion, respectively). Therefore, it was possible to reduce the photo-generated $[\text{Cp}_2\text{Ru}^{(\text{III})}]^+$ on FTO electrode to recover the original $\text{Cp}_2^*\text{Ru}^{(\text{II})}$. Results were corroborated by COMSOL simulation. The photo-activation enables the reduction of protons with $\text{Cp}_2^*\text{Ru}^{(\text{II})}$, an electron donor characterized by a redox potential more positive than the one of proton reduction in DCE. Thus, the regeneration of the photo-product happens at a potential 200 mV more positive than the direct reduction of protons on Pt. It represents a step forward for the water-splitting because $\text{Cp}_2^*\text{Ru}^{(\text{II})}$ can be recovered at a potential closer to OER compare to classical not photo-activated catalyst. A promising internal quantum yield of 25 % was observed. Further investigation about the spectroscopic phenomena involved will be provided in Chapter VI. Looking beyond $\text{Cp}_2^*\text{Ru}^{(\text{II})}$, these results could open an interesting new

research field for the development of metallocenes for H₂ photo-production. Indeed, ligands and metals of the metallocenes can be tuned to modify the metallocene properties such as the redox potential or the excitation wavelength.

In the meantime, Cp₂*Ru^(II) appears as a good electron donor to performed HER in the batch water-splitting as it can be recovered at a potential close to the oxidation of water (in comparison with catalyst processing without photo-activation) with a good quantum yield. Consequently, the next chapter focuses on the implementation of HER by Cp₂*Ru^(II) at polarised liquid||liquid interphases and characterised the mechanism involved.

4.6 References

- (1) Rivier, L.; Vannay, L.; Mendez, M.; Peljo, P.; Vrabel, H.; Corminboeuf, C.; Scanlon, M. D.; Girault, H. H. **2017**, submitted.
- (2) Jones, R. F.; Cole-Hamilton, D. J. *Journal of the Chemical Society, Chemical Communications* **1981**, 1245.
- (3) Pitman, C. L.; Miller, A. J. M. *ACS Catalysis* **2014**, *4*, 2727.
- (4) Gray, H. B.; Maverick, A. W. *Science* **1981**, *214*, 1201.
- (5) Bofill, R.; García-Antón, J.; Escriche, L.; Sala, X. *Journal of Photochemistry and Photobiology B: Biology* **2015**, *152, Part A*, 71.
- (6) Kamysheva, A. A.; Kreindlin, A. Z.; Rybinskaya, M. I.; Petrovskii, P. V. *Russian Chemical Bulletin* **1999**, *48*, 581.
- (7) Rybinskaya, M. I.; Kreindlin, A. Z.; Hoffmann, R.; Minyaev, R. M. *Russian Chemical Bulletin* **1994**, *43*, 1605.
- (8) Kamysheva, A. A.; Kreindlin, A. Z.; Rybinskaya, M. I.; Petrovskii, P. V. *Russian Chemical Bulletin* **2000**, *49*, 520.
- (9) Kreindlin, A. Z.; Rybinskaya, M. I. *Russian Chemical Reviews* **2004**, *73*, 417.
- (10) Hashidzume, K.; Tobita, H.; Ogino, H. *Organometallics* **1995**, *14*, 1187.
- (11) Swarts, J. C.; Nafady, A.; Roudebush, J. H.; Trupia, S.; Geiger, W. E. *Inorganic Chemistry* **2009**, *48*, 2156.
- (12) Trupia, S.; Nafady, A.; Geiger, W. E. *Inorganic Chemistry* **2003**, *42*, 5480.
- (13) Hill, M. G.; Lamanna, W. M.; Mann, K. R. *Inorganic Chemistry* **1991**, *30*, 4687.
- (14) Pellegrin, Y.; Odobel, F. *Comptes Rendus Chimie* **2017**, Vol 20, 3, 283..
- (15) Hawecker, J.; LEHN, J. M.; Ziessel, R. *Chemischer Informationsdienst* **1983**, *14*.
- (16) Bhattacharyya, K.; Das, P. K. *The Journal of Physical Chemistry* **1986**, *90*, 3987.
- (17) Chow, Y. L.; Danen, W. C.; Nelsen, S. F.; Rosenblatt, D. H. *Chemical Reviews* **1978**, *78*, 243.
- (18) Staško, A.; Brezová, V.; Biskupič, S.; Neudeck, A.; Bartl, A.; Dunsch, L. *Journal of Photochemistry and Photobiology A: Chemistry* **1998**, *116*, 97.
- (19) Tseng, T.-C.; Urban, C.; Wang, Y.; Otero, R.; Tait, S. L.; Alcamí, M.; Écija, D.; Trelka, M.; Gallego, J. M.; Lin, N.; Konuma, M.; Starke, U.; Nefedov, A.; Langner, A.; Wöll, C.; Herranz, M. Á.; Martín, F.; Martín, N.; Kern, K.; Miranda, R. *Nature Chemistry* **2010**, *2*, 374.
- (20) Skulason, H.; Frisbie, C. D. *Langmuir* **1998**, *14*, 5834.
- (21) Zhao, C.; Bond, A. M. *Journal of the American Chemical Society* **2009**, *131*, 4279.
- (22) Koelle, U.; Salzer, A. *Journal of Organometallic Chemistry* **1983**, *243*, C27.

- (23) O'Hare, D.; Green, J. C.; Chadwick, T. P.; Miller, J. S. *Organometallics* **1988**, *7*, 1335.
- (24) Kölle, V.; Grub, J. *Journal of Organometallic Chemistry* **1985**, *289*, 133.
- (25) Albery, W. J.; Archer, M. D. *Nature* **1977**, *270*, 399.
- (26) Bourdon, R.; Peljo, P.; Méndez, M. A.; Olaya, A. J.; De Jonghe-Risse, J.; Vrabel, H.; Girault, H. H. *The Journal of Physical Chemistry C* **2015**, *119*, 4728.
- (27) Rivier, L.; Stockmann, T. J.; Méndez, M. A.; Scanlon, M. D.; Peljo, P.; Opallo, M.; Girault, H. H. *The Journal of Physical Chemistry C* **2015**, *119*, 25761.
- (28) Adams, P.; Bengaouer, A.; Cariteau, B.; Molkov, V.; Venetsanos, A. G. *International Journal of Hydrogen Energy* **2011**, *36*, 2742.

5. Decamethylruthenocene Hydride and Hydrogen Formation at Liquid|Liquid Interfaces

Adapted with permission from Decamethylruthenocene Hydride and Hydrogen Formation at Liquid|Liquid Interfaces, *J. Phys. Chem. C*, **2015**, 119 (46), p 25761–25769, Copyright (2015) American Chemical Society.

5.1	Introduction.....	110
5.2	Experimental hydrogen evolution at liquid liquid interfaces	111
5.2.1	Shake-flask experiments.....	111
5.2.2	Cyclic voltammetric observations at w DCE interfaces	115
5.2.2.1	Mechanism involved for the proton transfer at w DCE interfaces.....	115
5.2.2.2	Control electrochemical experiments.....	116
5.2.2.2.1	[Cp ₂ *Ru ^(III)] ⁺ transfer across polarized w DCE interfaces.....	116
5.2.2.2.2	Influence of chloride and hydrogen ions presence.....	117
5.2.2.2.3	Influence of counter ion of the aqueous acid at polarized w DCE interfaces ..	118
5.2.2.2.4	Influence of the complexation rate of the hydride formation	119
5.3	Mechanistic analysis using simulated voltammetric curves	120
5.3.1	Influence of the rate of [Cp ₂ *Ru ^(IV) (H)] ⁺ formation in the organic phase.....	121
5.3.2	Simulation of the facilitated proton transfer.....	123
5.3.3	Influence of the rate of [Cp ₂ *Ru ^(IV) (H)] ⁺ dissociation in the organic phase.....	124
5.3.4	Influence of the rate of [Cp ₂ *Ru ^(IV) (H)] ⁺ dissociation in the aqueous phase.....	124
5.3.5	Influence of the rate of [Cp ₂ *Ru ^(IV) (H)] ⁺ association in the aqueous phase	126
5.4	Conclusions.....	126
5.5	References.....	129

5.1 Introduction

Coupling of the $\text{Cp}_2^*\text{Ru}^{(\text{II})}$ photocatalytic scheme with soft interfaces, as described in Figure 5.1, represents an interesting model platform to study the photo-production of H_2 towards the batch water-splitting and is the major focus of this Chapter.

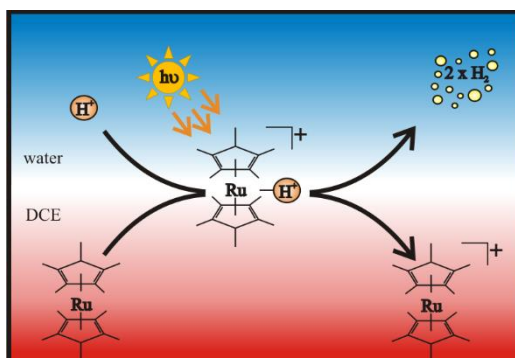


Figure 5.1. Photo-hydrogen evolution by $\text{Cp}_2^*\text{Ru}^{(\text{II})}$ at water|1,2-dichloroethane (w|DCE) interface

For this purpose, our group has developed an alternative strategy¹ to produce H_2 at ITIES, for example at a water|1,2-dichloroethane (w|DCE) interface, that relies on electron reductants (*e.g.* metallocenes), dissolved in an organic electrolyte solution and an acidic aqueous solution. In this way, product separation is inherent within the system, which is ultimately biomimetic. Upon polarisation of the interface, either *via* the application of an external voltage or by dissolving a common ion in both phases, protons are pumped into the organic phase. Thus, the potential dependent proton transfer step, with corresponding metal hydride formation, can be controlled and monitored electrochemically; thus, facilitating kinetic/thermodynamic investigations of the reactions. Furthermore, this methodology takes advantage of the fact that proton reduction in organic solvents, such as DCE, is thermodynamically more favourable than in aqueous media.¹ Consequently, milder organic donors, with higher (more positive) redox potentials, can be effectively coupled to proton pumping across the interface to produce H_2 . Additionally, the ITIES provides an alternative electrochemical perspective to investigate the HER. Different charge transfer reactions can be monitored by controlling the potential difference between the two phases.² Employing this utility, it is possible to investigate one key step of the HER: metal hydride formation.

Indeed, the understanding and the control of proton transfer – and possibly proton coupled electron transfer – to and from the metal hydride is particularly important in photochemical water

splitting³ and fuel cell electrocatalysis⁴ but also impacts a wide range of other catalytic, industrial, and biochemical reactions.⁵ Metal hydrides are crucial intermediates that allow for the transfer of a free proton to an organic molecule, such as for hydrogenation or hydroformylation.⁶ Therefore, this chapter provides the foundation of the production of H₂ by Cp₂*Ru^(II) in the batch water-splitting while also enhancing our mechanistic understanding of the metal hydride formation.

Here, the chapter presents HER by Cp₂*Ru^(II) at the liquid|liquid interface. The hydride formation was characterised by voltammetry and the biphasic mechanism elucidated through comparison of experimental and simulated CVs; the latter generated using a 1D geometry developed within COMSOL Multiphysics software. A modified electrochemical (E) – chemical (C), or EC mechanism, was the primary pathway evaluated, where the potential dependent interfacial proton transfer (from w to DCE) and the formation of the metal hydride within the bulk DCE phase constituted the electrochemical and chemical steps, respectively.

5.2 Experimental hydrogen evolution at liquid|liquid interfaces

As discussed in Chapter I, the liquid|liquid interface may be polarized like a conventional electrode-electrolyte interface by external polarization in a four-electrode cell or chemically by distribution of a common ion on either side of the interface. In a first stage, the production of H₂ at liquid|liquid interfaces was performed and characterised by applying a chemical polarisation. In a second stage, CVs were obtained by external polarisation to investigate the mechanisms involved.

5.2.1 Shake-flask experiments

The biphasic HER with Cp₂*Ru^(II) acting as an electron donor was initially probed by shake-flask experiments under anaerobic conditions and with moderate stirring, the w|DCE solution composition described for Vial 1 is shown in Figure 5.2. Two main conditions were varied: with/without i) light exposure and ii) electrochemical polarisation of the w|DCE interface. In order to polarise the interface, a phase transfer catalyst was employed, as previously described,⁷⁻⁹ using TB⁻ as the common ion initially dissolved in the aqueous phase. TB⁻ spontaneously transfers from (w) to (o) with the corresponding amount of Li⁺ and H⁺ and fixes the Galvani potential difference across the ITIES at positive values ($\Delta_o^w\phi \approx 0.50$ V). Simultaneously, protons are driven into the

organic phase and are available to react with $\text{Cp}_2^*\text{Ru}^{\text{(II)}}$. Further experimental details are specified in Chapter II, section 2.6.

2.5 mM $\text{Cp}_2^*\text{Ru}^{\text{(II)}}$	0.1 M HCl	Vial (1)
5 mM BATB	5 mM $[\text{Li}(\text{OEt}_2)_2]\text{TB}$	
(DCE)	(w)	

Figure 5.2. Schematic representation of the initial compositions of the aqueous and organic phases for shake flasks to perform photo-driven biphasic hydrogen evolution under chemical polarization.

Photographs taken of the reaction vial for the case where both light illumination and ITIES polarisation were used are displayed in Figure 5.3. Once solubilized in DCE, $\text{Cp}_2^*\text{Ru}^{\text{(II)}}$ produced a clear organic phase (Figure 5.3.(A)). After one hour of irradiation, the DCE phase exhibited a pink colour (Figure 5.3.(B)) with a strong UV/Vis absorption band at 500 nm (see Figure 5.3.), which agrees well with the absorption band for $[\text{Cp}_2^*\text{Ru}^{\text{(III)}}]^+$ as shown previously.¹⁰ If the reaction was stirred for 180 min, then the solution turned purple which agrees with the appearance of $[\text{Cp}_2^*\text{Ru}^{\text{(IV)}}(\text{C}_5\text{Me}_4\text{CH}_2)]^+$ (Figure 5.3.(C)) after prolonged photo-irradiation.¹⁰ In summary, $[\text{Cp}_2^*\text{Ru}^{\text{(III)}}]^+$ was seen for the transition from Ru(II) (colourless), to Ru(III) (pink), and finally to Ru(IV) (purple), as seen in Chapter III.

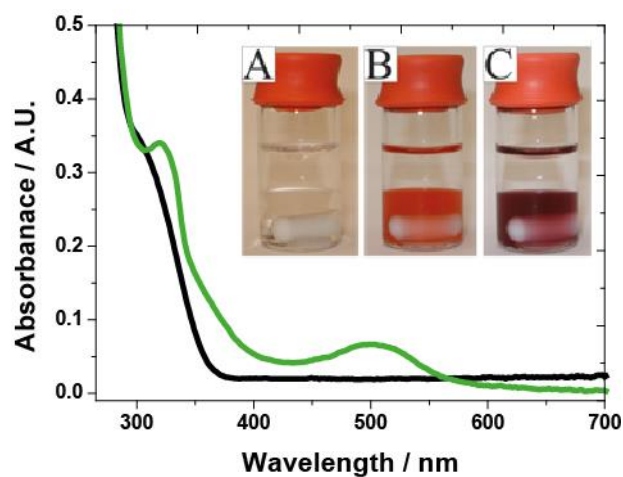


Figure 5.3. HER by $\text{Cp}_2^*\text{Ru}^{\text{(II)}}$ at liquid|liquid interface under white light illumination. UV/Vis absorbance spectra obtained using Vial 1 after first preparing the solution (black trace) and after stirring for 60 min under illumination (pink trace). In set pictures: Photographs taken of the reaction vial at various illumination time: (A) 0 min, (B) 60 min and, (C) 180 min.

Additionally, after 60 minutes of stirring, the head-space gas was sampled – as described in Chapter II, section 2.6 – and analysed using gas chromatography; chromatograms have been plotted in Figure 5.4 for each case as indicated inset. For the case of both ITIES, electrochemical

polarisation and light irradiation, a peak corresponding to H_2 gas was observed after ~ 2 min; however, no H_2 evolution was observed for the cases where either the phase transfer catalyst was omitted or the vial was kept in the dark. This indicates that $\text{Cp}_2^*\text{Ru}^{\text{III}}$ is a possible photo-active electron donor for H_2 evolution under biphasic conditions and that this HER is predominately performed in the bulk organic phase; therefore, $\text{Cp}_2^*\text{Ru}^{\text{III}}$ does not undergo appreciable interfacial electron transfer to aqueous protons.

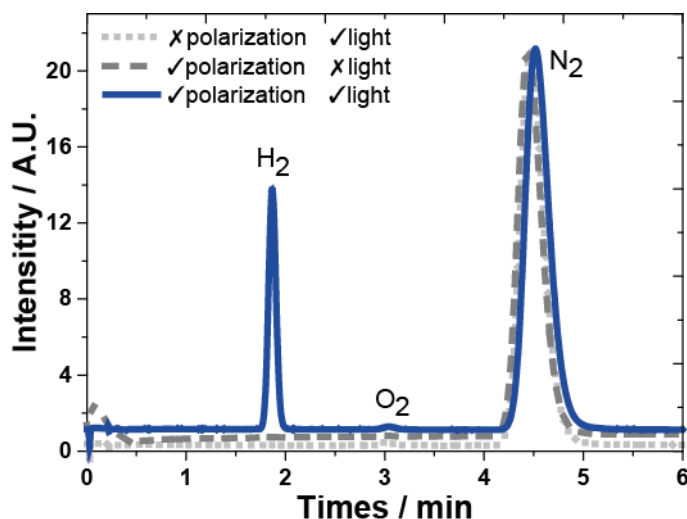


Figure 5.4. Gas chromatograms of the shake-flask headspace gas for experiments performed using Vial 1 recorded after 60 minutes of stirring under anaerobic conditions, in the dark (dashed curve), and under white-light illumination without $[\text{Li}(\text{OEt}_2)_2]\text{TB}$ (dotted trace) and with $[\text{Li}(\text{OEt}_2)_2]\text{TB}$ (solid line). Note that the presence of $[\text{Li}(\text{OEt}_2)_2]\text{TB}$ indicates ITIES polarisation at $\Delta_o^w\phi \approx 0.5$ V.

The amounts evolved of H_2 were recorded as a function of time using a calibrated GC with w|DCE (■) as well as w|trifluorotoluene (w|TFT, ●) liquid|liquid systems for comparison (Figure 5.5). The solution compositions were as outlined in Vial 1 but with an initial excess of $[\text{Li}(\text{OEt}_2)_2]\text{TB}$ present in (w) relative to $\text{Cp}_2^*\text{Ru}^{\text{III}}$ in (o), and therefore an excess of protons transferred from (w) to (o) as tetrakis(pentafluorophenyl)borate diethyl etherate acid $[\text{H}(\text{OEt}_2)_2]\text{TB}$. The quantity of H_2 evolved was observed to reach a plateau after 180 min at ~ 5.0 μmol . This value is twice the predicted stoichiometric amount of H_2 – estimated to be 2.5 μmol (Figure 5.5, dashed line) if each $\text{Cp}_2^*\text{Ru}^{\text{III}}$ molecule acts as a single electron donor. Therefore, these results are in good agreement with Chapter III studying the reaction mechanism of the photo-production of H_2 with $\text{Cp}_2^*\text{Ru}^{\text{III}}$ in a single acidified organic phase.¹⁰ Indeed, the first step involves the formation of the metal hydride, where a proton coordinates to the metal centre. The metal

hydride is oxidized under illumination and hydrogen is released. Then, the ruthenium core extracts a proton from one of its ligands (*e.g.* a proton from one of the methyl groups on the cyclopentadienyl rings), thus providing the second equivalent of protons needed to facilitate H₂ evolution as confirmed by ¹H and ¹³C NMR spectroscopy in Chapter III.

Additionally, the w|DCE biphasic system was compared to one using w|TFT. TFT has been previously proposed as an alternative solvent to study charge transfer across the interface,¹¹ as well as for H₂ and H₂O₂ formation in biphasic systems,¹² owing to its lower toxicity relative to DCE. The amount of H₂ evolved over time has been plotted in Figure 5.5. (●); however, the maximum yield approaches, but never exceeds, the quantitative yield calculated: 2.5 μmol. These results are similar to those made recently by Adamiak *et al.*¹² for the spontaneous HER in the dark using Cp₂*Fe^(II) as the electron donor. Therein,¹² they theorised that the low HER efficiency of the w|TFT *versus* w|DCE interface was owing to the lower degree of [H(OEt₂)₂]TB dissociation in TFT; this in turn limits the availability of H⁺. This could be the case here with Cp₂*Ru^(II), or alternatively, π-π interactions between the TFT molecules that can stabilize the [Cp₂*Ru^(IV)(H)]⁺ species through the Cp* ring; thereby, inhibiting the intramolecular abstraction of a Cp*-proton to form H₂.

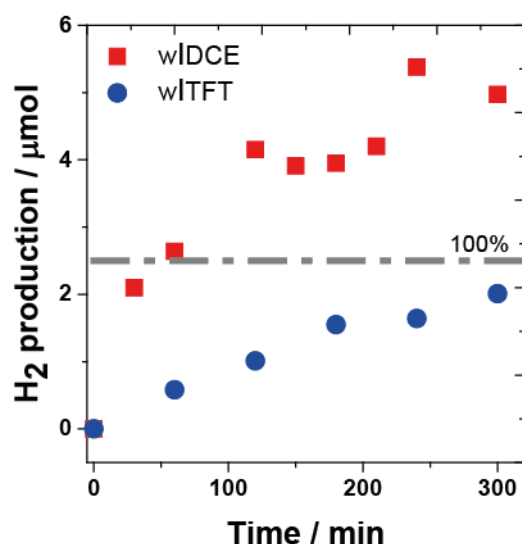


Figure 5.5. Plot of H₂ production over time obtained by quantification of the shake-flask headspace gas, as measured by gas chromatography, for w|TFT and w|DCE reactions under anaerobic conditions for experiments performed using Vial 1 (above) in the presence of excess [Li(OEt₂)₂]TB.

5.2.2 Cyclic voltammetric observations at w|DCE interfaces

In order to further investigate the mechanism involved at the interface, charge transfer reactions between w|DCE were characterised using a traditional four-electrode cell as described in Chapter II, section 2.2.4.

5.2.2.1 Mechanism involved for the proton transfer at w|DCE interfaces

Figure 5.6 depicts the CVs obtained at a scan rate of $0.050 \text{ V}\cdot\text{s}^{-1}$ using Cell 1 at varying pH, from 3 to 2 and 1 for the red, blue, and green traces, respectively, as well as in the absence of $\text{Cp}_2^*\text{Ru}^{\text{(II)}}$ (black trace) at pH = 3, which served as the blank. In the case of the blank, the potential window is limited by the transfer of protons from (w) to (o) at the positive end, and similarly chloride ion (Cl^-) transfer at negative potentials.

Upon closer inspection, the blank curve, without $\text{Cp}_2^*\text{Ru}^{\text{(II)}}$, differs from the CVs obtained in the presence of $\text{Cp}_2^*\text{Ru}^{\text{(II)}}$ in two respects. First, at the positive end, the CV potential profile for the blank has an expected return peak at 0.413 V, indicative of protons transferring back from (o) to (w); however, this curve feature is absent in the CVs acquired in the presence of $\text{Cp}_2^*\text{Ru}^{\text{(II)}}$ indicating irreversible proton transfer. This is in good agreement with the results of Samec *et al.*¹³ for ferrocene derivatives, along with our recent results¹⁴⁻¹⁶ using decamethylferrocene ($\text{Cp}_2^*\text{Fe}^{\text{(II)}}$) at a w|DCE interface. For the latter, proton transfer is followed by $[\text{Cp}_2^*\text{Fe}^{\text{(IV)}}(\text{H})]^+$ formation which subsequently reacts with dissolved O_2 to generate $[\text{Cp}_2^*\text{Fe}^{\text{(III)}}]^+$ as well as H_2O_2 and H_2O ; *i.e.* eliciting the oxygen reduction reaction (ORR). Therefore, for the present case, it is likely that protons are coordinating to $\text{Cp}_2^*\text{Ru}^{\text{(II)}}$ and generating $[\text{Cp}_2^*\text{Ru}^{\text{(IV)}}(\text{H})]^+$.

Secondly, after addition of $\text{Cp}_2^*\text{Ru}^{\text{(II)}}$ and during the cathodic scan in Figure 5.6(A), a peak-shaped wave emerges with a peak potential, $\Delta_o^w\phi_p$, at approximately -0.280 V for pH = 3. This ion transfer wave is likewise irreversible in that an analogous peak is not observed in the anodic scan. Fundamentally, this could be attributed to either transfer of a positively charged species from (o) to (w), or that of a negatively charged species from (w) to (o). An initial clue to the origin of this ion transfer peak was obtained when the CV potential range was manipulated (see Figure 5.6(B)) such that the initial CV was swept to moderate positive potentials while subsequent scans went to increasing positive potentials. The ion transfer wave at roughly -0.280 V was observed to increase in cathodic current intensity concomitantly with increases in the positive potential range.

Therefore, it can be concluded that there is a correlation between the occurrence of this peak, along with its intensity, and the amount of protons transferred. Indeed, after consideration of the control experiments discussed *vide infra*, this ion transfer wave is attributed to the transfer of $[\text{Cp}_2^*\text{Ru}^{\text{(IV)}}(\text{H})]^+$ from (o) to (w), the rate of formation of which is intimately linked to the quantity of protons transferred from (w) to (o).

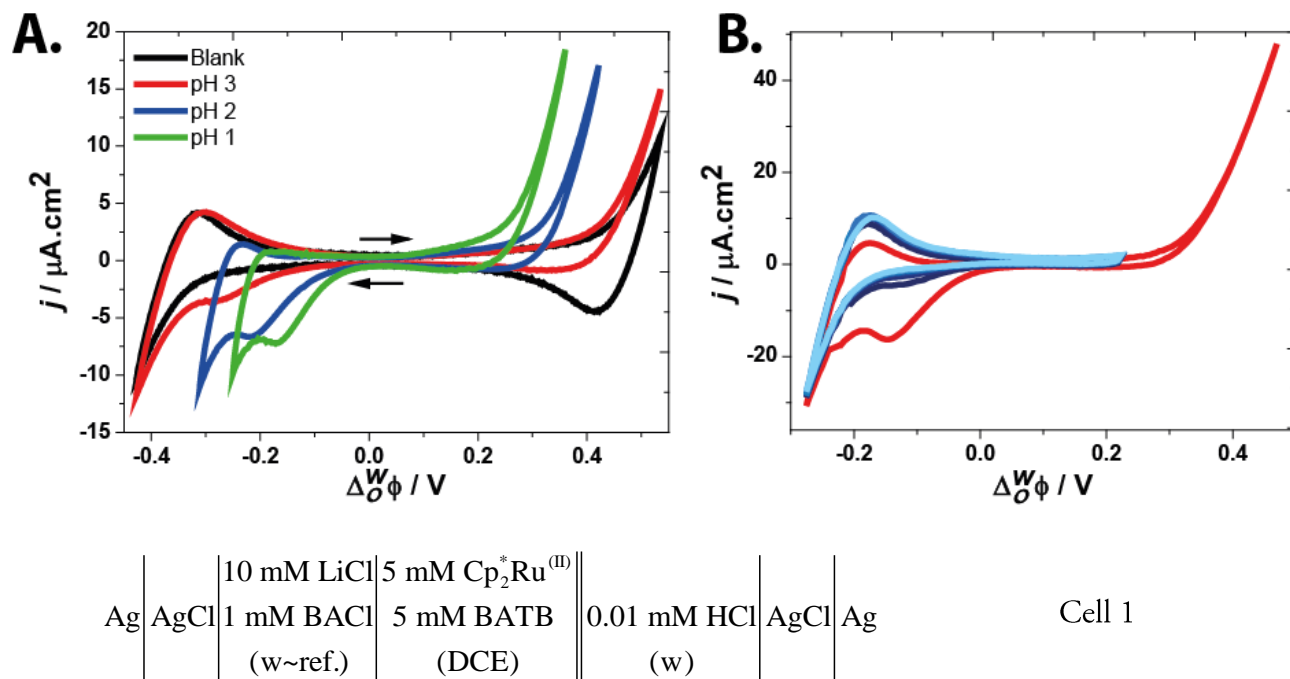


Figure 5.6. CVs obtained using Cell 1. (A) HCl concentration was varied as indicated, while the blank curve (—) was acquired in the absence of $\text{Cp}_2^*\text{Ru}^{\text{(III)}}$ with 0.001 M HCl. (B) Overlay of CVs recorded with z equal to 0.010 M HCl while increasing the limit of the positive potential range. All CVs were performed at a scan rate of 0.050 V.s^{-1} .

5.2.2.2 Control electrochemical experiments

5.2.2.2.1 $[\text{Cp}_2^*\text{Ru}^{\text{(III)}}]^+$ transfer across polarized w|DCE interfaces

One alternative positively charged species that may be present in DCE is the cationic $[\text{Cp}_2^*\text{Ru}^{\text{(III)}}]^+$ species. Therefore, the latter was synthesised by electrolysis, as described in Chapter II, and its formal ion transfer potential ($\Delta_o^w \phi_{[\text{Cp}_2^*\text{Ru}^{\text{(III)}}]^+}^{o'}$) determined through CV to be 0.005 V (see Cell 2 and Figure 5.7). Owing to the disparity between this value recorded for $[\text{Cp}_2^*\text{Ru}^{\text{(III)}}]^+$ and that found using Cell 1, one can conclude that the transfer wave at roughly -0.280 V is not due to $[\text{Cp}_2^*\text{Ru}^{\text{(III)}}]^+$. Two further possibilities are the transfer of $[\text{Cp}_2^*\text{Ru}^{\text{(IV)}}(\text{H})]^+$ from (o) to (w), or potential interactions between $\text{Cp}_2^*\text{Ru}^{\text{(III)}}$ and Cl^- that may facilitate Cl^- transfer from (w) to (o).

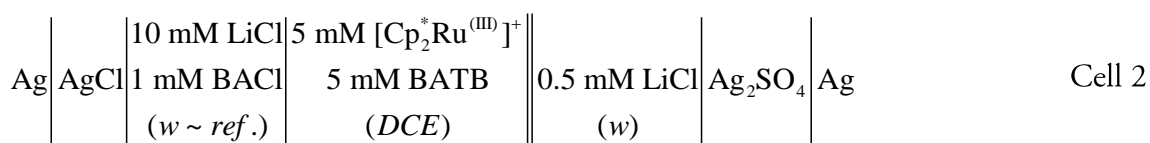
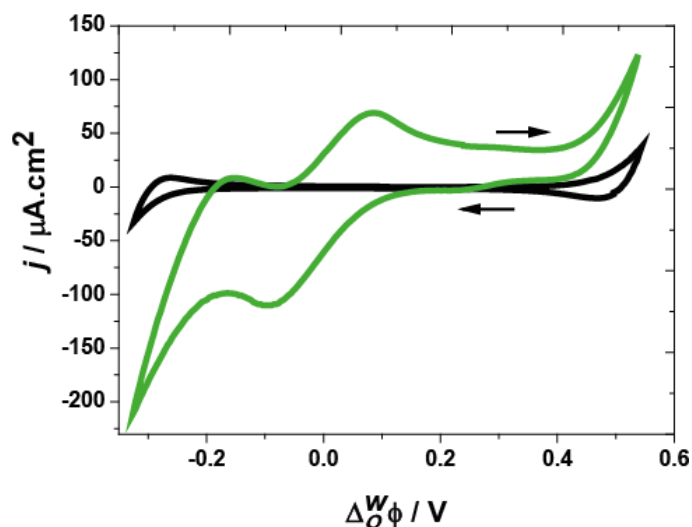


Figure 5.7. Experimental cyclic voltammograms recorded using Cell 2. With (green trace) and without (black trace) [Cp₂*Ru^(III)]⁺ dissolved in the DCE phase. All other instrument parameters were the same as in Figure 5.6.

5.2.2.2.2 Influence of chloride and hydrogen ions presence

In order to differentiate between these two possibilities, HCl was replaced by 5 mM of Li₂SO₄ and, subsequently, one drop of 0.5 M KCl solution was added (see Cell 3 and Figure 5.8). In the case of Cell 3 with Li₂SO₄, the CV was not affected by the presence of Cp₂*Ru^(II); this indicates that Li⁺ does not coordinate to Cp₂*Ru^(II) – nor do protons within its hydration sphere, as was recently discovered for Cp₂*Fe^(II).^{16,18} After addition of KCl, the potential window response narrowed owing to the reversible K⁺ and Cl[−] transfer at the positive and negative limits, respectively. No ion transfer wave was observed in the region of −0.280 V and a return peak was observed in the current-potential profile at the positive potential limit; therefore, one can conclude that Cl[−] does not interact with Cp₂*Ru^(II), at least in a manner observable by CV.

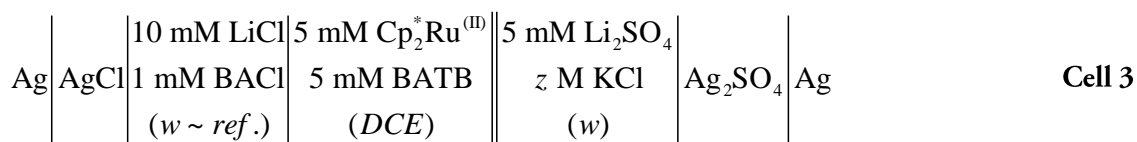
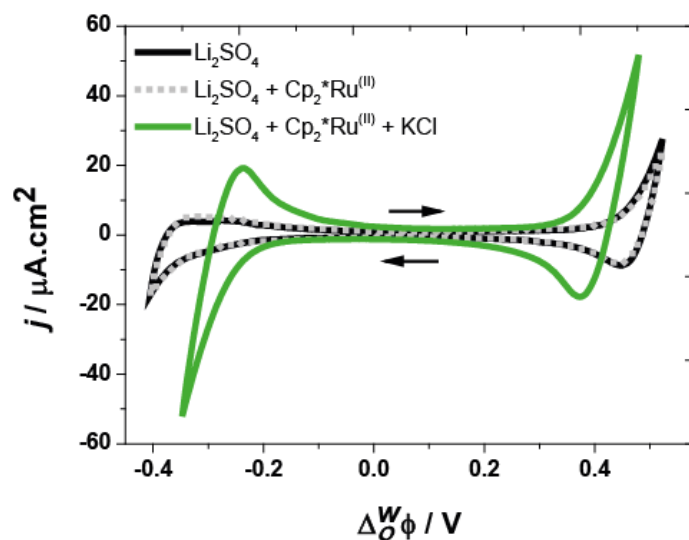
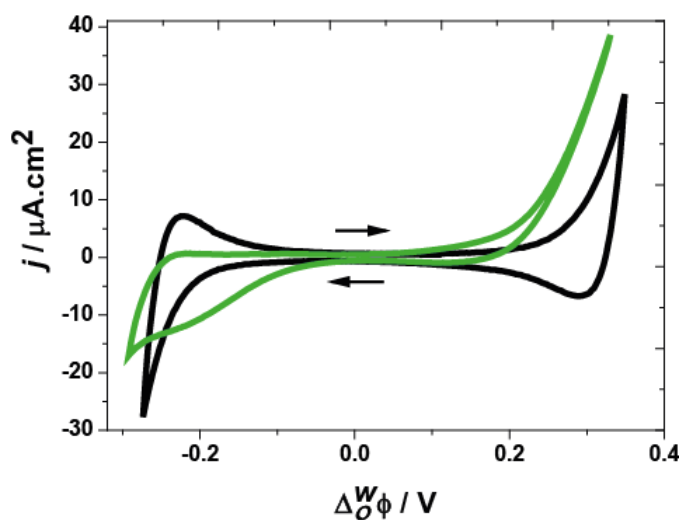


Figure 5.8. Experimental cyclic voltammograms recorded using Cell 3. With a drop of a solution of 0.5 M KCl added to the aqueous phase (green trace), without KCl (black trace) and without KCl and Cp₂*Ru^(III) (dashed curve). All other conditions were the same as in Figure 5.7.

5.2.2.2.3 Influence of counter ion of the aqueous acid at polarized w|DCE interfaces

However, when HCl (Cell 1) was replaced by H₂SO₄ (see Cell 4 and Figure 5.9.) the obtained CV generated a similar profile to that illustrated in Figure 5.6., *i.e.* irreversible proton transfer at the positive potential limit, as well as an asymmetric ion transfer wave at -0.280 V. Therefore, proton interaction with Cp₂*Ru^(III), generating [Cp₂*Ru^(IV)(H)]⁺, plays a key role in the observed CVs.



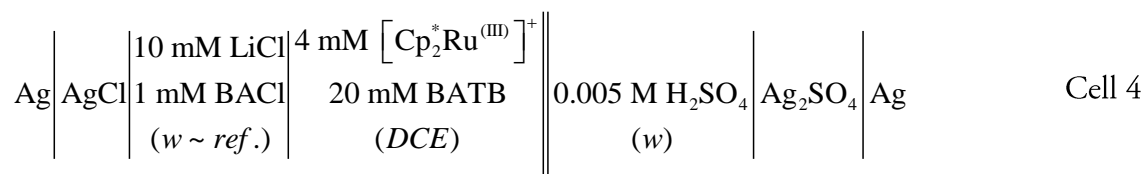


Figure 5.9. Cyclic voltammograms obtained using Cell 4. With (green trace) and without (black trace) $\text{Cp}_2^*\text{Ru}^{(\text{II})}$ dissolved in the DCE phase, along with 5 mM of H_2SO_4 in the aqueous phase. All other conditions were the same as in Figure 5.7.

5.2.2.2.4 Influence of the complexation rate of the hydride formation

To further explore the formation of $[\text{Cp}_2^*\text{Ru}^{(\text{IV})}(\text{H})]^+$, CVs were performed using Cell 5 and have been plotted in Figure 5.10. such that the concentration of $\text{Cp}_2^*\text{Ru}^{(\text{II})}$ in DCE was varied while $[\text{H}(\text{OEt}_2)_2]\text{TB}$ has been added to the organic phase. When the concentration of $[\text{H}(\text{OEt}_2)_2]\text{TB}$ is roughly equivalent to that of $\text{Cp}_2^*\text{Ru}^{(\text{II})}$ (*i.e.* 165 μM) the proton return peak is relatively unchanged relative to the blank trace (without HTB or $\text{Cp}_2^*\text{Ru}^{(\text{II})}$). However the transfer wave at $\Delta_o^w\phi_p \approx -0.280 \text{ V}$ is still present. Therefore, one can conclude that $[\text{Cp}_2^*\text{Ru}^{(\text{IV})}(\text{H})]^+$ is generated in the organic phase using dissolved $[\text{H}(\text{OEt}_2)_2]\text{TB}$ and that one equivalent of the acid is sufficient to fully convert $\text{Cp}_2^*\text{Ru}^{(\text{II})}$ to $[\text{Cp}_2^*\text{Ru}^{(\text{IV})}(\text{H})]^+$. Furthermore, as illustrated in Figure 5.10., the magnitude of the proton return peak decreases with increasing $\text{Cp}_2^*\text{Ru}^{(\text{II})}$ concentration as the $[\text{H}(\text{OEt}_2)_2]\text{TB}$ concentration remains static. One can consider as the $\text{Cp}_2^*\text{Ru}^{(\text{II})}$ concentration increases, the rate of complexation increases concomitantly (more $\text{Cp}_2^*\text{Ru}^{(\text{II})}$ are free to coordinate to protons) and the rate of dissociation decreases. This accounts for the decrease in magnitude of the proton return peak with a simultaneous increase in magnitude of the $[\text{Cp}_2^*\text{Ru}^{(\text{IV})}(\text{H})]^+$ transfer wave as the concentration of $\text{Cp}_2^*\text{Ru}^{(\text{II})}$ increases (Figure 5.10.). However, it was not possible to study the intensity of the current for the wave relative to $[\text{Cp}_2^*\text{Ru}^{(\text{IV})}(\text{H})]^+$ transfer quantitatively because the latter is highly sensitive to the proton concentration of the organic phase which is not stable owing to ITIES polarisation owing to the presence of $[\text{H}(\text{OEt}_2)_2]\text{TB}$.

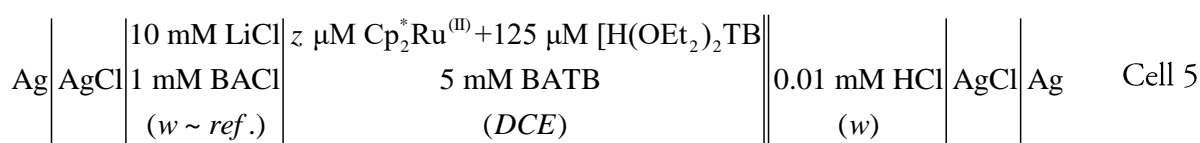
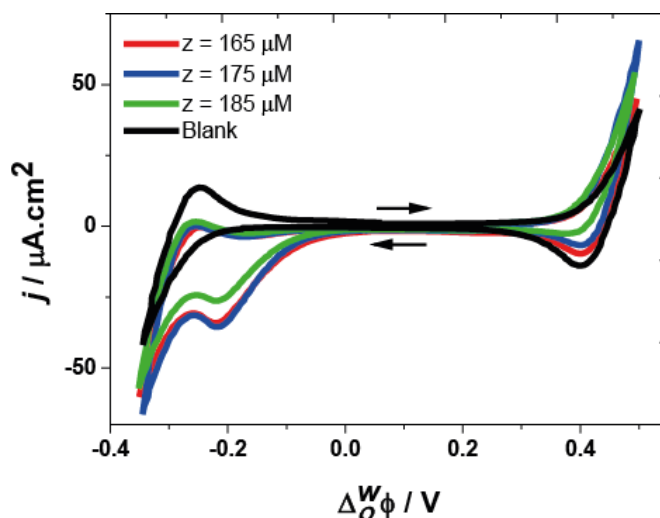


Figure 5.10. Cyclic voltammograms obtained using Cell 5. and z was varied as indicated while the blank curve (—) was acquired in the absence of $[\text{H}(\text{OEt}_2)_2]\text{TB}$ and $\text{Cp}_2^*\text{Ru}^{(\text{II})}$.

5.3 Mechanistic analysis using simulated voltammetric curves

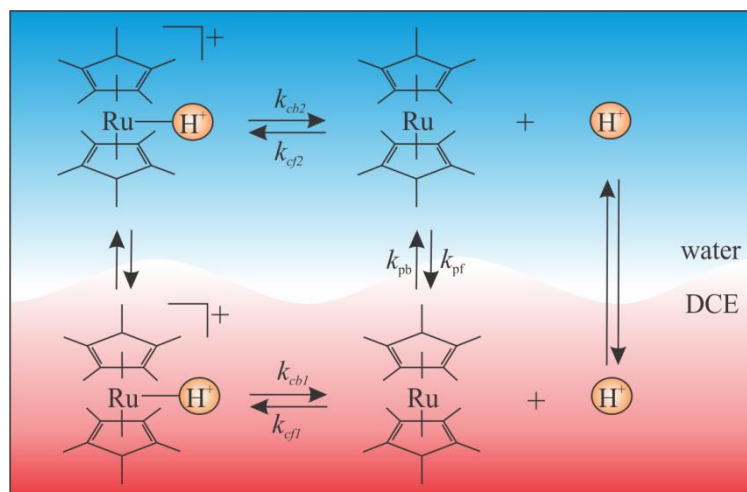


Figure 5.11. Biphasic decamethylruthenocene mechanism of hydride formation. The metal hydride is present in both aqueous and organic phases. The model includes potential dependent proton and $[\text{Cp}_2^*\text{Ru}^{(\text{IV})}(\text{H})]^+$ transfer steps as well as a potential independent partitioning of the neutral $\text{Cp}_2^*\text{Ru}^{(\text{II})}$ species.

In order to elucidate a possible reaction pathway, along with the associated kinetics/thermodynamics, a model was constructed within COMSOL Multiphysics software utilizing a simplified 1D geometry as described in detail elsewhere.¹⁴ Similar simulations have been employed to examine complex systems occurring at microelectrodes – indicating possible challenges with the use of ultramicroelectrodes,¹⁷ as well as the mechanistic elucidation and detection of short-

lived radical species coupled with scanning electrochemical microscopy.¹⁷ The diffusion of chemical species within the system was defined using Fick's laws, while the electrochemical flux of ions across the ITIES was defined using the Butler-Volmer series of equations as has been described previously.¹⁵ Further simulation details, along with the terms and coefficients, are provided in Chapter II, section 2.7.2.

The experimental data leads one to conclude that proton transfer is coupled to a bulk, organic phase reaction; whereby, protons are consumed in the organic phase and unavailable to undergo ion transport back across the ITIES – effectively generating an irreversible ion transfer process. With this in mind, the proposed mechanism (Figure 5.11.) includes a potential dependent proton transfer step followed by formation of the $[\text{Cp}_2^*\text{Ru}^{\text{(IV)}}(\text{H})]^+$. The ion transfer wave observed experimentally, at roughly -0.280 V, is dependent on the concentration of protons transferred (Figure 5.6(B)); therefore, one can conclude that it is associated with $[\text{Cp}_2^*\text{Ru}^{\text{(IV)}}(\text{H})]^+$. However, since this transfer wave is asymmetric (lacks a comparable return wave) and, as demonstrated by the shake-flask experiments for HER, is slow – relative to the timescale of the CV experiment – one can also conclude that the $[\text{Cp}_2^*\text{Ru}^{\text{(IV)}}(\text{H})]^+$ formed is not yet fully dissociated. Therefore, a potential dependent $[\text{Cp}_2^*\text{Ru}^{\text{(IV)}}(\text{H})]^+$ transfer step was explored in the model (rather than a $[\text{Cp}_2^*\text{Ru}^{\text{(III)}}]^+$ transfer step), followed by dissociation of the metal hydride in water – as the HER is not thermodynamically favoured in water – and finally partitioning of the neutral $\text{Cp}_2^*\text{Ru}^{\text{(III)}}$ species back to the organic phase.

5.3.1 Influence of the rate of $[\text{Cp}_2^*\text{Ru}^{\text{(IV)}}(\text{H})]^+$ formation in the organic phase

The effect of the rate of hydride formation was explored by systematically altering k_{cfl} (the rate of $[\text{Cp}_2^*\text{Ru}^{\text{(IV)}}(\text{H})]^+$ formation in the organic phase, see Figure 5.11.) and the resultant CVs have been plotted in Figure 5.12.; all other parameters were maintained as given in Table 2.2 in Chapter II. As k_{cfl} increases from $10^2 \text{ M}^{-1}\cdot\text{s}^{-1}$ up to $10^8 \text{ M}^{-1}\cdot\text{s}^{-1}$ (Figure 5.12 (A) and (B)) the ion transfer $[\text{Cp}_2^*\text{Ru}^{\text{(IV)}}(\text{H})]^+$ peak increases in magnitude from 0 to $-230 \mu\text{A}$. Simultaneously, the onset potential for proton transfer decreases and at k_{cfl} equal to $10^8 \text{ M}^{-1}\cdot\text{s}^{-1}$ an anodic peak was generated at ~ 0.410 V (Figure 5.12 B). This shift in the potential of protons transfer is due to the facilitated proton transfer, where protons coordinate to the $\text{Cp}_2^*\text{Ru}^{\text{(III)}}$ metal centre. Three mechanisms at the liquid|liquid interface have been recognized^{19,20}. As a reminder, the mechanism

of metallocene hydride formation can be regarded as an interfacial complexation reaction; whereby, the proton takes on the role of the ligand and coordinates to the metal centre of $\text{Cp}_2^*\text{Ru}^{\text{(II)}}$. Interfacial complexation reactions have been widely studied^{21,22} and offer insight into a possible mechanism for the ruthenocene hydride formation,^{19,23} either by transfer through interfacial complexation/decomplexation (TIC/TID); transfer of the proton, followed by organic phase complexation (TOC); or aqueous phase complexation, then transfer (ACT). Owing to the hydrophobicity of $\text{Cp}_2^*\text{Ru}^{\text{(II)}}$ and the dependence of the transfer wave at -0.280 V on the amount of protons transferred, as demonstrated in Figure 5.6 (B), as well as the need for a phase transfer catalyst in the shake flask experiments, a spontaneous ACT mechanism can be excluded. The effective ACT pathway included in Figure 5.11. is dependent on the hydride formation in the organic phase. Only then is a potential dependent $[\text{Cp}_2^*\text{Ru}^{\text{(IV)}}(\text{H})]^+$ transfer step possible; whereby, the externally applied Galvani potential difference is the driving force. For simplicity, the TIC/TID mechanism was not initially considered; however, is a possible mechanism, but unlikely since the shake-flask experiments required electrochemical polarisation in order to elicit H_2 production.

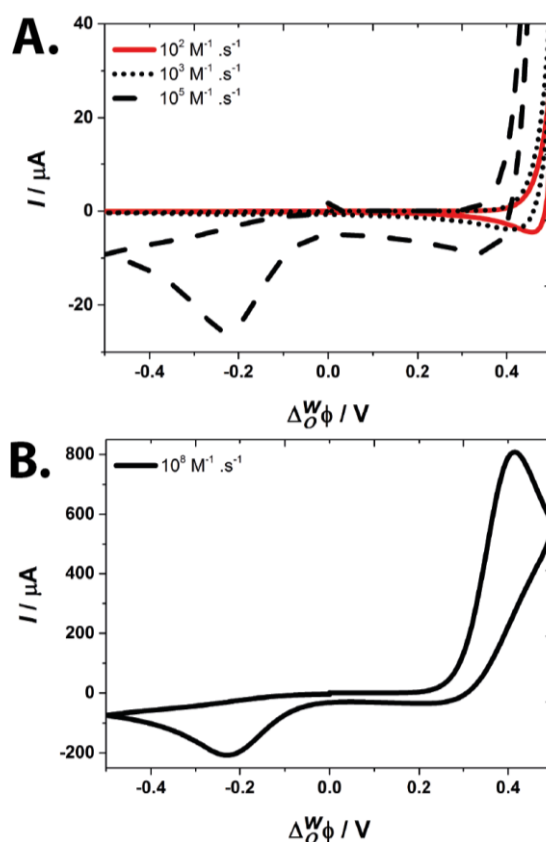


Figure 5.12. Simulated CVs generated using the mechanism illustrated in Figure 5.11. and using the parameters listed in Table 2.2, except that k_{fl} has been varied as indicated and $c_{\text{H}^+,aq}^*$ was maintained at 1 mM.

5.3.2 Simulation of the facilitated proton transfer

In order to elucidate this point further, a two-step EC (electrochemical, E, chemical, C) mechanism, with a potential dependent ion transfer step (E) of a generic species (i^{z+}) followed by an irreversible complexation step C, was employed, as provided below, within a similar simulation geometry:



In this comparatively simple system, the neutral ligand (L) is considered hydrophobic and does not undergo transfer across the ITIES with the same being true of the ion-ligand complex (iL^{z+}). The resulting CVs are given in Figure 5.13. with the formal ion transfer potential of i^{z+} , $\Delta_o^w \phi_{i^z}^{o'}$, set arbitrarily equal to 0.250 V.

As the rate of complexation increases, the half-wave potential decreases for the transfer of i^{z+} and the ion transfer wave becomes asymmetric (the ‘cathodic’ component disappears). This is in good agreement with the theory of facilitated ion transfer as has been previously established.^{19,23-25} This also serves to further illustrate that the lack of an observable proton transfer return peak within the edge of scan profile of the CV (Figure 5.6.(A)) can be satisfied by the irreversible coordination of protons to $\text{Cp}_2^*\text{Ru}^{(\text{II})}$.

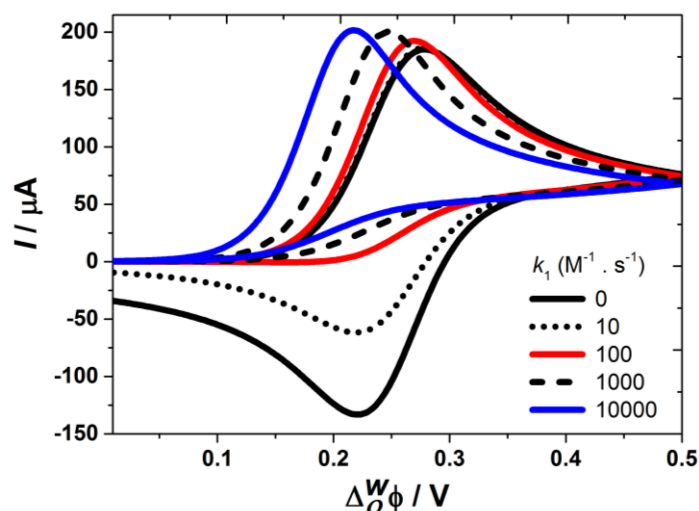


Figure 5.13. Simulated cyclic voltammograms generated using the EC mechanism (equation (5.1) and (5.2), above); here, the rate, k_1 , of the complexation step has been altered as indicated inset. The formal ion

transfer potential of \tilde{r}^z was 0.250 V, with $D_{i,w} = D_{i,o} = 1 \times 10^{-5} \text{ cm}^2 \cdot \text{s}^{-1}$, $c_{i,w} = 1 \text{ mmol} \cdot \text{L}^{-1}$, $c_{i,o} = 0 \text{ mmol} \cdot \text{L}^{-1}$, $L_o = 5 \text{ mmol} \cdot \text{L}^{-1}$, and $\nu = 0.020 \text{ V} \cdot \text{s}^{-1}$.

5.3.3 Influence of the rate of $[\text{Cp}_2^*\text{Ru}^{(\text{IV})}(\text{H})]^+$ dissociation in the organic phase

The effect of increasing k_{cb1} (the rate of $[\text{Cp}_2^*\text{Ru}^{(\text{IV})}(\text{H})]^+$ dissociation in the organic phase, Figure 5.11.) was also examined and the generated CVs have been plotted in Figure 5.14. With increasing k_{cb1} from 1 to 10 s^{-1} , the concentration of $[\text{Cp}_2^*\text{Ru}^{(\text{IV})}(\text{H})]^+$ in the vicinity of the interface decreases, the return peak for proton transfer re-emerges, and the cathodic wave for $[\text{Cp}_2^*\text{Ru}^{(\text{IV})}(\text{H})]^+$ transfer, (o) to (w), at -0.200 V decreases concomitantly. This demonstrates that the rate of complexation is high and effectively irreversible – *i.e.* negligible decomplexation.

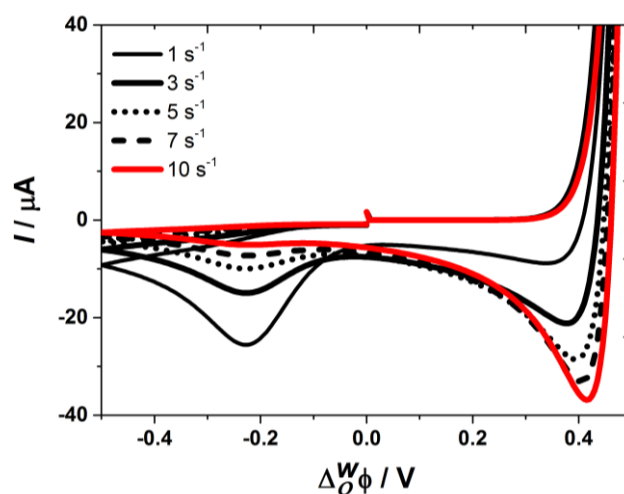


Figure 5.14. Simulated CVs employing the mechanism drawn in Figure 5.11. k_{cb1} was varied as indicated, inset; all other parameters are the same as those listed in Table 2.2.

5.3.4 Influence of the rate of $[\text{Cp}_2^*\text{Ru}^{(\text{IV})}(\text{H})]^+$ dissociation in the aqueous phase

Subsequently, the analogous reaction was investigated in the bulk aqueous phase by first examining the rate of decomplexation, k_{cb2} (Figure 5.11). Figure 5.15 illustrates that as k_{cb2} increases, from 50 to 10^8 s^{-1} , the half-wave potential of the cathodic wave shifts to more positive potentials, from -0.447 to -0.197 V , for the red and blue curves respectively, such that $k_{cb2} = 10 \text{ s}^{-1}$ provides a half-wave potential of -0.280 V . Half-wave potentials, $\Delta_o^w\phi_{1/2}$, have been calculated using the $[\text{Cp}_2^*\text{Ru}^{(\text{IV})}(\text{H})]^+$ transfer peak potential, $\Delta_o^w\phi_{p,c}$, and the following relationship: $\Delta_o^w\phi_{1/2} = \Delta_o^w\phi_p + (0.028 \text{ V})/z$; ²⁶ however, the ion transfer peaks in Figure 5.15 demonstrate a peak broadening with increasing k_{cb2} . For k_{cb2} equal to 50, 100, 1000, 10^5 , and 10^8 s^{-1} the peak width at -4 μA increases from 0.075 V to 0.080 , 0.090 , 0.105 , and 0.120 V , respectively. Additionally, the peak current intensity increases negatively until k_{cb2} equal to 10^5 s^{-1} , after which it decreases (Figure

5.15 (B)). The formal ion transfer potential for $[\text{Cp}_2^*\text{Ru}^{\text{(IV)}}(\text{H})]^+$ was approximated to be -0.500 V, which is just beyond the polarizable potential window (PPW). The simulated curves in Figure 5.15 (A) illustrate that the transfer potential of $[\text{Cp}_2^*\text{Ru}^{\text{(IV)}}(\text{H})]^+$ is effected in a similar way by the change of the aqueous decomplexation rate as the protons transfer potential was by k_{cf1} . That is, with increasing k_{cb2} the half-wave potential of $[\text{Cp}_2^*\text{Ru}^{\text{(IV)}}(\text{H})]^+$ shifts to more positive potentials. However, while altering k_{cb2} influences $[\text{Cp}_2^*\text{Ru}^{\text{(IV)}}(\text{H})]^+$ transfer, it does not alter the proton transfer potential; likewise, changing k_{cf1} does not impact the potential of $[\text{Cp}_2^*\text{Ru}^{\text{(IV)}}(\text{H})]^+$ transfer (Figure 5.12). Indeed, results obtained experimentally with Cell 5 (see above) show that when the $\text{Cp}_2^*\text{Ru}^{\text{(III)}}$ concentration and consequently, k_{cf1} and k_{cb1} , vary in the organic phase, the potential of $[\text{Cp}_2^*\text{Ru}^{\text{(IV)}}(\text{H})]^+$ transfer remains constant. Moreover, the potential of the proton transfer appeared dependant of k_{cf1} and k_{cb1} . The potentials switch to more negative values when more $\text{Cp}_2^*\text{Ru}^{\text{(III)}}$ are present because the transfer is facilitated by the proton complexation with the metallocene. However, like as was shown by simulation, the transfer potential is not expected to be dependant of k_{cf2} and k_{cb2} because the quantity of protons provided by $[\text{Cp}_2^*\text{Ru}^{\text{(IV)}}(\text{H})]^+$ is negligible compared to the amount of free protons in the aqueous phase. Therefore, the resulting simulated CVs are in good agreement with the phenomena observed experimentally (see Figure 5.10).

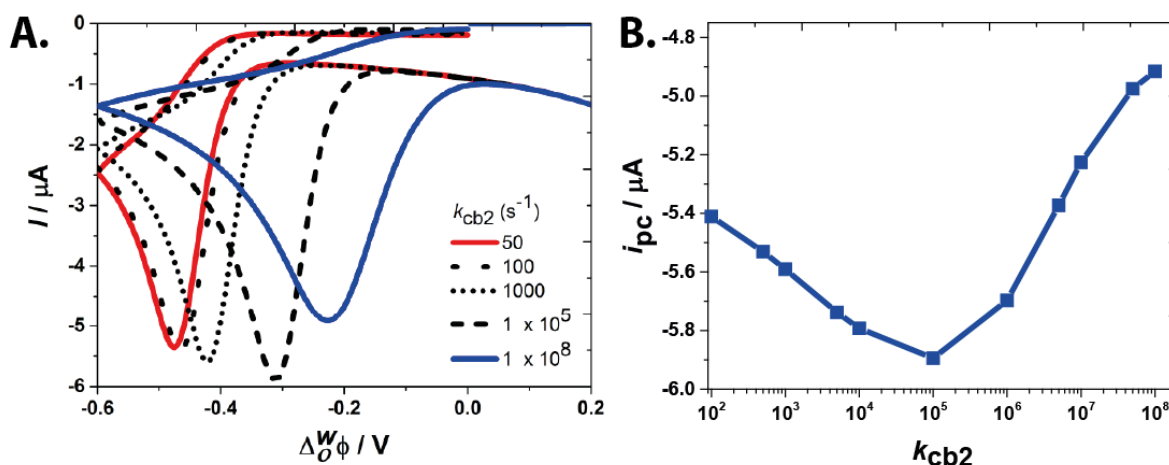


Figure 5.15. (A) CVs traces obtained using the simulation described in section 2. All parameters are the same as those described in Table 2.2 ($c_{\text{H}^+,aq}^* = 1 \text{ mM}$); however, here k_{cb2} has been altered as indicated inset. (B) Plot of the $[\text{Cp}_2^*\text{Ru}^{\text{(IV)}}(\text{H})]^+$ transfer peak current intensity versus k_{cb2} from (A).

5.3.5 Influence of the rate of $[\text{Cp}_2^*\text{Ru}^{\text{IV}}(\text{H})]^+$ association in the aqueous phase

Moving forward, k_{cf2} was iteratively altered while the other rate constants were maintained (Table 2.2); the resultant, simulated CVs have been plotted in Figure 5.16. As k_{cf2} increases, the stability of $[\text{Cp}_2^*\text{Ru}^{\text{IV}}(\text{H})]^+$ in the aqueous phase increases and, as k_{cf2} approaches k_{cb2} , the CVs become more reversible with an anodic wave becoming visible at $1000 \text{ M}^{-1}\cdot\text{s}^{-1}$ and continues to increase in anodic current intensity until $1 \times 10^5 \text{ M}^{-1}\cdot\text{s}^{-1}$. Simultaneously, the half-wave potential for $[\text{Cp}_2^*\text{Ru}^{\text{IV}}(\text{H})]^+$ decreased until $1 \times 10^8 \text{ M}^{-1}\cdot\text{s}^{-1}$, where it equals approximately the arbitrary value set in the simulation parameters.

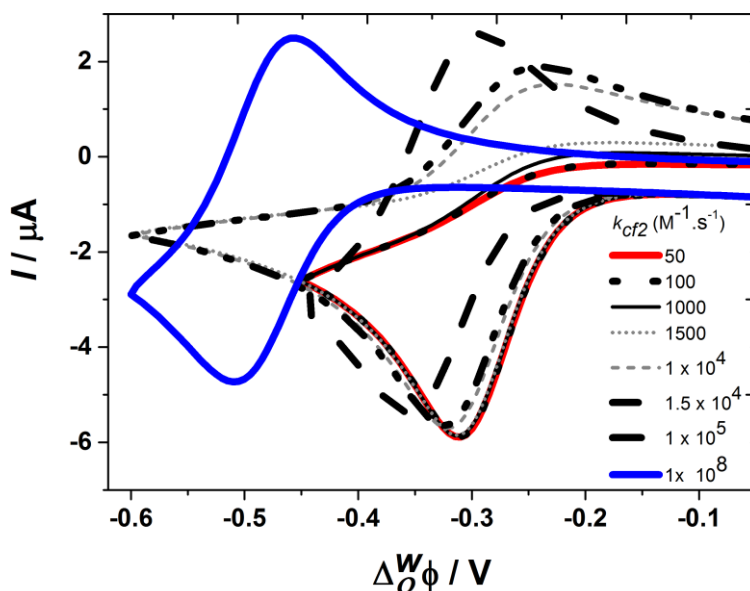


Figure 5.16. Simulated CV curves generated using the parameters given in Table 2.2, but with k_{cf2} augmented as indicated; $c_{\text{H}^+,aq}^* = 1 \text{ mM}$ and $k_{cb2} = 1 \times 10^5 \text{ s}^{-1}$.

The simulated data in Figure 5.15. and Figure 5.16 indicate that the aqueous reaction heavily favours the dissociation of $[\text{Cp}_2^*\text{Ru}^{\text{IV}}(\text{H})]^+$, therefore, based on the shift in the $[\text{Cp}_2^*\text{Ru}^{\text{IV}}(\text{H})]^+$ half-wave potential and the asymmetry of the anodic peak (or lack thereof) a value of k_{cf2} and k_{cb2} has been estimated to be $100 \text{ M}^{-1}\cdot\text{s}^{-1}$ and $1 \times 10^8 \text{ s}^{-1}$, respectively.

5.4 Conclusions

This chapter demonstrated $\text{Cp}_2^*\text{Ru}^{\text{III}}$ can act as a sacrificial electron donor to produce H_2 at polarised interfaces under light illumination employing DCE or TFT solvents.

The formation of $[\text{Cp}_2^*\text{Ru}^{\text{(IV)}}(\text{H})]^+$ at the w|DCE interface was investigated through cyclic voltammetry and subsequent comparison to simulated CVs generated using COMSOL Multiphysics software in order to elucidate the kinetics/thermodynamics. The proposed pathway follows a modified EC mechanism that involves a potential dependent proton transfer step (E), from (w) to (o), followed by favourable $[\text{Cp}_2^*\text{Ru}^{\text{(IV)}}(\text{H})]^+$ formation in the DCE phase (C). The HER is slow, however, and on the time scale of CV the $[\text{Cp}_2^*\text{Ru}^{\text{(IV)}}(\text{H})]^+$ transfers as the Galvani potential difference is swept to negative potentials (an asymmetric cathodic wave was observed) and rapidly dissociates in water. This is evidenced by two curve features in the recorded CVs: an irreversible transfer wave at the limit of the PPW for protons, along with the irreversible transfer wave at roughly -0.280 V that has been herein identified as $[\text{Cp}_2^*\text{Ru}^{\text{(IV)}}(\text{H})]^+$ transfer. This is the first time an irreversible ion transfer wave has been observed in relation to metallocene hydride formation at a liquid|liquid interface and is attributed to the slow rate of reaction relative to other metallocene analogs.

The shake-flask/GC experimental data corroborates those recorded using CV, as well as the postulated mechanism, in that $\text{Cp}_2^*\text{Ru}^{\text{(II)}}$ oxidation and H_2 production were only observed when both ITIES were polarised and the samples were illuminated. This indicates that the $[\text{Cp}_2^*\text{Ru}^{\text{(IV)}}(\text{H})]^+$ formation is a bulk organic phase reaction and also requires the formation of a $(\text{Cp}_2^*\text{Ru}^{\text{(II)}})^*$ or $([\text{Cp}_2^*\text{Ru}^{\text{(IV)}}(\text{H})]^+)^*$ excited species.

Furthermore, the investigations on the effect of the rate of hydride formation explain the irreversible nature of the proton transfer when the hydride is stable and that the cathodic irreversible peak, observed in the CV and never seen before with other metallocenes, can be attributed to $[\text{Cp}_2^*\text{Ru}^{\text{(IV)}}(\text{H})]^+$ transfer. The effect of the rate of hydride formation and dissociation was explored confirming that the rate of complexation is high ($\sim 10^5 \text{ M}^{-1}\cdot\text{s}^{-1}$), as confirmed through the simulations, and irreversible in the DCE phase. In contrast, the absence of an associated anodic peak related to $[\text{Cp}_2^*\text{Ru}^{\text{(IV)}}(\text{H})]^+$ transfer from (w) to (o), is due to the spontaneous decomplexation of the hydride in water which was determined to occur at a rate of $\sim 10^5 \text{ s}^{-1}$, while a rate of aqueous complexation was also estimated to be $100 \text{ M}^{-1}\cdot\text{s}^{-1}$. Furthermore, the transfer potential of the hydride is affected by the rate of the decomplexation of the hydride in the aqueous phase; however, it does not alter the proton transfer potential. Likewise, changing the rate of formation of the

hydride in DCE phase does not impact the potential transfer of $[\text{Cp}_2^*\text{Ru}^{\text{(IV)}}(\text{H})]^+$ transfer, but does influence the proton transfer potential.

This study proves the viability to perform photo-HER in batch-water splitting with $\text{Cp}_2^*\text{Ru}^{\text{(II)}}$. Next Chapter goes deeper inside the spectroscopic phenomena involved and characterize the formation of $[\text{Cp}_2^*\text{Ru}^{\text{(IV)}}(\text{H})]^+$ at the interface.

5.5 References

- (1) Méndez, M. A.; Partovi-Nia, R.; Hatay, I.; Su, B.; Ge, P. Y.; Olaya, A.; Younan, N.; Hojeij, M.; Girault, H. H. *Physical. Chemistry. Chemical. Physics*. **2010**, *12*, 15163.
- (2) Hung, L. Q. *J. Electroanalytical Chemistry*. **1980**, *115*, 159.
- (3) Du, P.; Schneider, J.; Luo, G.; Brennessel, W. W.; Eisenberg, R. *Inorganic Chemistry* **2009**, *48*, 4952.
- (4) Liu, T.; DuBois, D. L.; Bullock, R. M. *Nature Chemistry* **2013**, *5*, 228.
- (5) Naota, T.; Takaya, H.; Murahashi, S.-I. *Chem. Rev. (Washington, D. C.)* **1998**, *98*, 2599.
- (6) Nalesnik, T. E.; Freudenberg, J. H.; Orchin, M. *J. Organometallic Chemistry* **1982**, *236*, 95.
- (7) Hatay, I.; Ge, P. Y.; Vrubel, H.; Hu, X.; Girault, H. H. *Energy Environ. Sci.* **2011**, *4*, 4246.
- (8) Ge, P.; Todorova, T. K.; Patir, I. H.; Olaya, A. J.; Vrubel, H.; Mendez, M.; Hu, X.; Corminboeuf, C.; Girault, H. H. *Proceedings of the National Academy of Sciences* **2012**, *109*, 11558.
- (9) Ge, P.; Olaya, A. J.; Scanlon, M. D.; Hatay Patir, I.; Vrubel, H.; Girault, H. H. *ChemPhysChem* **2013**, *14*, 2308.
- (10) Rivier, L.; Vannay, L.; Méndez, M. A.; Peljo, P.; Scanlon, M. D.; Corminboeuf, C.; Girault, H. H. **2017**, Submitted.
- (11) Olaya, A. J.; Ge, P.; Girault, H. H. *Electrochemical Communication* **2012**, *19*, 101.
- (12) Adamiak, W.; Jedraszko, J.; Krysiak, O.; Nogala, W.; Hidalgo-Acosta, J. C.; Girault, H. H.; Opallo, M. *Journal of Physical Chemistry C* **2014**, *118*, 23154.
- (13) Trojánek, A.; Langmaier, J.; Samec, Z. *Electrochimica Acta* **2012**, *82*, 457.
- (14) Deng, H.; Stockmann, T. J.; Peljo, P.; Opallo, M.; Girault, H. H. *Journal of Electroanalytical. Chemistry* **2014**, *731*, 28.
- (15) Stockmann, T. J.; Deng, H.; Peljo, P.; Kontturi, K.; Opallo, M.; Girault, H. H. *J. Electroanalytical Chemistry*. **2014**, *729*, 43.
- (16) Deng, H.; Peljo, P.; Stockmann, T. J.; Qiao, L.; Vainikka, T.; Kontturi, K.; Opallo, M.; Girault, H. H. *Chemical Communication* **2014**, *50*, 5554.
- (17) Lin, C.; Compton, R. G. *J. Electroanalytical Chemistry*. **2015**, *743*, 86.
- (18) Cao, F.; Kim, J.; Bard, A. J. *Journal of the American Chemical. Society*. **2014**, *136*, 18163.
- (19) Peljo, P.; Girault, H. H. In *Encyclopedia of Analytical Chemistry*; John Wiley & Sons, Ltd: 2012.
- (20) Liu, S.; Li, Q.; Shao, Y. *Chem. Soc. Rev.* **2011**, *40*, 2236.
- (21) Stockmann, T. J.; Zhang, J.; Montgomery, A.-M.; Ding, Z. *Analytical Chimica Acta* **2014**, *821*, 41.
- (22) Nestor, U.; Wen, H.; Girma, G.; Mei, Z.; Fei, W.; Yang, Y.; Zhang, C.; Zhan, D. *Chemical Communication* **2014**, *50*, 1015.
- (23) Samec, Z.; Langmaier, J.; Kakiuchi, T. *Pure Applied Chemistry* **2009**, *81*, 1473.
- (24) Reymond, F.; Lagger, G.; Carrupt, P.-A.; Girault, H. H. *Journal Electroanalytical Chemistry* **1998**, *451*, 59.

- (25) Girault, H. In *Electroanalytical Chemistry*, Bard, A. J., Zoski, C. G., Eds.; CRC Press: 2010, p 1.
- (26) Bard, A. J.; Faulkner, L. R. *Electrochemical Methods: Fundamentals and Applications*, 2nd ed.; John Wiley: New York, 2001.

6. Photo-induced Decamethylruthenocene Hydride: a key intermediate to understand photo production of H₂ by metallocenes

6.1	Introduction	132
6.2	Spectroscopy and photochemistry of [Cp ₂ *Ru ^(IV) (H)] ⁺	132
6.2.1	Hydride formation: UV/vis investigations	132
6.2.2	Wavelength dependence of the excitation of [Cp ₂ *Ru ^(IV) (H)] ⁺	134
6.2.3	Computed absorption spectrum of [Cp ₂ *Ru ^(IV) (H)] ⁺	135
6.3	Clarification of the excitation photo-process involved in the mechanism	137
6.4	Second Harmonic Generation	138
6.4.1	Historical background of second harmonic generation	139
6.4.2	General strengths and limitations of second harmonic generation measurements.	140
6.4.3	Application of SHG to the study of assisted proton transfer	141
6.4.3.1	Experimental set-up	141
6.4.3.2	Preliminary results.....	142
6.4.3.3	Limitation and possibilities.....	145
6.5	Conclusions.....	146
6.6	References.....	148

6.1 Introduction

The protonation of the metal to form a hydride species is generally accepted as a key intermediate in the formation of H_2 .^{1,2} Indeed, the basicity of the metal has to be sufficient to allow the coordination of a proton on the metal center but at the same time, the formed bond should not be too strong as to hamper the elimination of H_2 . Thus, characterization of the hydride is critical but it was often obstructed due to their high reactivity. However, $[Cp_2^*Ru^{(IV)}(H)]^+$ has shown a high stability in the dark as a photo-activation is required to produce H_2 . Consequently, it was possible to study it dissolved in single phase by 1H NMR in chapter III and at liquid|liquid interfaces in Chapter V. In this chapter, we go in further into details by applying different spectroscopic methods in both single and a two-phase system.

Herein, spectroscopic measurements were performed to characterise $[Cp_2^*Ru^{(IV)}(H)]^+$ dissolved in single phase by UV/vis spectroscopy and at liquid|liquid interfaces by second harmonic generation (SHG). Spectroscopic characterisations provided information to clarify the excitation photo-process mechanism for the photo-hydrogen evolution by $Cp_2^*Ru^{(II)}$. The excitation wavelength of $[Cp_2^*Ru^{(IV)}(H)]^+$ was determined and results were corroborated by DFT calculations. Furthermore, the formation of $[Cp_2^*Ru^{(IV)}(H)]^+$ at the w|DCE interface was probed in depth.

6.2 Spectroscopy and photochemistry of $[Cp_2^*Ru^{(IV)}(H)]^+$

The protonation at the metal to form the cationic hydride in the dark was monitored by 1H NMR spectroscopy in Chapter III. Herein, the investigation metal hydride formation was pursued by UV/vis spectroscopy. Thereafter, the excitation wavelength was determined with information provided by the UV/vis characterization.

6.2.1 Hydride formation: UV/vis investigations

Spectroscopic characterization of the conversion of $Cp_2^*Ru^{(II)}$ to $[Cp_2^*Ru^{(IV)}(H)]^+$ with $[H(OEt_2)_2]TB$ organic acid, illustrated in Figure 6.1 (A), showed the appearance of a main absorption band at 243 nm as well as a broad absorption in the near-UV (between 300 and 350 nm). However, no isosbestic point was observed due to the absorption of $[H(OEt_2)_2]TB$ in this region (see Figure 6.2). To confirm the formation of $[Cp_2^*Ru^{(IV)}(H)]^+$ as a unique product, the titration was repeated with CF_3SO_3H , which does not absorb UV light (see Figure 6.1 (B)). In this case, a clear isosbestic point was observed at 231 nm. The main absorption band did not shift as

function of the counter ion of the acid and was still observed at 243 nm. Inconveniently, it appeared that the equilibrium constant of the reaction was dependent of the quantity of acid added for both acids. These results are in agreement with the NMR data recorded in Chapter III, Section 3.3.1.2. They indicated the formation of ion pairing and/or homo-association during the reaction. However, UV/vis spectroscopy data give new indications to precise the type of species present. Indeed, the main absorption band did not shift as function of the acid. It is a strong evidence that the counter ion is not involved in the formation of new species. Therefore, the formation of ion pairing can be excluded and presence of homo-association during the reaction is more likely.

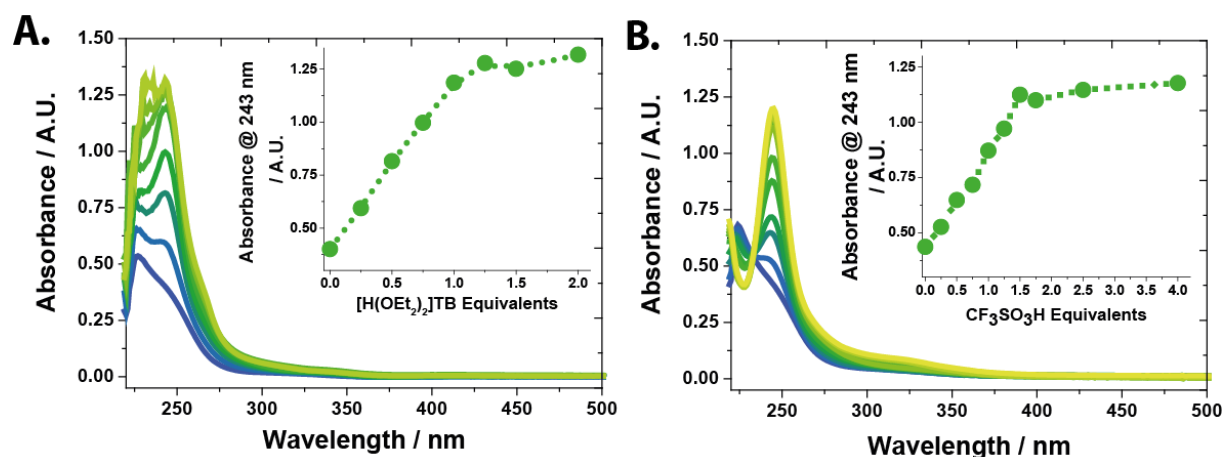


Figure 6.1. Metal hydride formation followed by UV/vis spectroscopy. The conversion of $\text{Cp}_2^*\text{Ru}^{\text{III}}$ (50 μM) to $[\text{Cp}_2^*\text{Ru}^{\text{IV}}(\text{H})]^+$ was monitored by UV/vis spectroscopy in the dark in the presence of various concentration of (A) $[\text{H}(\text{OEt}_2)_2]\text{TB}$ and (B) $\text{CF}_3\text{SO}_3\text{H}$. Inset, the absorbance at 243 nm corresponding to the appearance of $[\text{Cp}_2^*\text{Ru}^{\text{IV}}(\text{H})]^+$.

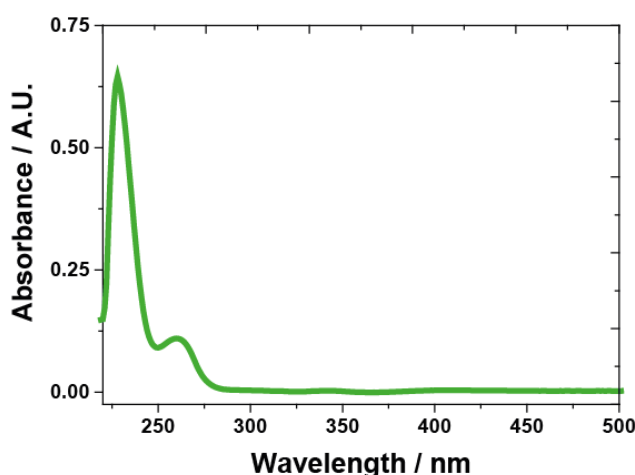


Figure 6.2. UV/vis spectrum of $[\text{H}(\text{OEt}_2)_2]\text{TB}$ organic acid. UV/vis spectrum recorded for a solution of 80 μM $[\text{H}(\text{OEt}_2)_2]\text{TB}$ in DCE.

6.2.2 Wavelength dependence of the excitation of $[\text{Cp}_2^*\text{Ru}^{\text{(IV)}}(\text{H})]^+$

The influence of the excitation wavelength was investigated to characterize the transition involved in the photo-reaction. A study was performed to analyse the IQY of the photo-reaction as a function of the wavelength of illumination. A maximum yield of 37 % was achieved at 243 nm corresponding to the maximum absorbance band of $[\text{Cp}_2^*\text{Ru}^{\text{(IV)}}(\text{H})]^+$ (Figure 6.3). This result firmly confirms that the mechanism involves the excitation of the hydride in the first stage of the reaction. The yield was divided by three at 229 nm and also decreased in the near UV region ($300 \text{ nm} < \lambda < 400 \text{ nm}$). No H_2 or $[\text{Cp}_2^*\text{Ru}^{\text{(III)}}]^+$ production was observed at 455 nm. Although care was taken to ensure a good illumination of the sample, the quantum yield obtained at 365 nm with a laser (*ca.* 7 %) is smaller than the one determined with an LED source (*ca.* 25 %). This can result from the different conditions of the experiment as well as the use of polarised laser light. Indeed, molecules which are oriented in such a way that their transition dipole moment is parallel to the k vector of the incident photons (and perpendicular to the plane of the polarisation vectors) are not excited.³ Herein, the cell was prepared inside the glove box and, taken out to be illuminated with the laser light. Thus, the cell may have been slightly contaminated by atmospheric O_2 (visible by GC). Consequently, a higher quantity of $[\text{Cp}_2^*\text{Ru}^{\text{(III)}}]^+$ was observed with UV/vis in comparison to the amount of H_2 detected with GC. Hence, UV/vis measurements show higher IQY than the GC measurements due to the production of $[\text{Cp}_2^*\text{Ru}^{\text{(III)}}]^+$ by the reduction of O_2 upon laser irradiation. Indeed, this reaction is thermodynamically more favourable than the reduction of a proton and the two reactions compete.^{4,5}

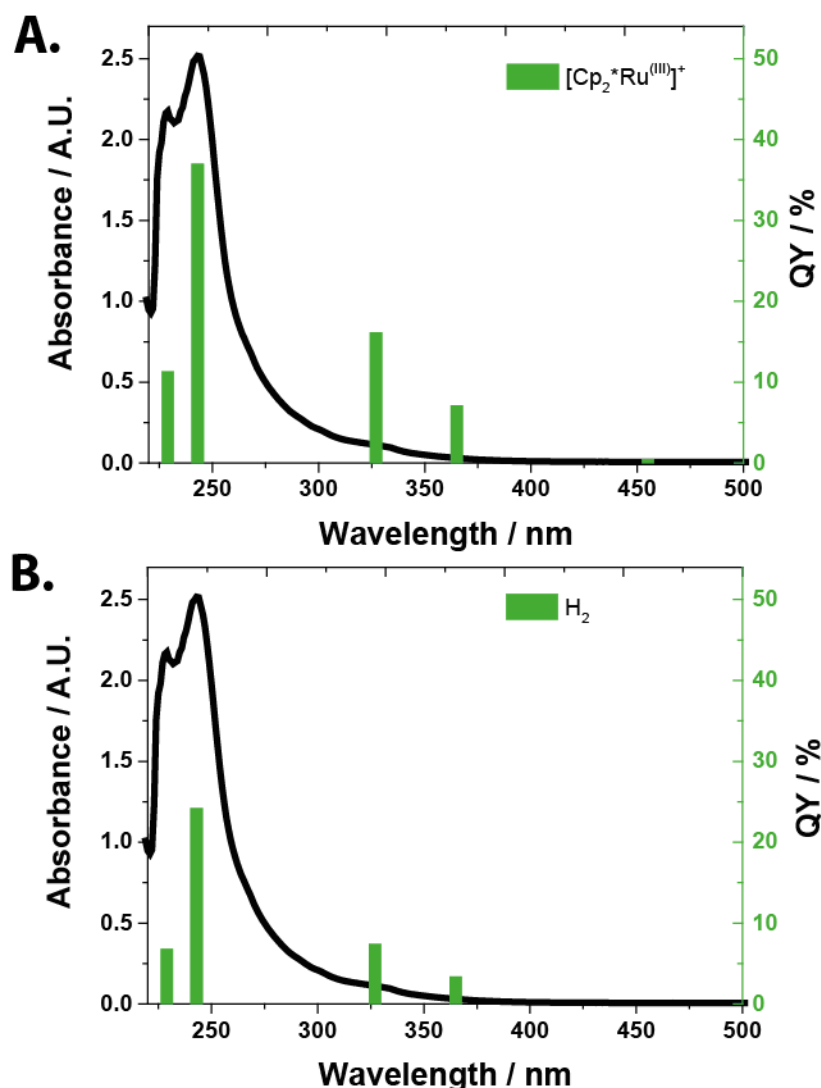


Figure 6.3. Wavelength dependence of the HER by $\text{Cp}_2^*\text{Ru}^{(\text{III})}$ as a function of the wavelength excitation. A solution of 6 mM $\text{Cp}_2^*\text{Ru}^{(\text{II})}$ with 12 mM $[\text{H}(\text{OEt}_2)_2]\text{TB}$ was prepared inside a glove box, sealed with a septa and illuminated outside the glove box under stirring conditions for 10 min. at various wavelengths. The power was modulated in order to keep the number of emitted photon constant and equal to 1.8 μmol . The EQY was obtained by determining the quantity of (A) $[\text{Cp}_2^*\text{Ru}^{(\text{III})}]^+$ produced by UV/visible spectroscopy and (B) H_2 produced by GC. Results are compared with the $[\text{Cp}_2^*\text{Ru}^{(\text{IV})}(\text{H})]^+$ spectrum (black line).

6.2.3 Computed absorption spectrum of $[\text{Cp}_2^*\text{Ru}^{(\text{IV})}(\text{H})]^+$.

DFT calculations were obtained in collaboration with Prof. Cl  mence Corminboeuf. The absorption spectrum of $[\text{Cp}_2^*\text{Ru}^{(\text{IV})}(\text{H})]^+$ was computed at the TD-  B97X-D/def2-TZVP level^{6,7} using the first 20 singlets excitation and a SMD solvation model⁸ for 1,2-dichloroethane ($\epsilon=10.125$). The geometry was optimized in the gas phase at the M06/def2-TZVP level.⁹ The natural transition orbitals¹⁰ and electron density difference are given below for the most intense

absorption band ($\lambda=227$ nm). The excited state density was obtained by adding to the converged DFT wave function the necessary Z-vector contribution derived from a coupled-perturbed Kohn-Sham (CPKS) calculation for state N .^{11,12} All computations were performed using Gaussian'09.¹³

The absorption spectrum computed at the TD- ω B97X-D level (Figure 6.4) shows a main band dominated by one transition at 227 nm. The result is in agreement with the experimental spectrum. The theoretical band at 227 nm induces an electronic enrichment on the hydride position after excitation (Figure 6.5). The contributions of the orbitals are mixed making the assignment cumbersome (Table 6.1). Nonetheless, the results seem consistent with a ligand to metal electron transfer character of the transition. Under excitation, the electronic density shift to the metal-hydride leading to weakening the bond. Thus, release of H_2 becomes thermodynamically more favourable.

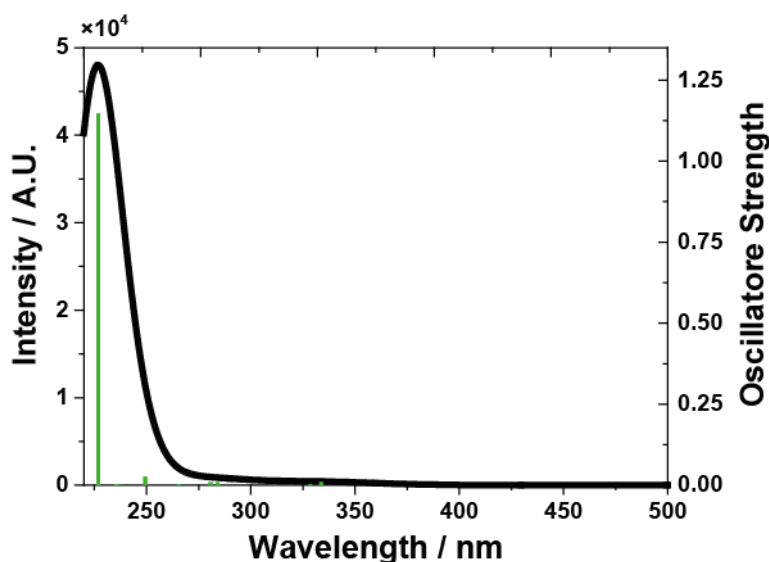


Figure 6.4. The absorption spectrum of $[Cp_2^*Ru^{(IV)}(H)]^+$ computed at the TD- ω B97X-D/def2-TZVP level using a SMD solvation model for 1,2-dichloroethane ($\epsilon=10.125$).

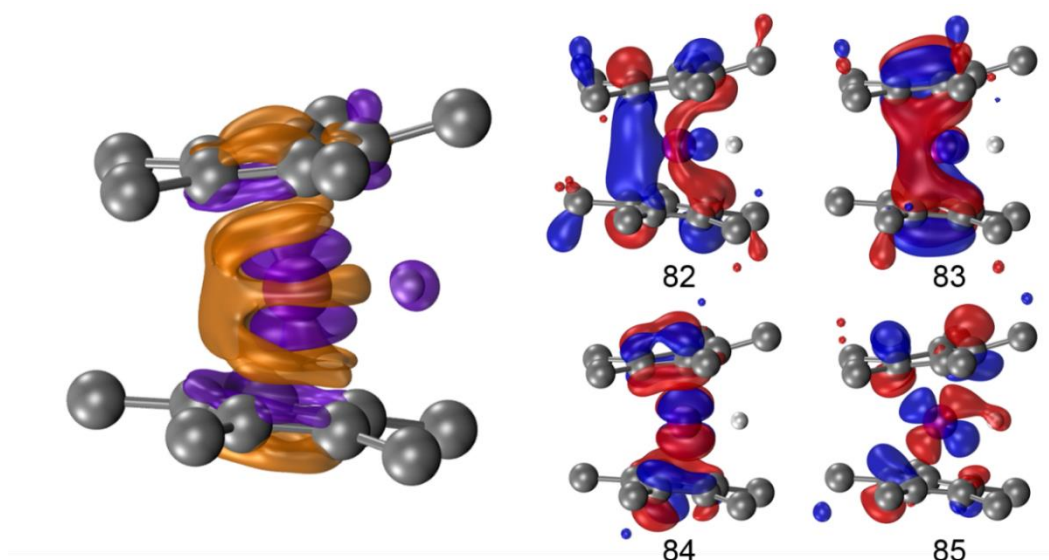


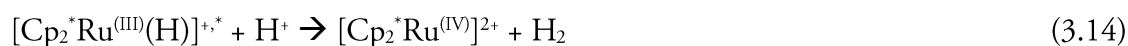
Figure 6.5. Density difference (excited – ground state) of $[\text{Cp}_2^*\text{Ru}^{\text{(IV)}}(\text{H})]^+$, isodensities = +0.002(violet) / -0.002(orange) (left). Natural Transition Orbitals participating to the $\lambda=227$ nm excitation (right). Densities and orbitals computed at the $\omega\text{B97X-D/def2-TZP}$ level using a SMD solvation model for 1,2-dichloroethane ($\epsilon=10.125$) on gas phase M06/def2-TZVP optimized geometry.

Table 6.1. Excitation energies, oscillator strengths and natural transition orbitals contributions for the excitation at $\lambda=227$ nm of $[\text{Cp}_2^*\text{Ru}^{\text{(IV)}}(\text{H})]^+$, computed at the $\omega\text{B97XD/def2-TZP}$ level using a SMD solvation model for dichloroethane ($\epsilon=10.125$) on gas phase ground state M06/def2-TZVP optimized geometry.

system	λ [nm]	f	transition	contribution
$[\text{Cp}_2^*\text{Ru}^{\text{(IV)}}(\text{H})]^+$	227	1.1466	83 → 84	58%
			82 → 85	38%

6.3 Clarification of the excitation photo-process involved in the mechanism

From the spectroscopic properties of $[\text{Cp}_2^*\text{Ru}^{\text{(III)}}(\text{H})]^+$ characterised in this Chapter, the HER by $\text{Cp}_2^*\text{Ru}^{\text{(II)}}$ was performed at various light power at a excitation wavelength $\lambda = 243$ nm (see Figure 6.6). The quantity of the produced hydrogen and $[\text{Cp}_2^*\text{Ru}^{\text{(III)}}]^+$ shows a linear dependence on the quantity of photons, which firmly excludes two-photon excitation processes to be involved in the H₂ elimination path described in the eq. (3.14):



Indeed, a two-photon process would have shown a quadratic dependence though the quantity of photon.

As the experiments were performed outside the glove box, the cell may have been slightly contaminated by atmospheric O₂ (visible by GC). Thus, a higher quantity of [Cp₂*Ru^(III)]⁺ (0.3 μmol) was observed due to the reduction of O₂ (O₂ reduction is thermodynamically more favourable than proton reduction)^{4,5} as already observed in section 6.2.2. In Figure 6.6, the 0.3 μmol of [Cp₂*Ru^(IV)(H)]⁺ were subtracted and the result shows a perfect fitting between H₂ and [Cp₂*Ru^(III)]⁺ production.

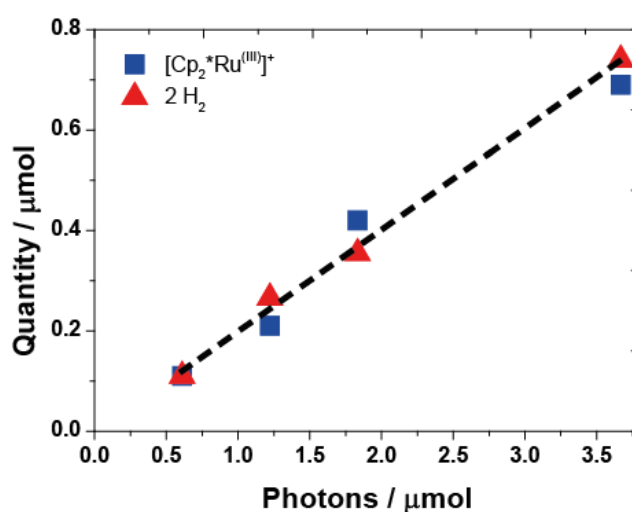


Figure 6.6. Quantity of H₂ produced as function of the quantity of photons. A solution of 6 mM Cp₂*Ru^(II) with 12 mM [H(OEt)₂]₂TB was prepared under anaerobic conditions in a glove box and in a quartz cell closed with a septum. The cell was taken out of the glove box to be illuminated by a laser at 243 nm under stirring. After 10 min, the appearance of [Cp₂*Ru^(III)]⁺ was followed by UV/vis spectroscopy and the H₂ produced was analysed by GC by sampling the headspace of the cell. The production of H₂ and [Cp₂*Ru^(III)]⁺ shows a linear dependence on the number of photon, typical for a one photon process (while a two photon process would have shown a quadratic dependence). An offset of 0.3 μmol [Cp₂*Ru^(IV)(H)]⁺ compared to the H₂ production was observed due to the rapid production of [Cp₂*Ru^(III)]⁺ from the reaction with O₂ contamination upon laser irradiation. This amount has been subtracted from the quantity of observed [Cp₂*Ru^(III)]⁺.

6.4 Second Harmonic Generation

Assisted ion transfer, presented in Chapter I, Section 1.2.2.2., was first investigated in 1979 by Koryta.¹⁴ He showed a shift in ion transfer potential, owing to a decrease in the Gibbs energy transfer, when a transferred ion complexes with an ionophore. This result gave rise to numerous studies to enhance our understanding on assisted ion transfer reactions especially because of the importance of complexation reactions in a wide range of natural phenomena.¹⁵⁻¹⁷ Consequently,

the characterization of assisted ion transfer is of major interest. In general, to understand the role played by biological membranes in the transfer of ion and, in particular, to investigate the processes involved at polarized interfaces while the proton transfer leads to the formation of $[\text{Cp}_2^*\text{Ru}^{(\text{IV})}(\text{H})]^+$ at the interface. So far, assisted ion transfers at the interface between two immiscible liquids have been extensively studied by electrochemical measurements. However, any study has addressed the direct and specific characterization of the complexation reaction product at the interface.

Optical second harmonic generation (SHG) is a powerful approach developed in the past decades to selectively probe the chemistry, physics and biology of gas|liquid, liquid|liquid, liquid|solid, gas|solid, and solid|solid interfaces.^{18,19} Indeed, a major problem encounter with linear classical optical techniques, such as absorption, emission, and Raman scattering, is the difficulty to separate the optical response of the interface from the optical response of the adjacent bulk species. For instance, if the species of interest is present in the bulk as well as at the interface, then, the optical signals due to absorption, fluorescence, and Raman scattering will most probably be dominated by most of the bulk molecules.²⁰ The second harmonic process converts two photons of frequency ω to a single photon of frequency 2ω . The latter is electric dipole forbidden in centrosymmetric media.²⁰⁻²² Therefore, regarding the interface between two liquids (*i.e.* two centrosymmetric media), only molecules involved in the asymmetry of the interface contribute to the SHG signal. Consequently, SHG is intrinsically surface-specific and has been extensively employed to investigate molecular absorption and organization as well as electron transfer at liquid|liquid interfaces.²²⁻²⁵

6.4.1 Historical background of second harmonic generation

SHG was first observed at liquid|air interface by Wang in 1969 who established the theoretical framework of non-linear optics at interfaces, and in particular the theory of SHG of such system.²⁶ Thereafter, Eisenthal *et al.* were the first to study the absorption and the orientation of molecular species at the water|air interface.²⁷ As consequence, similar studies were published at liquid|air interfaces²⁸ but the first SHG measurement at liquid|liquid interface was reported by Grubb *et al.* in 1988.²⁹ However, real systematic studies only arose in the 90's with the works of Higgins *et al.*^{22,30} in the group of Robert Corn. They described the absorption processes at ITIES

as function of the applied potential and showed the dependence of SHG signal to the orientation of the molecule at the interfaces.

In addition to follow orientation or absorption phenomena, SHG spectra can be recorded to characterize molecular species at the interface and study soft interfaces polarity as well as provide information on their thickness.³¹⁻³³ Furthermore, solute-solvent and solute-solute interactions can cause shifts of absorption SHG spectra. Consequently, SHG spectroscopy was also employed to study the formation of molecular aggregates at the liquid-liquid interfaces.³⁴⁻³⁸

Time resolved SHG follows the evolution of the system while light induced perturbations at the interface. One of the first measurement was reported in 1991 to measure the change of excited state lifetime of “rhodamine 6G” at the air|water interface.³⁹ Later, Shi *et al.*⁴⁰ studied the dynamics of malachite green at various interfaces including liquid|liquid interface. This work was followed by several time resolved investigation to study absorption,⁴¹ aggregation,⁴² reorientation^{43,44} and solvation dynamics^{44,45} at the interfaces.

6.4.2 General strengths and limitations of second harmonic generation measurements

Indeed, SHG has a great sensitivity to interfacial phenomena and it measures only reactions occurring at the interface. Thus, the measurements of interfacial complexation due to assisted ion transfer would mean that the reaction is heterogeneous. However, it does not mean that nothing occurs in the bulk solution.

The second advantage of SHG is that the signal intensity depends on the square of the interface concentration of the probed molecules. Consequently, the studied molecules can be identified by varying its concentration. Furthermore, the influence of the concentration on the interfacial reaction can be quantified and, therefore, kinetics can be investigated. Indeed, particular phenomena, absent in the bulk solution, can take place at the interface such as specific absorption or formation of molecular aggregates. Redox properties or excited state life time can be affected and, therefore, the kinetics can be different at the interface.

Finally, the method is simple as it does not require a model to extract rate constants of the reaction. Indeed, the investigated molecule is directly observed and therefore the result is not limited by the assumptions of a supporting model.

Nevertheless, SHG suffers of two main limitations: (i) its interface specificity leads to weak signals because only a small number of molecules are probed and, (ii) its dipole orientation specificity limits the detection to species that show non-linear optical properties.

6.4.3 Application of SHG to the study of assisted proton transfer

6.4.3.1 Experimental set-up

Herein, SHG technique was applied to investigate the formation of $[\text{Cp}_2^*\text{Ru}^{\text{IV}}(\text{H})]^+$ at a polarized w|DCE interface with the help of Grégoire Gschwend, a PhD student at LEPA. Charge transfer reactions between w|DCE were controlled using a four-electrode cell as described in Chapter II, Section 2.2.4. The cell used here was distinct from the one used in Chapter V because the faces were made of quartz for use in the wavelength range of UV light. **Figure 6.7** depicts the experiment carried out with 0.02 M HCl in the aqueous phase and 10 mM $\text{Cp}_2^*\text{Ru}^{\text{II}}$ in the organic phase. Under positive polarization, aqueous protons are driven to the DCE phase. Their complexation reaction with $\text{Cp}_2^*\text{Ru}^{\text{II}}$ forms $[\text{Cp}_2^*\text{Ru}^{\text{IV}}(\text{H})]^+$. The appearance of $[\text{Cp}_2^*\text{Ru}^{\text{IV}}(\text{H})]^+$ is probed at the interface in real time and as function of the potential, by SHG spectroscopy. The fundamental wavelength, set at 500 nm, was chosen to probe the appearance of $[\text{Cp}_2^*\text{Ru}^{\text{IV}}(\text{H})]^+$ at the interface. Thus, the wavelength of the photomultiplier was set at $\lambda = 250$ nm (because $\lambda_{[\text{Cp}_2^*\text{Ru}^{\text{IV}}(\text{H})]^+} = 248$ nm, as observed above).

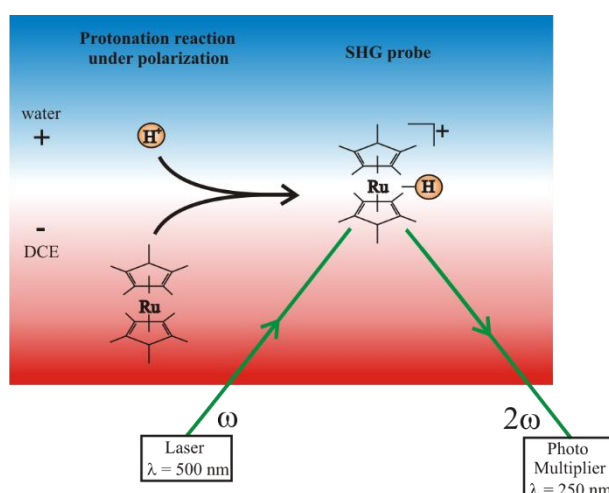


Figure 6.7. Schematic representation of the set-up to observe the formation of $[\text{Cp}_2^*\text{Ru}^{\text{IV}}(\text{H})]^+$ by second harmonic generation at w|DCE interface as function of the polarization.

6.4.3.2 Preliminary results

Caution has to be taken when recording a SH signal at polarised interfaces. Indeed, Conboy and Richmond⁴⁷ showed that SHG is sensitive to electric fields. Consequently, a control experiment, in absence of $\text{Cp}_2^*\text{Ru}^{\text{(II)}}$, was performed to first characterise the behaviour of the SHG signal as function of the polarization. However, this phenomenon, which is due to the potential-induced accumulation of electrolyte ions at the w|DCE interface, can be a useful tool to align the laser beam with the interface.

Thus, in a first stage, the fundamental wavelength was set at 900 nm and the generated SH signal was detected at 450 nm. A positive polarization was applied and the cell was aligned to get the highest SHG intensity.

In a second stage, the fundamental wavelength was set at 500 nm and the generated SH signal was detected at 250 nm to target the formation of $[\text{Cp}_2^*\text{Ru}^{\text{(IV)}}(\text{H})]^+$. A potential ramp from 0.2 V to 0.45 V and then from 0.45 V to -0.245 V was applied with a $2 \text{ mV}\cdot\text{s}^{-1}$ scan rate. The obtained CV is similar to those recorded in Chapter V. At positive potentials, the potential window is limited by the reversible transfer of protons from (w) to (o) (see the increase of current at 130 s in Figure 6.8, follow by a small current peak after the reversal of the scan direction due to the reversible proton transfer). Similarly, Cl^- ions transfer at negative potentials (see negative current at 480 s in Figure 6.1). In parallel, the SH signal was recorded as function of the time (Figure 6.8). A limited decrease of the signal was observed while protons were transferring and a small enhancement was observed during the interface polarization range due to TB^- polarization.

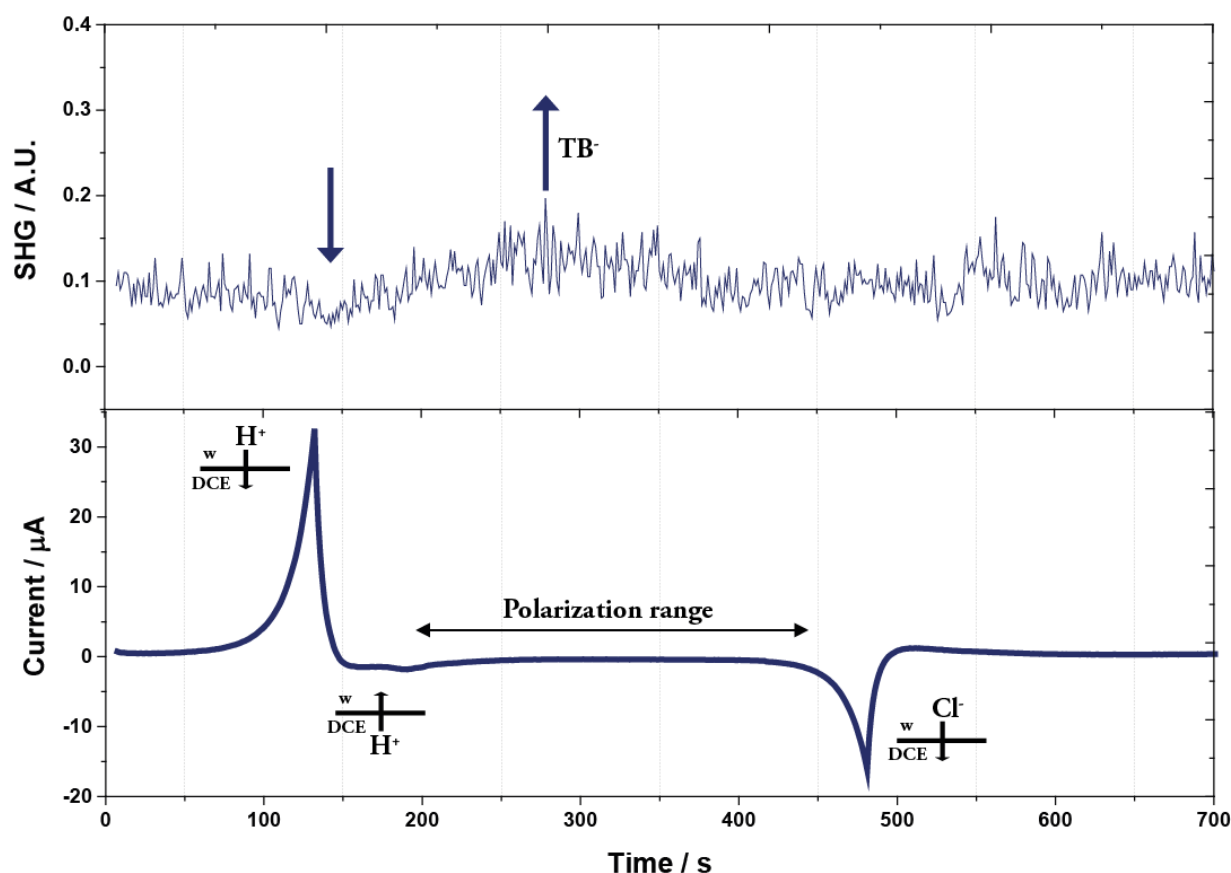


Figure 6.8. Control experiment obtained using the set-up described in Section 6.4.3.1 in absence of $\text{Cp}_2^*\text{Ru}^{\text{(II)}}$. Top, evolution of the SH signal recorded at w|DCE interface at $\lambda_{\text{SH}}=250$ nm as function of time, fundamental wavelength set at $\lambda_{\text{fond}} = 500$ nm. Bottom, current recorded as function of the time, scan rate 2 mV/s.

Similar experiments were recorded with $\text{Cp}_2^*\text{Ru}^{\text{(II)}}$ present in the organic phase. The cell was aligned thanks to the SH signal of TB^- , as described above. Then, the fundamental wavelength was set at 500 nm and the generated SH signal was detected at 250 nm to target the formation of $[\text{Cp}_2^*\text{Ru}^{\text{(IV)}}(\text{H})]^+$. A potential ramp was applied from 0 to 0.45 V and then, from 0.45 to -0.245 V at the same scan rate as above. As explained in Chapter V, Section 5.2.2., the current observed at positive potential corresponds to the proton transfer facilitated by the presence of $\text{Cp}_2^*\text{Ru}^{\text{(II)}}$. The transfer is now irreversible due to the formation of $[\text{Cp}_2^*\text{Ru}^{\text{(IV)}}(\text{H})]^+$ at the interface. At negative potentials, the first current wave was attributed to the transfer of $[\text{Cp}_2^*\text{Ru}^{\text{(IV)}}(\text{H})]^+$ from (o) to (w) by fitting simulated and experimental curves. The current limiting the negative end of the potential window was assigned to the transfer of Cl^- from (w) to (o) as observed in the blank. The CV was repeated several times and always the same SHG patterns were observed. The results provide

important information to strictly characterize $[\text{Cp}_2^*\text{Ru}^{\text{(IV)}}(\text{H})]^+$ formation at the interface and its transfer from (o) to (w) phase

First, the SH signal increased when protons transfer from (w) to (o) phase. Because of the wavelength specificity of SHG, the enhancement of the signal was clearly attributed to the formation of $[\text{Cp}_2^*\text{Ru}^{\text{(IV)}}(\text{H})]^+$ occurring during the facilitated proton transfer. However, the intensity of the signal increased as function of the transferred protons in a first time close to the onset potential of the proton transfer and then, decreased, despite the applied positive polarisation to supply protons. This signal extinction was attributed to the absorption of the SHG by $[\text{Cp}_2^*\text{Ru}^{\text{(IV)}}(\text{H})]^+$. Indeed, in the set-up configuration, $[\text{Cp}_2^*\text{Ru}^{\text{(IV)}}(\text{H})]^+$ is formed in the organic phase, located on the bottom of the cell. As can be seen in **Figure 6.7**, the interface is probed also from the bottom. Consequently, the SHG is generated in the DCE phase and is absorbed when a large amount of $[\text{Cp}_2^*\text{Ru}^{\text{(IV)}}(\text{H})]^+$ is produced.

The second signal enhancement was observed during the cathodic scan. It corresponds to the ions transfer wave attributed, by fitting with simulation data, to the transfer of $[\text{Cp}_2^*\text{Ru}^{\text{(IV)}}(\text{H})]^+$ from (o) to (w) in Chapter V. SHG spectroscopy provides here a direct characterization of the transfer and it definitively confirms the results obtained previously. In the meantime, it also validates the COMSOL method applied to investigate $\text{Cp}_2^*\text{Ru}^{\text{(III)}}$ transfer at polarized interfaces. Similarly to the SHG obtained for the formation of $[\text{Cp}_2^*\text{Ru}^{\text{(IV)}}(\text{H})]^+$ at the interface, the signal extinguished when a large concentration of $[\text{Cp}_2^*\text{Ru}^{\text{(IV)}}(\text{H})]^+$ was present.

Finally, the SH signal slightly increased between the two transfers of $[\text{Cp}_2^*\text{Ru}^{\text{(IV)}}(\text{H})]^+$. This signal is comparable to the one obtained in the control experiment (**Figure 6.1**) and was attributed to the polarisation of the electrolyte. Additionally, the signal gradually increases with the number of scan performed. This phenomenon has been observed with the different electrochemical cells prepared. It appeared that the experiment disturbs the interface, perhaps due to the accumulation of ions close to the interface, and increases the SHG signal making difficult the accumulation of the data.

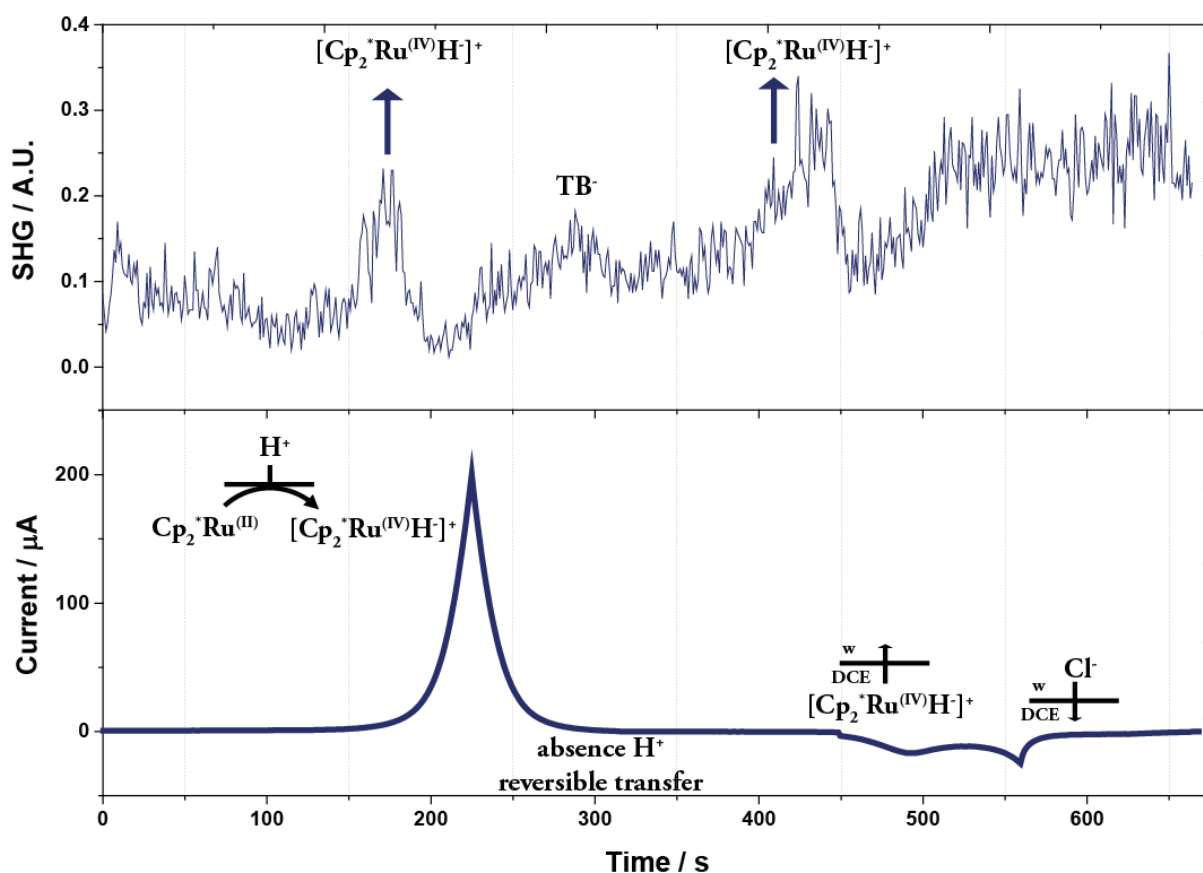


Figure 6.9. Current and SH signal obtained using the set-up described in Section 6.4.3.1. in presence of $\text{Cp}_2^*\text{Ru}^{(\text{III})}$. Top, evolution of the SH signal recorded at w|DCE interface at $\lambda_{\text{SH}}=250$ nm as function of time, fundamental wavelength set at $\lambda_{\text{fond}} = 500$ nm. Bottom, current recorded as function of the time, scan rate 2 mV/s.

6.4.3.3 Limitation and possibilities

For the first time an assisted ion transfer was characterized in real time and with a specific method. This is a direct proof of the heterogeneous formation of $[\text{Cp}_2^*\text{Ru}^{(\text{IV})}(\text{H})]^+$ at the interface from aqueous protons and organic $\text{Cp}_2^*\text{Ru}^{(\text{III})}$.

However, further characterizations (*i.e.* measure SHG spectra, investigate the concentration dependence) are obstructed due to the weak intensity of the SH signal recorded. As it was introduced above, because of the set-up configuration, the SH signal generated by $[\text{Cp}_2^*\text{Ru}^{(\text{IV})}(\text{H})]^+$ is absorbed by $[\text{Cp}_2^*\text{Ru}^{(\text{IV})}(\text{H})]^+$ itself when its concentration increases. Consequently, to increase the starting concentration of $\text{Cp}_2^*\text{Ru}^{(\text{III})}$ will disadvantage the signal intensity. Furthermore, the SHG is very sensitive to the ion present at the interface. After few CVs, the signal is disturbed by the

quantity of species that was moved to the interface. Therefore, it is not possible to accumulate spectra.

Nevertheless, these issues can be overcome by modifying the set-up configuration and setting the organic phase on the top of the cell. This would prevent the laser beam to pass through the organic phase, where $[\text{Cp}_2^*\text{Ru}^{\text{(IV)}}(\text{H})]^+$ is accumulated. From a practical point of view, it means to change DCE solvent for a solvent less dense than water. Electrochemistry at polarized interfaces has already been studied with lower density organic solvents containing nitrile and ketone functional groups such as valeronitrile, caprylonitrile, 2-octanone, 2-decanone, 3-nonanone and 5-nonanone.⁴⁸ The two last solvents appeared the most promising because of their large polarisation range. Butyronitrile is also a very attractive alternative within the scope of the batch water-splitting. Indeed, a recent work was published employing this solvent to catalyse the oxidation of water at a chemically polarized interface.⁴⁹

6.5 Conclusions

The $[\text{Cp}_2^*\text{Ru}^{\text{(IV)}}(\text{H})]^+$ was first studied in one phase. The protonation of $\text{Cp}_2^*\text{Ru}^{\text{(II)}}$ was monitored by UV/vis spectroscopy. The formation of a unique product, $[\text{Cp}_2^*\text{Ru}^{\text{(IV)}}(\text{H})]^+$, was observed at $\lambda = 243$ nm. However, homo-association occurred during the reaction and a direct determination of the pK_a was not possible. Additionally, the mechanism to evolve H_2 from $[\text{Cp}_2^*\text{Ru}^{\text{(IV)}}(\text{H})]^+$ was probed with unprecedented depth. Thus, the major H_2 (and, consequently, $[\text{Cp}_2^*\text{Ru}^{\text{(III)}}]^+$) production was recorded when the hydride was excited at $\lambda = 243$ nm. DFT computations seem consistent with electronic density transfer from ligands to the metal. It leads to weakening the metal-hydride bond and favour the H_2 release. Unequivocally, the linear increasing of H_2 and $[\text{Cp}_2^*\text{Ru}^{\text{(III)}}]^+$ production as function of the number of photon proves that one-photon excitation process is involved in the actual H_2 elimination path.

Thereafter, the formation of $[\text{Cp}_2^*\text{Ru}^{\text{(IV)}}(\text{H})]^+$ at polarised interfaces was investigated by SHG spectroscopy. The preliminary results obtained provide the direct characterization of the formation of the product during an assisted ion transfer. The results also confirmed irreversible $[\text{Cp}_2^*\text{Ru}^{\text{(IV)}}(\text{H})]^+$ transfer at negative potential predicted in Chapter V. However, the intensity of the SH signal was too low for further characterisation such as SHG spectra of $[\text{Cp}_2^*\text{Ru}^{\text{(IV)}}(\text{H})]^+$ and investigation of the dependence of the concentration. The possibility to inverse the phase was

discussed. Thus, in a next stage, Cp₂*Ru^(II) will be dissolved in a solvent with a density lower than DCE to inverse the aqueous and organic phase in order to record a higher signal and pursue the characterisations.

6.6 References

- (1) Du, P.; Schneider, J.; Luo, G.; Brennessel, W. W.; Eisenberg, R. *Inorganic Chemistry* **2009**, *48*, 4952.
- (2) Liu, T. B.; DuBois, D. L.; Bullock, R. M. *Nat. Chem.* **2013**, *5*, 228.
- (3) Fichtner, C.; van Gastel, M.; Lubitz, W. *Physical Chemistry Chemical Physics* **2003**, *5*, 5507.
- (4) Hatay, I.; Su, B.; Li, F.; Méndez, M. A.; Khoury, T.; Gros, C. P.; Barbe, J.-M.; Ersoz, M.; Samec, Z.; Girault, H. H. *Journal of the American Chemical Society* **2009**, *131*, 13453.
- (5) Hatay, I.; Su, B.; Li, F.; Partovi-Nia, R.; Vrubel, H.; Hu, X.; Ersoz, M.; Girault, H. H. *Angewandte Chemie International Edition* **2009**, *48*, 5139.
- (6) Chai, J.-D.; Head-Gordon, M. *Physical Chemistry Chemical Physics* **2008**, *10*, 6615.
- (7) Weigend, F.; Ahlrichs, R. *Physical Chemistry Chemical Physics* **2005**, *7*, 3297.
- (8) Marenich, A. V.; Cramer, C. J.; Truhlar, D. G. *The Journal of Physical Chemistry B* **2009**, *113*, 6378.
- (9) Zhao, Y.; Truhlar, D. *Theor Chem Account* **2008**, *120*, 215.
- (10) Martin, R. L. *J. Chem. Phys.* **2003**, *118*, 4775.
- (11) Wiberg, K. B.; Hadad, C. M.; Foresman, J. B.; Chupka, W. A. *J. Phys. Chem.* **1992**, *96*, 10756.
- (12) Handy, N. C.; Schaefer, H. F. *J. Chem. Phys.* **1984**, *81*, 5031.
- (13) Frisch, M. J.; Trucks, G. W.; Schlegel, H. B.; Scuseria, G. E.; Robb, M. A.; Cheeseman, J. R.; Scalmani, G.; Barone, V.; Mennucci, B.; Petersson, G. A.; Nakatsuji, H.; Caricato, M.; Li, X.; Hratchian, H. P.; Izmaylov, A. F.; Bloino, J.; Zheng, G.; Sonnenberg, J. L.; Hada, M.; Ehara, M.; Toyota, K.; Fukuda, R.; Hasegawa, J.; Ishida, M.; Nakajima, T.; Honda, Y.; Kitao, O.; Nakai, H.; Vreven, T.; Montgomery Jr., J. A.; Peralta, J. E.; Ogliaro, F.; Bearpark, M. J.; Heyd, J.; Brothers, E. N.; Kudin, K. N.; Staroverov, V. N.; Kobayashi, R.; Normand, J.; Raghavachari, K.; Rendell, A. P.; Burant, J. C.; Iyengar, S. S.; Tomasi, J.; Cossi, M.; Rega, N.; Millam, N. J.; Klene, M.; Knox, J. E.; Cross, J. B.; Bakken, V.; Adamo, C.; Jaramillo, J.; Gomperts, R.; Stratmann, R. E.; Yazyev, O.; Austin, A. J.; Cammi, R.; Pomelli, C.; Ochterski, J. W.; Martin, R. L.; Morokuma, K.; Zakrzewski, V. G.; Voth, G. A.; Salvador, P.; Dannenberg, J. J.; Dapprich, S.; Daniels, A. D.; Farkas, Ö.; Foresman, J. B.; Ortiz, J. V.; Cioslowski, J.; Fox, D. J.; Gaussian, Inc.: Wallingford, CT, USA, 2009.
- (14) Koryta, J. *Electrochimica Acta* **1979**, *24*, 293.
- (15) Girault, H. In *Modern Aspects of Electrochemistry*; Springer: **1993**, p 1.
- (16) Reymond, F.; Steyaert, G.; Carrupt, P. A.; Testa, B.; Girault, H. H. *Helvetica Chimica Acta* **1996**, *79*, 101.
- (17) Volkov, A. G.; Deamer, D. W. *Liquid-Liquid Interfaces Theory and Methods*; CRC press, **1996**.
- (18) Bloembergen, N. *Nonlinear optics, Chapter V*; World Scientific, **1996**.

- (19) Bloembergen, N.; Pershan, P. S. *Physical Review* **1962**, *128*, 606.
- (20) Eienthal, K. *Chemical Reviews* **1996**, *96*, 1343.
- (21) Eienthal, K. B. *Annual Review of Physical Chemistry* **1992**, *43*, 627.
- (22) Higgins, D. A.; Corn, R. M. *The Journal of Physical Chemistry* **1993**, *97*, 489.
- (23) Kott, K. L.; Higgins, D. A.; McMahon, R. J.; Corn, R. M. *Journal of the American Chemical Society* **1993**, *115*, 5342.
- (24) Wirth, M. J.; Burbage, J. D. *The Journal of Physical Chemistry* **1992**, *96*, 9022.
- (25) Bell, A. J.; Frey, J. G.; VanderNoot, T. J. *Journal of the Chemical Society, Faraday Transactions* **1992**, *88*, 2027.
- (26) Wang, C. C. *Physical Review* **1969**, *178*, 1457.
- (27) Hicks, J.; Kemnitz, K.; Eienthal, K.; Heinz, T. *The Journal of Physical Chemistry* **1986**, *90*, 560.
- (28) Higgins, D. A.; Abrams, M. B.; Byerly, S. K.; Corn, R. M. *Langmuir* **1992**, *8*, 1994.
- (29) Grubb, S. G.; Kim, M. W.; Rasing, T.; Shen, Y. R. *Langmuir* **1988**, *4*, 452.
- (30) Higgins, D. A.; Naujok, R. R.; Corn, R. M. *Chemical physics letters* **1993**, *213*, 485.
- (31) Wang, H.; Borguet, E.; Eienthal, K. *The Journal of Physical Chemistry A* **1997**, *101*, 713.
- (32) Wang, H.; Borguet, E.; Eienthal, K. *The Journal of Physical Chemistry B* **1998**, *102*, 4927.
- (33) Steel, W. H.; Walker, R. A. *Nature* **2003**, *424*, 296.
- (34) Nagatani, H.; Piron, A.; Brevet, P.-F.; Fermín, D. J.; Girault, H. H. *Langmuir* **2002**, *18*, 6647.
- (35) Nagatani, H.; Samec, Z. k.; Brevet, P.-F.; Fermín, D. J.; Girault, H. H. *The Journal of Physical Chemistry B* **2003**, *107*, 786.
- (36) Fujiwara, K.; Monjushiro, H.; Watarai, H. *Chemical physics letters* **2004**, *394*, 349.
- (37) Olaya, A. J.; Schaming, D.; Brevet, P. F.; Nagatani, H.; Xu, H. J.; Meyer, M.; Girault, H. H. *Angewandte Chemie* **2012**, *124*, 6553.
- (38) Olaya, A. J.; Schaming, D.; Brevet, P.-F.; Nagatani, H.; Zimmermann, T.; Vanicek, J.; Xu, H.-J.; Gros, C. P.; Barbe, J.-M.; Girault, H. H. *Journal of the American Chemical Society* **2011**, *134*, 498.
- (39) Castro, A.; Sitzmann, E. V.; Zhang, D.; Eienthal, K. B. *The Journal of Physical Chemistry* **1991**, *95*, 6752.
- (40) Shi, X.; Borguet, E.; Tarnovsky, A.; Eienthal, K. *Chemical physics* **1996**, *205*, 167.

- (41) Kunz, W.; Nostro, P. L.; Ninham, B. W. *Current Opinion in Colloid & Interface Science* **2004**, *9*, 1.
- (42) Fita, P.; Punzi, A.; Vauthey, E. *The Journal of Physical Chemistry C* **2009**, *113*, 20705.
- (43) Antoine, R.; Tamburello-Luca, A.; Hebert, P.; Brevet, P.; Girault, H. *Chemical physics letters* **1998**, *288*, 138.
- (44) Zimdars, D.; Eiseenthal, K. B. *The Journal of Physical Chemistry A* **1999**, *103*, 10567.
- (45) Zimdars, D.; Dadap, J. I.; Eiseenthal, K. B.; Heinz, T. F. *Chemical physics letters* **1999**, *301*, 112.
- (46) McArthur, E. A.; Eiseenthal, K. B. *Journal of the American Chemical Society* **2006**, *128*, 1068.
- (47) Conboy, J. C.; Richmond, G. L. *The Journal of Physical Chemistry B* **1997**, *101*, 983.
- (48) Toth, P. S.; Dryfe, R. A. W. *Analyst* **2015**, *140*, 1947.
- (49) Rastgar, S.; Pilarski, M.; Wittstock, G. *Chemical Communications* **2016**, *52*, 11382.

7. Biphasic Hydrogen Evolution Using Classical Systems

7.1	Introduction	152
7.2	First investigations on classical systems at soft interfaces	153
7.3	Cyclic voltammetry observations at w DCE interfaces	155
7.4	Mechanistic discussion	156
7.4.1	Energy transfer reactions.....	158
7.4.1.1	Characterisation of Ru(bpy) ₃ TB ₂	158
7.4.1.2	Electrochemical characterisations	159
7.5	Shake-flask experiments.....	161
7.5.1	Reaction and analysis.....	161
7.5.2	Comparison between the catalyst efficiencies at soft interfaces.....	162
7.5.3	Clarification of the proton source	163
7.6	Conclusions.....	163
7.7	References.....	165

7.1 Introduction

In 2011, Nieminen *et al.*¹ reported the functionalisation of liquid|liquid interfaces by platinum and palladium nanoparticles to catalysed the protons reduction by $\text{Cp}_2^*\text{Fe}^{\text{II}}$. Inspired by this study, a serie of non-noble, earth abundant MoS_2 -based catalyst was investigated at ITIES.^{2,3} It was observed that MoS_2 nanoparticles grown on carbon supports (such as carbon nanotubes or graphene) act as superior electrocatalysts towards HER as they provide conductive scaffolds that leads to (i) a significant decrease in the average NP size during the synthesis which increase the number of accessible catalyst edge size, (ii) an increase the dispersion of the catalyst which again maximize the availability of exposed surface catalytic sites, and (iii) a rapid electron transfer between the electron donor and the less conducting MoS_2 nanoparticles. Thereafter, the study was extended to Mo_2C nanowires and composites of Mo_2C nanoparticles formed on carbon nanotubes.⁴ A comparative kinetic study with other transition carbides (W_2C and WC), silicides (MoSi_2) and borons (MoB and B_4C) was published by Scanlon *et al.*⁵ in 2013 and highlighted the superior biphasic activity of Mo_2C and MoB . However, the use of nanoparticles at ITIES using $\text{Cp}_2^*\text{Fe}^{\text{II}}$ as a sacrificial donor, while highly efficient, has always been achieved in the dark, without photo-activation that could provide additional driving force towards water-splitting applications.

In 2013, Dr Peiyu Ge *et al.*⁶ investigated a biomimetic approach to produce H_2 at soft interfaces based on sacrificial electron donor and a photosensitizer combined with MoS_2 catalyst. Herein, the valuable knowledge accumulated in the past decades is employed to investigate the implementation of a 3-component model system based on homogeneous catalysts at polarised liquid|liquid interfaces. Such systems are interesting because they propose an alternative to metallocenes to produce H_2 in the batch water-splitting approach. Additionally, they could spread to diverse biomimetic photo-reactions such as water oxidation,⁷ carbon dioxide reduction⁸ but also for photodegradation reactions⁹ as well as organometallic photochemistry.¹⁰ Therefore, this study provides the foundation of an all-purpose interface, adaptable to various components and reactions.

In this work, a highly hydrophobic sensitizer consisting of a $\text{Ru}(\text{bpy})_3(\text{TB})_2$ salt was synthesised and introduced to the organic phase. In the presence of triethylamine (TEA), a sacrificial electron donor, the organic soluble molecular catalyst was tested under light illumination for its ability to catalyse hydrogen evolution. Two catalysts inspired by hydrogenase and composed of non-noble metals, were used for the first time at a liquid|liquid interface and experimented upon

to show the methods versatility (their molecular structures are illustrated in Figure 7.1. One of the advantages of this system is the ability to work in organic media (good solubility, low deactivation of catalysts and photosensitizers) but also with the benefit of using aqueous protons. This work complete Ge's study. It provides further details on the process that occur in the reaction and compare heterogeneous and homogeneous catalysis of proton reduction at liquid|liquid interface.

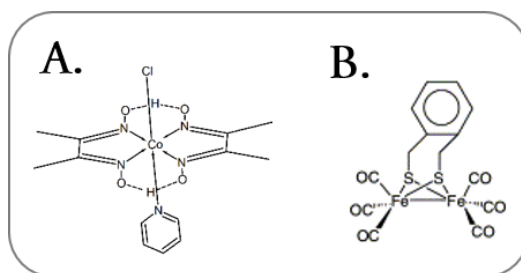
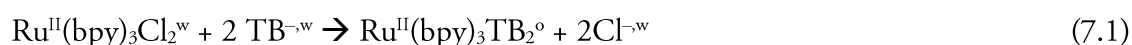


Figure 7.1: Molecular structure of: (A) $\text{Co}(\text{dmgh})_2(\text{py})\text{Cl}$ and (B) $\text{Fe}_2(\mu\text{-SCH}_2\text{C}_6\text{H}_4\text{CH}_2\text{S})(\text{CO})_6$

7.2 First investigations on classical systems at soft interfaces

Ge,⁶ from our laboratory, has described in her thesis the first attempt at using a classical system with an electron donor, a photosensitizer and a catalyst to perform hydrogen evolution at a w|DCE interface. $\text{Ru}^{\text{II}}(\text{bpy})_3\text{Cl}_2$ was solubilised in the aqueous phase and transferred to the organic phase thanks to $[\text{Li}(\text{OEt})_2]\text{TB}$ chemical polarisation through the formation of $\text{Ru}^{\text{II}}(\text{bpy})_3\text{TB}_2$ as shown below:



Thus, $\text{Ru}^{\text{II}}(\text{bpy})_3\text{TB}_2$ in the organic phase was employed as a photosensitizer. TEA and MoS_2 on mesoporous carbon (MoS_2/C) were added to play the role of electron donor and catalyst, respectively. Similarly, to the procedure presented in chapter V, section 5.2.1, the biphasic HER was investigated by performing shake-flask experiments. The optimised shake-flask conditions are described below:

0.05 μmol MoS_2/C

0.1 M HCl , 0.5 M TEA

5 mM $[\text{Li}(\text{OEt})_2]\text{TB}$

1 mM of $[\text{Ru}^{\text{II}}(\text{bpy})_3]\text{Cl}_2$

(DCE)

(w)

Vial (7.1)

The reaction occurred under exposure to 455 nm wavelength of illumination and mechanical agitation. After 2 hours, 7.6 μmol of H_2 was produced and quantified by gas chromatography as illustrated in Figure 7.2. During this study, the necessity of light and the increase in the efficiency of HER by addition of MoS_2 catalyst was demonstrated (Figure 7.2). Different parameters were studied such as the influence of the concentration of all the components. The reaction yield showed a linear dependence with photosensitizer concentration, required excess electron donor and had good efficiency with 0.05 μmol of added catalyst.

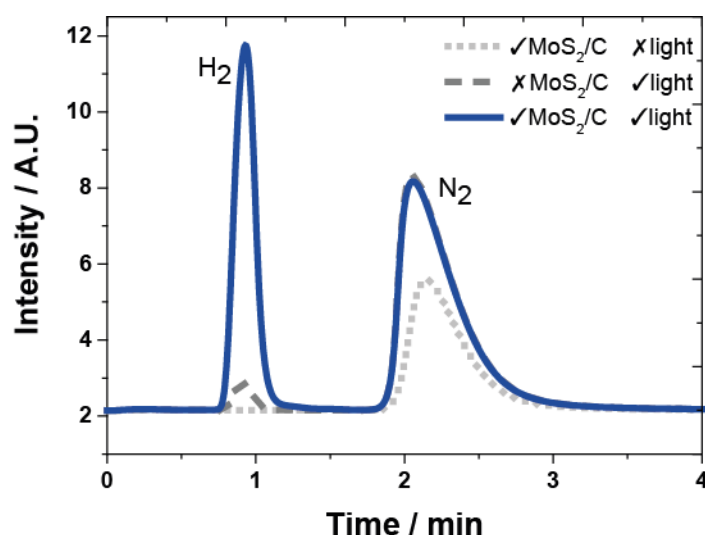


Figure 7.2. Gas chromatograms of the shake-flask headspace gas for experiments performed using Vial 7.1 recorded after 120 minutes of stirring under anaerobic conditions, in the dark (dotted curve), under white-light illumination without MoS_2/C (dashed trace) and with MoS_2/C (blue solid line).

Herein, the system is investigated using molecular catalysts, $\text{Fe}_2(\mu\text{-SCH}_2\text{C}_6\text{H}_4\text{CH}_2\text{S})(\text{CO})_6$ and $\text{Co}(\text{dmgh})_2(\text{py})\text{Cl}$ based on cheap and abundant metals. The first is a highly hydrophobic di-iron complex with a thiolate bridge and CO ligands that mimics the hydrogenase enzyme while the second is a simple cobaloxime complex. Similar conditions that Ge's study are used to evolve hydrogen at soft interfaces. Nevertheless, to make the understanding of the biphasic reaction easier, the system was simplified. Instead of being formed *in-situ*, a pre-synthesised organic soluble

$\text{Ru}^{\text{II}}(\text{bpy})_3\text{TB}_2$ was directly dissolved in the DCE phase (for the synthesis, see Chapter II, Section 2.1.2.3). While Ge's earlier study provided a model to integrate the HER based on 3-components system at soft interfaces, we propose a global and comprehensive study of the mechanisms involved. Thus, the following two sections encompass systematic electrochemical studies of the components in both one and two-phase systems. The last section presents the results obtained for the photo- H_2 production at a liquid|liquid interface using systems composed of an electron donor, a sensitizer and different catalysts.

7.3 Cyclic voltammetry observations at w|DCE interfaces

Control experiments, highlighting the impact of the interfacial polarisation on liquid|liquid voltammetry of $\text{Co}(\text{dmgh})_2(\text{py})\text{Cl}$ and $\text{Fe}_2(\mu\text{-SCH}_2\text{C}_6\text{H}_4\text{CH}_2\text{S})(\text{CO})_6$, were performed to prevent unexpected ion transfers from occurring during the reactions. Transfers between w|DCE were characterised using a traditional four electrode cell, as described in Chapter II, section 2.2.4.

First, voltammetric measurements at water|1,2-DCE interfaces were performed using Cell 1 in a glove box under anaerobic conditions. Figure 7.3 illustrates the cyclic voltammograms obtained in the absence (dark lines) and presence of $\text{Co}(\text{dmgh})_2(\text{py})\text{Cl}$ or $\text{Fe}_2(\mu\text{-SCH}_2\text{C}_6\text{H}_4\text{CH}_2\text{S})(\text{CO})_6$ (green lines). As discussed in Chapter V and VI, the blank curve, without catalyst in the organic phase, was limited at positive potentials by the transfer of protons from (w) to (DCE); whereas, at negative potentials, it was limited by the transfer of Cl^- . After addition of $\text{Co}(\text{dmgh})_2(\text{py})\text{Cl}$ or $\text{Fe}_2(\mu\text{-SCH}_2\text{C}_6\text{H}_4\text{CH}_2\text{S})(\text{CO})_6$ (Figure 7.3 (A) and (B) respectively) no significant modification of the curves was observed for both catalyst. It was previously presented (Chapters V and VI) that an irreversible positive current wave is observable where protons interact with complexes present in the aqueous phase. Thus, it could be envisaged that $\text{Co}(\text{dmgh})_2(\text{py})\text{Cl}$ or $\text{Fe}_2(\mu\text{-SCH}_2\text{C}_6\text{H}_4\text{CH}_2\text{S})(\text{CO})_6$ act as a lipophilic base and could be protonated facilitating thereby the proton transfer. However, no current increase was observed at positive potentials meaning that no apparent interaction with the catalysts are observed. It is in agreement with Dempsey and coworkers¹² results where a reduction of the $\text{Co}(\text{dmgh})_2(\text{py})\text{Cl}$ complex is required to subsequently, protonate the metal. Regarding $\text{Fe}_2(\mu\text{-SCH}_2\text{C}_6\text{H}_4\text{CH}_2\text{S})(\text{CO})_6$, the reaction pathway to catalyse the reduction of protons leads to successive electron and proton transfers. The sequence depends

on the nature of the terminal ligands of the di-iron complex and the strength of the acid used as a proton source.¹² Nevertheless, for all-CO derivatives, the first step in catalytic H₂ production was demonstrated to be an electron transfer.¹³ Thus, the result obtained with the 4-electrode cell is also in agreement with literature.

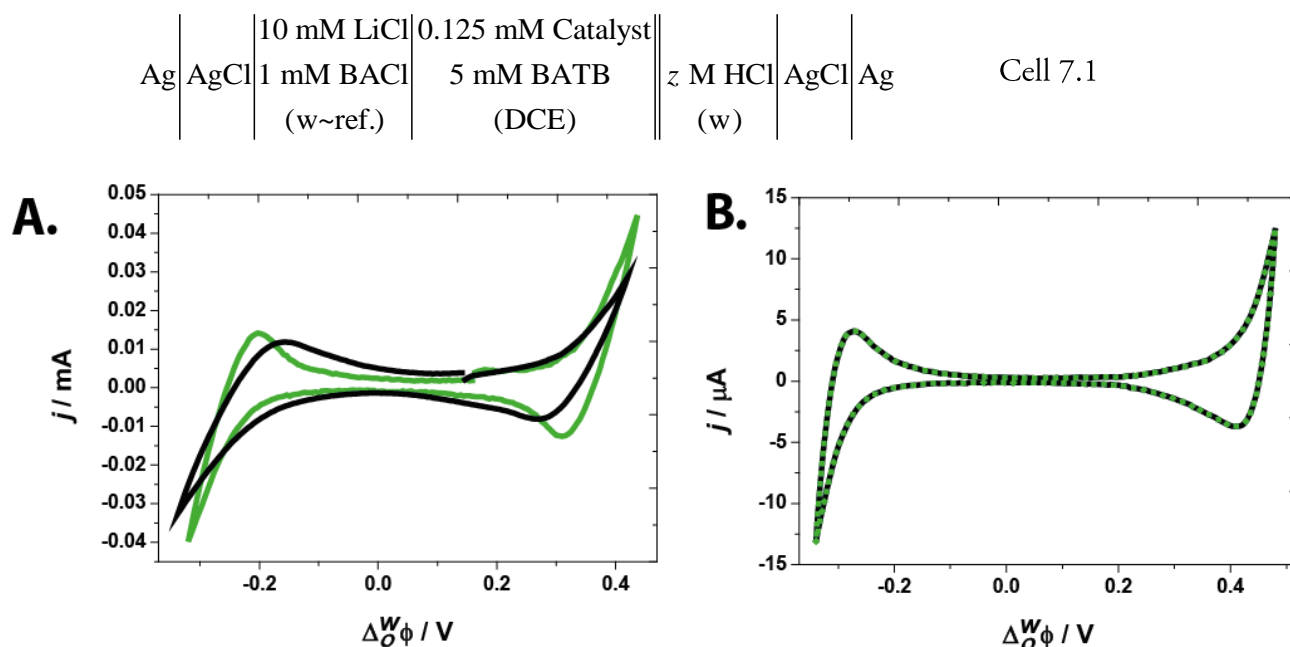
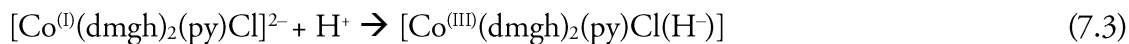
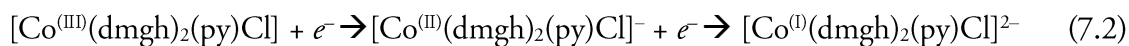
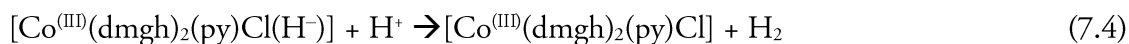
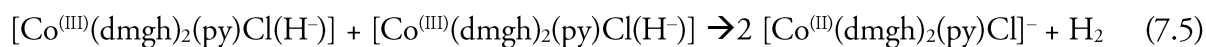
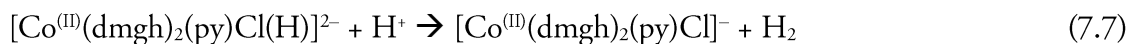
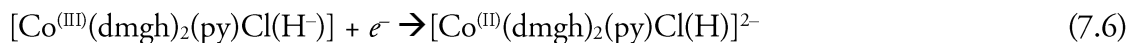


Figure 7.3. Cyclic voltammetry obtained using Cell 7.1 under aerobic conditions. The blank curves (black lines) were acquired in absence of catalyst. Then, the catalysts were added (green lines): (A) Co(dmgh)₂(py)Cl with 0.1 M HCl and (B) Fe₂(μ-SCH₂C₆H₄CH₂S)(CO)₆ with 1 mM HCl.

7.4 Mechanistic discussion

Despite numerous studies on cobaloxime complexes and their production of H₂, the mechanism has remained elusive.¹⁴⁻¹⁶ The first step is reduction of the cobalt to [Co^(I)(dmgh)₂(py)Cl]²⁻ followed by protonation of the complex to form [Co^(III)(dmgh)₂(py)Cl(H⁻)] (eq. 7.2 and 7.3). Consequently, the complex does not protonate without a first reduction, which agrees with CVs obtained at liquid|liquid interfaces. Subsequently, three different mechanisms are proposed similar to the production of hydrogen by metallocenes (see Chapter I, Section 1.4.3). The route, favoured by Fontecave and Artero,¹⁷ is a proton attack on [Co^(III)(dmgh)₂(py)Cl(H)]⁻ to form [Co^(III)(dmgh)₂(py)Cl] and H₂ by hetero-dissociation (eq. 7.4). Peters and Gray^{16,18} suggested another possibility based on a bimolecular reaction between two hydrides to eliminate H₂ and form [Co^(III)(dmgh)₂(py)Cl]⁻ by a homolytic pathway (eq. 7.5). To finish, Eisenberg *et al.*¹⁹ proposed the reduction of [Co^(III)(dmgh)₂(py)Cl(H)] to [Co^(II)(dmgh)₂(py)Cl(H)]²⁻, which can react *via* an analogous homolytic or heterolytic pathway (eq. 7.6, 7.7 and 7.8).

Reductions and protonation:**H₂ release:***Hetero-dissociation:**Bimolecular reaction:**Reduction follow by hetero-dissociation or bimolecular reaction:*

Similarly, the mechanism of H₂ evolution with the di-iron complexes mimicking natural hydrogenase can follow different pathways.^{20,21} The commonly accepted first step is the reduction of the di-iron complex to form a charge-separated state Fe⁰-Fe^I which, then, reacts with a proton to form the HFe^{II}-Fe^I complex. Nevertheless, the complex may also be protonated first and then reduced in a second stage. Which mechanism dominates depends on the properties of the ligands.¹³ As it was demonstrated above (see Section 7.3.2), Fe₂(μ-SCH₂C₆H₄CH₂S)(CO)₆ follows the first mechanism. Then, HFe^{II}-Fe^I is reduced a second time to form a hydride which could then be protonated to release H₂ and recover the Fe^I-Fe^I complex. A second scenario was also proposed. The HFe^{II}-Fe^I complex undergoes a second protonation to form a dihydride complex, which then releases H₂ through reductive elimination.²² Unfortunately, to date, no intermediate was observed in spectroscopy thus preventing researchers from validating either one of the proposed pathways.

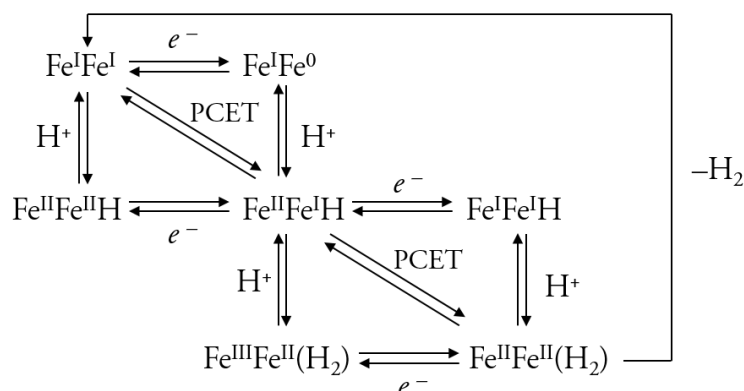


Figure 7.4: Possible pathway to evolve H_2 with di-iron complex (PCET = proton coupled electron transfer).²¹

7.4.1 Energy transfer reactions

7.4.1.1 Characterisation of $Ru(bpy)_3TB_2$

To have a better understanding of the system studied, the electron and energy transfer reactions involved were studied. To achieve this goal, the electronic properties of each component was studied using electrochemical measurements and fluorescence spectroscopy in collaboration with J. Hidalgo, a fellow PhD student at LEPA.

Excited $Ru(bpy)_3^+$ is both a better reductant and oxidant than ground state $Ru(bpy)_3^+$ owing to the higher energy content of the excited state.²³ Thus, electron transfer to an acceptor molecule (A) or electron transfer from a donor molecule (D) leads to the deactivation of the excited state *via* either reductive or oxidative pathway.



The mechanism depends on the properties of the donor and acceptor.

The ground state of the synthesized $Ru(bpy)_3TB_2$ was evaluated utilizing cyclic voltammetry. The reduction potential was found to be -1.07 V (*vs* SHE) and the oxidation 1.84 V (*vs* SHE) in DCE. The UV/vis spectrum indicates an absorption band at 452 nm and a fluorescence emission was observed at 583 nm. The zero-zero excitation energy, E^{0-0} , equal to 2.31 eV was used to calculate the redox potentials for the excited state, assuming the entropy change between the ground state and excited state is negligible.²⁴

The result, showing the two possible pathways of reductive or oxidative quenching, is summarised in Figure 7.5.

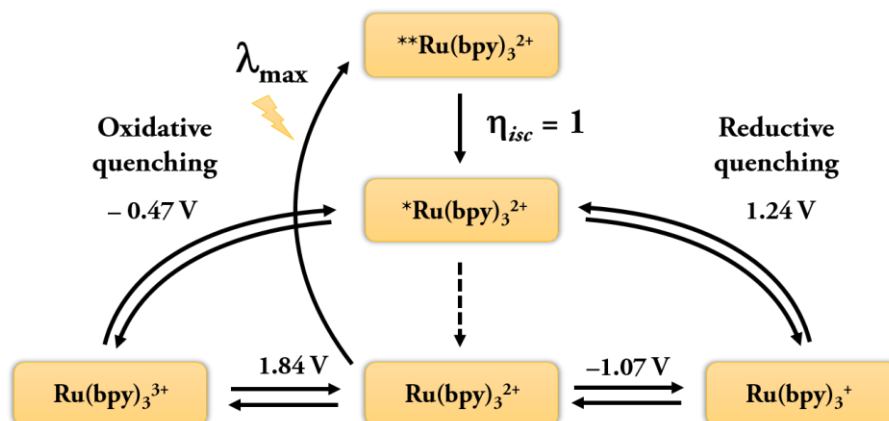


Figure 7.5: Schematic representation of Ru(bpy)₃(TB)₂ reductive and oxidative quenching. Reduction and oxidation potential was characterized using 25 μm diameter platinum microelectrode emerged in 5 mM Ru(bpy)₃(TB)₂ in DCE, with 10 mM BATB as supporting electrolyte. Absorption and fluorescence emission were recorded from a solution of 50 μM Ru(bpy)₃(TB)₂ in DCE.

7.4.1.2 Electrochemical characterisations

Cyclic voltammetry measurements provided information about the redox potential of the three components used. The formal redox potential of TEA was determined previously by J. Hidalgo to be $[E^{\circ}_{\text{TEA}^+/\text{TEA}}]_{\text{SHE}} = 1.11 \text{ V}$ in DCE. From the CVs presented in Figure 7.6 (B) of $\text{Fe}_2(\mu\text{-SCH}_2\text{C}_6\text{H}_4\text{CH}_2\text{S})(\text{CO})_6$, the latter's redox potential was determined at -0.88 V *vs.* SHE in DCE. The CV of $\text{Co}(\text{dmg})_2(\text{py})\text{Cl}$ was for the first time performed in DCE solvent (Figure 7.6 (A)). In acetonitrile, the complex shows one irreversible reduction assigned to a $\text{Co}^{(\text{III})}/\text{Co}^{(\text{II})}$ process at -0.43 V *vs* SHE, followed by a reversible reduction of $\text{Co}^{(\text{II})}$ to $\text{Co}^{(\text{I})}$ at -0.88 V .²⁵ In DMF, the complex exhibits similar redox waves with an anodic shift.²⁵ However, in DCE, a first reversible wave is observed at -0.03 V and two irreversible wave appeared at -0.40 and -1.00 V . Perhaps the first wave can be attributed to impurities in the commercial product. The two other peaks were assigned to $\text{Co}^{(\text{III})}/\text{Co}^{(\text{II})}$ and $\text{Co}^{(\text{II})}/\text{Co}^{(\text{I})}$ respectively. Further experiments would be required to entirely clarify the CV obtained.

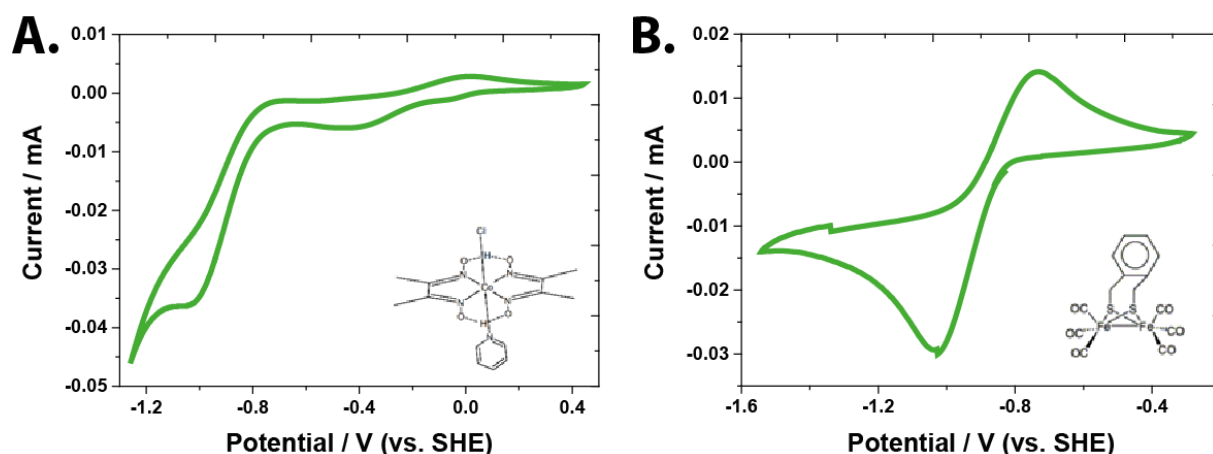


Figure 7.6. Cyclic voltammograms of catalysts in DCE on 2 mm diameter glassy carbon electrode under anaerobic conditions. (A) CV of 2.5 mM Co(dmgl)₂(py)Cl in DCE, with 10 mM tetrabutylammonium hexafluorophosphate as supporting electrolyte. (B) CV of 2.5 mM Fe₂(μ-SCH₂C₆H₄CH₂S)(CO)₆ in DCE, with 10 mM tetrabutylammonium hexafluorophosphate as supporting electrolyte.

These results suggest the reaction takes place *via* a reductive electron transfer pathway. A Jablonski diagram illustrates the different electronic processes occurring during the reaction in Figure 7.7. The process starts with the absorption of a photon. The later induces the excitation of Ru(bpy)₃²⁺ to Ru(bpy)₃^{2+,*}. Subsequently, the ground state is quenched by TEA and Ru(bpy)₃^{2+,*} gives its electron to the catalyst.

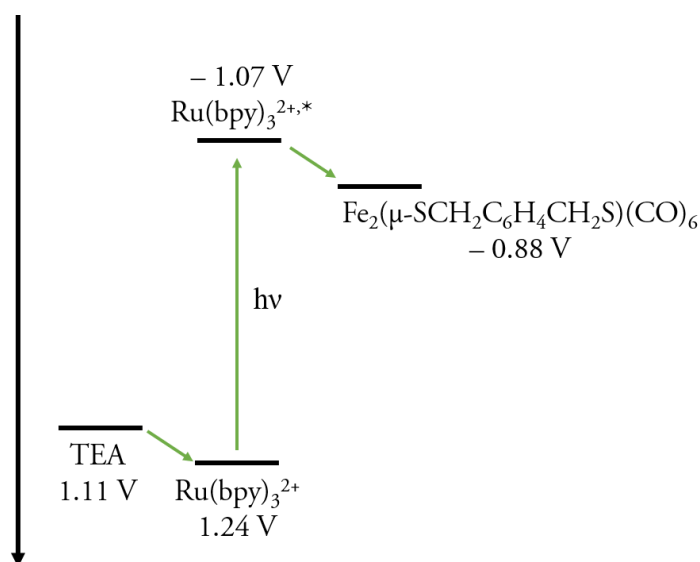


Figure 7.7: Schematic representation of electronic transfers.

7.5 Shake-flask experiments

7.5.1 Reaction and analysis

The reactivities of $\text{Fe}_2(\mu\text{-SCH}_2\text{C}_6\text{H}_4\text{CH}_2\text{S})(\text{CO})_6$ and $\text{Co}(\text{dmgh})_2(\text{py})\text{Cl}$ were studied by biphasic reactions with mechanical stirring under anaerobic conditions as previously optimized.⁶ Briefly, the flask was filled first with 2 mL of DCE solution containing 1 mM $\text{Ru}(\text{bpy})_3\text{TB}_2$ as photosensitizer and 0.05 μmol of $\text{Fe}_2(\mu\text{-SCH}_2\text{C}_6\text{H}_4\text{CH}_2\text{S})(\text{CO})_6$ or $\text{Co}(\text{dmgh})_2(\text{py})\text{Cl}$, followed by the addition of an aqueous solution containing 100 mM HCl, 5 mM $[\text{Li}(\text{OEt})_2]\text{TB}$ and 0.1 M TEA as electron donor. After stirring the two phases together for 2 hours in the dark, the headspace gas phase was analysed by gas chromatography. As presented in Figure 7.8 without light, no production of hydrogen was observed; however, under 455 nm irradiation, a H_2 peak appeared in the gas chromatogram at a retention time of *ca.* one minute confirming the necessity of illumination. As described in Table 7.1, $\text{Fe}_2(\mu\text{-SCH}_2\text{C}_6\text{H}_4\text{CH}_2\text{S})(\text{CO})_6$ and $\text{Co}(\text{dmgh})_2(\text{py})\text{Cl}$ produced 10.8 and 19.6 μmol of hydrogen, respectively, under these conditions.

For comparison, as revealed by Ge's previous study⁶ (Figure 7.2), the experiment performed without catalyst under illumination evolved only 0.4 μmol of H_2 , demonstrating the good efficiency of these two molecular catalysts. The reaction is accelerated 20 times with MoS_2/C , 30 times with $\text{Co}(\text{dmgh})_2(\text{py})\text{Cl}$ and 50 times with $\text{Fe}_2(\mu\text{-SCH}_2\text{C}_6\text{H}_4\text{CH}_2\text{S})(\text{CO})_6$.

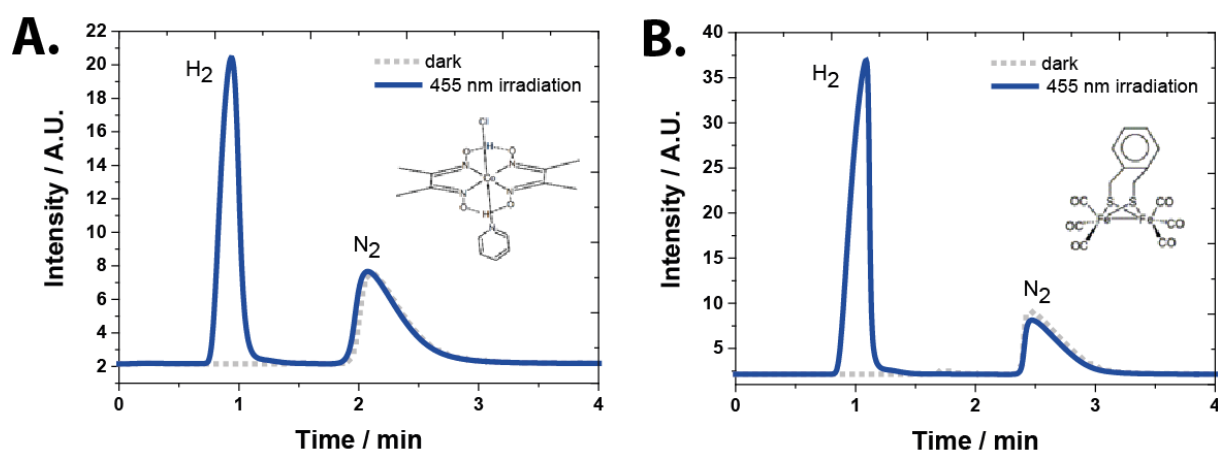


Figure 7.8: Gas chromatograms of the shake-flask headspace for two-phase reactions after 2 h, under anaerobic conditions: a. $\text{Co}(\text{dmgh})_2(\text{py})\text{Cl}$ as catalyst and b. $\text{Fe}_2(\mu\text{-SCH}_2\text{C}_6\text{H}_4\text{CH}_2\text{S})(\text{CO})_6$ as catalyst.

7.5.2 Comparison between the catalyst efficiencies at soft interfaces

The efficiency of the different catalysts to produce H_2 at soft interfaces were compared as shown in Figure 7.9 and Table 7.1. It appears that the heterogeneous catalysis with MoS_2/C particles is less efficient than homogeneous catalysis with molecular catalysts. Indeed, from a kinetic point of view, the probability for reagents meeting during homogeneous catalysis is higher. $\text{Co}(\text{dmgh})_2(\text{py})\text{Cl}$ is less soluble in DCE than $\text{Fe}_2(\mu\text{-SCH}_2\text{C}_6\text{H}_4\text{CH}_2\text{S})(\text{CO})_6$, thus making the reaction easier with the di-iron complex. This could explain the better performance of the di-iron complex. Moreover, the cobaloxime may be deactivated because of the presence of TEA. Indeed, cobalt metal has a high affinity for amines and the glyoxime ligands may be replaced by TEA, thus decomposing the catalyst. Furthermore, $\text{Fe}_2(\mu\text{-SCH}_2\text{C}_6\text{H}_4\text{CH}_2\text{S})(\text{CO})_6$ was synthesized by the group of “Chimie et Electrochimie de systèmes métal-soufre modèles” at Brest (France), and its ligands are specifically optimized to performed hydrogen evolution; they are rigid and unsaturated to stabilize the low oxidation states of metal ions¹³ contrary to cobaloxime which is a basic commercial chemical.

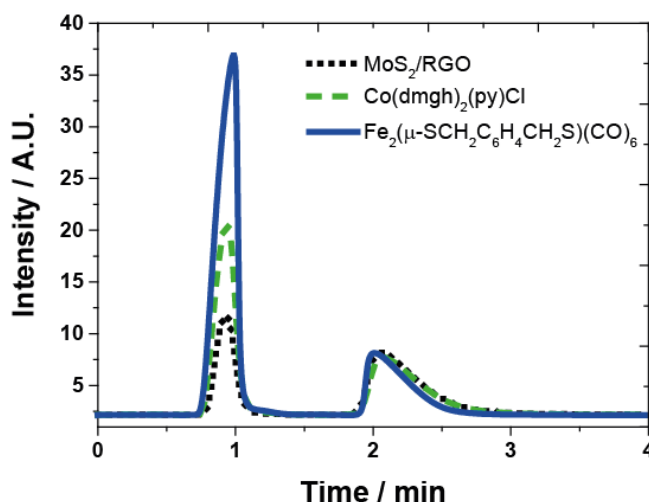


Figure 7.9 Comparison of gas chromatograms of the shake-flask headspace for two-phase reactions after 2 hours, under anaerobic conditions for different catalysts

Table 7.1: Comparison of H_2 production of the reaction after 2 h under anaerobic conditions for different catalysts

Catalysts	H_2 / μmol
MoS_2/C	7.6
$\text{Co}(\text{dmgh})_2(\text{py})\text{Cl}$	10.8
$\text{Fe}_2(\mu\text{-SCH}_2\text{C}_6\text{H}_4\text{CH}_2\text{S})(\text{CO})_6$	19.6

7.5.3 Clarification of the proton source

For this experiment, $[\text{Li}(\text{OEt}_2)_2]\text{TB}$ was added to the aqueous phase. It has been demonstrated in previous studies that the distribution of the common ion TB^- fixes a Galvani potential difference across the interface at a value of approximately 0.55 V. With such a chemically controlled polarization of the interface, the protons are driven from water to DCE. Additionally, TEA is a well-known electron donor but can also facilitate proton transfer across the ITIES as, at the pH values employed, it becomes protonated by HCl. Thus, there are two possible proton sources or interfacial proton carriers. This was confirmed by the amount of H_2 produced, which were higher than the quantity of protons which could be transferred. The quantity of protons present in the DCE phase due to the polarisation was not large enough to justify the yield obtained. Therefore, TEA plays an important role in this reaction. Additionally, the Galvani ion transfer potential of protonated TEA was measured (see paragraph 4.4.2.2.) and found to be 0.217 V. Consequently, the polarisation is enough to transfer protonated TEA in DCE. Thereafter, the later supplies protons for the HER.

Nevertheless, the presence of $[\text{Li}(\text{OEt}_2)_2]\text{TB}$ is required to keep $\text{Ru}(\text{bpy})_3\text{TB}_2$ in the organic phase. Indeed, without $[\text{Li}(\text{OEt}_2)_2]\text{TB}$, after 2 hours of reaction an orange coloration of the aqueous phase and a decrease of hydrogen yield were observed. This orange coloration may be due to the transfer of $\text{Ru}(\text{bpy})_3^{2+}$, into the aqueous phase, forming soluble orange coloured $\text{Ru}(\text{bpy})_3\text{Cl}_2$. Thus, the sensitizer was separated from its electron donor and its catalyst, which hindered electron transfer with the w|DCE interface acting as a barrier. The addition of $[\text{Li}(\text{OEt}_2)_2]\text{TB}$ polarises the interface sufficiently to retained the sensitizer in the organic phase producing high hydrogen yields.

7.6 Conclusions

The possibility to adapt a classical three-component system using homogeneous catalysts at polarised soft interface was investigated and their activity were compared to MoS_2/C heterogeneous catalysts. Thus, the behaviour of two molecular catalysts, $\text{Co}(\text{dmgh})_2(\text{py})\text{Cl}$ and $\text{Fe}_2(\mu\text{-SCH}_2\text{C}_6\text{H}_4\text{CH}_2\text{S})(\text{CO})_6$, towards the polarisation was studied at w|DCE interface. Cyclic voltammetry measurements confirmed there was no formation of a hydride with $\text{Co}(\text{dmgh})_2(\text{py})\text{Cl}$ and $\text{Fe}_2(\mu\text{-SCH}_2\text{C}_6\text{H}_4\text{CH}_2\text{S})(\text{CO})_6$ before their reduction. Results confirmed that the positive

polarisation is applied to perform HER and transfer protons across the w|DCE interface does not obstructed the interpretation of the obtained results.

The role of every components was investigated. Thus, the electrochemical measurements and the spectroscopic studies of $\text{Ru}(\text{bpy})_3\text{TB}_2$ provided a better understanding of the mechanisms occurring in the reaction.

$\text{Co}(\text{dmgh})_2(\text{py})\text{Cl}$ and $\text{Fe}_2(\mu\text{-SCH}_2\text{C}_6\text{H}_4\text{CH}_2\text{S})(\text{CO})_6$ were introduced to the ITIES platform their performances were investigated and compared with results obtained for MoS_2/C heterogeneous catalyst. The results showed that all the catalysts were able to produce H_2 at liquid|liquid interface under the chemical polarisation. A better efficiency was observed for the hydrogenase mimic complex. However, we believe that the polarisation induced by $[\text{Li}(\text{OEt})_2]\text{TB}$ species is not responsible for the proton transfer and TEA is certainly the dominant proton source. $[\text{Li}(\text{OEt})_2]\text{TB}$ chemical polarisation only participate to prevent $\text{Ru}(\text{bpy})_3^{2+}$ for escaping to the aqueous phase.

These investigations provide the foundation of the utilisation of 3-component at polarised liquid|liquid interface. Nevertheless, further investigations are required to obtain a sustainable system. To investigate the polarisation effects an electron donor that cannot be protonated would be preferred. It is possible to introduce semiconductors such as TiO_2 instead of $\text{Ru}(\text{bpy})_3\text{TB}_2$. and catalysts can also be optimised. Comparative kinetics studies and yield with one-phase system would also be required if this kind of systems are developed.

7.7 References

- (1) Nieminen, J. J.; Hatay, I.; Ge, P.; Mendez, M. A.; Murtomaki, L.; Girault, H. H. *Chemical Communications* **2011**, 47, 5548.
- (2) Hatay, I.; Ge, P. Y.; Vrubel, H.; Hu, X.; Girault, H. H. *Energy & Environmental Science* **2011**, 4, 4246.
- (3) Ge, P.; Scanlon, M. D.; Peljo, P.; Bian, X.; Vubrel, H.; O'Neill, A.; Coleman, J. N.; Cantoni, M.; Hu, X.; Kontturi, K.; Liu, B.; Girault, H. H. *Chemical Communications* **2012**, 48, 6484.
- (4) Bian, X.; Scanlon, M. D.; Wang, S.; Liao, L.; Tang, Y.; Liu, B.; Girault, H. H. *Chemical Science* **2013**, 4, 3432.
- (5) Scanlon, M. D.; Bian, X.; Vrubel, H.; Amstutz, V.; Schenk, K.; Hu, X.; Liu, B.; Girault, H. H. *Physical Chemistry Chemical Physics* **2013**, 15, 2847.
- (6) Ge, P. Y.; Girault, H. H. *Hydrogen Evolution in Biphasic Systems, Chapter 6* **2013**.
- (7) Dau, H.; Limberg, C.; Reier, T.; Risch, M.; Roggan, S.; Strasser, P. *ChemCatChem* **2010**, 2, 724.
- (8) Jessop, P. G.; Ikariya, T.; Noyori, R. *Chemical Reviews* **1995**, 95, 259.
- (9) Ameta, R.; Benjamin, S.; Ameta, A.; Ameta, S. C. In *Materials Science Forum*; Trans Tech Publ: **2013**; Vol. 734, p 247.
- (10) Narayanam, J. M. R.; Tucker, J. W.; Stephenson, C. R. J. *Journal of the American Chemical Society* **2009**, 131, 8756.
- (11) Savéant, J.-M. *Elements of molecular and biomolecular electrochemistry: an electrochemical approach to electron transfer chemistry*; John Wiley & Sons, **2006**; Vol. 13.
- (12) Gloaguen, F.; Rauchfuss, T. B. *Chemical Society Reviews* **2009**, 38, 100.
- (13) Quentel, F.; Passard, G.; Gloaguen, F. *Chemistry—A European Journal* **2012**, 18, 13473.
- (14) Chao, T.-H.; Espenson, J. H. *Journal of the American Chemical Society* **1978**, 100, 129.
- (15) Probst, B.; Kolano, C.; Hamm, P.; Alberto, R. *Inorganic Chemistry* **2009**, 48, 1836.
- (16) Dempsey, J. L.; Brunschwig, B. S.; Winkler, J. R.; Gray, H. B. *Accounts of Chemical Research* **2009**, 42, 1995.
- (17) Razavet, M.; Artero, V.; Fontecave, M. *Inorganic chemistry* **2005**, 44, 4786.
- (18) Hu, X.; Cossairt, B. M.; Brunschwig, B. S.; Lewis, N. S.; Peters, J. C. *Chemical communications* **2005**, 4723.
- (19) Du, P.; Knowles, K.; Eisenberg, R. *Journal of the American Chemical Society* **2008**, 130, 12576.

- (20) Bhugun, I.; Lexa, D.; Savéant, J.-M. *Journal of the American Chemical Society* **1996**, *118*, 3982.
- (21) Capon, J.-F.; Ezzaher, S.; Gloaguen, F.; Pétillon, F. Y.; Schollhammer, P.; Talarmin, J. *Chemistry – A European Journal* **2008**, *14*, 1954.
- (22) Wang, W.; Rauchfuss, T. B.; Bertini, L.; Zampella, G. *Journal of the American Chemical Society* **2012**, *134*, 4525.
- (23) Narayanam, J. M.; Stephenson, C. R. *Chemical Society Reviews* **2011**, *40*, 102.
- (24) Balzani, V.; Juris, A. *Coordination Chemistry Reviews* **2001**, *211*, 97.
- (25) Du, P.; Schneider, J.; Luo, G.; Brennessel, W. W.; Eisenberg, R. *Inorganic Chemistry* **2009**, *48*, 4952.

8. Conclusions and perspectives

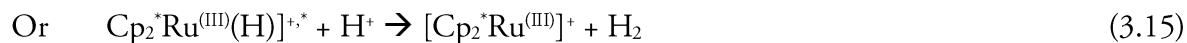
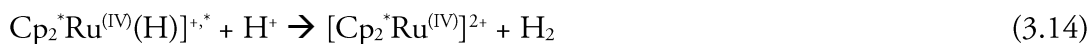
The increasing energy consumption all around the globe has prompted the scientific community to develop alternative ways to supply the energy demand. The strategies to exploit renewable energy (solar and wind in particular) face the problem of the intermittent nature of the energy production *via* these routes. In this context, the storage of energy through the formation of H₂ was proposed as a solution. Indeed, H₂ has the advantage that it may be readily obtained in large amounts by “splitting” water. Current approaches focus on the (photo)electrocatalytic production of H₂ at the surface of solid electrodes immersed in acidified aqueous or organic solutions utilizing highly engineered catalyst and photosensitizer combinations.^{1,2}

Our group has recently developed an alternative strategy to photo-produce H₂ at electrified liquidliquid interfaces with the use of a single molecule to achieve both proton reduction and photo-activation.³ Based on this method, the concept of batch water-splitting to produce H₂ and O₂ *via* a biomimetic approach at liquidliquid interfaces has been introduced. Basically, the set-up consists of two interfaces, one for photo-HER and another for photo-OER. The main objective of this work was to develop a simple and sustainable system that can be adapted to batch water-splitting. Therefore, we suggested the use of Cp₂*Ru^(II) as a simple molecule to performed the complex photo-HER at polarised liquidliquid interfaces. Indeed, from previous studies about the H₂ production by metallocenes, Cp₂*Ru^(II) appeared promising as it has an intermediate redox potential suitable to facilitate the efficient photo-production of H₂ as well as promote the rest of the photo-system through photo-OER.

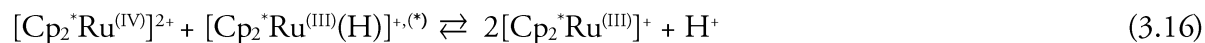
The reaction was studied and characterized in one phase by electrochemical, gas chromatographic and spectroscopic (UV/vis, ¹H and ¹³C NMR) experimental approaches, with corroboration by DFT. The first achievement was the investigation of every intermediate of the photo-reaction that leads to the resolution of the mechanism. Thus, the reaction shows the spontaneous formation of [Cp₂*Ru^(IV)(H)]⁺ in the dark as soon as Cp₂*Ru^(II) was placed in acidified media *via* the eq. (3.1):



The influence of the acid was investigated but unfortunately multiple interactions such as ion pairing or homo-association between the components during $[\text{Cp}_2^*\text{Ru}^{(\text{IV})}(\text{H})]^+$ formation was evidenced and prevented the reliable determination of $[\text{Cp}_2^*\text{Ru}^{(\text{IV})}(\text{H})]^+$. Thereafter, $[\text{Cp}_2^*\text{Ru}^{(\text{IV})}(\text{H})]^+$ releases H_2 under illumination forming a $[\text{Cp}_2^*\text{Ru}^{(\text{III})}]^+$ species. For the first time, it has been possible to study this key intermediate and, in particular, to follow its appearance by UV/vis spectroscopy thanks to its characteristic absorbance at $\lambda_{\text{max}} = 500 \text{ nm}$. The result provided clarification of the mechanism. A homolytic reaction (*i.e.* two $[\text{Cp}_2^*\text{Ru}^{(\text{IV})}(\text{H})]^+$ that react to release H_2) was excluded because the reaction was found to be first order with respect to $[\text{Cp}_2^*\text{Ru}^{(\text{IV})}(\text{H})]^+$. However, it was proposed that a proton could directly react with $[\text{Cp}_2^*\text{Ru}^{(\text{IV})}(\text{H})]^+$ or $[\text{Cp}_2^*\text{Ru}^{(\text{III})}(\text{H})]^+$:



Then, two possibilities exist that may explain the reduction of $[\text{Cp}_2^*\text{Ru}^{(\text{IV})}]^{2+}$ to the $[\text{Cp}_2^*\text{Ru}^{(\text{III})}]^+$ species observed by UV/vis. One possibility involves $[\text{Cp}_2^*\text{Ru}^{(\text{IV})}]^{2+}$ reacting with $[\text{Cp}_2^*\text{Ru}^{(\text{IV})}(\text{H})]^+$ or a photo-activated $[\text{Cp}_2^*\text{Ru}^{(\text{IV})}(\text{H})]^+$ to comproportionate into two equivalents of $[\text{Cp}_2^*\text{Ru}^{(\text{III})}]^+$ (eq. (3.16))



Alternatively, $[\text{Cp}_2^*\text{Ru}^{(\text{IV})}]^{2+}$ can react with the original $\text{Cp}_2^*\text{Ru}^{(\text{II})}$ species, eq. (3.1), the concentration of which depends on the equilibrium of eq. (3.17):



Both pathways are hindered by the presence of protons, thus the distinction between mechanisms was not possible from the recorded data.

In the same way, $[\text{Cp}_2^*\text{Ru}^{(\text{III})}(\text{H})]^+$ can be produced from the reaction of $[\text{Cp}_2^*\text{Ru}^{(\text{IV})}(\text{H})]^+$ with the original $\text{Cp}_2^*\text{Ru}^{(\text{II})}$.

Finally, results have shown the formation of $[\text{Cp}^*\text{Ru}^{(\text{IV})}(\text{C}_5\text{Me}_4\text{CH}_2)]^+$ at the end of the reaction. The presence of this irreversible product was not expected and must be avoided.

Consequently, the stabilization and the regeneration of $[\text{Cp}_2^*\text{Ru}^{(\text{III})}]^+$ to $\text{Cp}_2^*\text{Ru}^{(\text{II})}$ was a key challenge to obtain a sustainable way to produce H_2 from $\text{Cp}_2^*\text{Ru}^{(\text{II})}$.

The stabilization of $[\text{Cp}_2^*\text{Ru}^{(\text{III})}]^+$ was achieved with the use of a weakly coordinating solvent (DCE) and counter ion (TB^-). In a first stage, attempts to reduce $[\text{Cp}_2^*\text{Ru}^{(\text{III})}]^+$ and recover the initial $\text{Cp}_2^*\text{Ru}^{(\text{II})}$ were performed using TEA and TCNQ^- as sacrificial and non-sacrificial electron donor, respectively. TEA was not a strong enough reductant to reduce $[\text{Cp}_2^*\text{Ru}^{(\text{III})}]^+$. However, a positive result was obtained with TCNQ^- . Alan M. Bond *et al.*⁴ have shown the photo-oxidation of water to oxygen using TCNQ as a sacrificial electron acceptor. Consequently, coupling TCNQ with $\text{Cp}_2^*\text{Ru}^{(\text{II})}$ seems to be a promising way to achieve water-splitting. In a second stage, photo-production of H_2 by $\text{Cp}_2^*\text{Ru}^{(\text{II})}$ was combined with an electrochemical regeneration. Importantly, the regeneration of the photoproduct occurred at 200 mV higher potential than the direct reduction of protons on Pt. This represents a step forward for the water-splitting because $\text{Cp}_2^*\text{Ru}^{(\text{II})}$ can be recovered at a potential closer to OER in comparison with classical non-photo-activated catalysts. Additionally, a promising internal quantum yield of 25 % was observed.

In a second stage of the study, the implementation of $\text{Cp}_2^*\text{Ru}^{(\text{II})}$ at polarized liquid|liquid interfaces was achieved based on mechanistic results obtained. For the first time, H_2 was evolved by $\text{Cp}_2^*\text{Ru}^{(\text{II})}$ in a biphasic system. A similar mechanism was observed in one or two phases. Furthermore, ITIES was used as a platform to understand the heterogeneous formation of $[\text{Cp}_2^*\text{Ru}^{(\text{IV})}(\text{H})]^+$ at the interface. Indeed, protonation of the metal to form a hydride species is a key step in the formation of H_2 as the basicity of the metal has to be sufficient to guarantee the coordination of a proton on the metal centre but at the same time, the formed bond should not be too strong as to hamper the elimination of H_2 . Electrochemical measurements provided information about the effect of the hydride formation and dissociation confirming a high rate of complexation ($\approx 10^5 \text{ M}^{-1}\cdot\text{s}^{-1}$). A spontaneous decomplexation of the hydride in the aqueous phase was confirmed by fitting experimental and simulated data. Additionally, the hydride formation was investigated by spectroscopic methods in one phase by UV/vis as well as at the interface by SHG. The absorbance of $[\text{Cp}_2^*\text{Ru}^{(\text{IV})}(\text{H})]^+$ was characterized at 243 nm. This information was used to understand the role of the light excitation. Corroborated by DFT computations, the data seem consistent with an excitation of the hydride species. Therefore, the electronic density moves from

the ligands to the M-H bond. The M-H is weakened and the oxidation of $[\text{Cp}_2^*\text{Ru}^{\text{IV}}(\text{H})]^+$ and H_2 released is favoured. Secondly, the characterization of the number of photons involved in the photo-process provides further details about the photo-mechanism excluding two-photon excitation processes involved in the H_2 elimination path described in the eq. (3.14).

Finally, an alternative strategy to photo-produce H_2 at a polarised liquid|liquid interface based on three components (*i.e.* a photosensitizer, an irreversible electron donor and a catalyst) was presented. The main goal of this study was to evaluate the applicability of these systems and propose a way to investigate them. Different homogeneous and heterogeneous catalysts were compared and investigated for the first time at ITIES. This study provides to an all-purpose interface, adaptable to various components and reactions.

To conclude, $\text{Cp}_2^*\text{Ru}^{\text{II}}$ seems to be a non-sacrificial electron donor full of promise to perform photo-HER in the batch water-splitting. Results and investigations provided information to fully understand the process occurring in the reaction in the bulk or at the interface. Furthermore, a primary aim of this study was to evaluate the suitability of decamethylruthenocene as the metallocene of choice for applications in “batch-water splitting”. This demonstrates a possible “real world” application of such a system while also enhancing our understanding of the chemistry of metallocenes (in particular under illuminated conditions) and the hydrogen evolution reaction.

The next stages of the project are to perform photo-OER at polarized liquid|liquid interfaces and to associate together the photo-OER and photo-HER with $\text{Cp}_2^*\text{Ru}^{\text{II}}$. In this way, the details collected regarding the photoproduction of H_2 by $\text{Cp}_2^*\text{Ru}^{\text{II}}$ and in particular the generation, stabilization and reduction of the $[\text{Cp}_2^*\text{Ru}^{\text{III}}]^+$ intermediate, would provide crucial information to make the reactions work in tandem.

Regarding the oxygen evolution reaction, our group has published a first study about water oxidation in a biphasic water|acetonitrile mixtures.⁵ The reaction was catalysed by iridium oxide nanoparticles using $[\text{Ru}^{\text{III}}(\text{bpy})_3]^{3+}$. Recently, Wittstock *et al*⁶ used bismuth vanadate (BiVO_4) to carry the oxidation of water at a polarized liquid|liquid interface. Indeed, they demonstrated that hyperbranched nanostructured BiVO_4 , in the presence of $[\text{Co}(\text{bpy})_3](\text{PF}_6)_3$ as an organic soluble electron acceptor, and can achieve OER under visible light illumination. BiVO_4 is one of the most interesting visible-light-driven photocatalysts for water oxidation but it suffers from poor charge

transport properties, which cause high electron hole recombination. Furthermore, the hole transfer kinetics for OER are sluggish. However, the nanoscale branches and the polarization facilitate the electron transfers to the acceptor and, therefore, hinder the charge recombination. Consequently, we suggest to replace $[\text{Co}(\text{bpy})_3](\text{PF}_6)_3$ by $[\text{Cp}_2^*\text{Ru}^{(\text{III})}]^+$, which appears feasible from a thermodynamic point of view. The electron transfer across the interface as well as the behavior of the light activated BiVO_4 at the interface will have to be investigated by cyclic voltammetry and SHG measurements. The organic solvent is accepted to be a major limitation. Indeed, traditional DCE employed at ITIES is generally oxidized by OER reagents. Therefore, other solvents suitable for ITIES, such as valeronitrile, caprylonitrile, 2-octanone, 2-decadone, 3-nonanone and 5-nonanone⁷ have to be employed. In Wittstock *et al.*⁶ article, butyronitrile was used to catalyze water oxidation. Therefore, biphasic photo-HER by $\text{Cp}_2^*\text{Ru}^{(\text{II})}$ can be adapted to this new interface. Additionally, these solvents have a density lower than water and SHG investigation could be facilitated and could provide good conditions for complete SHG investigations.

To conclude, we believe that the batch water-splitting will enable the development of efficient systems based on a biomimetic approach. In the meanwhile, the development of this system provides important fundamental knowledge to understand the chemistry of photo-HER and photo-OER. It also enhances our understanding on process at ITIES and could be beneficial in the development and understanding of biomimetics processes.

8.1 References

- (1) Esswein, A. J.; Nocera, D. G. *Chemical Reviews* **2007**, *107*, 4022.
- (2) Dempsey, J. L.; Brunschwig, B. S.; Winkler, J. R.; Gray, H. B. *Accounts of Chemical Research* **2009**, *42*, 1995.
- (3) Rivier, L.; Peljo, P.; Vannay, L.; Grégoire, G.; Mendez, M.; Corminboeuf, C.; Scanlon, M. D.; Girault, H. *Angewandte Chemie International Edition* **2017**, *56*, 2324.
- (4) Zhao, C.; Bond, A. M. *Journal of the American Chemical Society* **2009**, *131*, 4279.
- (5) Hidalgo-Acosta, J. C.; Scanlon, M. D.; Méndez, M. A.; Peljo, P.; Opallo, M.; Girault, H. H. *ChemElectroChem* **2016**, *3*, 2003.
- (6) Rastgar, S.; Pilarski, M.; Wittstock, G. *Chem. Commun.* **2016**, *52*, 11382.
- (7) Toth, P. S.; Dryfe, R. A. W. *Analyst* **2015**, *140*, 1947.

Lucie Rivier

lucie.rivier@gmail.com / [LinkedIn](#)

French nationality

27 years old



EDUCATION

- PhD Student** **Ecole Polytechnique Fédérale de Lausanne (EPFL), Lausanne Switzerland**
(2012 – 2017) **Laboratory of Physical and Analytical Electrochemistry (LEPA)**
- MSc Chemist** **Université Paris Diderot, Paris, France**
(2010 – 2012) Academical degree specialised in physical chemistry
- BSc Chemist:** **Université du Maine, Institute of Technology, Le Mans, France**
(2009 - 2010) Professional degree specialised in organic chemistry
- Chem Tech** **Paul Sabatier Institute of Technology, Castres, France**
(2007 – 2009) Professional degree specialised in chemistry

RESEARCH EXPERIENCE

- 2012 – 2017** **Ecole Polytechnique Fédérale de Lausanne (EPFL), Lausanne Switzerland**
Laboratory of Physical and Analytical Electrochemistry (LEPA)
PhD research, development of photo-activated hydrogen evolution reaction at the liquid|liquid interfaces.
- 2012** **Industrial Physics and Chemistry Higher Educational Institution (ESPCI ParisTech), Paris, France**
Laboratory of Analytical, Bioanalytical Sciences and Miniaturization
6 month internship, development of new immunoassays on microchips with a label-free optical detection.
- 2011** **Guangdong University of Technology, Guangzhou, China**
Prof. Cheng's group
4 month internship, study of polymerisation and post-functionalisation of dopamine on carbon nanotubes to develop a new hybrid biomaterial for bones substitution.
- 2010** **French Alternative Energies and Atomic Energy Commission (CEA), Saclay, France**
Laboratory for Molecular Electronics (LEM)
4 month internship, synthesis of porphyrin and phthalocyanin dendrimers and functionalization of carbon nanotubes by “click-chemistry” and diazonium salts.

2009 **Université de Montréal, Canada**
Prof. Skene's Group

3 month internship, synthesis and study of new functional polymers for their photophysical and electrochemical properties.

AWARDS AND ACHIEVEMENTS

- 2014** 1st Poster Prize winner for the poster "Elucidation of Multi-Step Photoproduction of Hydrogen by Decamethylruthenocene at Liquid|Liquid Interfaces", *LightChEC Summer School*, Switzerland.
- 2014** Doctoral Teaching Assistant Prize from the Section of Chemistry and Chemical Engineering, EPFL

PUBLICATIONS

- [1] P. Peljo, M.D. Scanlon, A. Olaya, L. Rivier, E. Smirnov, H. H. Girault, Redox Electrocatalysis of Floating Nanoparticles: Determining Electrocatalytic Properties Without the Influence of Solid Supports, submitted.
- [2] M.D. Scanlon, P. Peljo, L. Rivier, H.H. Girault, Water splitting by Electrolysis Utilizing Polarized Liquid-Liquid Interfaces, submitted.
- [3] L. Rivier, L. A.C. Vannay, M.A. Méndez, P. Peljo, H. Vrubel, C. Corminboeuf, M.D. Scanlon, H.H. Girault, Photo-generation of Hydrogen by Decamethylruthenocene: a non-sacrificial electron donor and sensitizer, submitted.
- [4] L. Rivier, P. Peljo, L.A.C. Vannay, G.C. Gschwend, M.A. Méndez, , C. Corminboeuf, M.D. Scanlon, H.H. Girault, Photoproduction of Hydrogen by Decamethylruthenocene Combined with Electrochemical Recycling, *Angew. Chem. Int. Ed.*, **2017**, 56 (9), 2324.
- [5] L. Rivier, J. Stockmann, M.A. Méndes, M.D. Scanlon, P. Peljo, M. Opallo, H.H. Girault, Decamethylruthenocene Hydride and Hydrogen Formation at Liquid|Liquid Interfaces, *J. Phys. Chem. C*, 2015, 119 (46), 25761-25769.
- [6] K.H. Le Ho, I. Hijazi, L. Rivier, C. Gautier, B. Jousselme, G. Miguel, C. Romero-Nieto, D.M. Guldi, B. Heinrich, B. Donnio, S. Campidelli, Host–Guest Complexation of [60] Fullerenes and Porphyrins Enabled by "Click Chemistry", *Chemistry - A European Journal*, **2013**, 34, 11374.
- [7] A. Bolduc, L. Rivier, S. Dufresne, W.G. Skene, Spectral investigation of conjugated azomethines: A large palette of colors possible with acid and oxidant doping, *Mater. Chem. Phys.*, **2012**, 132 (2-3), 722.
- [8] K.H. Le Ho, L. Rivier, B. Jousselme, P. Jégou, A. Filoramo, S. Campidelli, Zn-porphyrin/Zn-phthalocyanine dendron for SWNT functionalisation, *Chem. Commun.*, **2010**, 46, 8731.